Computer Modelling of Electromagnetics for Brine Layer Detection near Potash Mines

Todd LeBlanc

A Thesis Submitted to the
College of Graduate and Postdoctoral Studies

In the Department of the Geological Sciences
University of Saskatchewan

Supervisor

Samuel Butler

In partial fulfillment of the requirements for the degree of

Master of Science in Geology

© Copyright Todd LeBlanc, February, 2020. All rights reserved.

PERMISSION TO USE

In presenting this thesis/dissertation in partial fulfillment of the requirements for a Post-graduate degree from the University of Saskatchewan, I agree that the Libraries of this University may make it freely available for inspection. I further agree that permission for copying of this thesis/dissertation in any manner, in whole or in part, for scholarly purposes may be granted by the professor or professors who supervised my thesis/dissertation work or, in their absence, by the Head of the Department or the Dean of the College in which my thesis work was done. It is understood that any copying or publication or use of this thesis/dissertation or parts thereof for financial gain shall not be allowed without my written permission. It is also understood that due recognition shall be given to me and to the University of Saskatchewan in any scholarly use which may be made of any material in my thesis/dissertation.

DISCLAIMER

Reference in this thesis/dissertation to any specific commercial products, process, or service by trade name, trademark, manufacturer, or otherwise, does not constitute or imply its endorsement, recommendation, or favoring by the University of Saskatchewan. The views and opinions of the author expressed herein do not state or reflect those of the University of Saskatchewan, and shall not be used for advertising or product endorsement purposes.

Requests for permission to copy or to make other uses of materials in this thesis/dissertation in whole or part should be addressed to:

Head of the Department of Geological Sciences
University of Saskatchewan
Geology Building, 114 Science Place
Saskatoon, SK S7N 5E2 Canada

OR

Dean

College of Graduate and Postdoctoral Studies

University of Saskatchewan

116 Thorvaldson Building, 110 Science Place

Saskatoon, Saskatchewan S7N 5C9 Canada

Acknowledgements

First I would like to acknowledge and thank my supervisor, Dr. Sam Butler, for integrating me into his research group as a graduate student. I have learned much of a technical nature from him over the years; his approach to scientific inquiry and problem solving have positively and permanently changed the way I operate as a scientist today.

Next, I would like to acknowledge *Nutrien* - formerly *Potash Corporation of Saskatchewan Inc.* (*PotashCorp*) - for their support, including supplying EM data for analysis and providing research funding for this project. Specifically, I would like to thank Craig Funk, Director of *Nutrien*'s GeoServices and Land division, for his encouragement and for bringing me on for several of his team's projects over the years. Next I would like to thank Randy Brehm, my supervisor both when I was a student employee and later during my *Mitacs Accelerate* project with *PotashCorp*. It is only through his guidance, initiative, and patience that this project has even become a reality. I would also like to thank Tanner Soroka, James Isbister, and Matthew van den Berghe for their exceptional expertise and advice on all matters related to mining, geology, geophysics, and technical writing. It was a great pleasure working with you all.

I would like to thank the Geological Sciences department here at the University of Saskatchewan. The number of people that have contributed to my study and work here over the years in both my undergraduate and graduate studies are too many to count; however, I would like to thank the faculty, specifically, Dr. Jim Merriam, Dr. Bruce Englington, Dr. Kevin Ansdell, and Tim Prokopiuk, for their mentorship and support over the years. Lastly, I would like to thank my fellow students in the Butler Research Group for their insight and assistance -

especially, Zoë Vestrum and Leon Ang Li.

Finally, I would like to thank the *Mitacs* program for their funding of my internship with *PotashCorp*. Their efforts to create partnerships between industry and academia have and will continue to greatly benefit students like myself.

I dedicate this work to Amanda, my girlfriend; my brothers, Michael and Ryan; my parents, Raymond and Jeanette; and my grandparents, Irene and Origene; without their support and understanding I would not be the man I am today.

Abstract

Safe mine expansion has been a reoccurring issue for potash mines in Saskatchewan over the years. One of the key issues facing mining operations is the potential for water inflow; this concern is even more serious specifically for potash mines due to the solubility of halite and sylvite minerals of which potash mines are largely comprised. The source of water in-flows are porous sedimentary formations above the mine. In this project we are proposing, through computer modelling, the possibility of remotely detecting the presence of these zones of water bearing strata, specifically water bearing carbonates, specifically using geophysical electromagnetic methods.

Normally the sedimentary layers near potash mines in Saskatchewan are considered low-hazard for having porous water-bearing characteristics. However, under certain conditions there is the potential for unsaturated water to have been introduced both into the carbonates above the mine, and even into the salt of the prairie evaporate formation itself, enhancing and even creating porosity in the lithology. Areas of higher porosity have been identified in core samples and have been spatially tied to areas of absent overlying salt layers. Historically, several different geophysical techniques have been proposed to determine the presence of water-bearing anomalies near mine. The techniques that have been tested for this purpose include 3D resistivity, frequency-domain electromagnetics, and time-domain electromagnetics. In many cases these efforts have produced effective results.

This project sought to investigate the potential of using time-domain electromagnetics to determine the presence of water-bearing anomalies within the carbonates of the Dawson Bay Formation which lie above the Prairie Evaporite Formation.

This project consisted of two principal components. One is computer modelling of time-domain electromagnetics in a full-space or mine environment performed in *COMSOL Multiphysics*, the other, as part of a Mitacs Accelerate internship that the student author participated in concert with *Nutrien*, under the joint supervision of Dr. Samuel Butler of the University of Saskatchewan and Randy Brehm of *Nutrien*, is an in-mine time-domain electromagnetics survey conducted in an area of suspected Dawson Bay water-bearing anomalies. The survey found a decisive conductive zone in the vicinity of the suspected carbonate anomaly. Subsequent computer modelling, both forward and inverse, has been performed to attempt to constrain the location of this anomaly relative to the Prairie Evaporite salt.

Contents

List of Figures

List of Tables

Glossary of Symbols

Variable	Description	Units
ϕ	Azimuthal coordinate	—
r	Radial coordinate	—
z	Vertical coordinate	—
x	Horizontal coordinate orthogonal to y	—
y	Horizontal coordinate orthogonal to x	—
$\mathbf{H}$	Magnetic field	A m^{-1}
$\mathbf{J}$	Current density	A m^{-2}
$\mathbf{D}$	Electric displacement field	C m^{-2}
$\mathbf{E}$	Electric field density	V m^{-1}
$\mathbf{B}$	Magnetic flux density	T
i	Imaginary number	$\sqrt{-1}$
ω	Angular frequency	Hz
δ	Skin depth	m
ρ	Resistivity	Ω m
σ	Conductivity	S m^{-1}
μ	Magnetic permeability	H m^{-1}
μ_0	Magnetic permeability of free space	$4\pi 10^{-7}$ H m^{-1}
μ_r	Relative magnetic permeability	—
z_d	Diffusion distance	m
v_d	Diffusion velocity	m s^{-1}
t	Time	s
h	Thickness of electrically distinct layer	m
j	Index for layers in EM models	—
k	Index for time-gates in time-domain	—
l	Index for frequency domain segments	—

$\hat{i}$	Index for stations points along survey lines	—
F	General integral constant	—
λ	Hankel transform variable	m^{-1}
κ	Spatial frequency wave number	m^{-1}
J_α	Bessel function of the first kind and α number	—
A^+ or A^-	Downward and upward looking admittance coefficients	A m^3
Y	Input admittance	m^{-1}
Γ	Reflection coefficients	—
γ		m^{-1}
a	Time-domain transformation coefficients	—
$\mathbf{A}$	Magnetic vector potential	V s m^{-1}
$\tilde{r}$	Distance	m
m	Magnetic dipole moment	A m^2
k	Wave number	m^{-1}
θ	Time-domain wave number	m^{-1}
I	Current	A
I_t	Current multiplied by number of turns in wire	A
Ψ	Time derivative of the magnetic field ($\frac{\mathrm{d}H}{\mathrm{d}t}$)	A m^{-1} s^{-1}
S	EM model sensitivity	S m^{-1}
$\bar{X}$	Sample mean	—
s	Sample standard deviation	—

Chapter 1

Introduction

1.1 Motivations

The principal motivations behind this project are to enhance the contribution of geophysics in geotechnical fields related to potash mining and to develop an understanding of electromagnetics in full-space environments. Potash mining has made extensive use of geophysics over the course of many decades. Geophysical techniques that have already been used range from seismic to ground penetrating radar to various galvanic and inductive electrical methods (Gendzwill, 1978; Gendzwill and Pandit, 1980; Krivochieva and Chouteau, 2002; Eso and Oldenburg, 2006). Their applications include clay seam detection, mapping mounds in the Winnipegosis, and investigating the thicknesses and properties of near-mine geological formations. There also exists substantial geophysics performed on the surface near mine tailings and over solution mine piping (see Siemon et al., 2010; Campbell and Fitterman, 2000; Smith et al., 2000). This is mostly done as an environmental monitoring check on contaminant leaking.

Electromagnetics as a geophysical technique has been well-understood and modelled when on the surface of the Earth. This operation has the benefit of only producing signal responses from the ground below. This has a variety of benefits when it comes to modelling and predicting responses. Of course, as it is an inductive technique, when surveying underground in a mine there exists inhomogeneity in the lithology both above and below the transmitter. This causes response signals to behave in a more complex way than surveys on the surface.

In addition, in-mine surveys also suffer from low transmitter power that surface surveys usually do not. The geometry of the mine panels offer a severe spatial restriction on the size and shape of the transmitting loop, while powerful diesel generators, common on the surface, are not used underground because of air quality concerns - forcing survey operators to use lower voltage current sources. Both of these restrictions limit the signal-to-noise of in-mine surveys. As such, it is important to fully model the near-mine electromagnetic parameters to get an understanding of the expected signal response change when varying these relevant parameters.

1.2 Context of the Study

Brine in-flows into potash mines have been a recurring issue for mine planners and operations over the years in Saskatchewan. These situations can result in mine temporary or partial closure, conversion to a solution-based mine, and countless lost dollars and man-hours. These in-flows are thought to have their origin in the carbonates above the mine.

The genesis of these phenomena are complex and discussed in greater detail elsewhere in this report, but loosely put there are three broad cases that these geologically anomalous areas fall into. The first of which is when brine is located in large collapse structures above the mine. These collapse structures are often large enough to be seen in 3D surface seismic and are geospatially tied to the edges of mounds in the Winnipegosis formation below the mine (Gendzwill, 1978). These mounds in turn can also be detected confidently from in-seam (in-mine) seismic. The combination of the strong geospatial link with the geophysical coverage means detecting and avoiding these troublesome areas is both well-understood and is a common procedure.

Another instance of mine in-flow comes from saturated brine located in voids in the salt above the mine. These voids have been detected using a large host of geophysical tools, from 3D resistivity to frequency and time-domain electromagnetics. For an example of one such study, see Eso and Oldenburg (2006). The high physical contrast between wet and dry salt allows for this distinct geophysical signature. This contrast increases with porosity, but broadly ranges between 100 to $10,000$ Ωm for dry salt and 1 to 100 Ωm for wet salt

(Ezersky and Goretsky, 2014). The presence of clay seams can also contribute to an elevated conductivity in salt. The resistivity of clays ranges between 2 to 14 Ωm (Salem, 2001). Clays in the salt are not common in the area that this project focuses on, but are present in other Saskatchewan potash mining areas. The particular case of salt-locked brine is not considered an overly serious phenomenon due to the limited volume of the void brine - as long as there is no linking path from the void to an additional aquifer source - and the fully-saturated nature of the brine. This combination of low volume and low leeching capability make this particular phenomenon less of a concern.

The third case of brine in-flow occurs when the normally tight and plugged Dawson Bay carbonate (located just above the formation with the mined ore) becomes porous and filled with water. Typical resistivity of the Dawson Bay formation varies, but is commonly around 20 to 50 Ωm. This phenomenon is a concern due to the fact that the brine is usually sub-saturated and very high-volume. It is also a concern because of the difficulty in detecting such an anomalous layer of brine in the carbonates near-mine. The resistivity contrast is smaller when it comes to wet-dry carbonate when compared with wet-dry salt. There is also often a time delay between mining and when the area becomes a known concern. This project seeks to investigate the potential of using geophysics to assist in detecting the third of these phenomena, principally the use of time-domain electromagnetics.

1.3 Objectives

The main objectives for this project broadly include developing an understanding of the physical effects of using electromagnetics in-mine to detect conductive bodies. In-mine electromagnetics has the challenge of being full-space (i.e. response signals from above and below) rather than the traditional half-space signal when performing surveys on the surface of the Earth. One of the objectives of this project will be understanding the effects of this full-space signal. Another objective will be to analyze the effect of near-mine parameterization on the response signal. This near-mine parameterization has a variety of challenging issues with it. One is detecting conductive bodies in geologically realistic environments - i.e. between two conductive shale bodies, another is detecting conductive bodies at close

range (within the salt), and lastly detecting especially thin conductive bodies. For all of these problems the issues are not strictly reducible to measuring a change in the response - after all we know there will be a physical difference in the model that will generate a variation in the response, but rather the degree of response variation from the normal near-mine parameters. Lastly, through developing a realistic set of near-mine parameters, we aim to perform a thorough sensitivity analysis to better understand the propagation of electromagnetic diffusion and the time we would expect responses originating in each layer to arrive at the receiver.

Another objective involved analyzing in-mine time-domain electromagnetics data supplied by Potash Corporation of Saskatchewan Inc. (now Nutrien Ltd.). This data was collected as part of a 2017 internship that the student author partook in collaboration with the Mitacs Accelerate program. This survey was performed in an area with a suspected Dawson Bay anomaly. This anomaly resides in the carbonates 40 to 60 meters from the mine. This data has the potential to help us refine near-mine parameters and illustrate the degree to which they change over a suspicious area. One aspect to this side of the project lies in data processing and visualization. Another aspect is applying a set of inversions to the survey data to improve on and fine-tune forward model parameterization. This will allow us to improve on the first set of objectives related to the effects of near-mine parameterization on signal response and improve on future pre-survey predictive forward modelling.

1.4 Overview

This work is subdivided into five chapters. These chapters will aim to provide an overview, outline the history and background behind geophysics in potash mining, detail the approaches taken by this project in computer modelling design and surveying, detail the results, and summarize the conclusions. The project has three main components to it: forward electromagnetic computer modelling, in-mine survey data, and linking the computer modelling with the data through inversions. The methods and the results sections (chapters 3 and 4) are subdivided into these three broad categories in order to aid the reader. There are additional subsections on topics that are ancillary to the main three, and these are kept separate

for clarity. Each of these three main categories have sections detailing the creation, processing, validation, and visualization techniques. In the case of computer modelling, a significant amount of effort was made to insure each individual model set-up was accurate and efficient. As such model validation was a key component to the process once the individual model was created. For the survey data, an additional step of data processing was required to convert the data into a suitable form for the inversion code. Each of the main three components have sections detailing the results from a variety of perspectives, including comparing the measured or calculated signal against position, time, and transmitter/receiver separation.

Chapter 2

Theory and Background

Summary

This chapter will cover areas of background knowledge for this research topic, as well as give an historical context for the efforts made during this project. The topics in this section will include first a basic overview of the physics behind geophysical electromagnetic investigation. Next, I will cover the lithology near potash mines in Saskatchewan; detailing the features present in such formations. Lastly, an outline of the potential hazards in potash mining, as well as the historical applications of geophysics to delineated such near-mine hazards.

2.1 Basics of Electromagnetics

Electromagnetics is a geophysical induction technique that responds to spatial variations in the electrical properties of rocks. These variations are stimulated via a time-varying magnetic field. The magnetic field is created and observed through the placement of two loops of electrical wire. One of these loops (Tx) transmits a magnetic field - known as the primary field - into the Earth by producing electric currents at a specific frequency, using the principle of Ampère's Law. This phenomenon can be examined in both frequency- and time-domains (West, 2001). The following equations use **H**, **J**, **D**, **E**, and **B** as the magnetic field (in amperes per metre), current density (amperes per square metre), electric displacement field (coulombs per square metre), electric field (volts per metre), and magnetic flux density

(teslas) respectively. Upper case indicates the respective phenomena in frequency domain, while in lower case (**h**, **j**, **d**, **e**, and **b**) the phenomena is described in time-domain. The symbol i is the square root of -1. Equations 2.1 and 2.2 resolve Ampère's and Faraday's laws in frequency-domain, while equations 2.3 and 2.4 resolve Ampère's and Faraday's laws in time-domain.

$$\nabla \times \mathbf{H} = \mathbf{J} + i\omega\mathbf{D}. \tag{2.1}$$

$$\nabla \times \mathbf{E} = -i\omega\mathbf{B}. \tag{2.2}$$

$$\nabla \times \mathbf{h} = \mathbf{j} + \frac{\mathrm{d}\mathbf{d}}{\mathrm{d}t}. \tag{2.3}$$

$$\nabla \times \mathbf{e} = -\frac{\mathrm{d}\mathbf{b}}{\mathrm{d}t}. \tag{2.4}$$

The magnetic field produced by the transmitter turn-off induces eddy-currents within the Earth acting to oppose the change in the magnetic field. The resulting eddy-currents, in-turn, induce their own magnetic field - known as the secondary field - which is measured along with the primary field by a second loop referred to as the receiver (Rx). These eddy-currents are stronger and diffuse slower in material that is conductive, and are weaker and diffuse faster in material that is resistive.

The propagation distance of the EM signals (both frequency-domain and time-domain) are controlled through the same property, though are optimally described mathematically through slightly different means. In frequency-domain, the property of concern is the skin depth (δ). Skin depth is the distance an induced electromagnetic field travels before it decays to e^{-1} or 36.8% of the original magnitude of the signal. Skin depth is both a function of the host rock resistivity ρ and magnetic susceptibility of the material μ, as well as the operating

frequency of the EM system ω.

$$\delta(\omega, \rho, \mu) = \sqrt{\frac{2\rho}{\mu\omega}}. \tag{2.5}$$

In time-domain, the propagation distance is controlled by the time parameter instead of by the frequency. For any time-domain measurement, it is assumed the current is in "long time". This means the displacement currents are negligible, and the wave component of Maxwell's equations disappear and the diffusion term dominates. This phenomenon is described by both the diffusion distance, z_d, shown in equation 2.6, and diffusion velocity, v_d, shown in equation 2.7. When "long time" occurs depends on the material. For most rock ($\approx 25\ \Omega$ m) "long time" will likely be in the order of tens or hundreds of nanoseconds, while for salt ($\approx 1000\ \Omega$ m) this would occur somewhat later in time - likely on the order of microseconds. If the host material is strongly magnetic (as such, $\mu \neq \mu_0$), these terms also depend on a varying μ, though, in most cases, this is not a significant consideration.

$$z_d(t, \rho) = \sqrt{\frac{2\rho t}{\mu}}. \tag{2.6}$$

$$v_d(t, \rho) = \frac{\mathrm{d}z_d}{\mathrm{d}t} = \sqrt{\frac{\rho}{2\mu t}}. \tag{2.7}$$

These two phenomena, diffusion distance and skin depth, allow the creation of sounding measurements of the Earth by taking measurements at a series of varying times or frequencies, depending on the system. These sounding measurements are usually taken in parallel profiling lines.

There are principally two systems of electromagnetic investigation. They operate differently in the moments that they sample the secondary field. A diagram illustrating the setup and the physics behind these two systems can be seen in figure 2.1 (Dentith and Mudge, 2014). In frequency-domain (FEM), sampling occurs as the current in the loop is on and oscillating - using most commonly a sinusoidally varying current (a.c.). This means that both primary and secondary fields are measured. However, using the analytical solution for

a field in a perfectly insulating full-space, the primary field can be subtracted out of the measured response, leaving only the signal produced by variations in the Earth as the result. In time-domain or transient electromagnetics (TEM), the system operates by measuring the magnetic field after a sudden turn-off of a constantly running - or direct current (d.c.) - transmitter loop. This means that the measured response in a standard induction coil receiver is exclusively, in principle, that of the time derivative of the secondary field. However, given the constraints of the amount of power in the wire, the number of turns in the wire, and the method of operational communication between transmitter and receiver, the actual turn-off time can never be instantaneous and will vary, leading the initial measured time windows to be noisy with the remnants of the primary field. Figure 2.2 illustrates the different time-varying electrical current outputs for transient (time-domain) and harmonic (frequency-domain) systems. The waveform in figure 2.2.a shows the sudden turn off in TEM transmitting current from a steady on state, allowing for a measurement of the decaying secondary magnetic fields in the off-time for a TEM system. Figure 2.2.b shows a typical FEM system where the transmitter is operating with an alternating current output. This constant change in current generates a magnetic field.

2.2 Geology Surrounding Potash Mines

Lithology surrounding potash mines consist of formations with various evaporite, shale and carbonate members. Several conflicting nomenclatures and varied interpretations of these members exist in the literature. However, since this project has a physics-based interest in these bodies, the simplest geological interpretations available will typically be used as the basic framework for subsequent computer modelling. Formations of interest that will be discussed in future chapters, beyond the mining ore zone formation of the Prairie Evaporite, include the Dawson Bay, Souris River, and the Winnipegosis. All of these formations consist of segments of transgression and regression of sea levels which led to their deposition. Typical basal features (due to the initial transgression of sea level) are shale to carbonate bodies, while cap members feature carbonate to anhydrites or halites deposited during regression of the sea levels (Lane, 1964).

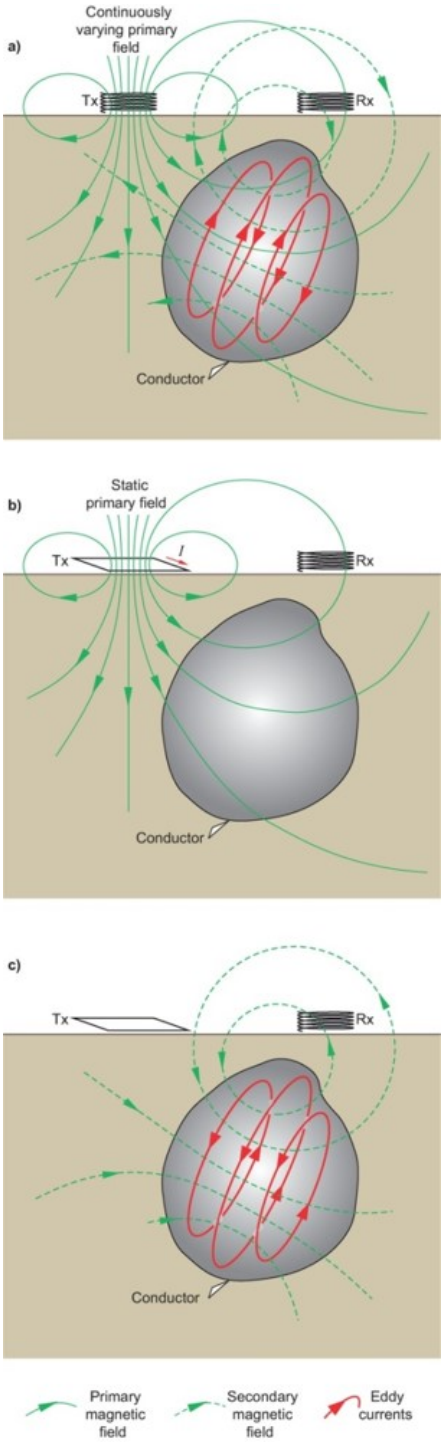

Figure 2.1: **Basic physical principles behind electromagnetic measurements. a) shows a frequency-domain system sampling both the primary and secondary fields, b) shows a time-domain system at a time while the current is on and in a steady state, and c) shows a time-domain system at some time after current turn-off (Dentith and Mudge, 2014).**

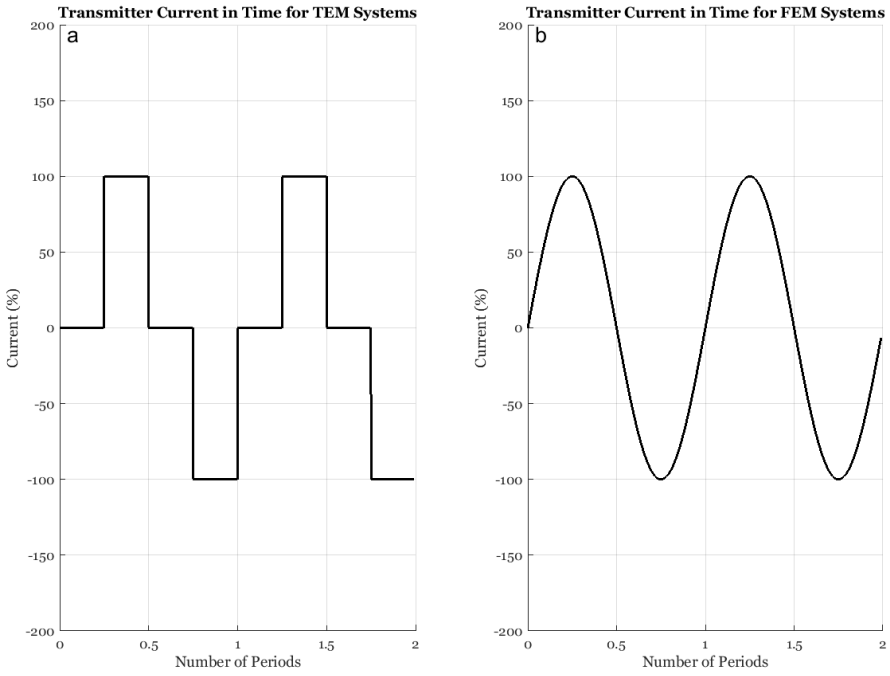

Figure 2.2: **Transmitter forms for a typical time-domain system (TEM) in *a*) and frequency-domain system (FEM) in *b*). The y-axis depicts the percent of maximum current in the transmitting wire. The time-domain system shown here is using a 50% on square-wave form.**

2.2 Geology Surrounding Potash Mines

This project will be focusing primarily on the Dawson Bay formation. Historically, the Dawson Bay has been of significant interest for potash mine operations and safety in Saskatchewan (Gendzwill 1982; Gendzwill and Stead, 1991; Duckworth, 1992). The Dawson Bay lies just above the Prairie Evaporite formation, the upper portion of which supplies the ore zone for potash mining. Various classifications for the Dawson Bay have been proposed. These segregate the formation into anywhere between 4 and 6 members. The classification system used principally for this project, as well as for the physical computer modelling, will be based on the one put forward by Dunn (1982) rather than the one devised several decades earlier by Lane (1959) both for its simplicity and for better correlation with geophysical parameters.

Figure 2.3 shows the broad view, high level sequence of geological layers surrounding the Prairie Evaporite formation throughout southern and central Saskatchewan. The figure was modified from the stratigraphic column constructed by the North Dakota Geological Survey (Murphy, Nordeng, Juenker, and Hoganson, 2009). Above the Dawson Bay lies the Souris River formation. Both of these formations belong to the Manitoba group of the Middle Devonian (Lane, 1964). The Souris River lies near the point where delineating various layer members with distinct physical properties begins to lose benefit from an electromagnetic modelling perspective, however, the lower member, the Davidson, has uniquely porous properties that made modelling it as distinct from the overlying Souris River members advantageous. As such it will be discussed below. Other formations of interest are the ones below the Prairie Evaporite including the Winnipegosis and the Ashern. These, along with the Prairie Evaporite, belong to the Elk Point group of the Middle Devonian (Lane, 1964). The Winnipegosis was partly modelled as a separate layer independent of the lower half-space in order to supply the EM model with a variation below the transmitting layer in addition to the ones above. Little conclusive evidence from the resulting models indicated that this lower layer was a significant contributor to the measured signal, but it was retained to provide the inversions with another option below the transmitting layer.

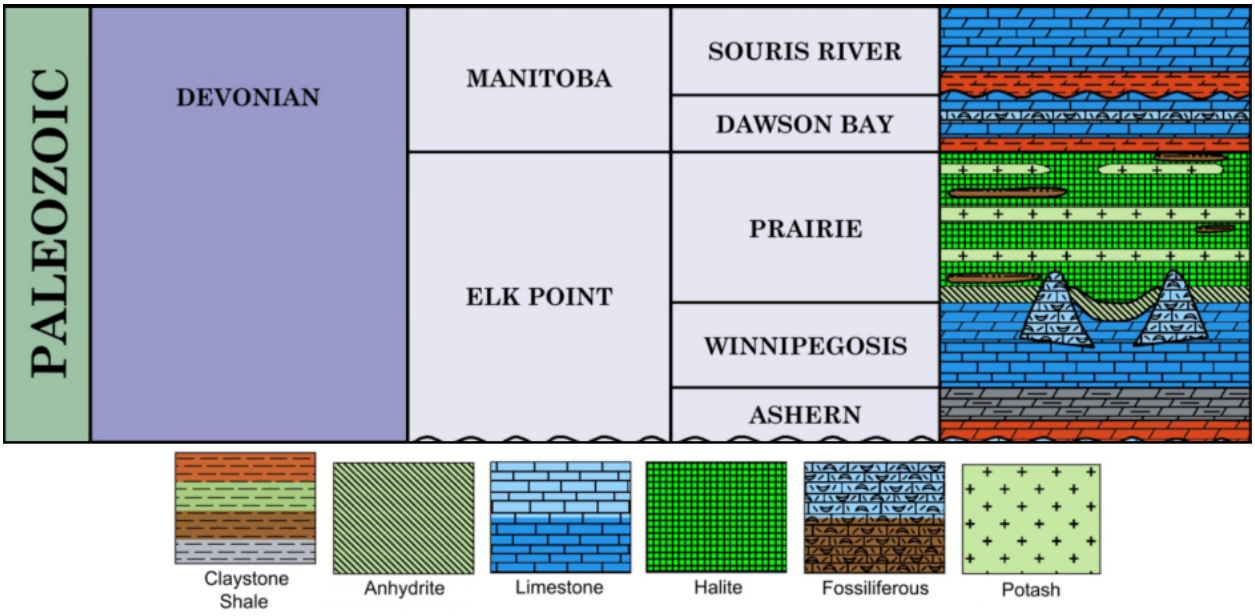

Figure 2.3: **High level stratigraphy of the geological formations common across south-central Saskatchewan. Diagram modified from Murphy et al. (2009).**

2.2.1 The Dawson Bay formation

Dunn divides the Dawson Bay into four distinct members. The lowermost member is the Second Red Bed, a dolomitic green-red shale body roughly 4 metres in thickness (Lane, 1959). It lies disconformably above the Prairie Evaporite formation. Above this is a succession of carbonate limestone with various lithofacies noted, from black and bituminous in the upper end, to grey and buff to the lower. There are also variations in texture between fragmental in the upper end to cryptocrystalline in the lower. This complexity has led to several conflicting classifications of the middle members of the Dawson Bay. Dunn chose to classify the limestone members into two groups, the lower Dawson Bay limestone member referred to as the Burr Member and the upper Dawson Bay limestone member referred to as the Neely Member. Above these middle members lies the Hubbard Evaporite, a primarily halite member that is locally present across the Dawson Bay (Dunn, 1982).

Lane (1959) classifies the Dawson Bay into six members. The middle four (DB-2 to DB-5) refer to the limestone carbonate members. Lane noted slight variations in texture between DB-2 and DB-3, changing from microgranular in the DB-5 to microcrystalline in the DB-4. However, the two textures are gradational between one another and occur to some extent

in both, leading Dunn to group them together into one member, the Neely. The property that Lane used as the dividing principle between DB-2 and DB-3 was the sharp resistivity contrast that can be seen in some well-logs between the DB-2 and the DB-1 (Second Red Bed) and the DB-3. It was noted by Dunn (1982, p.4-5), that while the contrast between DB-2 and Second Red Bed can be seen in the gamma logs, making them consistently distinct, the resistivity low observed in the DB-3 corresponds with the amount of halite impregnation in the member, which in turn corresponds with the degree that dolomitization produced pore space for the impregnation to occur. This is a post-depositional effect and varies in degree from well to well. Hence, Dunn proposed DB-2 and most of DB-3 together in one member (the Burr). The top of the Burr Member is defined by a sharp spike in the gamma often seen in the argillaceous carbonate at the top of the DB-3.

For the purposes of modeling the full-space, near mine conditions, the model proposed by Dunn appears more useful from an EM perspective. Section 3.4 analyzes geophysical logs from a well site near a potash mine. Interpretations on the geophysical lithology that informed the subsequent modelling are also detailed in that section.

2.2.2 The Souris River formation

The Souris River formation lies disconformably above the Dawson Bay (Lane, 1964). They are both members of the Manitoba group and belong to the Middle Devonian. The Souris River is marked according Lane (1964) as the carbonates (Neely) or evaporites (Hubbard) of the Dawson Bay transition to the green-grey or red shales of the First Red Bed. The Souris River is divided into several sequences of sea level transgression and regression depositions. These sequences are from oldest to youngest, the Davidson, Harris, and Hatfield members. The only layer considered of importance to this project is the Davidson. This is due to it being typically the largest of the three; it is also the most proximal to the mining layer; and, finally, it contains a large conductive shale body (the First Red Bed), as well as a fairly porous lower carbonate member in the area of interest to this project. Both of these fairly large and conductive bodies were thought to be extremely important to the constructed EM models. Lane (1964) subdivides the carbonate middle members of the Davidson into b-unit and c-unit members, as well as a d-unit evaporite cap. For the purposes of modelling,

the only layers individually defined are the First Red Bed and the porous Lower Davidson (b-unit) carbonate.

2.2.3 The Winnipegosis formation

Another important formation is the Winnipegosis. This formation is a Middle Devonian carbonate deposit located below the Prairie Evaporite. The Winnipegosis is divided into two layers. The lower portion is relatively uniform in thickness (ranging from 9 - 20 m) and consistently present across most of central-southern Saskatchewan. The upper portion of the Winnipegosis consists of regionally accumulated "banks" or mounds that can extend upwards of 100 m and vary laterally usually between 1 to 10 km (Wardlaw and Reinson, 1971). Section 2.3 will go into detail on the history and current understanding of mine in-flow threats to potash mining. However, put briefly, one of these in-flow threats is spatially tied to these mounds in the Winnipegosis due to groundwater moving through the mounds in the Devonian which led to salt dissolution and subsidence in the younger lithology above (Gendzwill, 1978).

Including this formation in this project had two purposes. One was that it provided a spatially constrained zone below the Prairie Evaporite salt body. This allowed forward models and inversions to interact with a spatially constrained layer below the transmitting layer - allowing a degree of flexibility to the full-space analysis. The other was analyzing the effects on electromagnetic responses in areas of Winnipegosis mounds.

2.3 Hazards in Potash Mining and Mine Geometry

Potash mining in Saskatchewan is conducted exclusively in the upper zone of the Prairie Evaporite formation (Holter, 1969). The Prairie Evaporite formation is a Devonian salt deposit up to 200 metres in thickness and consisting of anhydrite near the base, with predominately halite throughout the rest of the deposit. Near the top of the formation, sylvite begins to dominate. The geometry of a Saskatchewan potash mine can vary; however, mine panels share a few characteristics such as very long lengths (often more than a kilometre), extremely straight with near insignificant vertical variation to the panel over their lengths.

The width and height of these panels can vary from mine to mine, but the geometry used for modelling in this project, as well as the geometry of the mine that was surveyed as part of this project, has dimensions of between 2 and 3 metres in height, and 20 metres width (Gendzwill and Stead, 1992).

Historically, potash mining has suffered from mine flooding. Notable potash mine flooding events include the one that forced the Cominco potash mine to halt production between 1970 and 1972, and caused the shutdown and subsequent conversion to a solution mine of Patience Lake in 1987 (Gendzwill and Stead, 1992). The potential mechanisms behind mine in-flow have been found to fall into one of three categories:

1. Collapse structures: large or small bodies of brecciated shale, salt, and limestone. In-flow may not be immediate, but often will follow in time once a collapse structure has been cut into by the mining machine.

2. Brine in pores between the salt crystals can be released via mining. The dissolving power, and therefore the threat, of this source is low due to the saturated nature of the brine in contact with the salt. Typically, the discharge from a source in the salt is low volume.

3. Aquifers in the carbonates above the mine can be leached into the mine due to fracturing over time of the salt and shale from mining operations. This mechanism is the primary focus of this project's investigation.

The first of these sources (collapse structures) is thought to have been created near mounds in the Winnipegosis carbonate below the Prairie Evaporite during compaction of the salt. Expelled water from the Winnipegosis mounds dissolved some of the deposited salt, allowing for collapse structures to form subsequently on the edges of these features. Seismic is an extremely useful tool in determining the presence of these areas of threat due to the high velocity difference between dolomite of the Winnipegosis and the salt of the Prairie Evaporite. Historically, a mixture of surface 3D and in-mine 2D seismic surveys have been used successfully to delineate these features (Gendzwill and Stead, 1992).

The second of the inflow threats, that of trapped saturated water in the salt itself, is the least dangerous of all the sources. This is because saturated water has lower dissolving

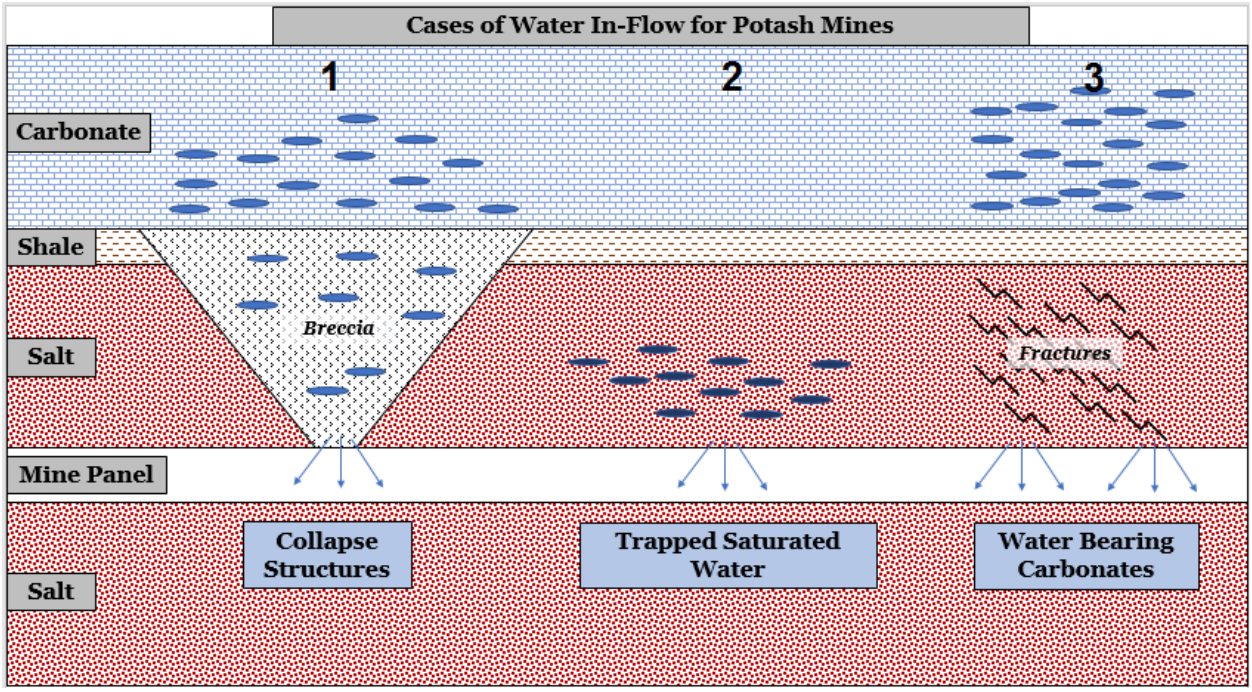

Figure 2.4: **Simplified and idealized mine panel in profile view and the surrounding geology above and below the mine illustrating the cases of water in-flow threats for potash mining in Saskatchewan. The geological layers are not to scale. The blue ellipses denote the presence of sub-saturated or saturated water (light to darker). The black lines denote minor fracturing induced from mining operations.**

power compared with the other sources and often has much lower volume. It is has been demonstrated (Gendzwill, 1982; Duckworth, 1992; and Eso and Oldenburg, 2006) that detecting these phenomena is possible using a variety of galvanic and inductive geophysical techniques, as the conductivity contrast between wet salt and dry salt is many orders of magnitude. These studies and others are outlined in section 2.4.

The third of these cases, the situation where water lies above the shale body in the carbonate is the primary topic of discussion for this project. Seismic investigations typically have limitations in detecting these types of anomalies because of the relatively low velocity contrast between wet and dry carbonates. Both frequency-domain electromagnetics and time-domain electromagnetics have been considered for this purpose, though the time-domain method has been preferred due to certain benefits over frequency-domain. The main advantage of time-domain lies in not requiring exact knowledge of the receiver location and thereby avoiding significant potential primary field noise that occurs in frequency-domain measurements due to frequency-domain operating while the primary field is active (Dentith and Mudge, 2014). Galvanic techniques, such as DC resistivity, while successful in detecting brine in the salt, are cumbersome to deploy and require a very large amount of voltage to penetrate a dry salt layer. Figure 2.5 shows a series of DC resistivity computer models. Sub-figures 2.5.a, 2.5.c, 2.5.e show the current distribution around each of the three models. Sub-figures 2.5.b, 2.5.d, 2.5.f illustrate each respective model geometry and resistivity variation. The first of these is designed to simplistically model the near mine geological environment. This includes a mostly resistive lower half-space, and a thin resistive layer insulating the more conductive half-space above. When comparing the first case with the second where the conductive upper half-space is removed completely we see that the log of the current distribution shows not a large difference of current penetration in the upper half-space between the conductive and the resistive one. When we compare with even just a slightly more conductive insulating layer (around 100 Ωm), we see a large change in the amount of current that penetrates into the upper-half space. This would indicate that DC Resistivity would be a good choice if the conductive water had already reached the salt above the mine, but not as much in detecting conductive changes in the layers above the mine if the salt-back is still intact. An additional interesting alternative means of water detection

is induced polarization (IP). Chargeability responses have been potentially observed in areas where water near the mine comes in contact with clay layers (El-Kaliouby et al., 1995; Chouteau et al., 1997). This makes IP a possible avenue of exploration in the future, but not as a reliable, consistent replacement for traditional inductive techniques such as TEM for this purpose.

2.4 History of Geophysics in Potash Mines

One of the areas of interest in potash mining is mapping and detecting salt-back thickness - or the distance from the top of the mine panel to the Second Red Bed above. Thin salt-backs are considered a safety and operational hazard. Early techniques used to measure this distance were electromagnetic. A report created by Gendzwill (1967) consisted of several frequency-domain measurements underground using a Ronka Mark III system. It was a dual-frequency system operating at 615 and 2400 Hz. Several separations were used in this study, ranging from 100 to 300 feet. These results were compared with modified analytical half-space solutions originally proposed by James Wait. Wait's solutions were created to assist airborne electromagnetics by shifting the source into the air above the homogeneous half-space of the Earth (Wait, 1956). Gendzwill applied these solutions by treating the salt as infinitely resistive. This method used the transition from salt to the Second Red Bed as the boundary of the conductive half-space. Results showed some degree of agreement between the theoretical and measured values (Gendzwill, 1967).

Several years later, Gendzwill and Pandit (1980) performed a computer modelling study using frequency-domain systems for determining salt-back thickness. They found that an optimal operating frequency of around 30-40kHz should be used. At lower frequencies the signal over-penetrates the targeted shale body and introduces signals from conductive bodies from above the shale, while higher frequencies have significant interference from clay seams in the salt as well as introducing unwanted displacement currents. The optimal array setup was found to be horizontal co-planar with a small underground transmitter-receiver separation of 8 metres.

For detecting the increased conductivity of anomalous water bearing zones near potash

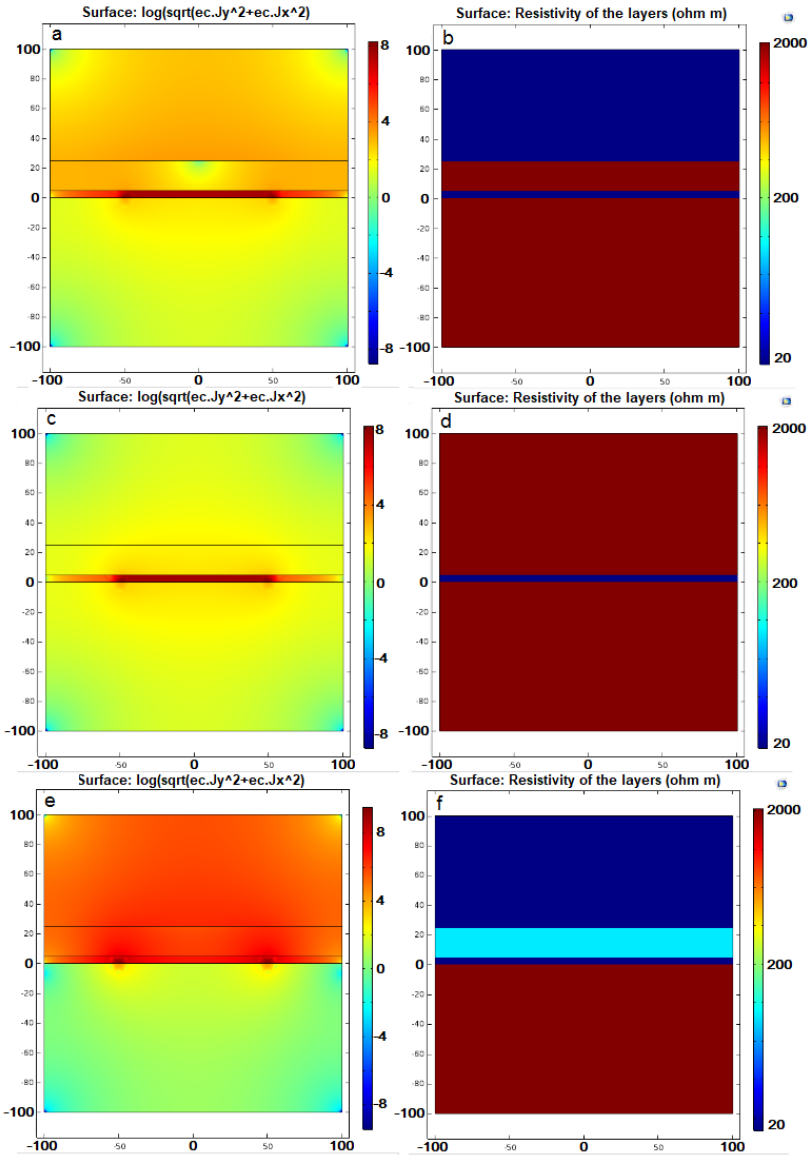

Figure 2.5: **Series of cross-section computer models created in COMSOL illustrating the difficulty in injecting current through a highly resistive layer. Current is injected in this model through the placement of two potential nodes (one positive, one negative) that introduce a voltage difference at $(-50,0)$ and $(50,0)$ respectively. The left figures are the log of the current densities and the right ones are the layer resistivities. The top set is the case of injecting current upward through a 20m resistive layer. The middle illustrates the case where there is no conductive half-space above the resistive layer. The lowest one is the case where the resistive layer has been reduced in resistivity.**

mines, various galvanic and induction techniques have been used. Eso and Oldenburg (2006) used a 3D Direct Current Electrical Resistivity Imaging (DC ERI) survey in an area of known water in-flow through the Second Red Bed and into the Prairie Evaporite. This survey identified the wet salt roughly 10 metres above the mining horizon, as well as a known void in the salt near the in-flow. It was noted by Eso and Oldenburg that the use of standard 3D resistivity surveys is difficult to perform, both in the availability of the geometry for the arrays and the quality of that available geometry.

In another survey, Duckworth (1992) conducted both time-domain (TEM) and frequency-domain (FEM) electromagnetic surveys in a known geological anomalous zone. This survey found a significant conductive response in the radial field in both frequency and time domains in this anomalous zone - the radial field being the horizontal field in-line with the survey. The frequencies measured ranged from 222 to 1777 Hz. Both the in-phase and quadrature responses were measurable. The time-domain measurements ranged in time from 0.15 to 6.4 milliseconds. Only the radial field responses were published. The source of this response appeared to be a conductive layer located in the Prairie Evaporite formation just below the Second Red Bed. The magnitude of the signal appeared to suggest a layer in the salt of similar conductivity of a body of shale. In the case of the vertical field, Duckworth suggested the coil separation of 100 metres was too large to produce any variation in response. Duckworth also warned against having mining machines and equipment near any EM surveys conducted in the mine as they produce electromagnetic noise. The systems used in this survey were the Max-Min for frequency and the Crone PEM for time-domain. It was noted that the time-domain system produced smoother profiles. A likely possible explanation proposed by the authors for this was that the PEM used a more powerful transmitting magnetic moment.

Krivochieva and Chouteau (2002) performed 1D TEM forward computer modelling using the numerical techniques put forward by Umesh Das (1995) and analyzed TEM survey data from a potash mine in Taquari-Vassouras, Brazil. Krivochieva and Chouteau discovered that both the vertical and radial components of the magnetic field carried responses from conductive layers, but only the radial field showed distinct shape and polarity when the layer was above compared to when it was below. Variations in conductivity, thickness and distance could also be accounted for in the computer modelling. In-mine data collected for

that survey found no significant conductive bodies near the mine. A test was also done using the transmission survey technique (source on surface, receivers in-mine) for this project. This test found that at a depth of 400 metres the transmitted signal was detectable and compared favourably with in-mine TEM and borehole log data.

Chapter 3

Methodology

Summary

This project focused on three key areas of interest designed to explore the problem of performing electromagnetics in mine environments. The initial step of this project was to create and thoroughly test a set of full-space and half-space electromagnetic models both in *COMSOL Multiphysics* and in *Mathworks Matlab*. These computer modelling tools were of principal importance toward our purpose of understanding and predicting in-mine electromagnetic signals and how they respond to changing geological environments. The second was analyzing electromagnetic survey data produced in potash mines. This data was supplied via a *Mitacs Accelerate* internship that the student author took part in with *Potash Corporation of Saskatchewan Inc.* (*PotashCorp*) - now called *Nutrien* - under the supervision of Randy Brehm, Senior Geophysicist at *Nutrien*. This internship included participating in an underground time-domain electromagnetic survey being performed in an area of a suspected conductive anomaly near-mine. The data from this survey was made available to the *Butler Research Group* by *PotashCorp* for the purposes of this research project. The third aspect to the project was constructing an inversion system using *Matlab*'s in-built minimization search algorithms and COMSOL Multiphysics 2-dimensional axisymmetric geometric settings as our forward modelling software. These software systems were connected via COMSOL Multiphysics LiveLink with Matlab tool.

The computer software tools constructed in the first part of this project allowed us to

assist with survey planning and initial predictive modelling prior to conducting in-mine surveys. This includes both the survey conducted as part of the *Mitacs* program as well as other later surveys conducted at other sites by *Nutrien*. The survey data from the *Mitacs* program was tied to inversion scripts to produce plausible near-mine parameter estimations. Several different approaches were used to control the parameters during the aforementioned inversions. In order to produce these inversion products, the forward modelling systems were tied to minimization techniques in *Matlab* via a rudimentary objective function.

3.1 Electromagnetic Forward Modelling Design

As with any numerical modelling, the required discretization of the geometry and mathematics introduces the problem of the trade-off between speed and accuracy. When it comes to accuracy, rigorous testing was performed comparing our models to analytic solutions devised by Nabighian (1988) in frequency- and time-domain and in both full- and half-space environments. This was done specifically to achieve the highest degree of accuracy with the smallest possible run-time. The analytic electromagnetic solutions are limited to environments with homogeneous resistivity, and for half-space environments solutions only exist in the plane of the transmitter.

For the purposes of electromagnetic forward modelling performed during this project, it was thought that having two independent software tools, using two different solving methods, would be ideal. Having two independent solving tools would allow for mutual verification when outside of the homogeneous environments that purely analytic solutions are exclusive to. The first of these tools chosen for this task was a spectral semi-analytic solution redesigned by Das (1995) for use in full-space environments which calculates a spatial frequency magnetic and electric field response to EM stimulus. This method will be referred to as the spectral semi-analytic solving method for the purpose of this project. The second tool used for this project was the magnetic field solver in *COMSOL Multiphysics*. *COMSOL* uses Partial Differential Equations (PDEs) determined over a series of spatially defined points for its method of resolving magnetic and electrical fields. This method will largely be referred to as the PDE-based numerical method for the rest of this document. Section 3.1.1 goes over

the design of the 1D spectral semi-analytic layered-space solutions in *Matlab Mathworks*. The modelling code for this was written by the author, but was originally based on work by Das (1995). Section 3.1.2 goes over the parameterization of the layered-space Partial Differential Equation (PDE)-based numerical *COMSOL Multiphysics* models. Section 3.1.3 will go over the analytic solutions to various homogeneous models in detail. Comparisons between the analytic solutions and simple homogeneous numerical models from both Matlab and COMSOL are found in section 3.1.4.

3.1.1 One-Dimensional Spectral Semi-Analytic Modelling of Electromagnetics in *Matlab*

Das (1995) proposed a method of calculating 1D electromagnetic full-space layered Earth - i.e. resistivity varying - forward models that reformulated the already existing techniques but avoided the instability inherent in previous propagation matrices. Through recursion, input admittances at the interfaces are calculated at the upper and lower ends of the model and moved inward to the source layer. This produces a spatial frequency solution for the magnetic and electric fields. Through a pair of conversions, this spectral solution is converted into a real-space, frequency-domain EM solution; and finally into a real-space, time-domain EM solution. This technique was also used by Krivochieva and Chouteau (2002) as part of their investigation using time-domain electromagnetics at the Taquari-Vassouras potash mine in Brazil.

This project created a forward electromagnetic modelling script using *Matlab* based on Das' method. In this method, each layer with a distinct resistivity is assumed to lie flat and stretch to infinity in the horizontal directions. This makes this modelling approach one dimensional. Figure 3.1 shows the inputs for this script. Any number of layers can be input. Each layer is assigned a thickness h and a resistivity ρ. For both the first and last layer, the assigned thicknesses are infinite to create the edge of the half-space in both directions for the modeling script ($h_0 = h_n = \infty$). From the thickness values, depth z to each layer can be determined. One of the layer horizons is assigned to be the source layer LS. The position of the receiver is assigned (x, y, z) positions relative to that source.

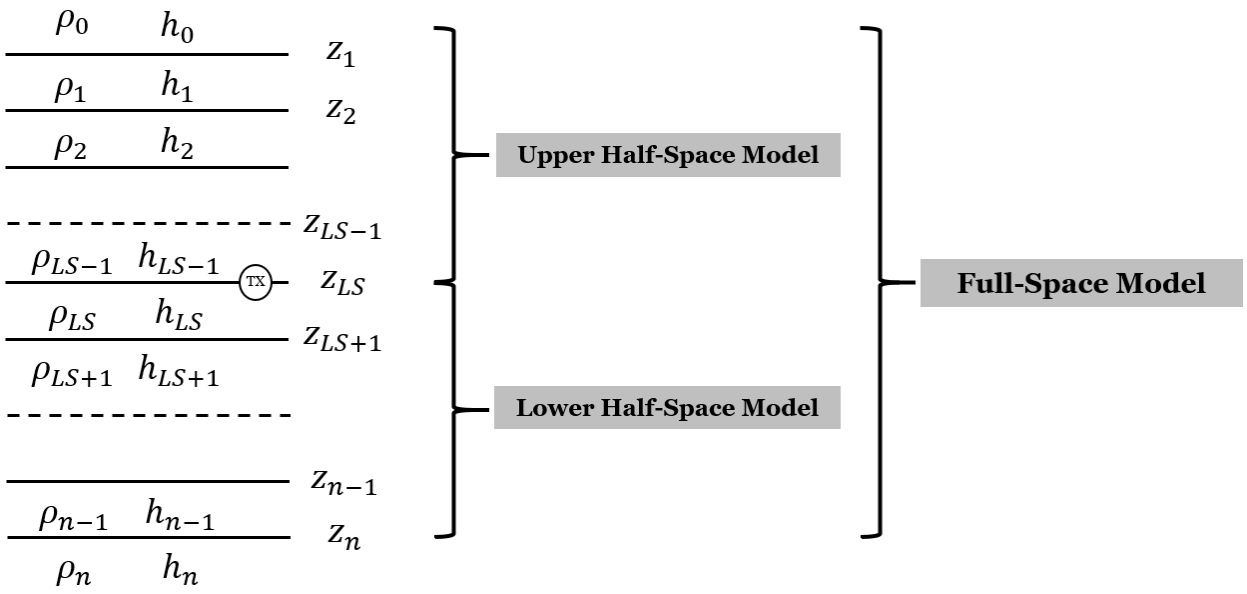

Figure 3.1: **Diagram showing the layer input values for the 1D forward model devised by Das.**

The formulation needs to solve for the tangential electric and radial magnetic fields in frequency-domain. The tangential field is perpendicular to the vertical and radial fields and represents the horizontal across-line field. This is done by applying boundary conditions at layer interfaces sequentially throughout the model which impose continuity of the horizontal components of the magnetic and electric fields. Equations 3.1 and 3.2 show the conversion of the tangential electric field E_ϕ and radial magnetic field H_r from spatial frequency domain to real space. Here λ is the Hankel transformation variable, r is the total transmitter receiver separation, and J_1 is the Bessel function of the first kind and order 1. The $\tilde{E}_\phi$ and $\tilde{H}_r$ terms are the electric and magnetic fields transformed to spatial frequency space. See Equations 3.3 and 3.4 for their expressions. Here, γ is a function of both the Hankel transform variable, λ, and κ. The κ term is the same as the k wave number term used by Nabighian in his analytical solution (1988); κ is a function of both frequency and resistivity. Equation 3.5 shows the expression for γ and equation 3.6 shows the expression for κ. Both of these vary with each layer. The layer conductivity is denoted by σ. The terms A^+ and A^- are admittance coefficients that need to be determined for each layer. The layer index is denoted

by j.

$$E_{\phi,j}(r,z) = \frac{i\omega\mu}{2\pi}\int_0^\infty \lambda^2 \tilde{E}_{\phi,j}(\lambda,z)J_1(\lambda r)\mathrm{d}\lambda. \tag{3.1}$$

$$H_{r,j}(r,z) = \frac{1}{2\pi}\int_0^\infty \lambda^2 \tilde{H}_{r,j}(\lambda,z)J_1(\lambda r)\mathrm{d}\lambda. \tag{3.2}$$

$$\tilde{E}_{\phi,j}(z) = A_j^+ exp\big(-\gamma_i(z-z_j)\big) + A_j^- exp\big(-\gamma_i(z_{j+1}-z)\big). \tag{3.3}$$

$$\tilde{H}_{r,j}(z) = \gamma_j\Big(A_j^+ exp\big(-\gamma_j(z-z_j)\big) - A_j^- exp\big(-\gamma_j(z_{j+1}-z)\big)\Big). \tag{3.4}$$

$$\gamma_j(\omega,\sigma) = \sqrt{\lambda^2 - \kappa(\omega,\sigma)_j^2}. \tag{3.5}$$

$$\kappa_j(\omega,\sigma)^2 = -i\omega\mu\sigma_j. \tag{3.6}$$

To calculate these admittance coefficients, the input admittances (Y^+ and Y^-) within each layer need to be calculated (see equations 3.7 and 3.8). Note that $Y_j^-(z)$ is calculated in layers below the transmitting source layer (i.e. for $-\infty < z \leq z_{LS}$), while $Y_j^+(z)$ is calculated in layers above the source transmitting layer (i.e. $z_{LS} < z < \infty$).

$$Y_j^-(z) = -\frac{\tilde{H}_{r,j}(z)}{\tilde{E}_{\phi,j}(z)} = -\frac{\gamma_j\Big(A_j^+ exp\big(-\gamma_j(z-z_j)\big) - A_j^- exp\big(-\gamma_j(z_{j+1}-z)\big)\Big)}{A_j^+ exp\big(-\gamma_j(z-z_j)\big) + A_j^- exp\big(-\gamma_j(z_{j+1}-z)\big)}. \tag{3.7}$$

$$Y_j^+(z) = \frac{\tilde{H}_{r,j}(z)}{\tilde{E}_{\phi,j}(z)} = \frac{\gamma_j\Big(A_j^+ exp\big(-\gamma_j(z-z_j)\big) - A_j^- exp\big(-\gamma_j(z_{j+1}-z)\big)\Big)}{A_j^+ exp\big(-\gamma_j(z-z_j)\big) + A_j^- exp\big(-\gamma_j(z_{j+1}-z)\big)}. \tag{3.8}$$

Since we know there is no influence of the downward travelling signal on the uppermost half-space and vice versa ($A_0^+ = 0$ and $A_n^- = 0$), the input admittance for the uppermost (layer 0) and lowermost (layer n) half spaces can be reduced to much simpler formulas as shown in equations 3.9 and 3.10.

$$Y_0^-(z) = -\frac{\gamma_0\Big(- A_0^- exp\big(- \gamma_0(z_1 - z)\big)\Big)}{A_0^- exp\big(- \gamma_0(z_1 - z)\big)} = \gamma_0. \tag{3.9}$$

$$Y_n^+(z) = \frac{\gamma_n\Big(A_n^+ exp\big(- \gamma_n(z - z_n)\big)\Big)}{A_n^+ exp\big(- \gamma_i(z - z_n)\big)} = \gamma_n. \tag{3.10}$$

Now that we have the uppermost and lowermost input admittances reduced to their respective γ_0 and γ_n terms, we can begin to solve for the input admittance for each layer in a descending and ascending direction for each half-space. From above moving downward, we solve for the second (and subsequent) layers via the formula found in equation 3.11, and from below moving upward we can solve for $n - 1$ layer and previous layers via the formula found in equation 3.12. The Γ^- and Γ^+ terms are the reflection coefficients of the interfaces between layers. Their expressions are shown in equations 3.13 and 3.14.

$$Y_{j+1}^-(z_{j+1}) = \gamma_j \frac{1 - \Gamma_j^- exp(-2\gamma_j h_j)}{1 + \Gamma_j^- exp(-2\gamma_j h_j)}. \tag{3.11}$$

$$Y_j^-(z_j) = \gamma_j \frac{1 - \Gamma_j^+ exp(-2\gamma_j h_j)}{1 + \Gamma_j^+ exp(-2\gamma_j h_j)}. \tag{3.12}$$

$$\Gamma_j^- = \frac{\gamma_j - Y_j^-(z_j)}{\gamma_j + Y_j^-(z_j)}. \tag{3.13}$$

$$\Gamma_j^+ = \frac{\gamma_j - Y_j^+(z_{j+1})}{\gamma_j + Y_j^+(z_{j+1})}. \tag{3.14}$$

Finally, to return to the issue of calculating the spatial frequency coefficients, A_j^+ and A_j^-, we use the principle that the electric field is continuous across the interfaces (equation

3.15), while the magnetic field makes a non-zero jump over the source layer boundary of the value shown in equation 3.16. M is the magnetic moment of the source and a is the transmitting loop radius. These two equations are valid only at the source layer. Equation 3.17 shows the solution for the spatial frequency coefficient for the layer directly above the source layer (LS) boundary from the signal travelling upward, and equation 3.18 shows the solution for the layer directly below from the signal travelling downward.

$$\lim_{z \to z_L S^-} \tilde{E}_\phi - \lim_{z \to z_L S^+} \tilde{E}_\phi = 0. \tag{3.15}$$

$$\lim_{z \to z_L S^-} \tilde{H}_r - \lim_{z \to z_L S^+} \tilde{H}_r = \frac{2MJ_1(\lambda a)}{a}. \tag{3.16}$$

$$A^-_{LS-1} = \frac{MJ_1(\lambda a)}{\lambda a \gamma_{LS-1}} \frac{\gamma_{LS-1} + Y^-_{LS}(z_{LS})}{Y^-_{LS}(z_{LS}) + Y^+_{LS}(z_{LS})}. \tag{3.17}$$

$$A^+_{LS} = \frac{MJ_1(\lambda a)}{\lambda a \gamma_{LS-1}} \frac{\gamma_{LS} + Y^+_{LS}(z_{LS})}{Y^-_{LS}(z_{LS}) + Y^+_{LS}(z_{LS})}. \tag{3.18}$$

In order to solve for both upward and downward travelling signal coefficients for all layers, we need to propagate the solution from either side of the source layer. Equations 3.19 and 3.20 show the propagation of solutions for all layers above the source layer boundary (i.e. for layers $j = LS-1, LS-2, LS-3, ..., 2$).

$$A^-_{j-1} = \frac{1 + \Gamma^-_j}{1 + \Gamma^-_{j-1} e^{-2\gamma_{j-1} h_{j-1}}} A^-_j exp(-\gamma_j h_j). \tag{3.19}$$

$$A^+_j = \Gamma^-_j A^-_j exp(-\gamma_j h_j). \tag{3.20}$$

Equations 3.21 and 3.22 show the propagation of the solution to the layers below the source layer (i.e. layers $j = LS, Ls+1, LS+2, ..., n-1$).

$$A^+_{j+1} = \frac{1 + \Gamma^+_j}{1 + \Gamma^+_{j+1} exp(-2\gamma_{j+1} h_{j+1})} A^+_j exp(-\gamma_j h_j). \tag{3.21}$$

$$A_j^- = \Gamma_j^+ A_j^+ exp(-\gamma_j h_j). \tag{3.22}$$

Now that frequency solutions for the tangential electric field and the radial magnetic field have been derived, all that remains is to calculate the vertical magnetic field response. This can be done using equation 2.2 with the derived tangential electric field. This simplifies to equation 3.23. Combining equations 3.23 and 3.1 we get equation 3.24, keeping in mind the derivative of a first order Bessel function which is shown in equation 3.25.

$$H_z = \frac{1}{i\omega\mu_0}\left(\frac{\partial E_\phi}{\partial \rho} + \frac{E_\phi}{r}\right). \tag{3.23}$$

$$H_{z,j}(z) = -\frac{1}{2\pi}\int_0^\infty \lambda^2 E_{\phi,j}(z)\left(\lambda\left(\frac{J_0(\lambda r) - J_2(\lambda r)}{2}\right) + \frac{J_1(\lambda r)}{r}\right)\mathrm{d}\lambda. \tag{3.24}$$

$$\frac{\mathrm{d}J_v(x)}{\mathrm{d}x} = \frac{J_{v-1}(x) - J_{v+1}(x)}{2}. \tag{3.25}$$

Now that the responses were calculated in frequency-domain, the last remaining step is to convert to time-domain. This is done, as shown by Farquharson (2006), by integrating over the imaginary components of the magnetic field frequency-domain solution sets as shown in equations 3.26 and 3.27 - the former of which is the evaluation for the magnetic field and the latter the time derivative of the magnetic field. The time derivative of the magnetic field is the primary equation of interest, as it is the phenomenon that is measured with typical TEM receivers. This solution can be performed for any time t. Time-gates typically used for this project were between 10 μs to 100 ms.

This integration was initially performed with *Matlab*'s in-built *trapz* and *integral* functions. These functions work on discretizing and sampling the integrand numerically. In the case of *trapz* it is a trapezoidal solution taking two points in the sample and integrating over the trapezoid they create. *integral* is also numerical but uses a global adaptive quadrature method to resolve the integral. In both of these cases the solution had a long run time and was less accurate than required. This inaccuracy increased in later time. This is due to the

$sin(\omega t)$ factor in equation 3.27. At late time-gates the integrand oscillates at rates orders of magnitude higher than at early time gates, and, as such, requires a much higher sampling density.

$$\mathbf{h} = -\frac{2}{\pi}\int_0^\infty \mathbf{H}_{imaginary}(\omega)\cdot\frac{1}{\omega}\cdot cos(\omega t)\cdot \mathrm{d}\omega. \tag{3.26}$$

$$\frac{\mathrm{d}\mathbf{h}}{\mathrm{d}t} = \frac{2}{\pi}\int_0^\infty \mathbf{H}_{imaginary}(\omega)\cdot sin(\omega t)\cdot \mathrm{d}\omega. \tag{3.27}$$

To avoid this issue, the magnetic field frequency-domain solution sets were replaced by a series of curve segments of 3rd order polynomials. The coefficients for these 3rd order curve segments (a_1, a_2, a_3, a_4) were approximated using *Matlab*'s *polyfit* function. The function was created step-wise where each segment consisted of four discrete points over which the 3^{rd} order *polyfit* was applied. This transformed equation 3.27 to that of equation 3.28. The number, n, of segments the frequency solution were divided into varied between sets. The index for each segment is denoted by l. This integral function can then be integrated by parts. The final function is shown in equation 3.29 (F is the integration constant).

$$\frac{\mathrm{d}\mathbf{h}}{\mathrm{d}t} = \frac{2}{\pi}\sum_{l=1}^{n}\int_{\omega_l}^{\omega_{l+1}}(a_{l,1}\omega^3 + a_{l,2}\omega^2 + a_{l,3}\omega + a_{l,4})\cdot sin(\omega t)\cdot \mathrm{d}\omega. \tag{3.28}$$

$$\begin{aligned}\frac{\mathrm{d}\mathbf{h}}{\mathrm{d}t} = \frac{2}{\pi}\sum_{l=1}^{n}\Bigg[t^{-4}\Bigg(&sin(t\omega)(3a_{l,1}(t^2\omega^2-2)+t^2(2a_{l,2}\omega+a_{l,3}))\\ &-tcos(t\omega)(a_{l,2}t^2\omega^3 - 6a_{l,1}\omega + a_{l,2}(t^2\omega^2-2) + a_{l,3}t^2\omega + a_{l,4}t^2)\Bigg) + F\Bigg]_{\omega_l}^{\omega_{l+1}}.\end{aligned} \tag{3.29}$$

This increased the accuracy of the conversion and decreased the processing time to a couple of seconds, regardless of the size of the original frequency-domain solution set. The primary limiting factors in terms of accuracy and time in the code is the original Hankel transforms in the frequency-sweep function. This somewhat reduced applicability of the 1D semi-analytical method in Matlab to early time EM modelling and confirming the accuracy

of the faster COMSOL models. Figure 3.2 shows a frequency solution set with the function consisting of a sequence of cubic splines plotted along with it. This demonstrated the excellent fit between the constructed functions with the original calculated fields. While the long run time and other difficulties with the spectral semi-analytic method prevented it from being widely used for this project, it was - however - vital in confirming accuracy of layered space solutions produced by the numerical PDE-based method in *COMSOL Multiphysics*. Comparisons of solutions from both of these methods are presented in section 3.1.4.

3.1.2 COMSOL Multiphysics Model Design

Modelling in *COMSOL* was performed using the in-built Magnetic Fields functionality in the alternating and direct currents (AC/DC) module. The Magnetic Fields function within *COMSOL* uses Ampére's Law as its foundation for the electromagnetic solver as shown in equation 3.30, where the B-field is generated via the initial magnetic vector potential $\mathbf{A}$ (the relationship between $\mathbf{B}$ and $\mathbf{A}$ is shown in equation 3.31). The σ, μ_0 and μ_r terms are the conductivity of the model slice, the magnetic susceptibility of free space, and relative magnetic susceptibility, respectively. The decay solution is calculated from an initial magnetic vector potential, $\mathbf{A}$, emulating a vertical magnetic dipole at the origin of the model space. The equation in cylindrical coordinates over the unit vectors $\mathbf{r}$, ϕ, and $\mathbf{z}$ for this is shown in equation 3.32. The relationship between the B-field and the magnetic vector potential is shown in equation 3.31.

$$\mathbf{J_e} = \sigma \frac{\mathrm{d}\mathbf{A}}{\mathrm{d}t} + \nabla \times (\mu_0 \mu_r \mathbf{B}). \tag{3.30}$$

$$\mathbf{B} = \nabla \times \mathbf{A}. \tag{3.31}$$

$$\mathbf{A} = \frac{m\mu_0 r}{4\pi (r^2 + z^2)^{\frac{3}{2}}} \boldsymbol{\phi}. \tag{3.32}$$

Numerical solutions in *COMSOL* are determined in a series of time steps following a set of

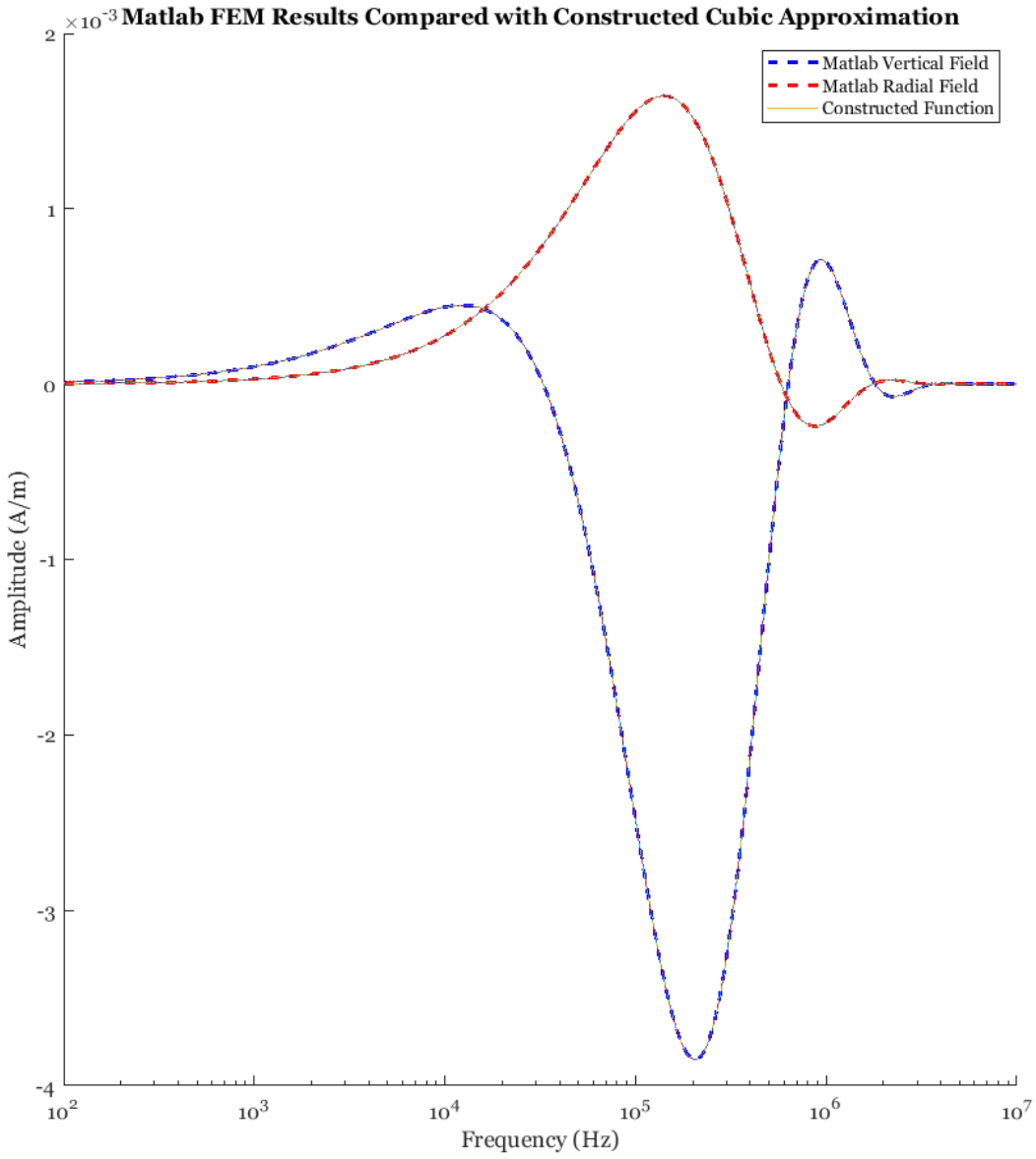

Figure 3.2: **Forward model frequency sweep results for both the radial and vertical magnetic field plotted against the constructed set of 3rd order polynomial functions.**

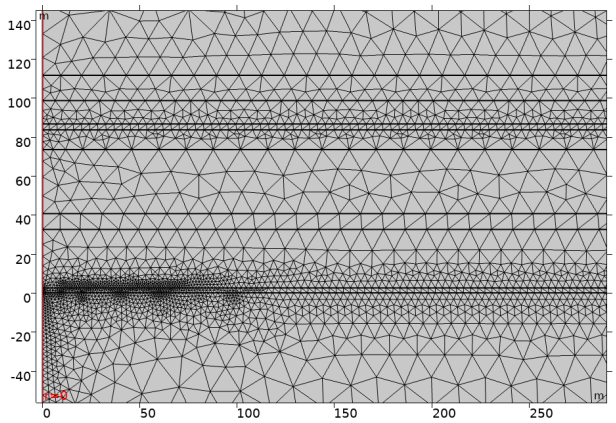

Figure 3.3: **Image showing the mesh assignment in COMSOL for the constructed near mine layers. On the y-axis is the elevation from mine floor in metres. On the x-axis is position from transmission point in metres. The points of intersection of the black lines are the mesh points where the model resolves the magnetic and electric field PDEs.**

initial conditions. The AC/DC module uses the Weyl gague with the electric scalar potential set to 0. The solving time step was defined over 10^{-7} to 10^{-2} seconds with exponential increments of 0.005. In general, the spatial mesh in *COMSOL* was kept at the default "normal" setting. However, much higher densities were set near points of transmission and reception. In addition, when geometric layers with varying physical properties were introduced, a minimum number of vertical mesh points were defined in each layer. This was done so that layers would be resolved no matter how thin they were. In general, with homogeneous conditions and not considering points of transmission and reception, increasing the density of the spatial nodes did not have enough of a quantifiable effect on the accuracy of the solutions to justify increasing the density of mesh points further. Figure 3.3 shows the mesh as defined near the magnetic dipole transmission point.

In order to reduce the degrees evaluated and the computational requirements for the forward models in *COMSOL*, the 2D axisymmetric space dimension was used for the majority of the modelling process. This decreased the time to evaluate each model significantly from the fully 3D geometry. The 2D axisymmetric geometry in *COMSOL* allows the software to shift from a 2D-Cartesian geometry to a 2D-cylindrical one. 2D-Cartesian geometry treats the across profile axis as infinite. The 2D-axisymmetric geometry treats all properties and

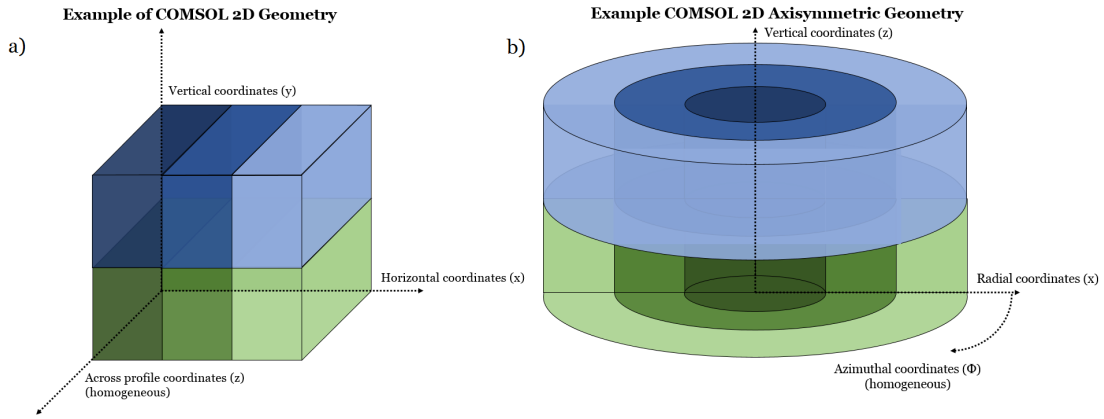

Figure 3.4: **Idealized figure demonstrating the difference between 2D-axisymmetric geometry compared with standard 2D geometry. Colour variation denotes variance in the physical properties in each respective dimension. The figure *a* shows the standard 2D geometry invariant with translation in the z-axis, while the figure *b* shows 2D-axisymmetric geometry invariant with rotation about the z-axis.**

solutions as symmetric about a rotation about the z-axis. 2D-cylindrical geometry is an effective method of modelling magnetic fields due to the dipole nature of magnetic fields and the restriction of using 1D resistivity variation. This would not be easily duplicated in 2D-Cartesian space. A simple visual expression of both 2D and 2D-axisymmetric geometry is shown in figure 3.4. This geometry was used with physical variations only in the vertical direction. Another limitation is that the magnetic dipole used to simulate the response to current in a EM transmitter loop is restricted to the centre of the geometry ($r = 0$ m, $z = 0$ m) and the dipole axis must coincide with the z-axis. This effectively renders the geometry one-dimensional - with some restricted two-dimensional possibilities. This was considered appropriate as the lithology near potash mines in Saskatchewan tends to be fairly consistent in elevation and thickness. Lateral changes in resistivity near mine are the primary focus of this project.

All of the *COMSOL* models are essentially similar to an out-of-loop configuration (or slingram-type in frequency domain), since the transmission point is a simple magnetic dipole. Due to the reciprocity theorem, changing the leading component in the profile line - either receiver or transmitter - has no effect on the measurements. One of the controls on signal

response is the transmitter receiver separation. The numerical model in *COMSOL* solves for the magnetic field at all points in space. Time varying magnetic fields were typically evaluated at 10, 20, 40, 60 and 100 m transmitter-receiver separations. Certain surface (2D) and volumetric (3D) analysis is also performed at times and is possible due to *COMSOL*'s partial differential equation (PDE) solving method. This type of visualization enables us to understand the interaction of the entire domain at any point in time (or frequency).

3.1.3 Analytic Electromagnetic Solutions

Analytic solutions for electromagnetic fields in a homogeneous Earth are made possible through coupling Maxwell's equations to empirical constitutive relations relevant to the Earth subsurface. Typical constitutive relations that are used and assumed to be valid for the Earth are isotropy, homogeneity, linearity, and the independence of electrical parameters with varying temperature, pressure and time. In addition, the magnetic permeability is also assumed to be equal to that of free space. The full steps in deriving an analytic solution are described in Ward and Holmann (1987). These analytic solutions were used to verify both the spectral semi-analytic solutions derived in *Matlab* and the PDE-based numerical solutions in *COMSOL*. Each of these equations are described mathematically in Cartesian coordinates, and are based on a magnetic dipole vertically orientated in the z-axis at the point of origin ($x = 0$ m, $y = 0$ m, $z = 0$ m).

The analytic solutions for harmonic magnetic dipoles are shown in equations 3.33 and 3.34. Since there is assumed homogeneity, there is no component of the electric field in the vertical direction. The σ term is the host material electrical conductivity and the k term is the wave number, shown in equation 3.35, where the real and imaginary components of the dielectric permittivity are absorbed into the real and imaginary components of the electrical conductivity through a magnitude of $|\sigma(\omega)|$ and conductivity phase of $\phi(\omega)$. The $\tilde{r}$ term is the total distance from the magnetic dipole point ($\tilde{r} = \sqrt{x^2 + y^2 + z^2}$).

$$\mathbf{E} = \frac{i\omega\mu m}{4\pi\tilde{r}^2} exp(-ik\tilde{r})\big(ik\tilde{r} + 1\big)\left(\frac{y}{\tilde{r}}\hat{\mathbf{x}} + \frac{x}{\tilde{r}}\hat{\mathbf{y}}\right). \tag{3.33}$$

$$\mathbf{H} = \frac{m}{4\pi\tilde{r}^3} exp(-ik\tilde{r}) \left[\left(\frac{xz}{\tilde{r}^2}\hat{\mathbf{x}} + \frac{yz}{\tilde{r}^2}\hat{\mathbf{y}} + \frac{z^2}{\tilde{r}^2}\hat{\mathbf{z}} \right) \big(-k^2\tilde{r}^2 + 3ik\tilde{r} + 3 \big) + \big(k^2\tilde{r}^2 - ik\tilde{r} - 1 \big)\hat{\mathbf{z}} \right]. \quad (3.34)$$

$$k = \sqrt{-i\mu|\sigma(\omega)|exp(i\phi(\omega))}. \quad (3.35)$$

The step response of a transient magnetic dipole for both the electric and magnetic fields are shown in equations 3.36 and 3.37. In these formulae, the step response is representing a current turn-on. As with the harmonic magnetic dipole solutions, the space is assumed to be electrically homogeneous. Taking the time derivative of equation 3.37 gives us the change in magnetic field in time calculated from measuring a voltage change response in a typical transient electromagnetic receiver system. The analytic solution for a homogeneous full-space is given in equation 3.38. The time-domain wave number used for each of these solutions is θ; the expression of which is given by equation 3.39.

$$\mathbf{e} = \frac{\mu m\theta^3\tilde{r}}{2\pi^{\frac{3}{2}}t} exp(-\theta^2\tilde{r}^2) \bigg(-\frac{y}{\tilde{r}}\hat{\mathbf{x}} + \frac{x}{\tilde{r}}\hat{\mathbf{y}} \bigg). \quad (3.36)$$

$$\begin{aligned} \mathbf{h} = \frac{m}{4\pi\tilde{r}^3} exp(-\theta^2\tilde{r}^2) \Bigg(\Bigg[\bigg(\frac{4}{\pi^{\frac{1}{2}}}\theta^3\tilde{r}^3 + \frac{6}{\pi^{\frac{1}{2}}}\theta\tilde{r} \bigg) exp(-\theta^2\tilde{r}^2 + 3erfc(\theta\tilde{r}) \Bigg] \\ \times \Bigg[\frac{xz}{\tilde{r}}\hat{\mathbf{x}} + \frac{yz}{\tilde{r}}\hat{\mathbf{y}} + \frac{z^2}{\tilde{r}^2}\hat{\mathbf{z}} \Bigg] - \Bigg[\bigg(\frac{4}{\pi^{\frac{1}{2}}}\theta^3\tilde{r}^3 + \frac{2}{pi^{12}}\theta\tilde{r} \bigg) exp(-\theta^2\tilde{r}^2) + erfc(\theta\tilde{r}) \Bigg]\hat{\mathbf{z}} \Bigg). \end{aligned} \quad (3.37)$$

$$\frac{\mathrm{d}\mathbf{h}}{\mathrm{d}t} = \frac{m\theta^3}{\pi^{\frac{3}{2}}t} exp(-\theta^2\tilde{r}^2) \left[\theta^2\tilde{r}^2 \left(\frac{xz}{\tilde{r}^2}\mathbf{u}_x + \frac{yz}{\tilde{r}^2}\mathbf{u}_y + \frac{z^2}{\tilde{r}^2}\mathbf{u}_z) \right) + (1 - \theta^2\tilde{r}^2)\mathbf{u}_z \right]. \quad (3.38)$$

$$\theta = \left(\frac{\mu\sigma}{4t} \right)^{\frac{1}{2}}. \quad (3.39)$$

The half-space analytic solutions are slightly more complicated to arrive at, but Ward and Hohmann (1987) derived a workable set of solutions that are valid only in the plane of the transmitter. These solutions use cylindrical coordinates instead of Cartesian. This introduces an additional term into the solution sets of r which is the distance in the plane of the transmitter. These half-space solutions assume half of the space is infinitely resistivity, while the other half is set at some value of conductivity (σ). Harmonic magnetic dipole half-space solutions for the tangential electric field, and the vertical and radial magnetic fields are shown in equations 3.40, 3.41, and 3.42 respectively. Transient magnetic dipole half-space solutions for the time step response for the tangential electric field and the vertical and radial magnetic fields are shown in equations 3.43, 3.44, and 3.45 respectively. Time derivatives of the magnetic fields (vertical and radial) are shown in equations 3.46 and 3.47. The time step radial magnetic field responses use modified Bessel functions of the first and second kind (I_α and J_α respectively) of order α.

$$E_\phi = \frac{-m}{2\pi\sigma r^4}\left[3 - \left(3 + 3ikr - k^2r^2\right)exp(-ikr)\right]. \tag{3.40}$$

$$H_z = \frac{-m}{2\pi k^2 r^5}\left[9 - \left(9 + 9ikr - 4k^2r^2 - ik^3r^3\right)exp(-ikr)\right]. \tag{3.41}$$

$$H_r = \frac{-mk^2}{4\pi r}\left[I_1\left(\frac{ikr}{2}\right)K_1\left(\frac{ikr}{2}\right) - I_2\left(\frac{ikr}{2}\right)K_2\left(\frac{ikr}{2}\right)\right]. \tag{3.42}$$

$$e_\phi = \frac{-m}{2\pi\sigma r^4}\left[3erf(\theta r) - \frac{2}{\pi^{\frac{1}{2}}}\theta r\left(3 + 2\theta^2r^2\right)exp(-\theta^2r^2)\right]. \tag{3.43}$$

$$h_z = \frac{m}{4\pi r^3}\left[\frac{9}{2\theta^2r^2}erf(\theta r) - erf(\theta r) - \frac{1}{\pi^{\frac{1}{2}}}\left(\frac{9}{\theta r} + 4\theta r\right)exp(-\theta^2r^2)\right]. \tag{3.44}$$

$$h_r = \frac{-mk^2}{4\pi r}\left[I_1\left(\frac{ikr}{2}\right)K_1\left(\frac{ikr}{2}\right) - I_2\left(\frac{ikr}{2}\right)K_2\left(\frac{ikr}{2}\right)\right]. \tag{3.45}$$

$$\frac{\partial h_z}{\partial t} = -\frac{m}{2\pi\mu_0\sigma r^5}\left[9erf(\theta r) - \frac{2\theta r}{\pi^{\frac{1}{2}}}(9 + 6\theta^2r^2 + 4\theta^4r^4)e^{-\theta^2r^2}\right]. \tag{3.46}$$

$$\frac{\partial h_r}{\partial t} = -\frac{mr\theta^2}{2\pi r} exp(\frac{-\theta^2 r^2}{2}) \left[I_1\left(\frac{\theta^2 r^2}{2}\right) - I_2\left(\frac{\theta^2 r^2}{2}\right) \right]. \tag{3.47}$$

3.1.4 Forward Modelling Validation

In order to validate the accuracy of the spectral semi-analytical solutions produced in *Matlab* as well as the numerical PDE-based solutions produced in *COMSOL*, several homogeneous models were constructed and compared with analytic calculations from the solutions seen in section 3.1.3. Figures 3.5 and 3.6 show the PDE-based magnetic and electric field responses at 40 m and 100 m transmitter-receiver horizontal separation (1 m vertical position) to a transient magnetic dipole turn-on of 1 A m^2; the full-space used both 10 Ω m and 100 Ω m resistivity. All other PDE-based solutions were constructed using a magnetic dipole turn-off in order to duplicate actual transient electromagnetic systems. However, when it comes to the time derivative of the magnetic field response, the only change a turn-off/turn-on system would cause would be to change the polarity of the calculated or measured response. Either approach would work for the bulk of our purpose in this project.

Figures 3.7 and 3.8 show the PDE-based time derivative magnetic field solutions to a magnetic dipole turn-off calculated using magnetic vector potential initial conditions, comparing them with analytic solutions for 10 Ω m and 100 Ω m resistive full-spaces. As with the previous figures, both 40 m and 100 m transmitter/receiver horizontal separations are depicted. Vertical location of the receiver is also at 1 m. There is a some degree of noise in very early time, especially at 100 m Tx-Rx separation in a full-space of 10 Ω m. This is due to the larger distance and slower diffusion speed leading to a later time for the current to pass the receiver location and allow the field response to enter late time. In general, the numerical PDE-based solutions appear to struggle during early time polarity changes in the magnetic field decay. This was not seen as a concern as time-derivative magnetic field analysis commonly focuses on the late time decay. The time to build a PDE-based numerical model in *COMSOL* depended on the resistivity and the length of time observed, but for the complex, mostly conductive models used in the forward models the build time was around 65 s.

Figures 3.9 and 3.10 show spectral semi-analytic solutions produced by the *Matlab* func-

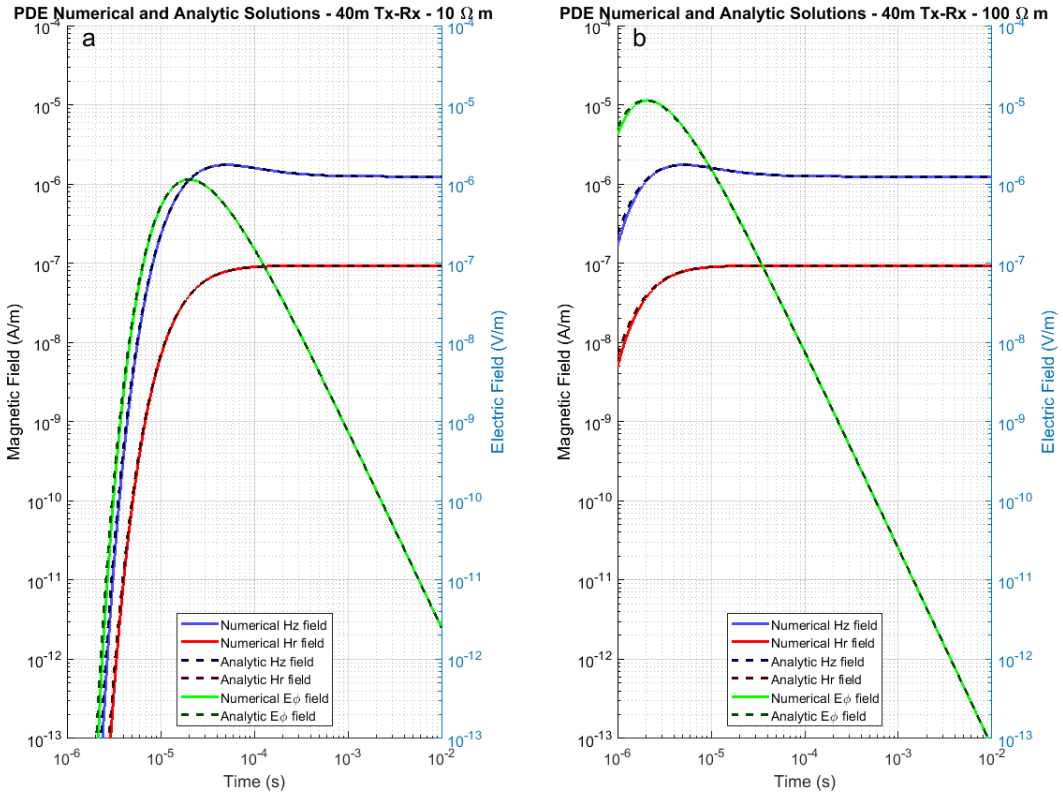

Figure 3.5: **Comparing the PDE-based numerical magnetic and electric field solutions produced in** $COMSOL$ **to homogeneous analytic solutions. Full-space resistivity was set at** $10\ \Omega$ **m in figure a) and** $100\ \Omega$ **m in figure b). Receiver position was set at** $r = 40$ **m and** $z = 1$ **m. Response is to a** 1 **A m**^{2} **magnetic dipole turn-on.**

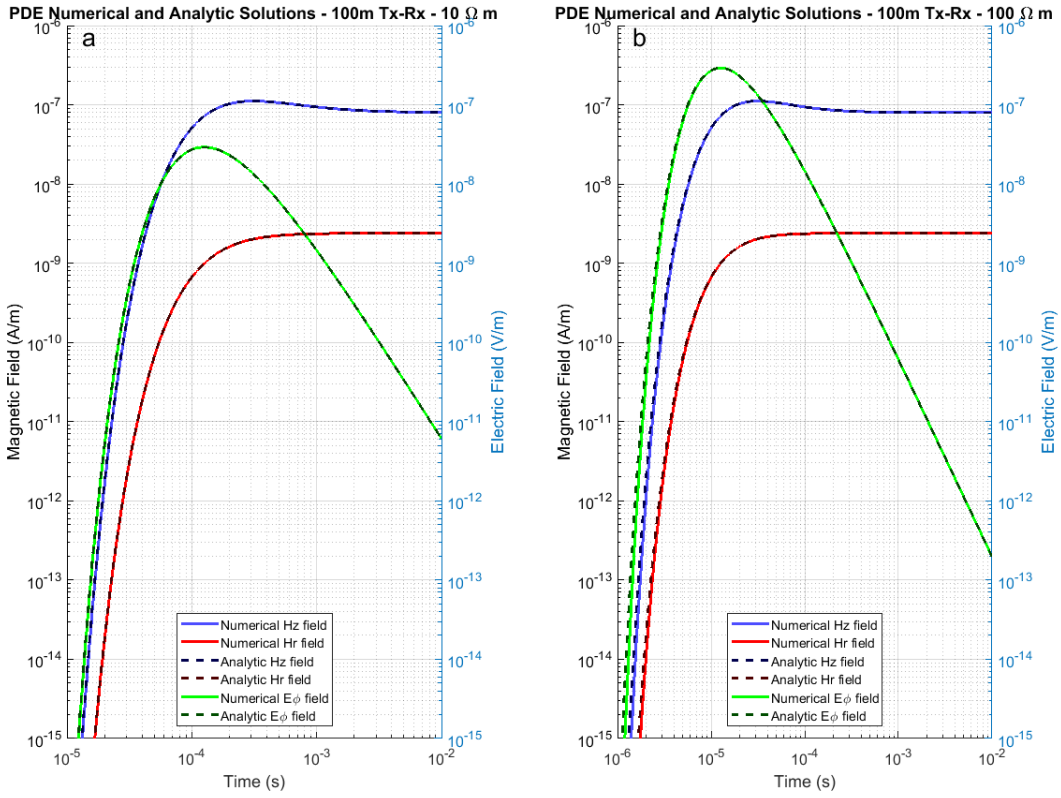

Figure 3.6: **Comparing the PDE-based numerical magnetic and electric field solutions produced in** $COMSOL$ **to homogeneous analytic solutions. Full-space resistivity was set at** $10\ \Omega$ **m in figure a) and** $100\ \Omega$ **m in figure b). Receiver position was set at** $r = 100$ **m and** $z = 1$ **m. Response is to a** 1 **A m**^{2} **magnetic dipole turn-on.**

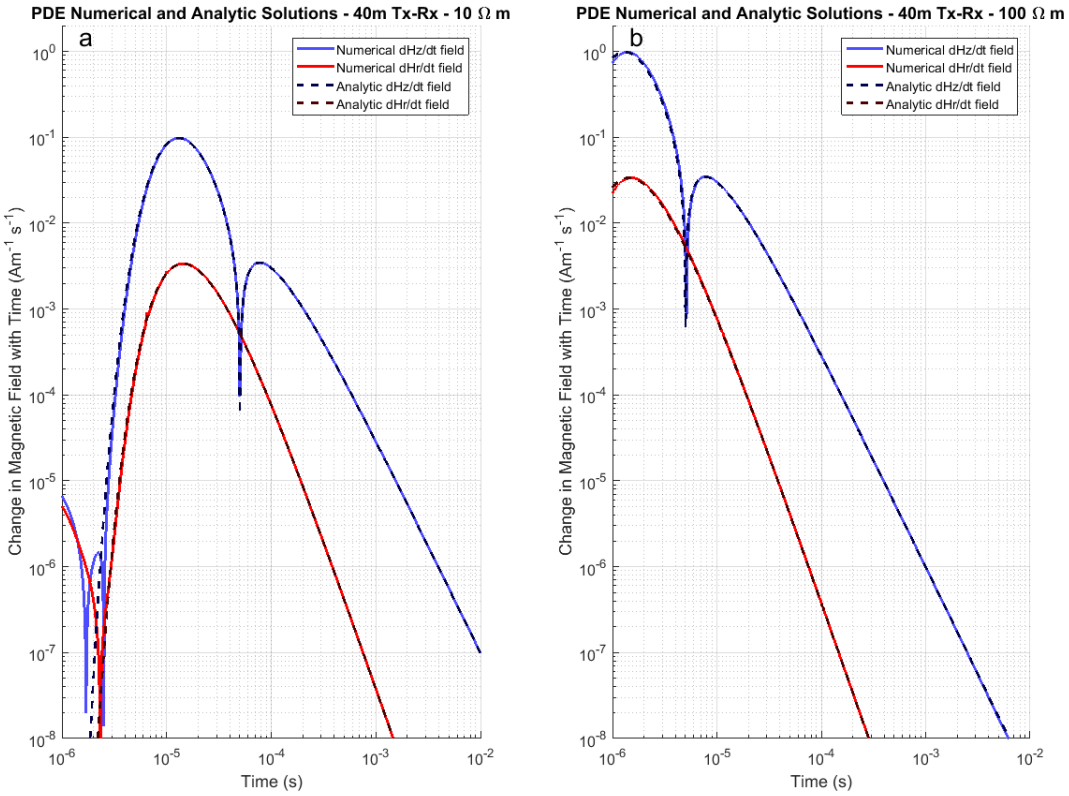

Figure 3.7: **Comparing the PDE-based numerical time derivative of the magnetic field solutions produced in $COMSOL$ to homogeneous analytic solutions. Full-space resistivity was set at $10\ \Omega$ m in figure a) and $100\ \Omega$ m in figure b). Receiver position was set at $r = 100$ m and $z = 1$ m. Response is to a 1 Am^2 magnetic dipole turn-off, duplicated through magnetic vector potential initial conditions.**

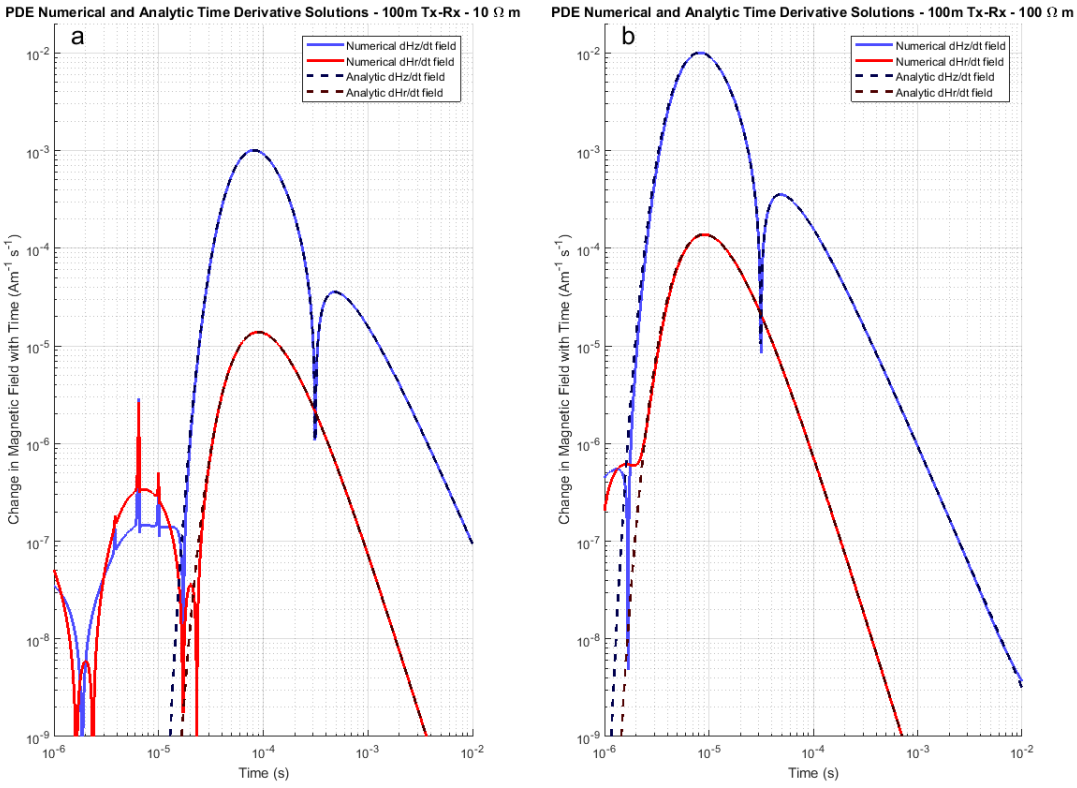

Figure 3.8: **Comparing the PDE-based numerical time derivative of the magnetic field solutions produced in *COMSOL* to homogeneous analytic solutions. Full-space resistivity was set at 10 Ω m in figure a) and 100 Ω m in figure b). Transmitter-receiver separation was set at 40 m. Response is to a 1 Am^2 magnetic dipole turn-off, duplicated through magnetic vector potential initial conditions.**

tions created to replicate Das' formalism as described in section 3.1.1 being compared with analytic solutions for both frequency domain responses as well as time-derivative magnetic field responses. The locations of the receiver and full-space resistivity were set at $r = 40$ m, $z = 1$ m, $\rho = 100$ Ω m and $r = 100$ m, $z = 1$ m, $\rho = 10$ Ω m respectively. The first example is a situation of a near receiver in a high electromagnetic diffusion speed environment, and the second for a far receiver in a low electromagnetic diffusion speed environment. The early time response matches the analytic solutions fairly well, including matching the polarity shift near perfectly. As the late time signal approaches 10 ms the calculated signal begins to show obvious signs of fluctuation in amplitude and no longer matches the analytic decay curve, especially in the low signal radial field. The time to produce these calculations depend on the number of layers, but for homogeneous environments, the run time was around 55 s. Each build only calculates the signal at one point in space.

A point of interest when comparing full-space environments to the traditional half-space environments of electromagnetics performed on the surface of the Earth is that the full-space vertical field decay response has a higher amplitude in signal as well as a corresponding later transition between early and late time when compared to the half-space model. This is due to the increase in conductivity above the survey, as even resistive rock will be more conductive than air. The implication is that, given a comparable Earth resistivity, electromagnetic surveys conducted underground would benefit from a higher signal-to-noise ratio when compared to a similar survey on the surface. To illustrate this, figure 3.11 shows two models - one is full-space and the other is half-space - both with a homogeneous resistivity of 100 Ω m. This signal contrast would be even higher if the full- and half-space resistivity were lower.

Another note of interest is the shape that the current "smoke-rings" that are produced by time-domain EM pulses. In traditional surface surveys, the half-space environment introduces a high enough resistivity contrast between the sub-surface below and the air above that the current diffuses outward and down. Figure 3.12 shows the current distribution and magnetic field streamlines at 0.01 s in a half-space homogeneous environment of 30 Ω m. In contrast, a pure full-space environment (with homogeneous resistivity above and below the transmitting plane) will produce a "smoke-ring" that diffuses laterally. Figure 3.13 also

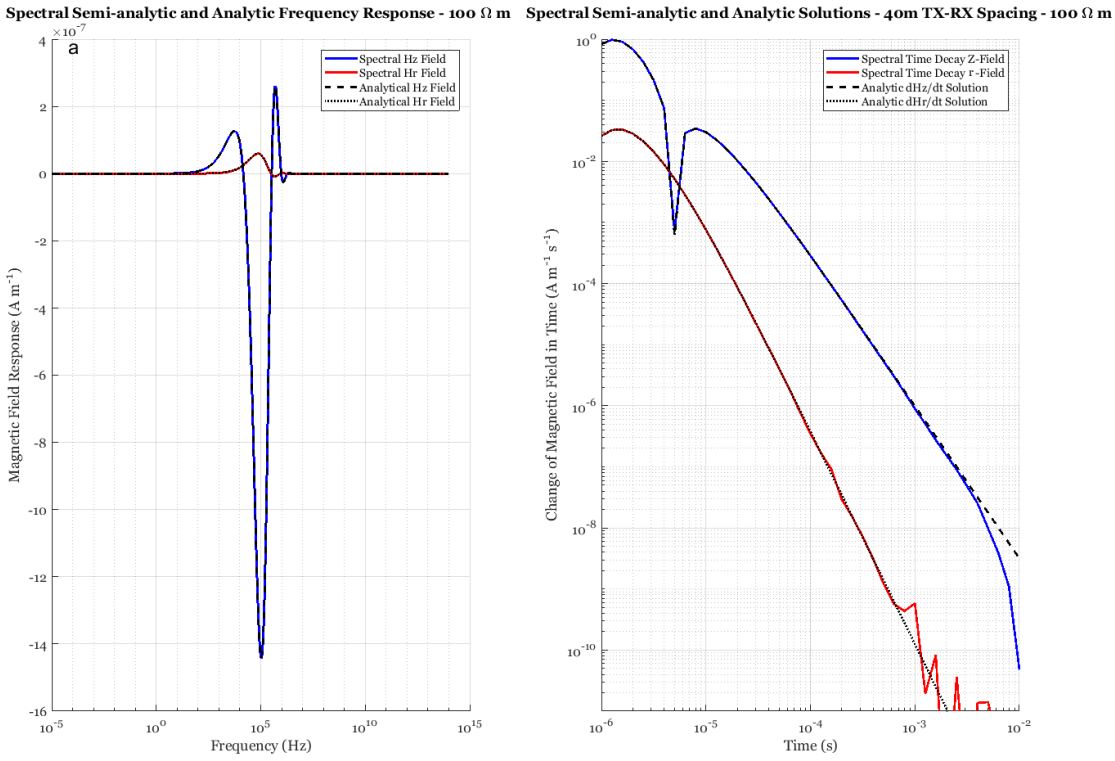

Figure 3.9: **Comparing the spectral semi-analytic solutions derived in *Matlab Mathworks* to homogeneous analytic solutions. Full-space resistivity was set at** 100 Ω **m. Transmitter-receiver separation was set at** 40 **m. Figure a) shows the frequency dependant response and figure b) shows the time dependant response.**

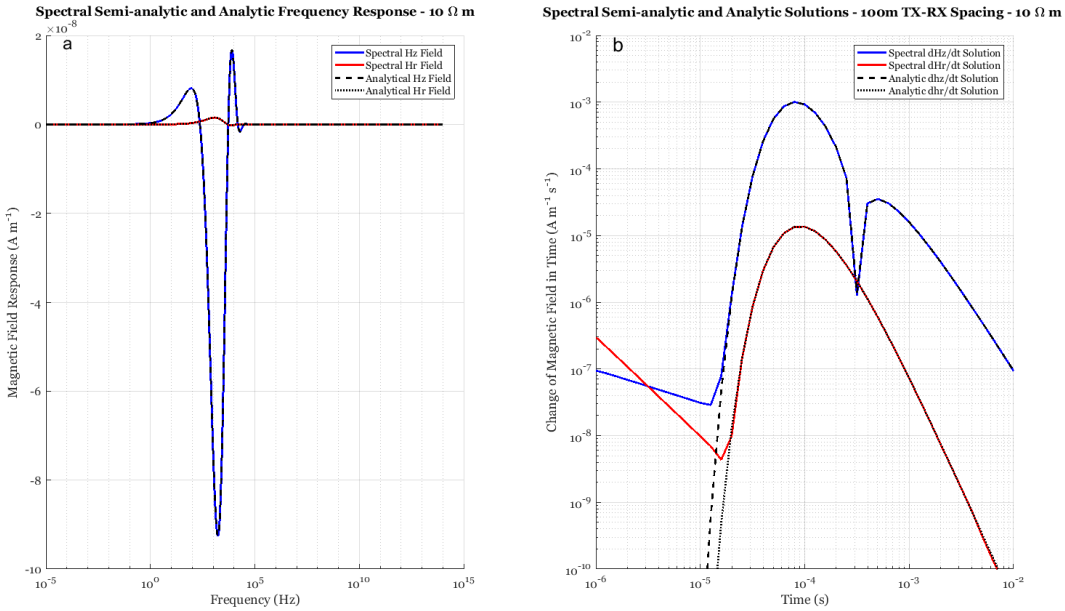

Figure 3.10: **Comparing the spectral semi-analytic solutions derived in *Matlab Mathworks* to homogeneous analytic solutions. Full-space resistivity was set at** 10 Ω **m. Transmitter-receiver separation was set at** 100 **m. Figure a) shows the frequency dependant response and figure b) shows the time dependant response.**

shows the current distribution and magnetic field streamlines in a homogeneous environment of 30 Ω m, although this time it is in full-space.

Lastly, a couple of layered Earth tests were done by comparing both layered spectral models with layered PDE-based numerical models. Figure 3.14 shows the time decay signal from both models at 40 m and 100 m transmitter/receiver separation. This layered model was a simple construction of a single conductive layer directly below the transmitting layer within a resistive full-space ($\rho = 100$ Ω m). The conductive layer was 100 m wide and had a resistivity of 10 Ω m. Another model was also constructed, this time featuring a resistive layer in a conductive full-space. All parameters were the same as the previous example, except that the resistivity of the 100 m layer and the full-space were switched. The results of these models can be seen in figure 3.15. For both of these models the results match extremely well. They give a degree of confidence that the PDE-based numerical layered models are accurate for the purposes outlined in sections 3.1 and 3.3.

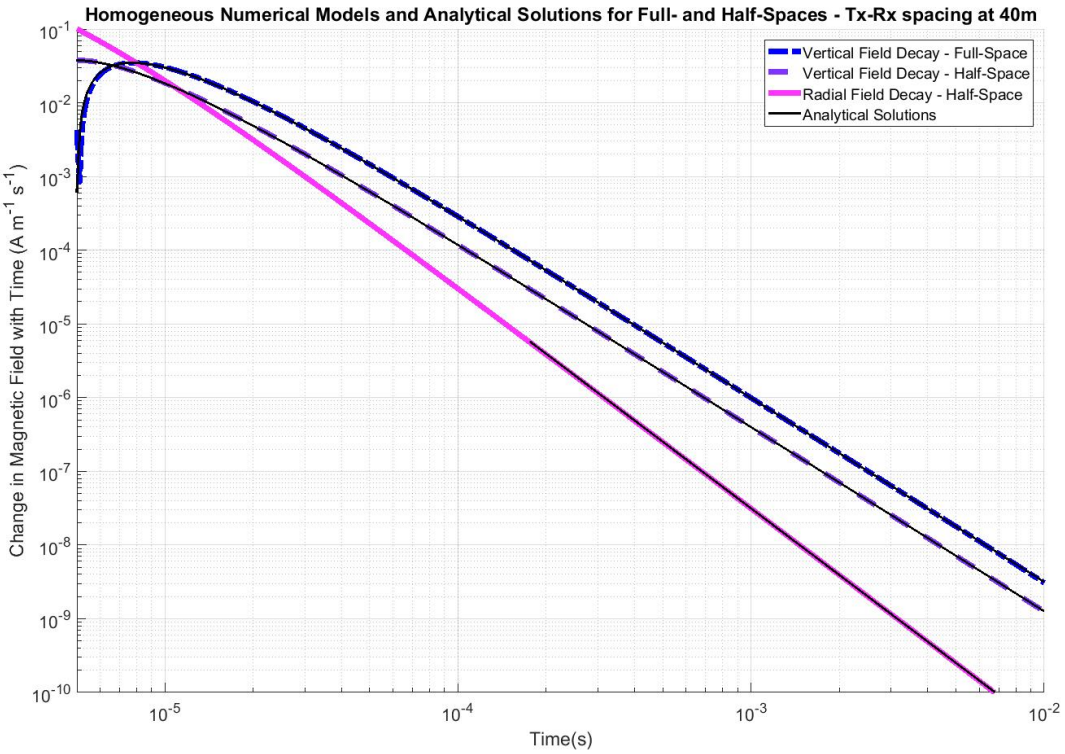

Figure 3.11: **Illustrating the difference between full-space and half-space responses. Both models are homogeneous, set at** $100\ \Omega$ **m, and have the receiver in the plane of the transmitter at** 40 **m distance.**

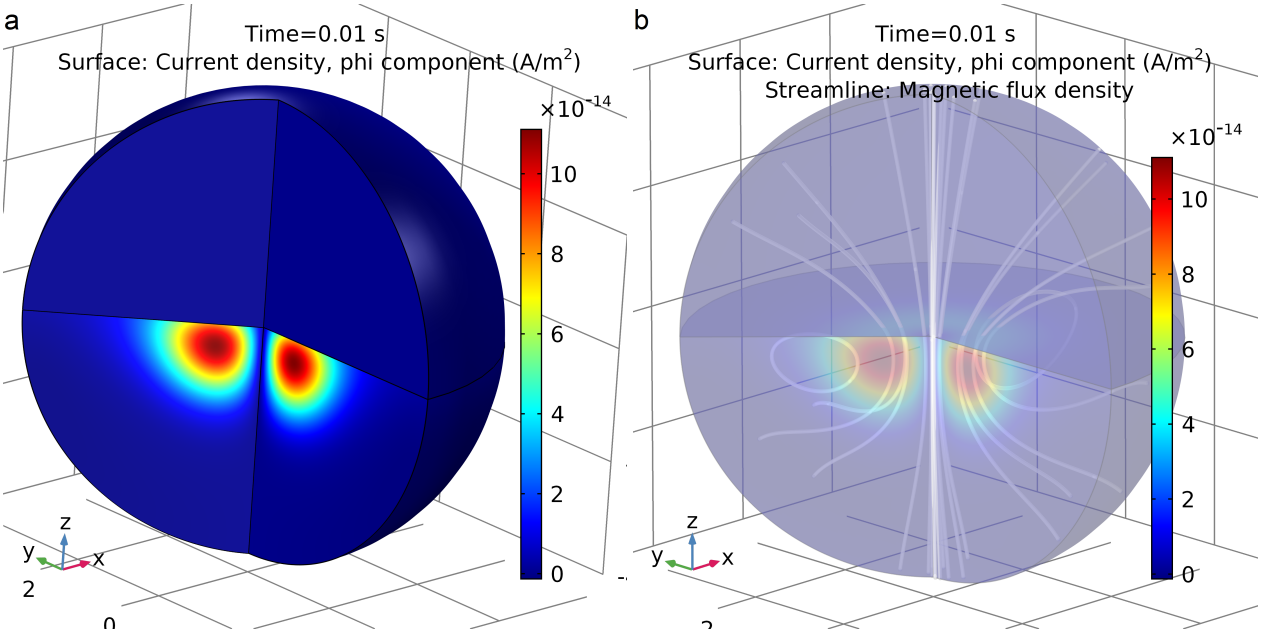

Figure 3.12: **Half-space homogeneous environment** 0.01 **s after a time-domain EM pulse (**$\rho = 30\ \Omega$ **m). Colour contours show current density and the streamlines in b) show the direction of the magnetic field.**

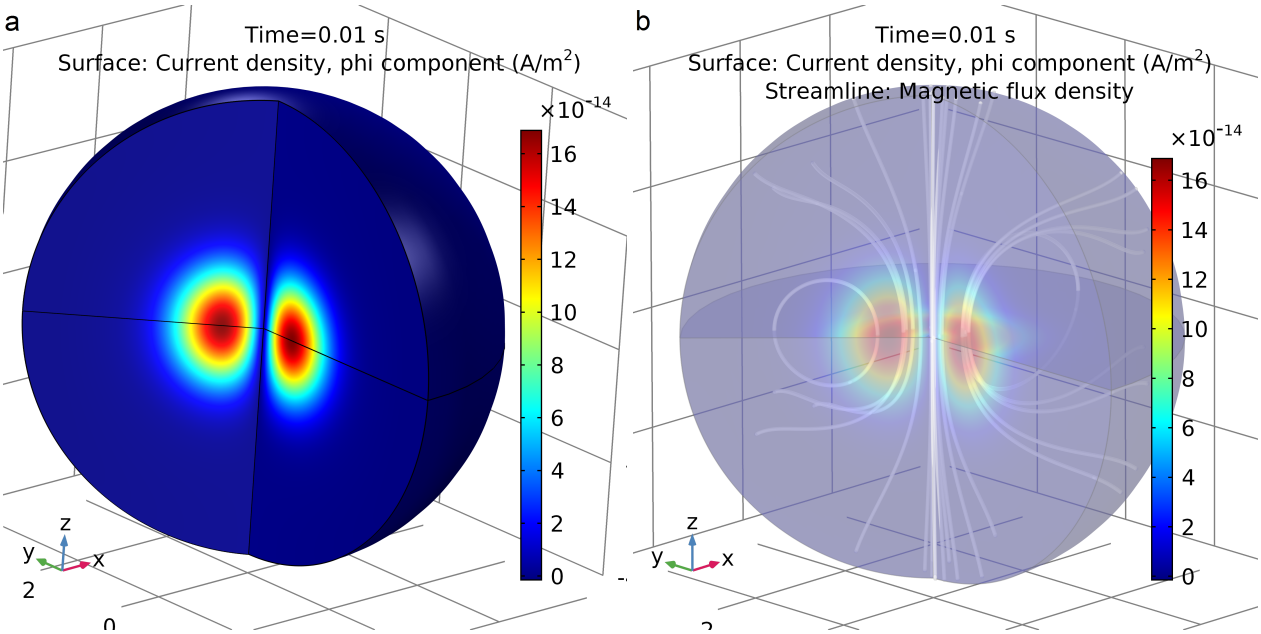

Figure 3.13: **Full-space homogeneous environment** 0.01 **s after a time-domain EM pulse (**$\rho = 30\ \Omega$ **m). Colour contours show current density and the streamlines in b) show the direction of the magnetic field.**

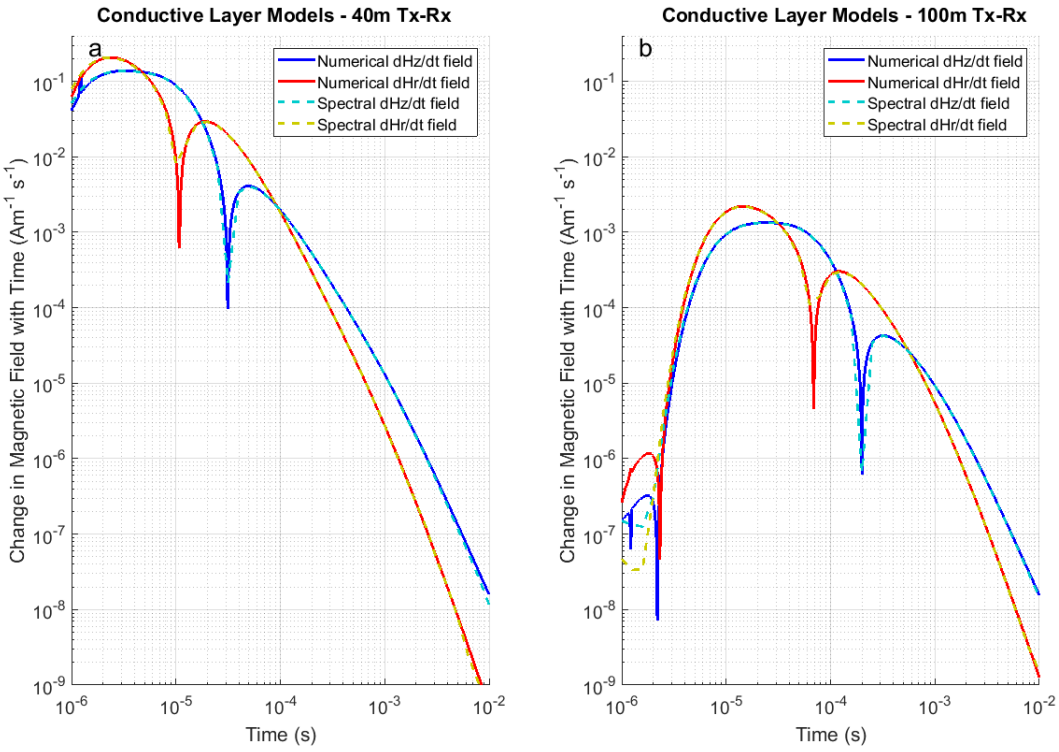

Figure 3.14: **Example of a set of non-homogeneous models of a conductive layer within a resistive full-space, comparing both semi-analytic spectral and PDE-based numerical solutions. The parameters of the conductive layer were** 100 **m thick and** 10 Ω **m resistive. The layer was placed directly below the transmitting plane. The full-space had a resistivity of** 100 Ω **m.**

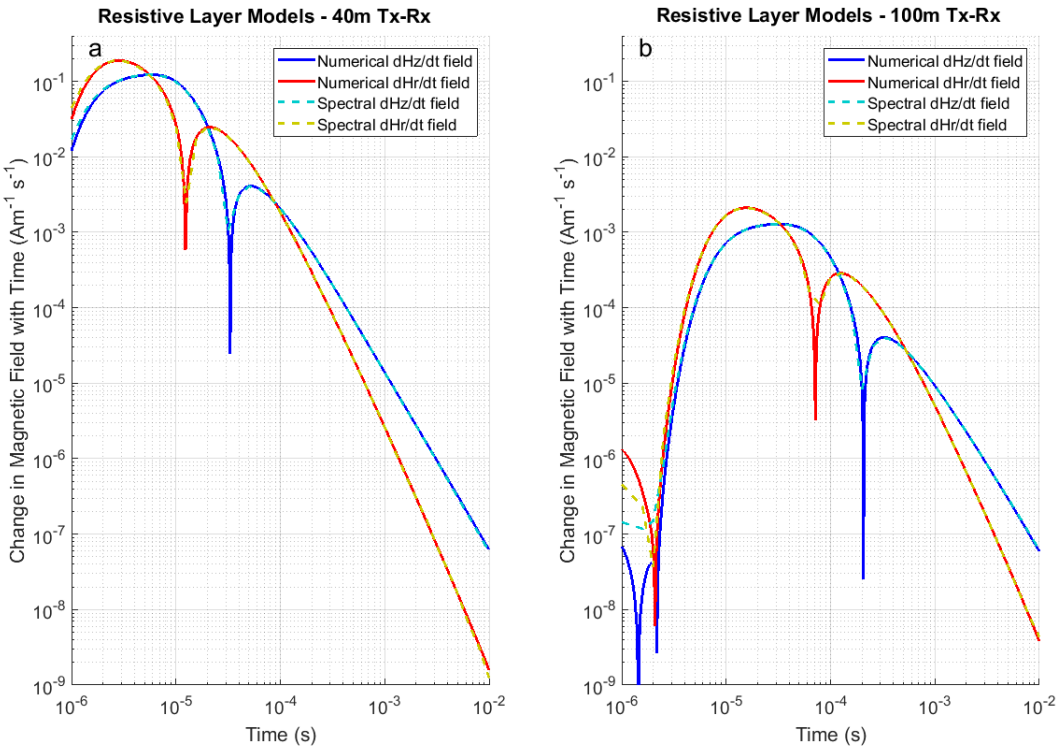

Figure 3.15: **Example of a set of non-homogeneous models of a resistive layer within a conductive full-space, comparing both semi-analytic spectral and PDE-based numerical solutions. The parameters of the resistive layer were** 100 **m thick and** 100 Ω **m resistive. The layer was placed directly below the transmitting plane. The full-space had a resistivity of** 10 Ω **m.**

3.1.5 Visualizing Current Density and Magnetic Fields

For the purposes of illustrating the effects of current distribution in varying environments, a series of time-slices were constructed using the PDE-based numerical modelling in *COMSOL Multiphysics*. These time-slices were selected around polarity changes of the vertical magnetic field decay observed at $r = 60$ m and $z = 1$ m in two homogeneous half-space environments. One half-space environment was selected to represent a resistive environment (120 Ω m), while the other was conductive (30 Ω m). The time decay signal received at the location of $r = 60$ m and $z = 1$ m is shown in figure 3.16 while the dashed lines indicate the selected time-slices. Figures 3.17, 3.18, and 3.19 show the distribution of current in two different half-space homogeneous environments - one conductive (30 Ω m) and one resistive (120 Ω m). Sub-figure a) shows the surface vertical magnetic field time derivative at the point in time analyzed as well as the current density at a depth approximate to the maximum current density below the surface in that specific model. The depth of the line graph of current density varied, but the line always stayed at a constant depth and extended from $r = 0$ m to $r = 120$ m. Sub-figures b) and c) show a cross-section contour of the current density against depth and position around the receiver point for both the conductive and resistive models respectively. Note that the position just to the right of the high current density (in the centre of the magnetic flux streamlines) correlates to the horizontal position of the polarity change in the magnetic field signal decay in the plane of the transmitter. This diffusion of current in the subsurface is downward (and, in the case of an in-mine survey, upward as well) and outward from the transmitting point. In 3D geometry this diffusion of current would form "smoke-rings" in the subsurface.

3.1.6 Current Density and Full-space Resistivity

The role resistivity plays in a full-space environment for inductive geophysical tools is interesting. With both traditional galvanic and surface electromagnetic surveys there is a degree of direction that the operators have on the signal. However, with electromagnetic surveys in full-space environments the signal travels in both directions on either side of the plane of the transmitting loop. The degree to which the signal does travel in each direction is directly

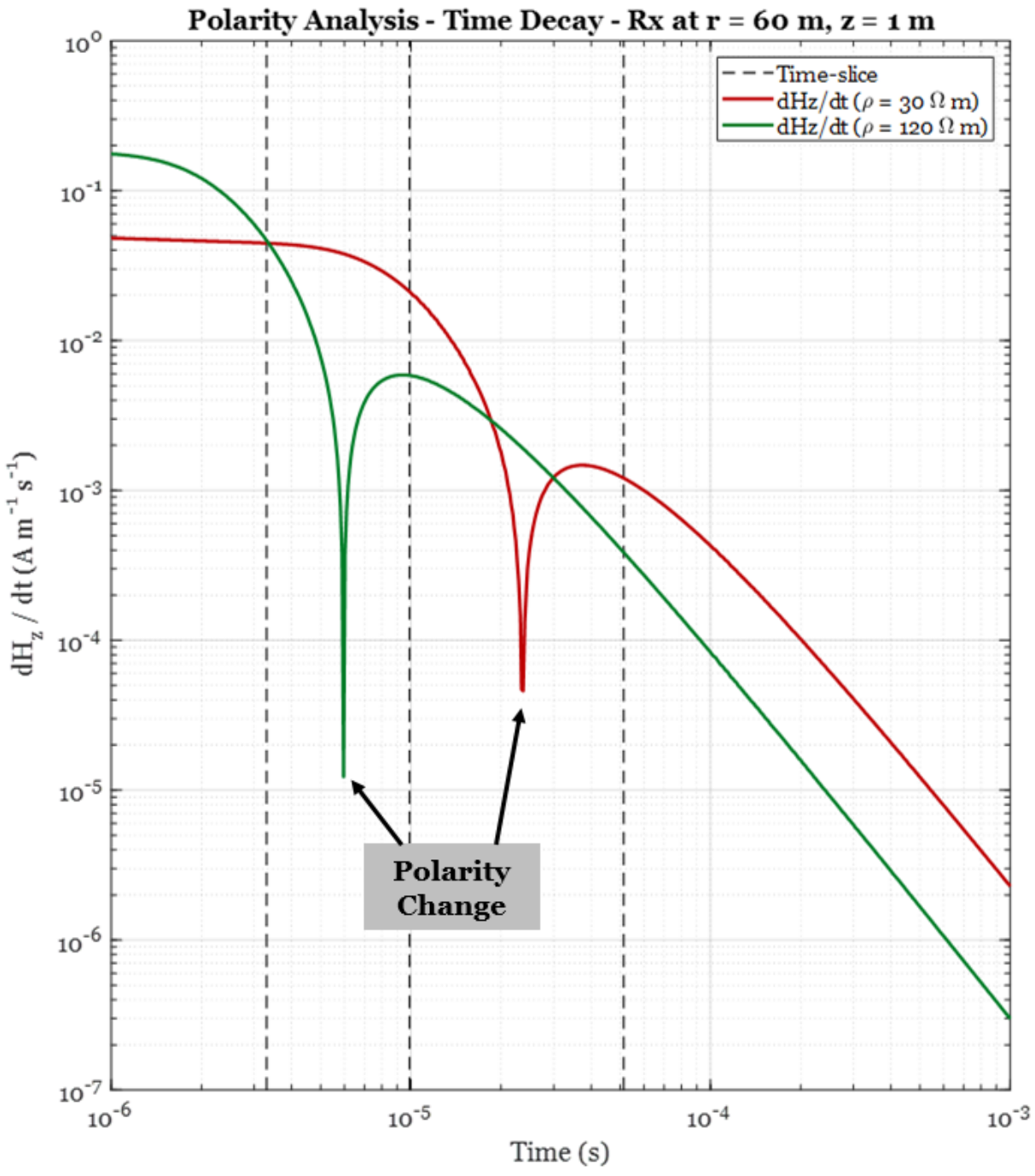

Figure 3.16: **Polarity change and current density analysis. Comparing two homogeneous models (at 30 Ω m and 120 Ω m). The time-slices highlighted are shown on figures 3.17, 3.18, and 3.19.**

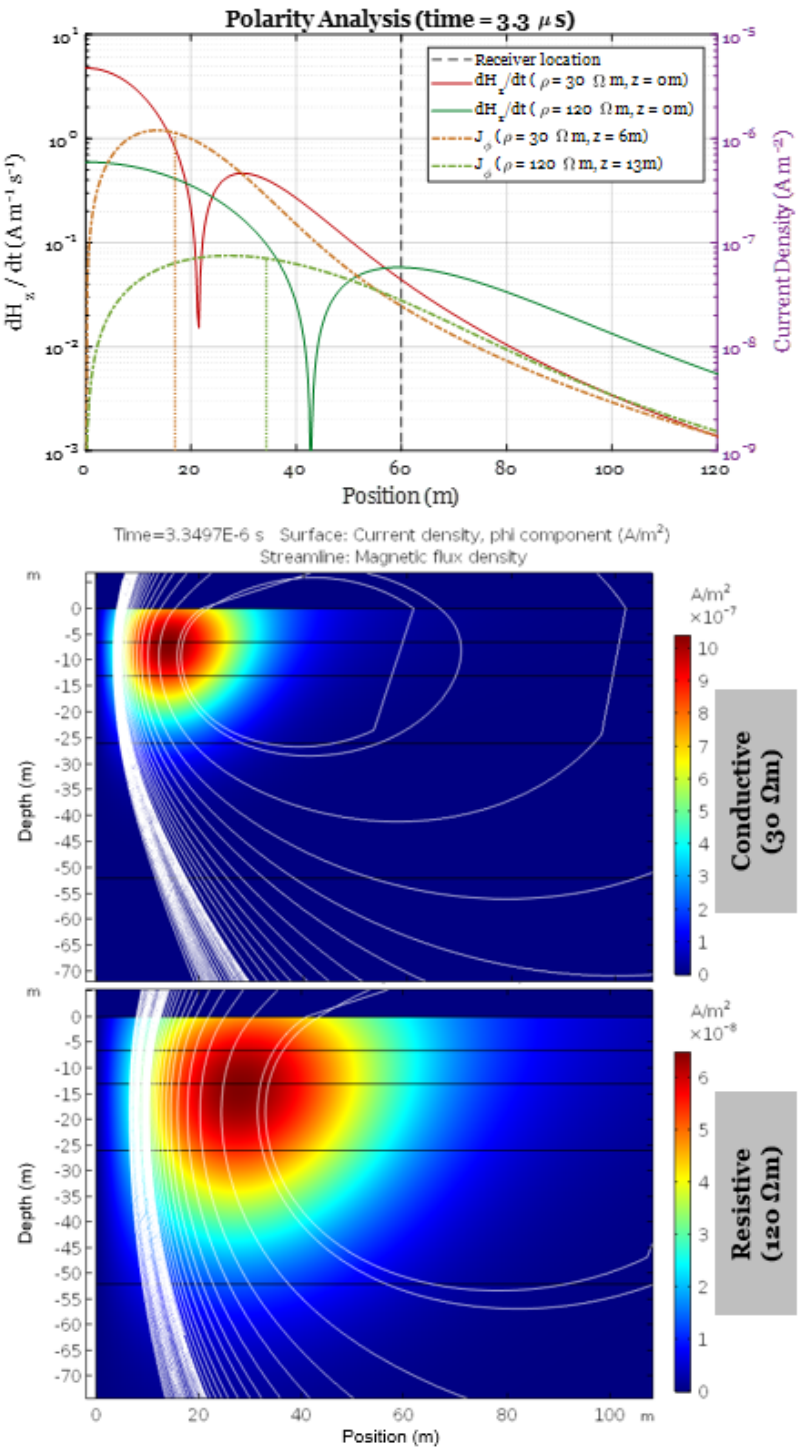

Figure 3.17: **Polarity change and current density analysis. Comparing the magnitude of the current density and magnetic field time decay around a receiver at 60 m Tx-Rx separation at 3.3 μs for two homogeneous models at 30 Ω m and 120 Ω m. Tx-Rx plane at 0 m. Streamlines in b) and c) represent the direction of the magnetic flux density.**

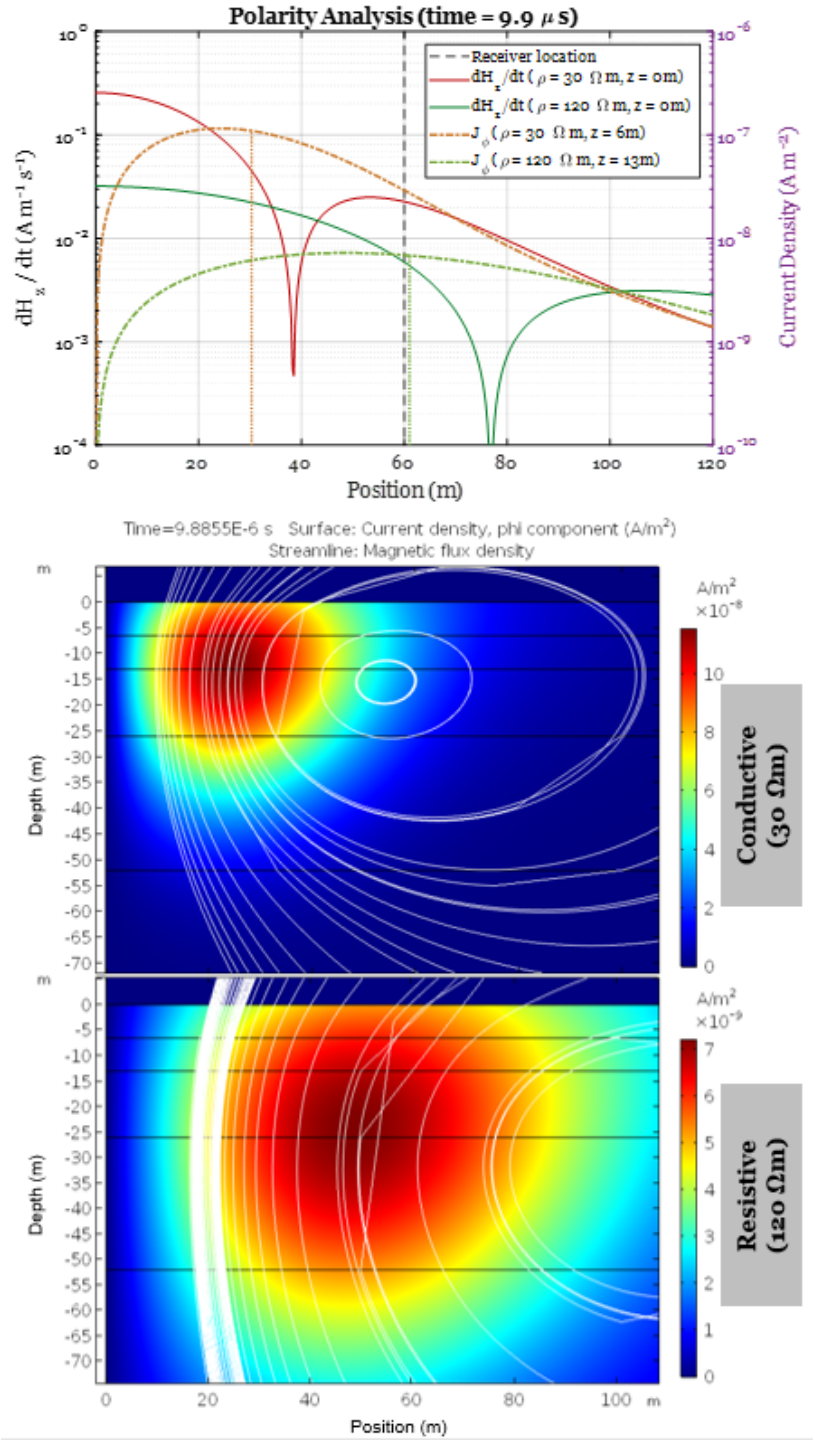

Figure 3.18: **Polarity change and current density analysis. Comparing the magnitude of the current density and magnetic field decay around a receiver at 60 m Tx-Rx separation at 9.9 μs for two homogeneous models at 30 Ω m and 120 Ω m. Tx-Rx plane at 0 m. Streamlines in b) and c) represent the direction of the magnetic flux density.**

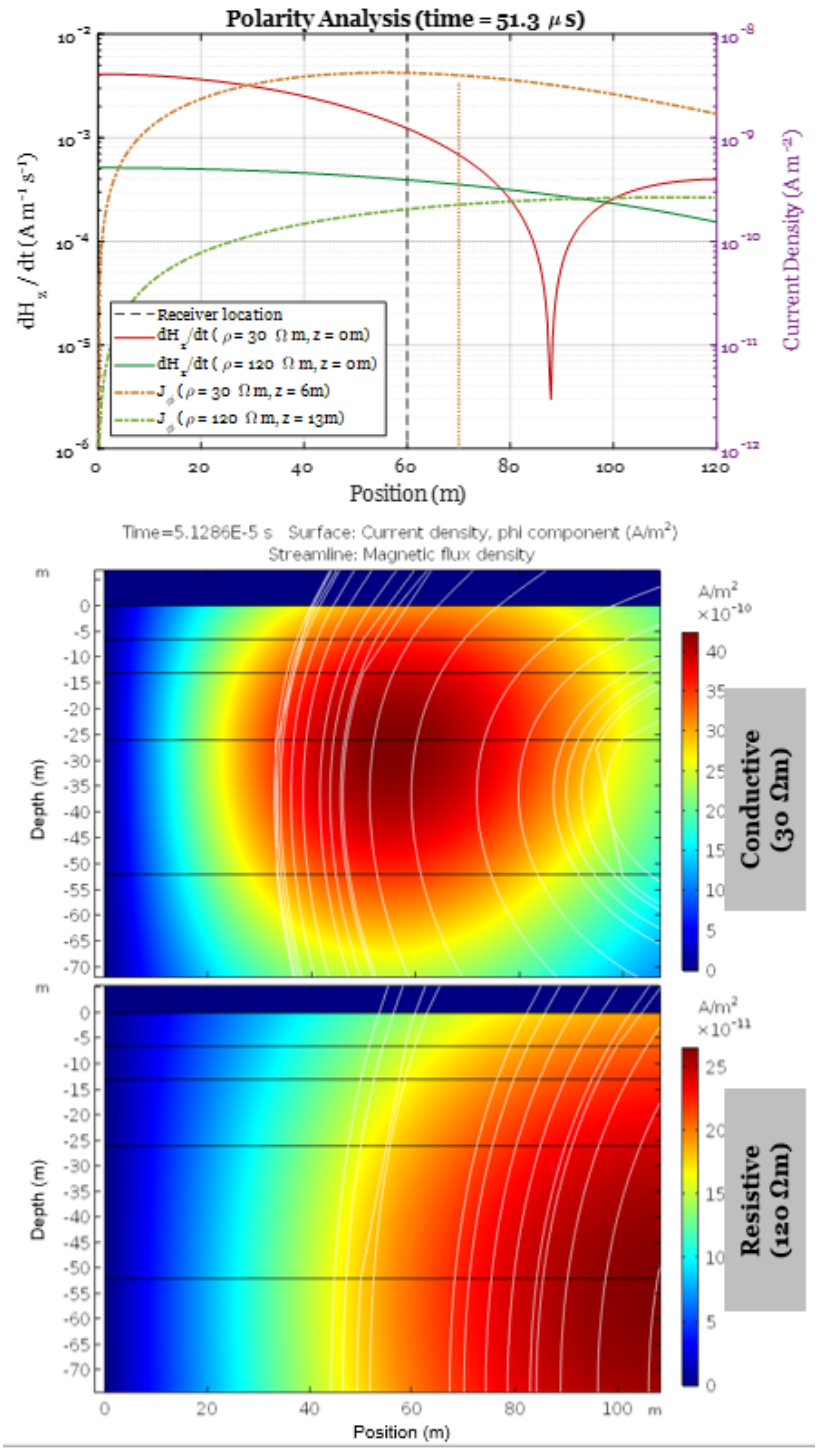

Figure 3.19: **Polarity change and current density analysis. Comparing the magnitude of the current density and magnetic field decay around a receiver at 60 m Tx-Rx separation at 51.3 μs for two homogeneous models at 30 Ω m and 120 Ω m. Tx-Rx plane at 0 m. Streamlines in b) and c) represent the direction of the magnetic flux density.**

related to the resistivity of the environment. To illustrate this phenomenon in a very simple and general way, a series of forward full-space heterogeneous resistivity models were constructed. These models were sets of two resistivity homogeneous half-spaces built together in opposite directions around the transmitting layer. The resistivity of the upper half-space was set unchangingly at 10 Ω m. The lower half-space resistivity was set to varying values ranging from 10 Ω m to 1280 Ω m. In order to analyze the current distribution in each of the half-spaces, the ϕ-component of the current density was integrated over each half-space. Since the 2D-axisymmetric models in COMSOL do not produce current density in either the r- or z-directions, the integration of J_ϕ over the half-space is an appropriate representation of the amount of current - or signal - in the half-space. Figure 3.20.a shows the total current in the lower and upper half-spaces for each of the models. Current decreases in time in both half-spaces at roughly the same rate in every instance. However, the more resistive the lower half-space becomes the less amount of current it retains. In contrast, there appears to be a slight increase in current in the upper-half space as the lower half-space becomes more resistive. In this figure the red solid curves are the lower (changing) half-space, and the blue dashed curves are the upper (unchanging) half space. For both of these curves the darker curves represent the more conductive lower half-space models and the lighter represent the more resistive models. Figures 3.20.b and 3.20.c show the distribution of the current density of the end case models at time equal to 0.01 s.

Figure 3.21 illustrates the ratio of the current in the upper half-space to the lower half-space (blue curves - left axis). This relationship is relatively consistent over time (as suggested in figure 3.20); however, the ratio of current in the half-spaces is plotted over several instances of time to indicate the small changes that do occur. In the end extreme case, the ratio increases to roughly between 35 and 45, depending on the time slice analyzed. On the right y-axis is plotted the absolute current density in both half-spaces at the time slice 0.0001 s or 0.1 ms. The scale on this axis is linear which helps highlight the noticeable increase in current in the upper half-space as the resistivity in the lower half-space increases. Despite this increase in the upper-half space, the total current in the model does decrease overall as resistivity increases.

A second set models were constructed analyze the effects of proximity of resistivity varia-

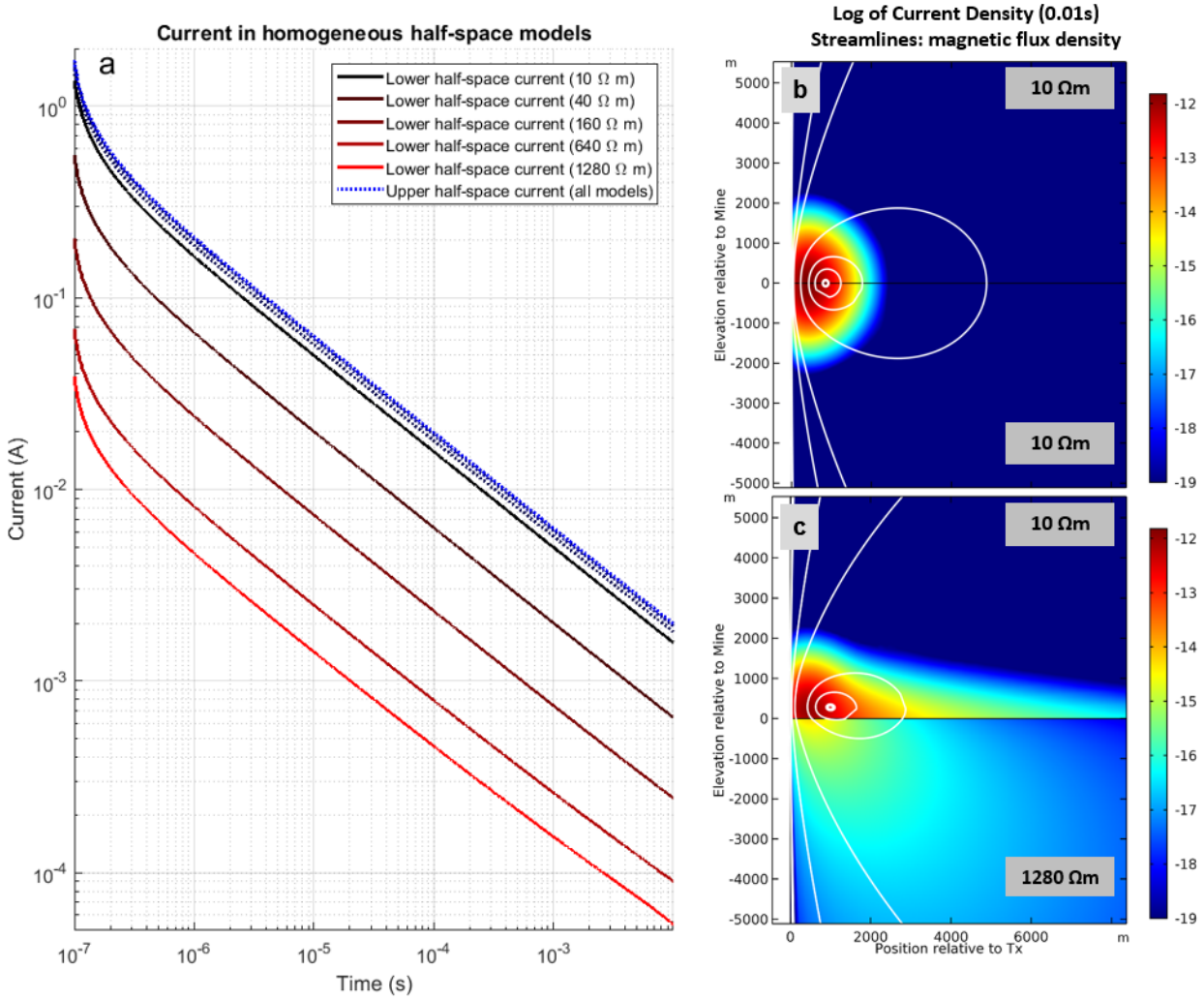

Figure 3.20: **Current in half-space models with varying resistivity in one of the half-spaces. a) shows the current (integrated from the current density of the area that comprises the respective half space) for both half-spaces in each of the models. b) and c) show the log of the current density at 0.01 s for the model where each half-space was set at 10 Ω m and for the model when the lower half-space was changed to 1280 Ω m.**

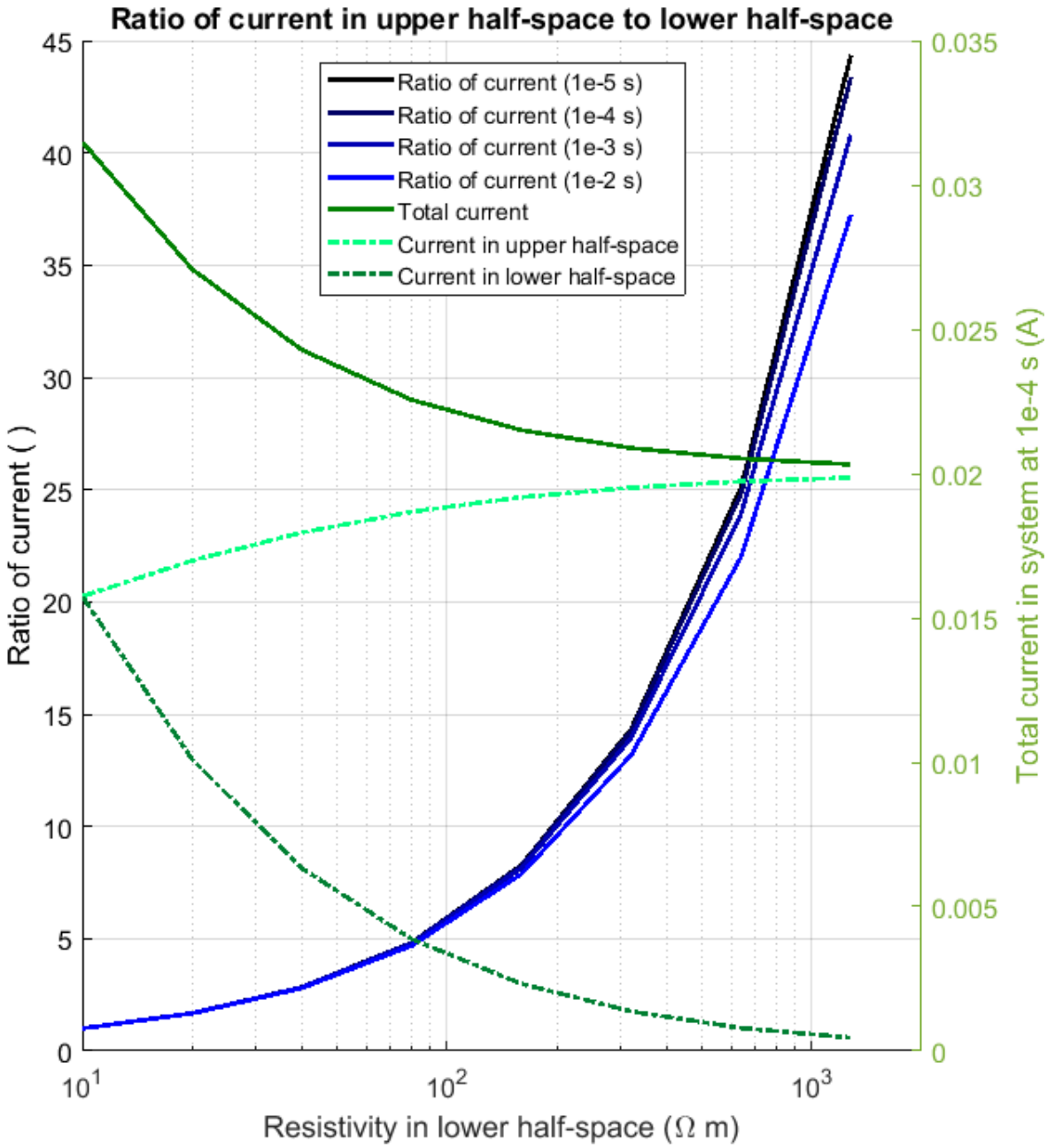

Figure 3.21: **Ratio of the current in the upper half-space with respect to the current in the lower half-space over changing resistivity of the lower half-space at specific time-gates. The green curves show the current in the system at 0.1 ms including the total, upper half-space, and lower half-space.**

tion to current distribution. This set varied resistivity in two horizontal 100 m layers within an otherwise homogeneous full-space environment (set at 10 Ω m). One of these 100 m layers was placed just below the transmitting plane, within the lower half of the model space. The other 100 m layer was placed 100 m above the transmitting plane, within the upper half of the model space. This placed two identical anomalous 1D targets within the 10 Ω m full-space on either side of the transmitting plane but off-set by 100 m distance. These 1D targets were varied from the background full-space resistivity of 10 Ω m to a much higher resistivity of 1280 Ω m. As with the previous figures (3.20 and 3.21), the current in the half-spaces on either side of the transmitting plane over time and the current density distribution are shown in figure 3.22 and the ratio of the current in the upper-half space (distal anomaly) to the current in the lower half-space (proximal anomaly) is shown in figure 3.23.

3.2 Data Acquisition

Time-domain electromagnetic (TEM) survey data was acquired in a potash mine during the fall of 2017. This data was collected by *Potash Corporation of Saskatchewan Inc.* in collaboration with the *Mitacs Accelerate* program. The student author partook in this survey as an operator and processor. The survey data collected was made available to the Butler Research team for the purposes of this master's project. The data from this internship was the focus of much of the analysis described in sections 4.1 and 4.3. This includes the data inversions that were performed afterward for this project.

This section will detail the equipment used for both the transmitter and receiver arrays. The general mine geometry and survey set-up, as well as the various sources of noise. Lastly, the operational parameters will be listed and detailed.

3.2.1 In-mine Time-domain Electromagnetics (TEM) Survey Details

The geometry of potash mine panels do not allow for in-loop surveying, as the panels are cut far too narrow (no more than 15-25 m wide). As such, an out-of-loop configuration had to

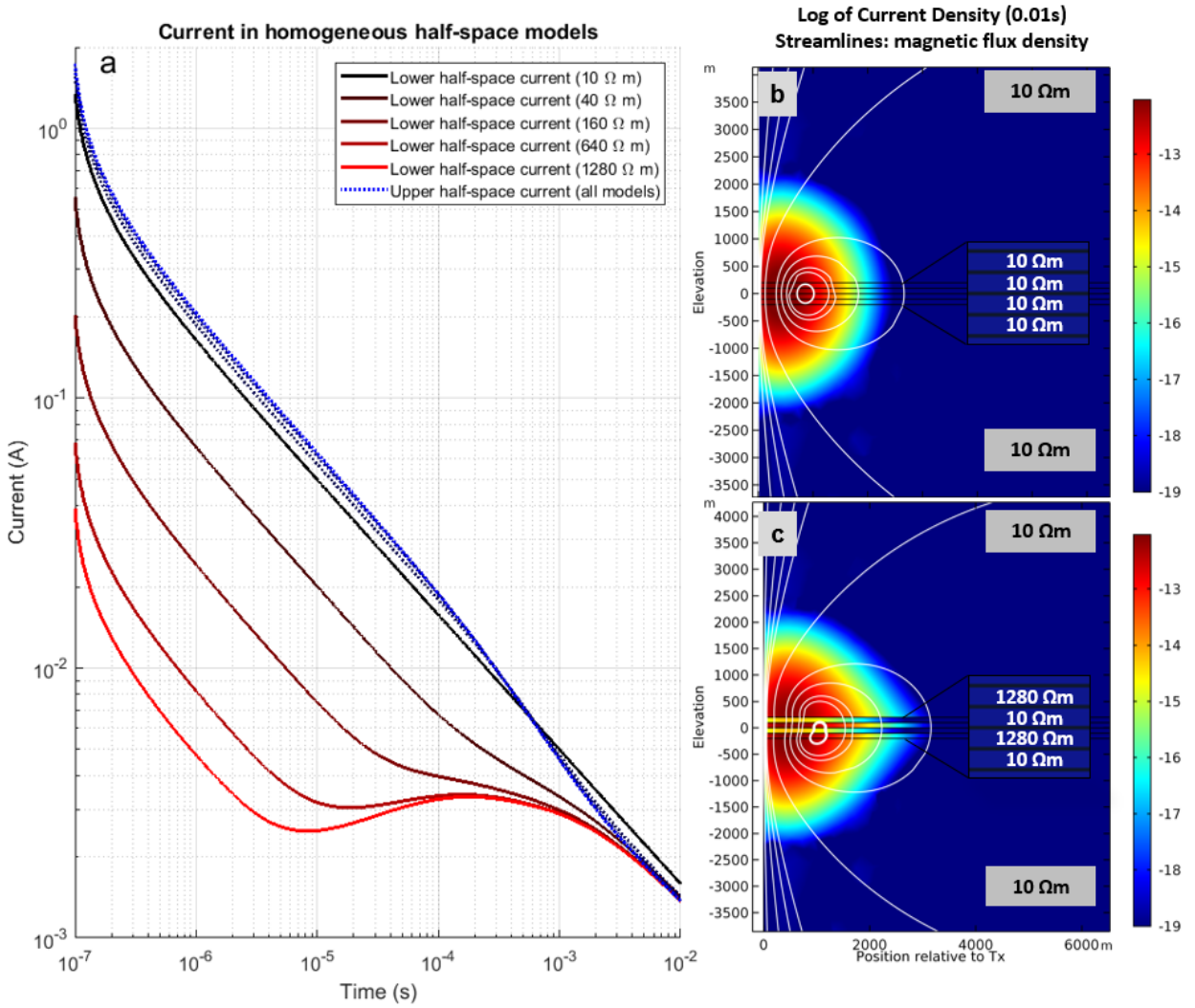

Figure 3.22: **Current in half-space models with varying resistivity in one of the half-spaces. a) shows the current (integrated from the current density of the area that comprises the respective half space) for both half-spaces in each of the models. b) and c) show the log of the current density at 0.01 s for the model where each half-space was set at 10 Ω m and for the model when the lower half-space was changed to 1280 Ω m.**

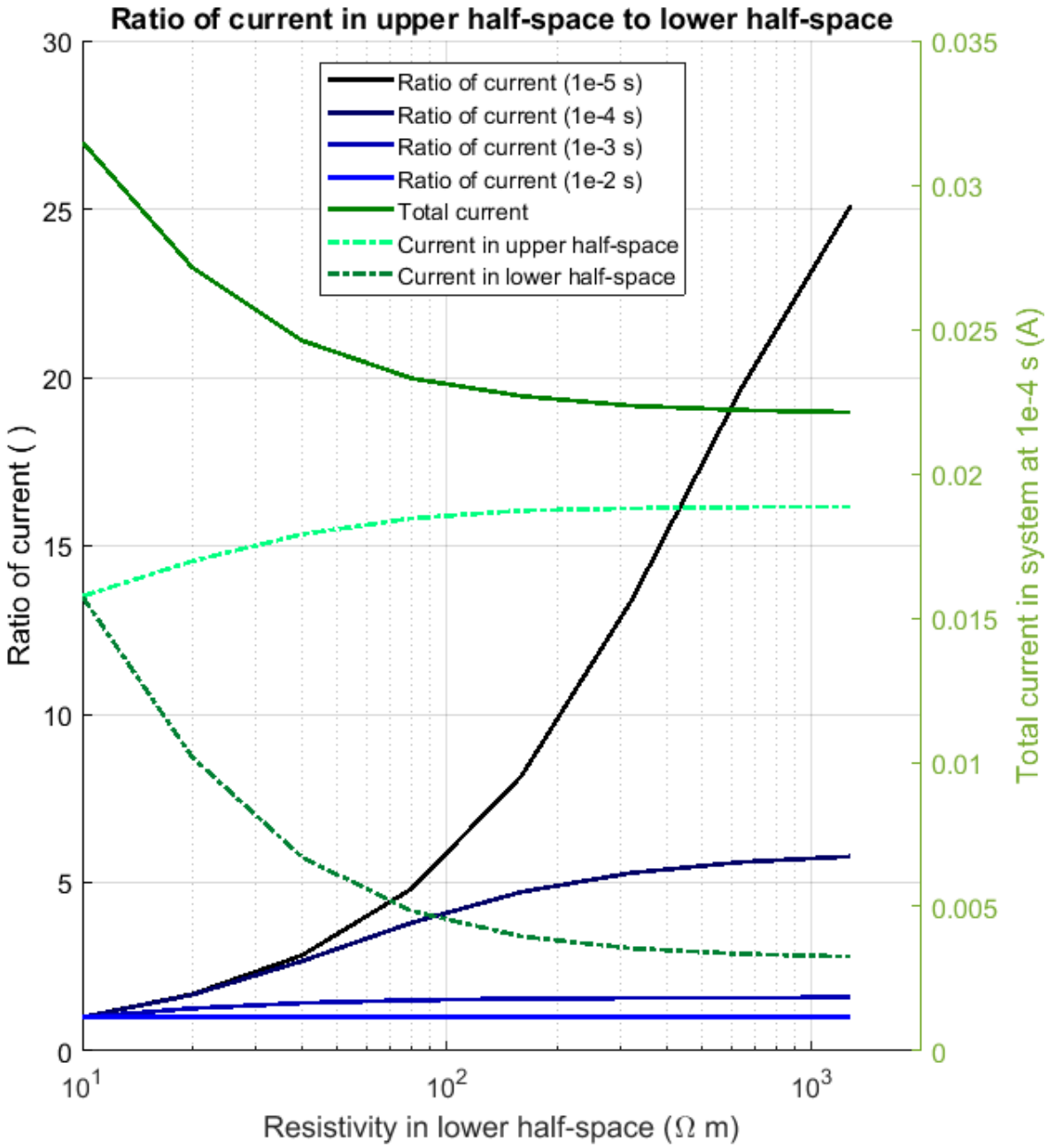

Figure 3.23: **Ratio of the current in the upper half-space with respect to the current in the lower half-space over changing resistivity of the lower half-space at specific time-gates. The green curves show the current in the system at 0.1 ms including the total, upper half-space, and lower half-space.**

be used. This is also commonly known as "slingram" when observing in frequency-domain. The two general controls surveyors have on TEM surveys in out-of-loop configurations are the power in the transmitter and the distance between the receiver and transmitter. The transmitter power controls the amplitude of the initial signal and consequently the amplitude of the measured response. This increase in measured response allows for deeper penetration of the measurable signal before it drops below the noise level. More power is usually preferable, though too much power will induce self-inductance in the transmitter wires that can be detected by the receiver. These small oscillating electrical currents will produce signals that will dominate early time measurements in the receiver, though they are small enough that moving the receiver further away can reduce their effects to sufficiently low enough levels.

The other control is transmitter and receiver separation. Increasing this has the effect of losing some lateral resolution as the signal travels through a wider variety of material. Other effects include increasing the time the bulk of the current diffuses in the inner range between transmitter and receiver, pushing the time of transition from early to late time later on in the time-gate measurements. Late time signal is easier to analyze and model effectively due to its consistent and smooth decay.

In-mine TEM survey data was collected in two parallel survey lines roughly 320 metres from one another. The lines ran east-west for 1000 and 550 metres respectively. The equipment used for this survey included a GDD NordicEM24 digital receiver linked to Geonics high-resolution 3D receiver coils. The transmitter was a Geonics TEM57-MK2 transmitter, powered by two 12 V batteries in series, controlled by a GDD EM-IP Tx Controller. The transmitter coil was a 16-gague, 8-turn 5-by-5 metre square loop. Reference between the transmitter and receiver was initially achieved through a cable; during survey operation the link was synchronized through a crystal timer. The cable was reintroduced every hour and the drift was noted. This drift was not noted to exceed acceptable levels at any point during the survey. The current produced by the transmitter was maintained around 13 A, producing in turn a magnetic moment of roughly 2600 Am^2 - although this signal did drop over time as the batteries lost power. Batteries were replaced once the drop in current became noticeable between readings. Types and number of measurements varied between the two survey lines, but included taking the vertical, radial, and tangential fields, at transmitter-receiver

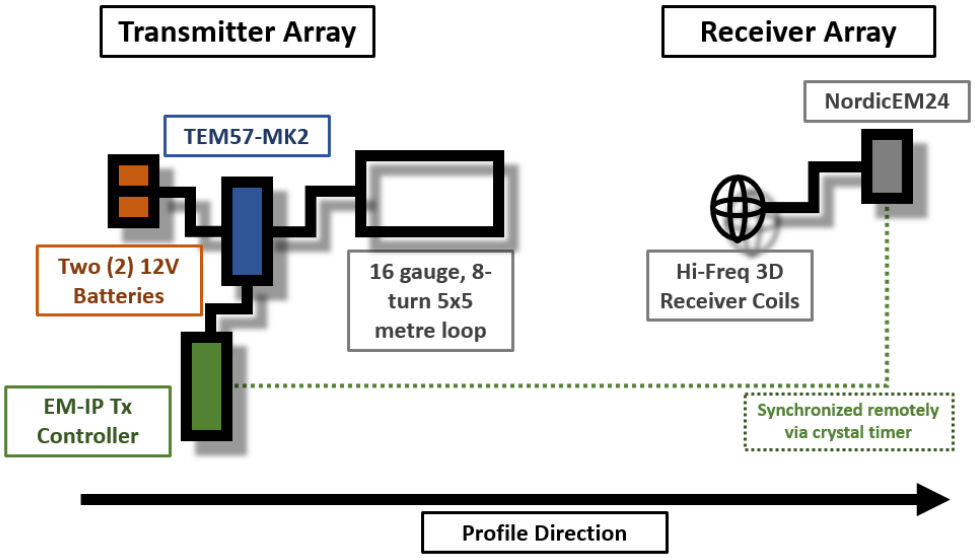

Figure 3.24: **Survey set-up and instrument relative positioning. Diagram not made to scale.**

separations of 40, 60, and 100 metres. The details of the parameters of the two survey lines are shown in table 4.1.

These survey lines were profiled into an area with an anomalous Dawson Bay signature detected via earlier surface seismic surveys. On each line, the expected point of entering the anomalous zone was roughly at the mid-point of the survey profile. Due to the speed at which the electromagnetic response was expected to enter late-time in the resistive environment of a salt mine, transmitter receiver separations of 100 metres were performed. On the low end, however, it was discovered in preliminary tests that a separation of 20 metres was too small to avoid substantial noise from self-induction in the transmitter that was being detected by the receiver. This was not observed when using the TEM47 transmitter in earlier surveys. The TEM47 has a much smaller power output of only 2 A. With the TEM57-Mk2, it was determined that 40 m separation between the transmitter and receiver was large enough that the self-induction issue was resolved.

Gate times were selected to match the 120 kHz sampling rate of the NordicEM24. The latest time gate (7.22 ms) was restricted by the operational frequency of the transmitter (which was set at 85 Hz). This allowed for 1024 measurements to be stacked to increase the signal to noise ratio, combined with four repeat measurements at each station to alert

the surveyors to any large millisecond-to-second scale temporal external EM noise, all to be performed in around 30 s per station. Table 3.1 shows the selected gate-time windows and their widths. The centre of each gate window was the gate-time assigned to the measurement.

3.3 Inversion Tools and Method

In an effort to apply a more mathematical approach to constraining the parameters behind the survey results, complimenting the user-directed forward modelling techniques described in section 3.1, a rudimentary inversion technique was created using forward modelling tools designed in *COMSOL Multiphysics* and tying them with objective function minimization calculation scripts in *MATLAB*. This was done via *COMSOL*'s *LiveLink* for *MATLAB* functionality. *LiveLink* allows *MATLAB* to interface with *COMSOL*, defining parameters, running models, and receiving results. The *MATLAB* scripts that were used for this purpose are described in the sections 3.3.1 and 3.3.2. The first of these details the minimization technique that was used, while the second details the objective function itself. Section 3.3.3 shows the inversion validation methods that were used to test the accuracy and capabilities of the designed system.

3.3.1 Simplex Inversion in Matlab

The simplex method used by the $fminsearch$ function in *MATLAB* was chosen to be used as the iterative method for solving for this minimum. This function uses the Nelder-Mead simplex algorithm put forward by Nelder and Mead (1965) and follows the outline used by Lagarias, Reeds, M. Wright, and P. Wright (1998). Initially, the simplex is formed around the initial list of parameter values x_0 by modifying each of the n parameters by 5%. This forms the basis for the starting simplex algorithm with $n + 1$ points from the n parameters and the initial starting point. The algorithm then orders the parameter sets in order of lowest objective function (best) to highest (worst), with the parameter set with the highest value objective function being discarded in favour of another estimate. This new estimate is then either found via reflecting, expanding, contracting outside or inside, or shrinking the value in parameter-space. Reflection is generated by equation 3.48, where m is the middle

Gate	Start (ms)	Centre (ms)	End (ms)	Width (ms) / (samples)	
1	0.0083	**0.0125**	0.0167	0.0083	1
2	0.0167	**0.0208**	0.0250	0.0083	1
3	0.0250	**0.0292**	0.0333	0.0083	1
4	0.0333	**0.0375**	0.0417	0.0083	1
5	0.0417	**0.0458**	0.0500	0.0083	1
6	0.0500	**0.0542**	0.0583	0.0083	1
7	0.0583	**0.0625**	0.0667	0.0083	1
8	0.0667	**0.0708**	0.0750	0.0083	1
9	0.0750	**0.0792**	0.0833	0.0083	1
10	0.0833	**0.0875**	0.0917	0.0083	1
11	0.0917	**0.0958**	0.1000	0.0083	1
12	0.1000	**0.1083**	0.1167	0.0167	2
13	0.1167	**0.1292**	0.1417	0.0250	3
14	0.1417	**0.1583**	0.1750	0.0333	4
15	0.1750	**0.1958**	0.2167	0.0417	5
16	0.2167	**0.2417**	0.2667	0.0500	6
17	0.2667	**0.2958**	0.3250	0.0583	7
18	0.3250	**0.3583**	0.3917	0.0667	8
19	0.3917	**0.4292**	0.4667	0.0750	9
20	0.4667	**0.5083**	0.5500	0.0833	10
21	0.5500	**0.5958**	0.6417	0.0917	11
22	0.6417	**0.6917**	0.7417	0.1000	12
23	0.7417	**0.8000**	0.8583	0.1167	14
24	0.8583	**0.9292**	1.0000	0.1417	17
25	1.0000	**1.0875**	1.1750	0.1750	21
26	1.1750	**1.2833**	1.3917	0.2167	26
27	1.3917	**1.5250**	1.6583	0.2667	32
28	1.6583	**1.8208**	1.9833	0.3250	39
29	1.9833	**2.1792**	2.3750	0.3917	47
30	2.3750	**2.6083**	2.8417	0.4667	56
31	2.8417	**3.1167**	3.3917	0.5500	66
32	3.3917	**3.7125**	4.0333	0.6417	77
33	4.0333	**4.4042**	4.7750	0.7417	89
34	4.7750	**5.2042**	5.6333	0.8583	103
35	5.6333	**6.1333**	6.6333	1.0000	120
36	6.6333	**7.2208**	7.8083	1.1750	141

Table 3.1: **Selected NordicEM24 receiver gate-times for the 2017 in-mine TEM survey. The centre of each gate window was the gate-time assigned to the measurement.**

point (centroid) in the parameter space between the first n parameters (equation 3.49). This middle point excludes the parameter of the worst point (x_{n+1}) in its calculation.

$$r = 2m - x_{n+1}. \tag{3.48}$$

$$m = \frac{\sum_{l=1}^{n} x_l}{n}. \tag{3.49}$$

If the objective function at $f(r)$ is better than at $f(x_{n+1})$, but still worse than $f(x_1)$, then the process is terminated and the reflection is used. If the reflection is better than all $f(x_l)$ values, including $f(x_1)$, then the expansion point s is calculated as shown in equation 3.50. If the expansion provides a better objective value than the reflection, then it is taken, used, and the process is terminated. If not, the reflection is used instead.

$$s = m + 2(m - x_{n+1}). \tag{3.50}$$

If the reflected parameter provides a worse objective value than $f(x_n)$, a contracted value is calculated in the direction of either r or x_{n+1} depending on which one provided a better objective function to begin with. If $f(r)$ is better, the contraction (represented by c) occurs outside the current parameter space (closer to r) as shown in equation 3.51. So long as the objective function is better at c than at r, the process is terminated and c is used. If not, the shrink method is applied. If $f(x_{n+1})$ is better than $f(r)$, an inside contraction (represented by cc) is used as shown in equation 3.52. Like for c, if cc provides a better objective function than x_{n+1}, then cc is used, otherwise the shrink method is applied.

$$c = m + \frac{r - m}{2}. \tag{3.51}$$

$$cc = m + \frac{x_{n+1} - m}{2}. \tag{3.52}$$

The shrink method pulls all parameters toward the best performing one x_1. This creates

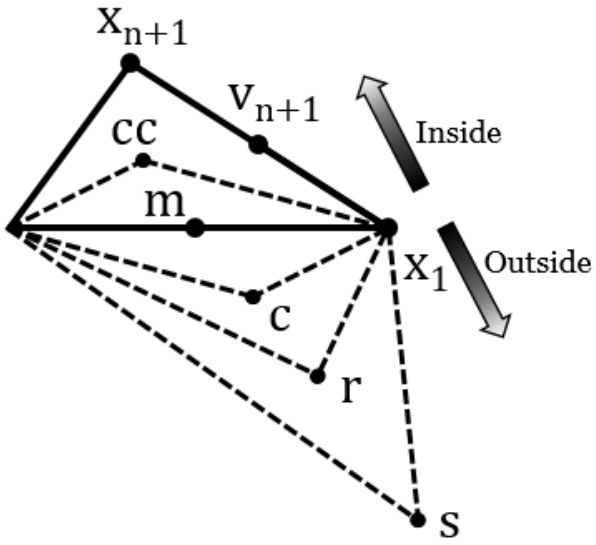

Figure 3.25: **Diagram illustrating the Nelder-Mead approach. Modelled after images created by Lagarius et. al (1998).**

a new set of parameter values for the next simplex. the new values are $x_1, v_2, v_3, ..., v_{n+1}$. This is shown in equation 3.53.

$$v_l = x_1 + \frac{x_l - x_1}{2}. \tag{3.53}$$

Figure 3.25 shows the method of iteration of solving for parameters via the simplex method.

3.3.2 Building the Inversion Objective Function

The objective function that the simplex minimization sought to minimize was a modified least-squares (or L2-norm). This function was defined in *MATLAB* as having two parts (equation 3.54). One is the square of the error, or difference between the model and the measured values, normalized to the amplitude of the response, and summed over all time-gates. The other was a parametric damping term applied to keep the parameters from shifting too far from their starting values. This was used as the inversion system had a tendency to allow sets of parameters in the resistive end of the spectrum to shift out even

further in the resistive direction, beyond anything geologically realistic (in excess of 10^6 Ω m). This was partly expected as electromagnetic systems struggle with resolving resistive targets due to the speed with which the EM signal diffuses through them. However, there could be additional computational or mathematical reasons for this. Future work should be done to determine the extend of this undesirable feature. This damping term was kept as small as possible, constraining large excesses of parameter shift, while still contributing as little as possible to the overall objective function value.

$$obj.fun. = minimum\{residual + damping\}. \tag{3.54}$$

The residual function is shown in equation 3.55. It sums the squares of the difference between the time derivative of the magnetic field of both calculated model and the measured survey data over each of the k-th time-gates. This difference is normalized to the magnitude of the calculated model in order to scale each time-gate with equal weighting in the residual calculation. Due to the noise at the later time gates, as well as the difficulty in matching the early time direction change, the time-gates from the survey that were used were set between 0.079 ms and 2.6 ms. Equation 3.56 shows the damping term, where ρ_j is the iterative resistivity of the j-th layer, $\rho_{0,j}$ is the initial starting value of the corresponding layer, m is the number of layers, and C is a arbitrary constant applied to the damping term to appropriately scale it with the magnitude of the residual value. The value used for this purpose varied with the inversion being performed, but for the purpose of inverting the survey data across the survey lines and when every layer was allowed to change resistivity, a value of 0.0038 was used for C.

$$residual = \frac{\sqrt{\sum_{k=1}^{n} \left(\frac{\frac{\mathrm{d}H}{\mathrm{d}t}_{k,model} - \frac{\mathrm{d}H}{\mathrm{d}t}_{k,measured}}{\frac{\mathrm{d}H}{\mathrm{d}t}_{k,model}} \right)^2}}{n}. \tag{3.55}$$

$$damping = C\left(\frac{\sum_{j=1}^{m} \left| \frac{\rho_j - \rho_{0,j}}{\rho_{0,j}} \right|}{m} \right). \tag{3.56}$$

$$obj.fun. = min\left[\frac{\sqrt{\sum_{k=1}^{n}\left(\frac{\frac{\mathrm{d}H}{\mathrm{d}t}_{k,model}-\frac{\mathrm{d}H}{\mathrm{d}t}_{k,measured}}{\frac{\mathrm{d}H}{\mathrm{d}t}_{k,model}}\right)^2}}{n}+C\left(\frac{\sum_{j=1}^{m}\left|\frac{\rho_j-\rho_{0,j}}{\rho_{0,j}}\right|}{m}\right)\right]. \tag{3.57}$$

3.3.3 Inversion Validation

A synthetic dataset was constructed in COMSOL Multiphysics as a way of testing the simplex inversion method in Matlab. This synthetic model had three horizontal layers and was set in a full-space environment. The layers as well as the produced forward model for this synthetic dataset are shown in figure 3.26. The transmitter as always was located at the origin of the model ($z = 0$, $r = 0$). The receiver was set in the plane of the transmitter, parallel to the layers, and at 40 metres distant. Layer 1 acts as the upper half-space and extends from 150 metres above the transmitting plane to the upper end of the model space. Layer 2 is the only bounded layer for this dataset and extends from 0 to 150 metres. The last layer, layer 3, forms the lower half-space and extends from 0 metres to the bottom of the model space. The resistivity of layers 1, 2, and 3, were set at 10, 100, and 1000 Ω m respectively. The slight kink in the decay curves between 0.1 and 1.0 ms seen in figure 3.26.b indicates the time that the diffusing signal reached the conductive layer 1.

Two separate inversions on this synthetic dataset were performed. One was a two-parameter inversion that only allowed the upper two layer's resistivities to vary, keeping the lower half-space (layer 3) resistivity at 1000 Ω m. The other was a three-parameter inversion where all three layer resistivities were allowed to change. In all cases, the layer thicknesses and elevation were hard-set in the model at their respective correct values.

This first test aimed at isolating and illustrating the principles behind the simplex method, principally by changing the starting parameter values and by keeping the number of parameters low. The damping coefficient C (shown in equation 3.56) was set to zero for this set of inversions, making the only contributing term in the objective function the residual. However, a large penalty was placed on the objective function if either parameter drifted larger than 1000 Ω m. This would redirect any wayward inversion path back down

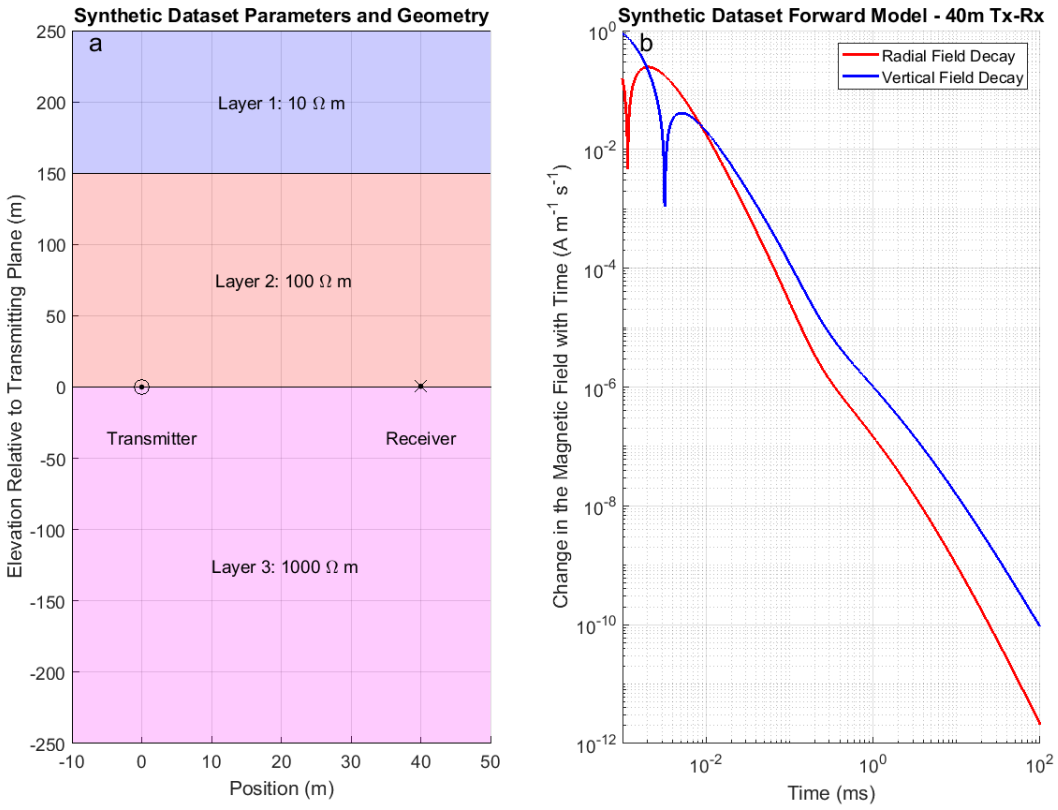

Figure 3.26: **Detailing the parameters of the forward model that generated the synthetic dataset used for the inversion validation. Figure a shows the thickness, distance, and resistivity of the horizontal layers, while figure b shows the forward model response at 40 m Tx-Rx separation.**

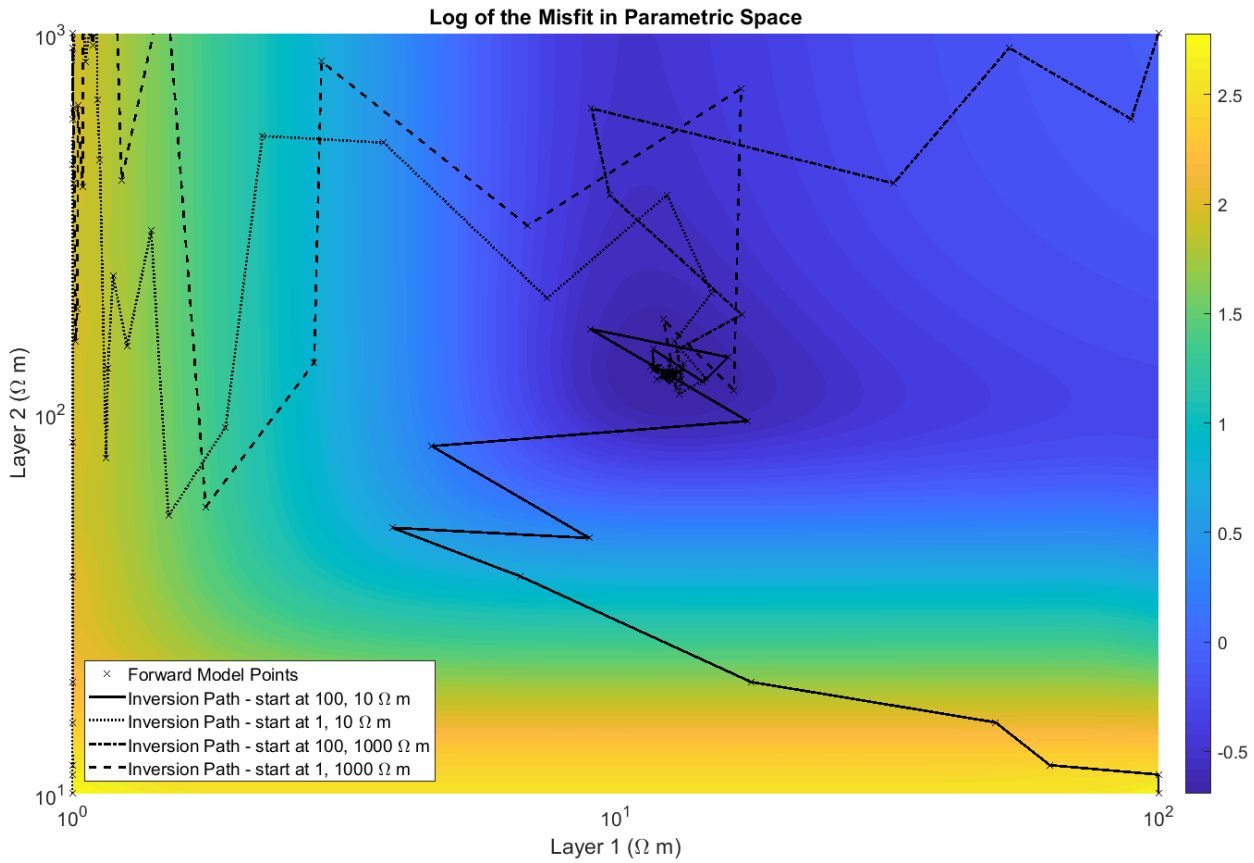

Figure 3.27: **Map of the misfit for the 2-layer synthetic inversion, showing the mapping paths for four different starting points of the inversion in parametric space. The log of the misfit is contoured here to highlight the lower end of the misfit that encompasses the majority of the displayed space. The conductive end of the space for both layers has a much higher misfit.**

toward more reasonable numbers. This was only needed for inversions with certain initial conditions. Figure 3.27 shows the results of these inversions in parametric space. The contours denote the logarithm of the residual (the grid for which was calculated separately). In each iteration of the inversion, the parameters were initialized in a different quadrant of parametric space. This space was constructed around the values of the parameters used in the initial forward model (100 Ω m and 10 Ω m) that created the synthetic dataset. The various lines show the inversion paths taken by the SIMPLEX algorithm from the different starting conditions.

The values of the parameters and the objective function over the course of each of these inversions are shown in table 3.2. Inversions #1 and #2 had much smaller starting residuals

	Starting			Final			
#	ρ_1 (Ω m)	ρ_2 (Ω m)	**Res.**	ρ_1 (Ω m)	ρ_2 (Ω m)	**Res.**	**Iterations**
1	1000	1	99.29	12.40	126.5	0.203	55
2	1000	100	0.82	12.40	126.5	0.203	43
3	10	1	610.74	12.38	126.5	0.203	67
4	10	100	494.29	12.40	126.5	0.203	40

Table 3.2: **Results of the inversions performed on a synthetic dataset. It shows the starting values of each set, including the residual (res.), the final conditions, and the number of iterations to arrive at the completion of the inversion.**

than the others. Inversion #2 especially, located in the northeast corner of parametric space, where both layers were set initially more resistive than those used in the synthetic data creation, had a very small initial residual (0.8 compared with the final residual found by the inversions of 0.2). Inversions #2 and #4 were the most efficiently determined (lower iteration count). They also did not induce the penalty on the objective function by exceeding the 1000 Ω m ceiling placed on the resistivity parameters. In both of these inversions, the half-space (layer 1) was set initially more resistive. When the half-space was set more conductive, the inversion was much more inefficient in reaching the objective function minimum. This was compounded when the intermediate layer (layer 2) was also set more conductive. This inversion (#3) was the only one to incur the objective function penalty for exceeding the space allotted for the parameters.

Figure 3.28 illustrates the process for a three-parameter inversion on the same dataset as the previous section described. This inversion allowed all three layer's resistivities to vary. The starting values for the parameters in the inversion were set at 78.0 Ω m, 230.0 Ω m, 460.0 Ω m for layers 1, 2, and 3 respectively. No damping term was used for this inversion and no penalty was placed on the parameters. However, a termination flag was placed once a certain number of iterations was reached. Figure 3.28.a shows the geometry and parameters of the forward model that generated the synthetic data. Figure 3.28.c and 3.28.e show the values produced through the inversion process for both the objective function and the parameters within the inversion respectively. The x-axis is the inversion iteration count; the y-axis values are the calculated objective function value and the parameters used for the layers. The dashed lines in figure 3.28.e highlight the forward model resistivities. Figures

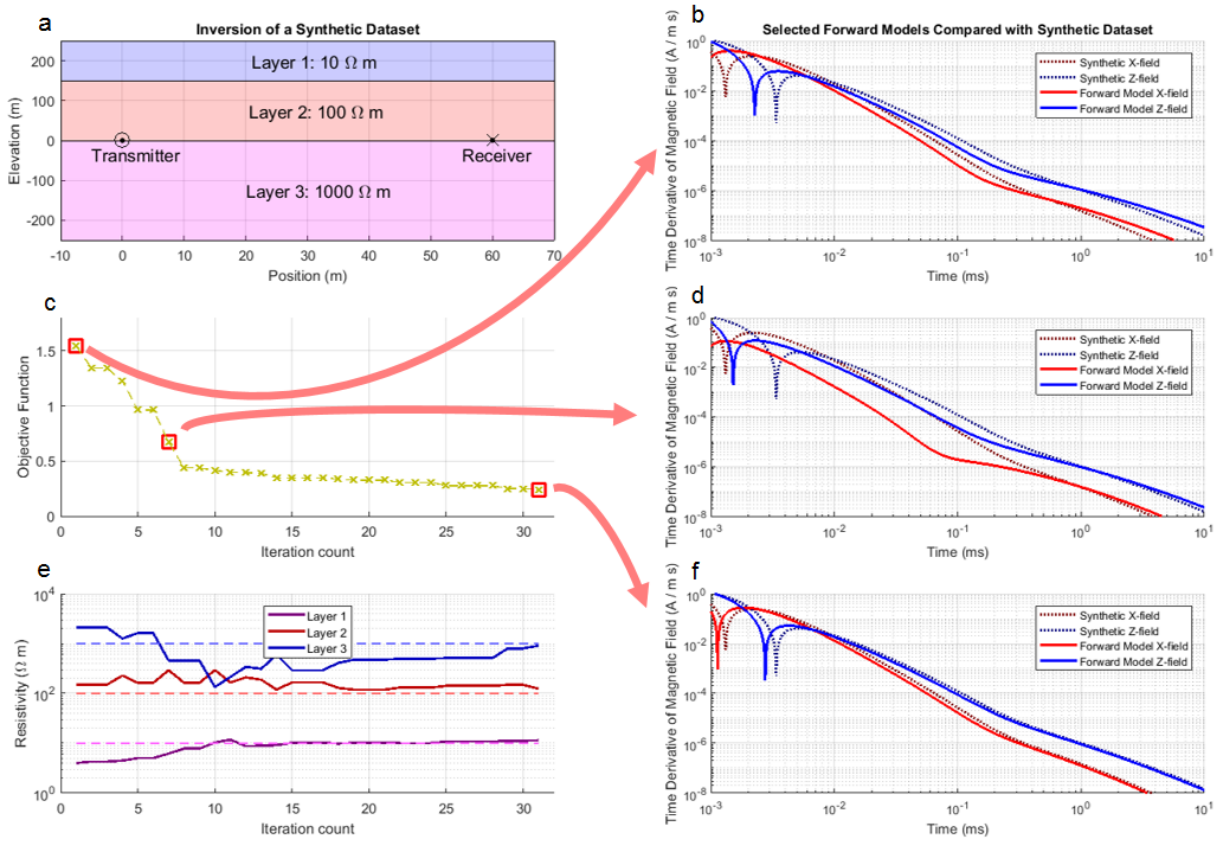

Figure 3.28: **Illustrating a 3-layer inversion process. Figure a) shows the parameters and geometry of the initial forward model that constructed the data used in the inversion. Figure c) shows the iteration of the objective function over the inversion process. The forward models in the highlighted iterations are shown in figures b), d), and f). Figure e) shows the resistivities of each layer over the iterations in the inversion.**

3.28.b, 3.28.d, and 3.28.f on the right are various time-decay graphs of the synthetic dataset (dashed lines) and the respective forward models found at specific points in the inversion (solid lines).

3.4 Well-log Analysis

Parameters for the initial model were determined from well-log borehole data near the location of the mine site that was surveyed as part of this project. One of the wells analyzed was PCS Ste. Martha 16-14-73-30. This particular modern well-log included a host of tools,

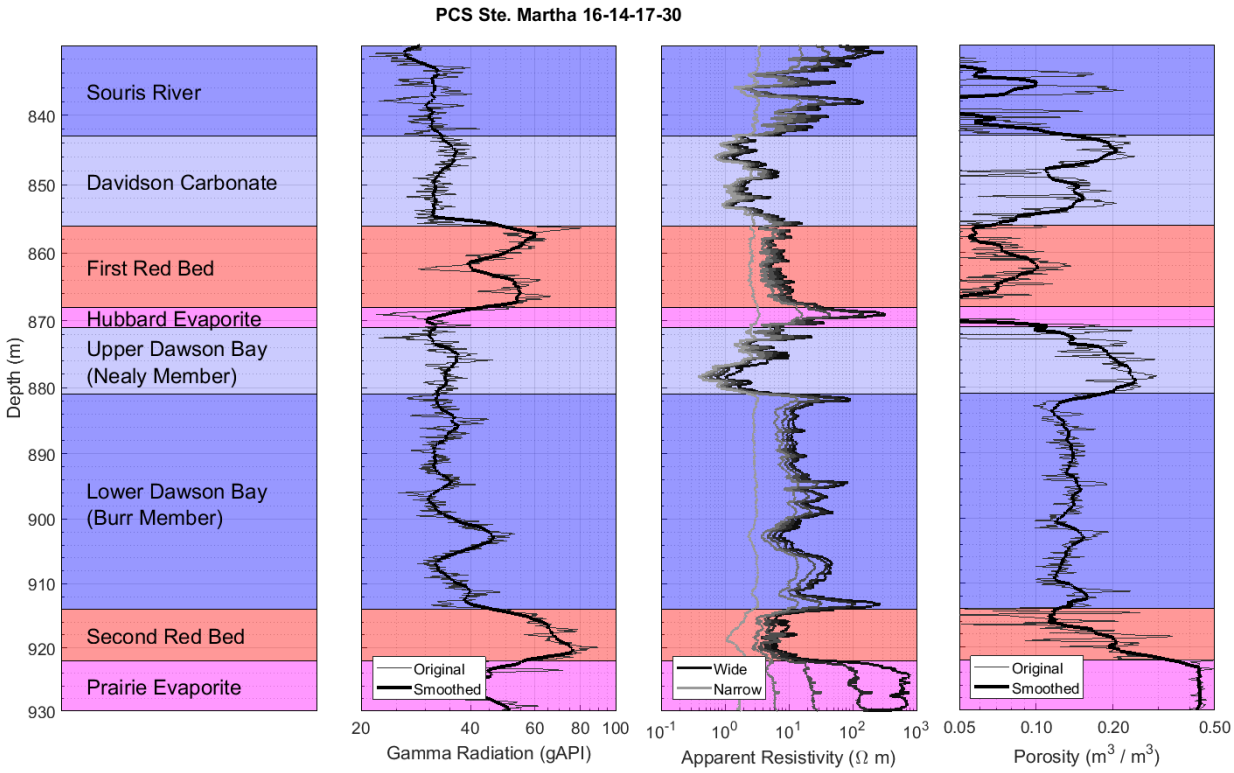

Figure 3.29: **PCS Ste. Martha 16-14-73-30 well-logs. Includes gamma, apparent resistivity, and porosity calibrated to limestone. The layer horizons match those used for the EM models and were picked from the well-logs. These horizons are not meant to perfectly match the geological ones as they are an approximation of the physical properties of the rocks.**

the principal of which included gamma-ray radiation, resistivity, and neutron porosity logs. Gamma-ray measurements can assist with constraining the thicknesses of the Red Beds (shale bodies), while the resistivity and porosity logs can assist with constraining the thicknesses of the other beds (carbonates and evaporates). The resistivity logs also provide a good starting point for resistivities of the various layers in the EM model. Figure 3.29 shows well-log data for gamma-ray radiation, resistivity, and limestone calibrated neutron porosity logs.

Note that neutron porosity logs do not measure porosity directly. They approximate porosity by emitting neutron particles into the rock and measure the neutron response rate. This is made useful by the principle that hydrogen's low mass and relatively large scattering cross-section produce a slowing effect on neutron particles. Hydrogen is disproportionately represented in pore spaces with water or hydrocarbons and, as such, is seen as a good

indicator of pore space. In order for the neutron count rate to have any meaning, the tool requires extensive calibration and correction to align with the lithology and water content of the host rock. The lithology calibration for this log was Limestone. This makes the porosity values only valid in the blue shaded areas of the log (the carbonate-limestone layers). Even within the carbonates, however, the water content in the rock will also shift the results around. Despite all this, the porosity log can aide in a relative understanding of porosity changes, as well as in delineating layer thicknesses, especially within the carbonate rocks.

The gamma spikes ($50 - 67$ gAPI) from 856 to 868 and from 914 to 922 metres depth are indicative of shale bodies and are thought to effectively delineate the Red Beds above the mine workings (First and Second respectively) from the surrounding layers. These zones also show relatively consistent apparent resistivity compared with the carbonate layers (both between different carbonate layers and internally within each one). The carbonate layers within the Souris River and Dawson Bay formation show multi-layering on both the porosity and resistivity sections. The Souris River has a section of much higher localized porosity (14% versus 5%) in the lower section. This section can loosely be correlated to the Lower Davidson carbonate - or the Davidson Member B-unit from Lane's report on the Souris River (1964). The other carbonate zone that demonstrates similar qualities is the Upper Dawson Bay (871 - 881 metres). This zone is markedly different from the Lower Dawson Bay in both porosity (19% compared with 13%) and resistivity (29 Ω m compared with 4 Ω m). This zone - along with the Lower Davidson - has the most conductive response of all of the layers above the mining zone. This response is even higher than the shale bodies. It follows that there is a degree of correlation between porosity and conductivity within these carbonate layers. Statistical analysis of the well-log, including means and standard deviations can be found in table 3.3. Of additional interest, the Prairie Evaporite layer showed slightly anomalous values in both the porosity and resistivity logs. While the porosity log is calibrated for carbonates specifically, the fact that it detected such a strong response suggests the presence of some water in the salt. The resistivity log on the other hand displayed a resistivity of 770 Ω m which is lower than pure salt which typically ranges between 10^3 and 10^5 Ω m (Ezersky and Goretsky, 2014). This might also suggest some disseminated water or other impurities in the salt.

		Gamma (gAPI)		
Layer	**Thickness (m)**	$\bar{X}$	**s**	$100 \cdot \mathbf{s} \cdot \bar{X}^{-1}$
Souris River	40	34.3	10.5	30.5%
Lower Davidson	13	33.4	3.1	9.2%
First Red Bed	12	51.8	9.5	18.4%
Hubbard Evaporite	3	32.9	7.6	23.1%
Upper Dawson Bay	10	33.8	3.6	10.7%
Lower Dawson Bay	33	35.4	5.1	14.5%
Second Red Bed	8	67.1	9.0	13.4%
Prairie Evaporite	30	89.3	72.0	80.5%
		Apparent Resistivity (Ωm)		
Layer	**Thickness (m)**	$\bar{X}$	s	$100 \cdot \mathbf{s} \cdot \bar{X}^{-1}$
Souris River	40	52.6	88.6	168.5%
Lower Davidson	13	3.4	2.4	71.1%
First Red Bed	12	8.4	4.8	57.0%
Hubbard Evaporite	3	90.7	102.8	113.3%
Upper Dawson Bay	10	4.3	3.6	83.1%
Lower Dawson Bay	33	28.8	35.7	123.9%
Second Red Bed	8	9.8	6.4	65.8%
Prairie Evaporite	30	770.8	255.4	33.1%
		Porosity ($\frac{m^3}{m^3}$)		
Layer	**Thickness (m)**	$\bar{X}$	s	$100 \cdot \mathbf{s} \cdot \bar{X}^{-1}$
Souris River	40	0.046	0.084	183.1%
Lower Davidson	13	0.143	0.052	36.2%
First Red Bed	12	0.071	0.030	41.8%
Hubbard Evaporite	3	0.014	0.076	527.7%
Upper Dawson Bay	10	0.193	0.067	34.8%
Lower Dawson Bay	33	0.135	0.020	14.9%
Second Red Bed	8	0.169	0.069	41.1%
Prairie Evaporite	30	0.454	0.041	9.0%

Table 3.3: **Statistical analysis of the well-logs from PCS Ste. Martha 16-14-73-30. Mean values ($\bar{X}$), standard deviations (s), and percent standard deviations are shown for each layer used in the geological electromagnetic computer modelling.**

Chapter 4

Experimental Results

Summary

This chapter will summarize the results acquired over the course of this project. As mentioned in Chapter 3, the project had three broad categories of focus. The first of these was processing and analyzing in-mine survey time-domain electromagnetics (TEM) data from an active potash mine (section 4.1). The second in forward modelling full-space EM signals in both *COMSOL Multiphysics* and *Mathworks Matlab* (section 4.2). The third in mathematical inversions on the survey data to derive approximations of near mine geological parameters (section 4.3).

While these three sections to the project are separated for the sake of clarity in this text, each section strongly relied on material from other sections for their operation. Before any surveying was performed, extensive forward modelling was performed to get an idea of optimal survey parameterization. The inverse modelling required forward modelling tools properly optimized for efficiency and accuracy, as well as reliable and repeatable survey data. Lastly, even the forward modelling described in section 4.2 relied on the inverse modelling products as a baseline for the parameters in each model set. It was considered best practice to analyze forward models with the closest approximation to in-mine environments as possible. In addition, well-log analysis performed by both the author as well as by *Nutrien* informed each step of the project, both as a starting point for the predictive forward modelling and the data inversions, as well as a guide for the extent of expected parametric change in anomalous

areas.

4.1 In-Mine Survey Results

The in-mine time-domain electromagnetics (TEM) data collected as part of the *Mitacs* student internship as an ancillary part of this project was performed within a potash mine in an area of a suspected large Dawson Bay anomaly. A prior surface seismic survey provided the initial indicators for this anomaly. The in-mine TEM survey included two parallel out-of-loop east-west profile lines. The coordinates and parameters used for the in-mine survey lines are shown in table 4.1. The northing and easting coordinates used for the survey are not tied to any specific grid UTM (Universal Transverse Mercator). They are spatially accurate relative to the survey but were artificially created to protect the anonymity of the location and the mine site. Preliminary modelling suggested that measuring the radial field would be highly beneficial. In addition, it was thought that underground the noise level for the radial field would be substantially lower than at the surface. Initial in-mine background tests confirmed this theory.

The position of the north line was 1056 metres north of the south profile line, and was profiled from 7391 m to 8391 m east with the receiver leading. The second line, the south one, was profiled east to west with the receiver leading. The position of the second line was at 7228 m north, and profiled from 8671 m to 8121 m east. The numbering on the stations of these lines reflect the order with which they were taken. The north line is numbered as the first line (01−) and the south line is the second (02−). At each transmitter set-up, multiple readings were taken, measuring the vertical, radial, and, occasionally, the tangential field decays, each at various different separations between the transmitter and the receiver. The separations included 40, 60, and, occasionally, 100 metres. At each separation only the receiver was moved. This effectively shifted the centre point between the transmitter and receiver and allowed for short mini-profiles to be created at each transmitter set-up. The survey lines were conducted in mining panels away from the main access corridors. There was no operating machinery or non-survey personnel on the survey lines or in the nearby secondary mine panels. In addition, effort was made to keep the areas free of mining

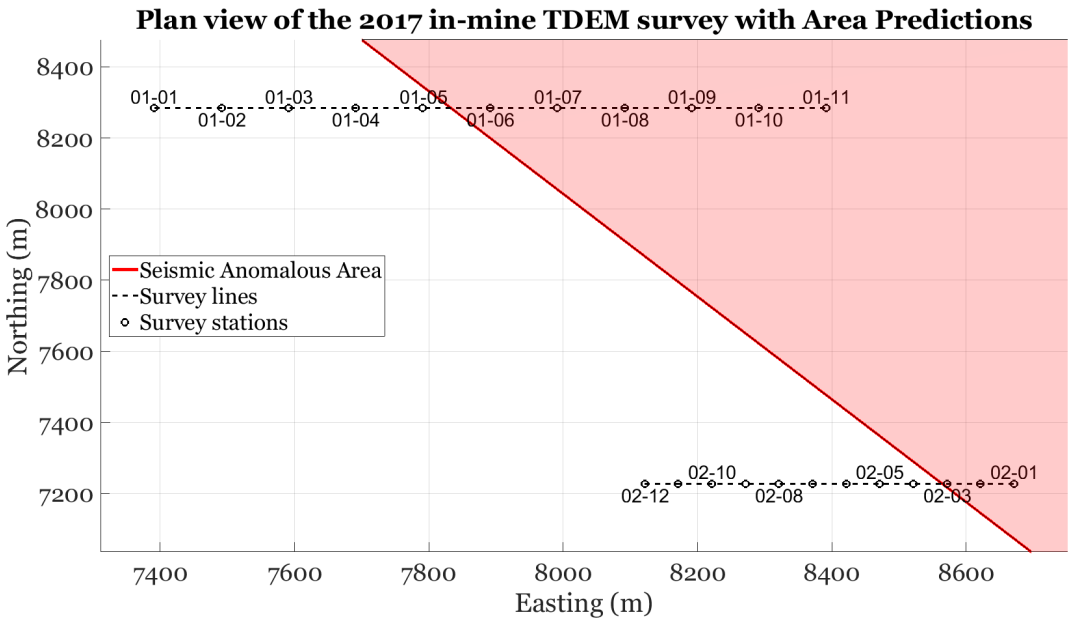

Figure 4.1: **Plan view of the TEM survey area. Transmitter station designations are shown alongside their locations. The red shaded zone shows the general area of the seismically detected anomaly.**

structure or non-operating machinery. Figure 4.1 shows the positioning of both survey lines relative to one another and the predicted anomalous area.

The parameters for the south line were different from the north line so as to mimic an earlier study performed with different equipment in the same southern mine panel. The parameters for the north line were designed to be more optimal for the purpose of the survey. The north profiled line exclusively measured the radial and vertical fields, including taking measurements at 100 m transmitter-receiver separation (thereby extending the mini-profiles created by moving only the receiver), and extended the distance between transmitter station points. This allowed the north line to cover a much longer stretch of distance than would otherwise be possible in the time allowed for the survey. In general, receiver relocation takes a very small amount of time compared to a transmitter relocation and set-up due to the large amount of power and equipment used in the transmitter array.

Figures 4.2, 4.3, and 4.4 show the decay signals from the north profile line at the transmitter-receiver separation of 40 m, 60 m and 100 m respectively, while figures 4.5 and 4.6 show the decay curves from the south line at 40 m and 60 m transmitter-receiver separations. Figure 4.7 shows the tangential field measurements on the south profile line at

both 40 m and 60 m transmitter-receiver separations. Tangential field measurements were not performed on the north line. The lighter decay curves on these figures are survey stations on the east side of the survey lines (generally from within the anomaly), and the darker curves are stations on the west side of the survey lines (generally outside of the anomaly). Blue shaded curves are the vertical field decay and red the radial field decay. There is a marked increase in response indicative of a conductive layer in time gates from both survey lines as early as 0.1 ms on the stations to the east of the surveyed area. The numbering for these eastern stations are higher value ones for the north line (01-xx) and lower values for the south line (02-xx). The exact point in time is not easily discernible due to the noisy fluctuations in the early time gates. The peak increase in amplitude is higher on the north line than on the south. The north line also contains a higher number of survey points displaying this marked increase in signal as the north panel was cut farther into the anomalous zone than the south line was. In both cases, the eastern terminus of the surveyed lines were the mining face of the cut panels.

The next set of figures look at the decay response from a profile view. Figures 4.8, 4.9, 4.10, 4.11, and 4.12 display the decay response over all timegates. There is a general trend that begins at the middle time-gates (between 129 μs and 1.087 ms) to a higher amplitude response toward the east of the survey lines. There also appears to be broadly three different areas being mapped on each survey line: (1) a baseline resistive response on the west end of the survey lines, (2) a transition zone where the signal begins to rise and is changing from station to station, and (3) an anomalous conductive zone on the east end of the survey lines where the signal is no longer changing and a conductive response is observed. By observing the decay responses in profile, we can get an idea of the lateral extent of the anomalous area, including both the transition zone and the anomalous zone; as well as it allows us to more easily display all of the stations' decay responses on the same figures. Figure 4.13 shows the tangential field readings on the south line in profile.

In order to get a better idea of the response variation across time and the profiled points, the log of the relative (or residual) decay response was calculated (see equation 4.1). This is simply the log of the decay response at each station ($\frac{\mathrm{d}H_{\hat{i}}}{\mathrm{d}t}$) divided by a base station (or regional) decay response ($\frac{\mathrm{d}H_0}{\mathrm{d}t}$). This is also known as the target response (Dentith and

	North Line (Profile #1)	South Line (Profile #2)
Line Position (northing)	8284 m	7228 m
Start point (easting)	7391 m	8671 m
End point (easting)	8391 m	8121 m
Profile Length	1000 m	550 m
Profile Direction	East	West
Rx position	leading	leading
Tx station spacing	100 m	50 m
Tx-Rx Separations	40, 60, 100 m	40, 60 m
Rx Components	vertical (z), radial (ρ)	vertical (z), radial (ρ), tangential (ϕ)
Tx Orientation	horizontal	horizontal

Table 4.1: **Survey parameters for both profile lines. Profile 1 is the northern line and profile 2 is the southern one. The parameters vary between the two survey lines partly due to the desire to test the various alterations as well as geological features and time considerations between the two lines.**

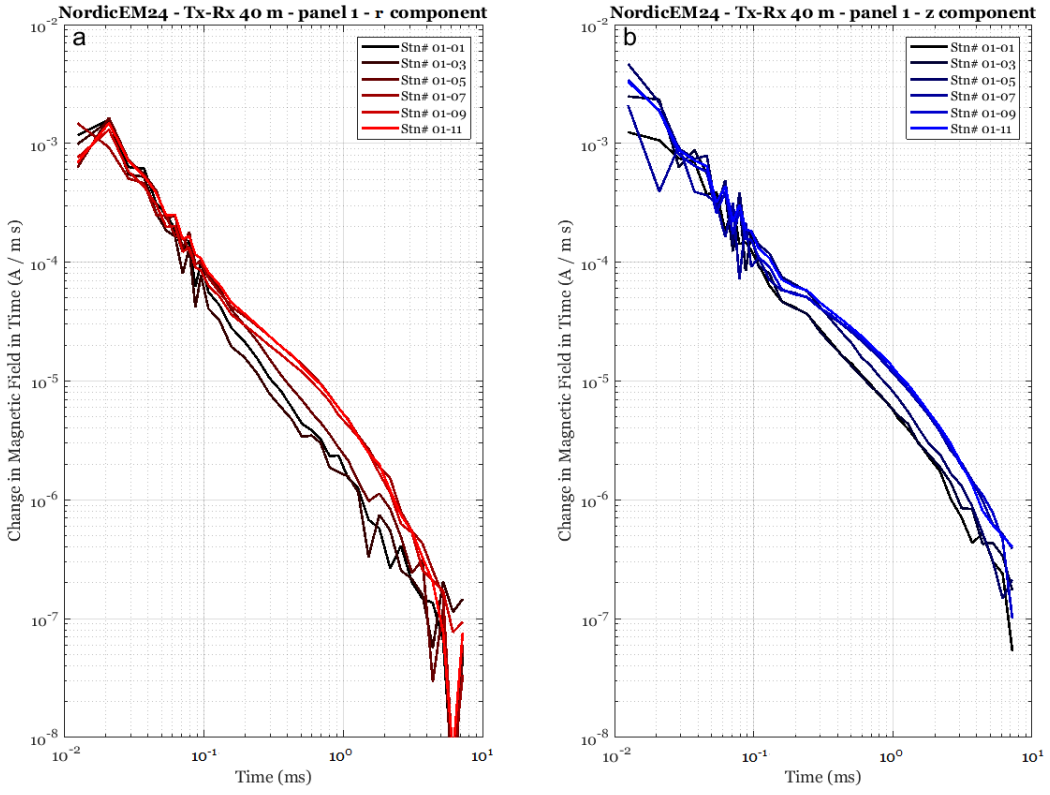

Figure 4.2: **2017 survey data. Decay view. Profile line 1; transmitter receiver separation of 40 metres. Figure 4.2.a shows the radial field decay and figure 4.2.b shows the vertical field decay.**

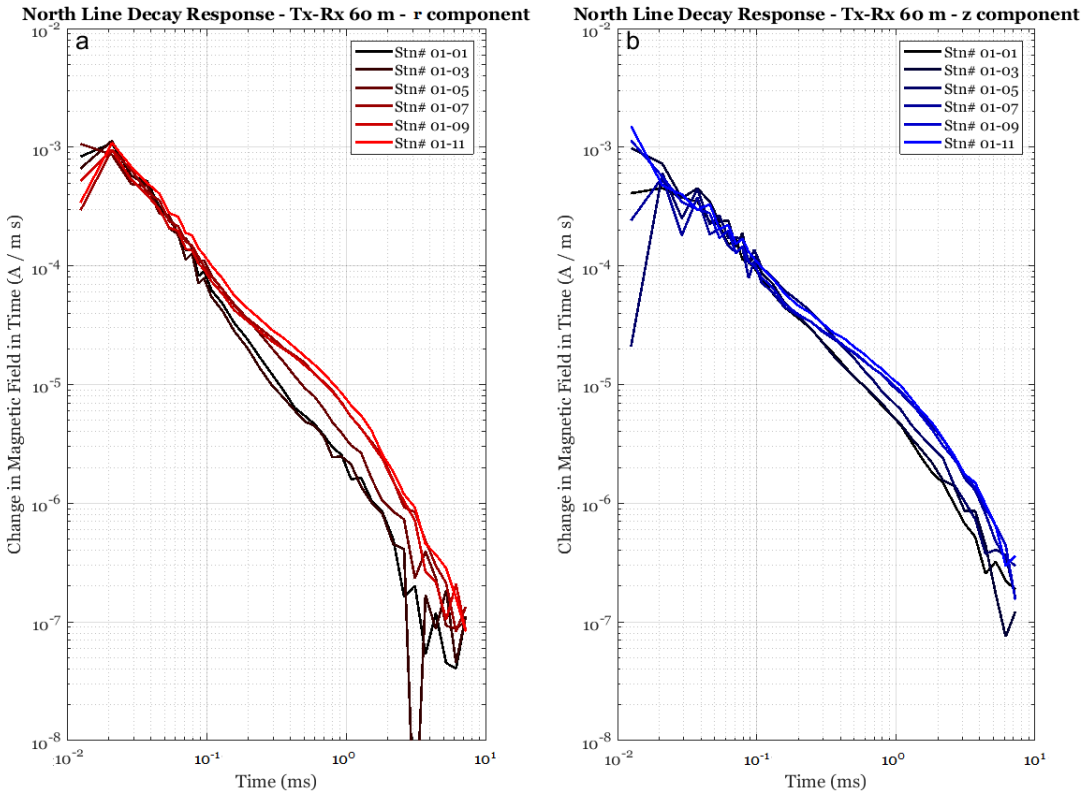

Figure 4.3: **2017 survey data. Decay view. Profile line 1; transmitter receiver separation of 60 metres. Figure 4.3.a shows the radial field decay and figure 4.3.b shows the vertical field decay.**

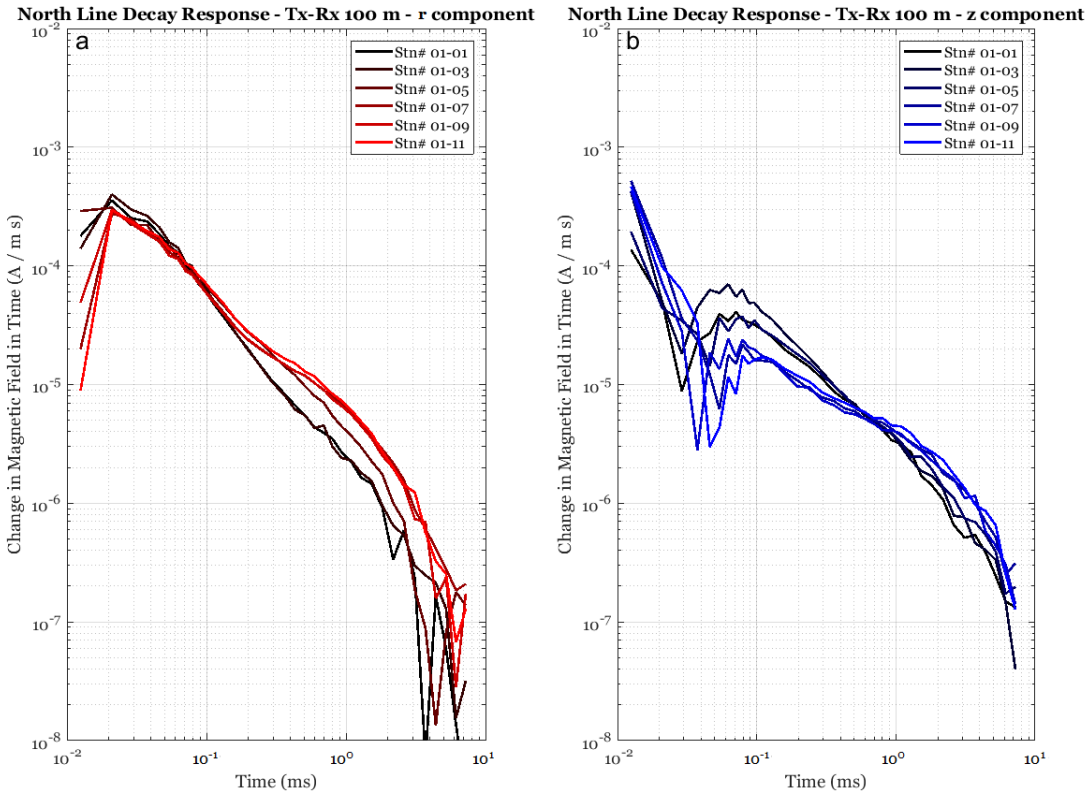

Figure 4.4: **2017 survey data. Decay view. Profile line 1; transmitter receiver separation of 100 metres. Figure 4.4.a shows the radial field decay and figure 4.4.b shows the vertical field decay.**

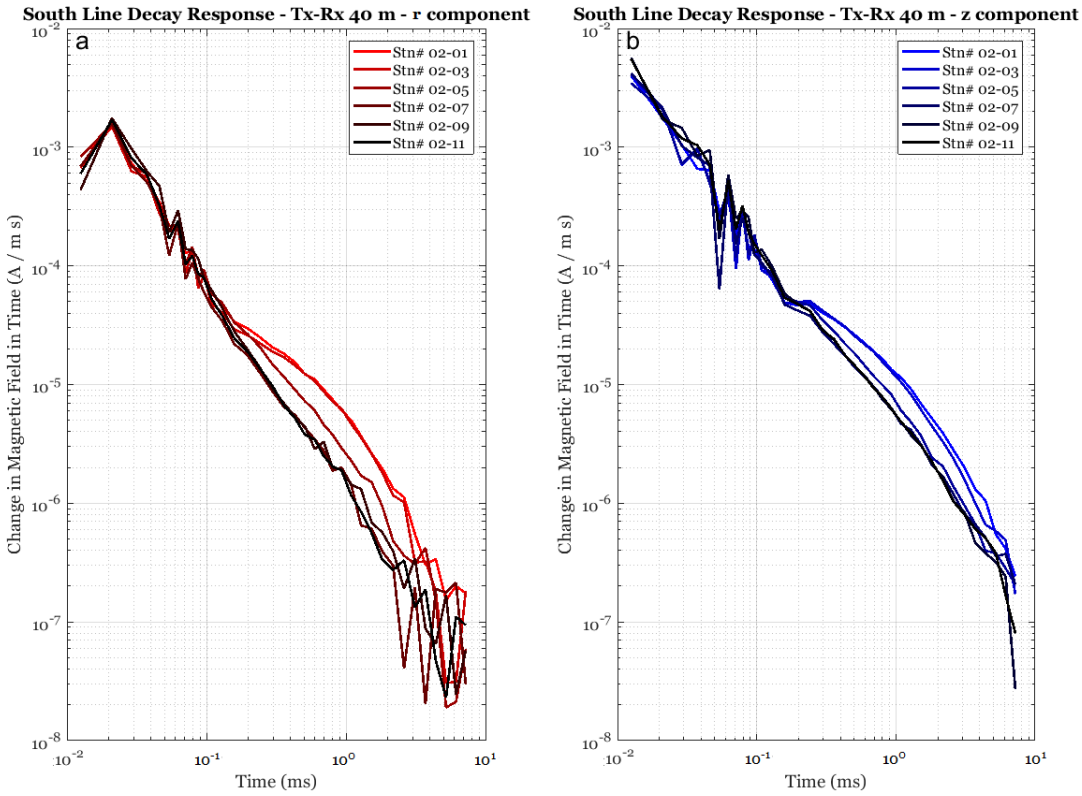

Figure 4.5: **2017 survey data. Decay view. Profile line 2; transmitter receiver separation of 40 metres. Figure 4.5.a shows the radial field decay and figure 4.5.b shows the vertical field decay.**

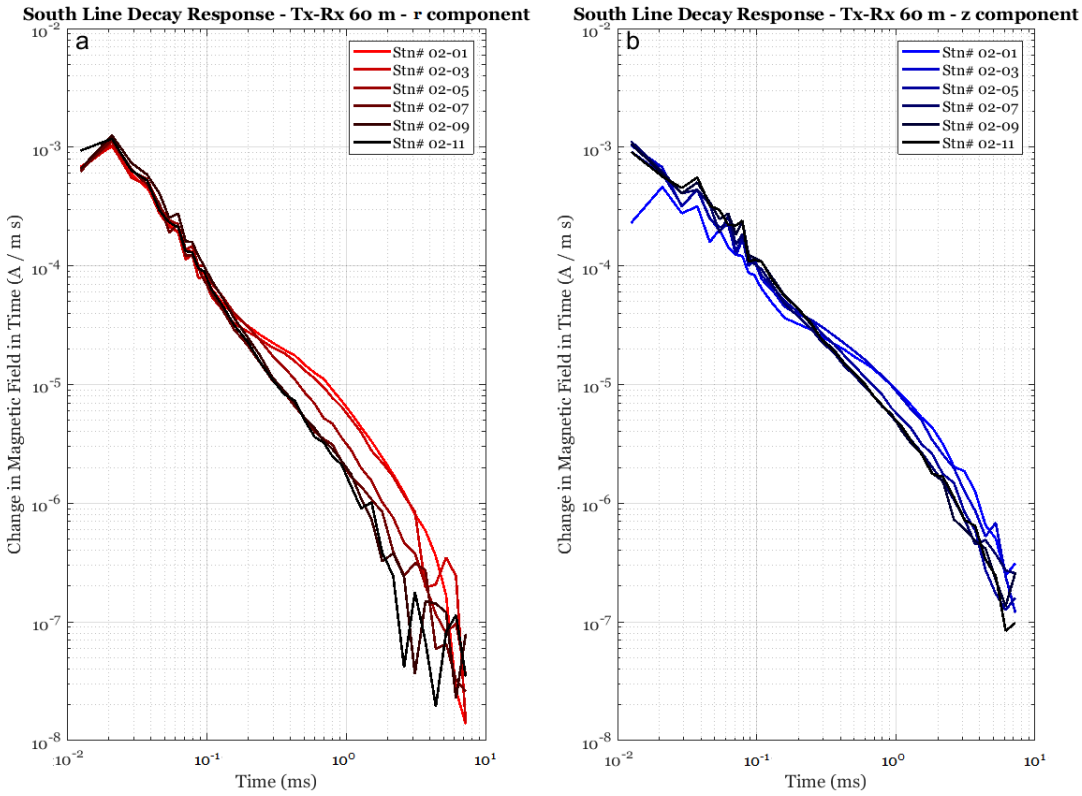

Figure 4.6: **2017 survey data. Decay view. Profile line 2; transmitter receiver separation of 60 metres. Figure 4.6.a shows the radial field decay and figure 4.6.b shows the vertical field decay.**

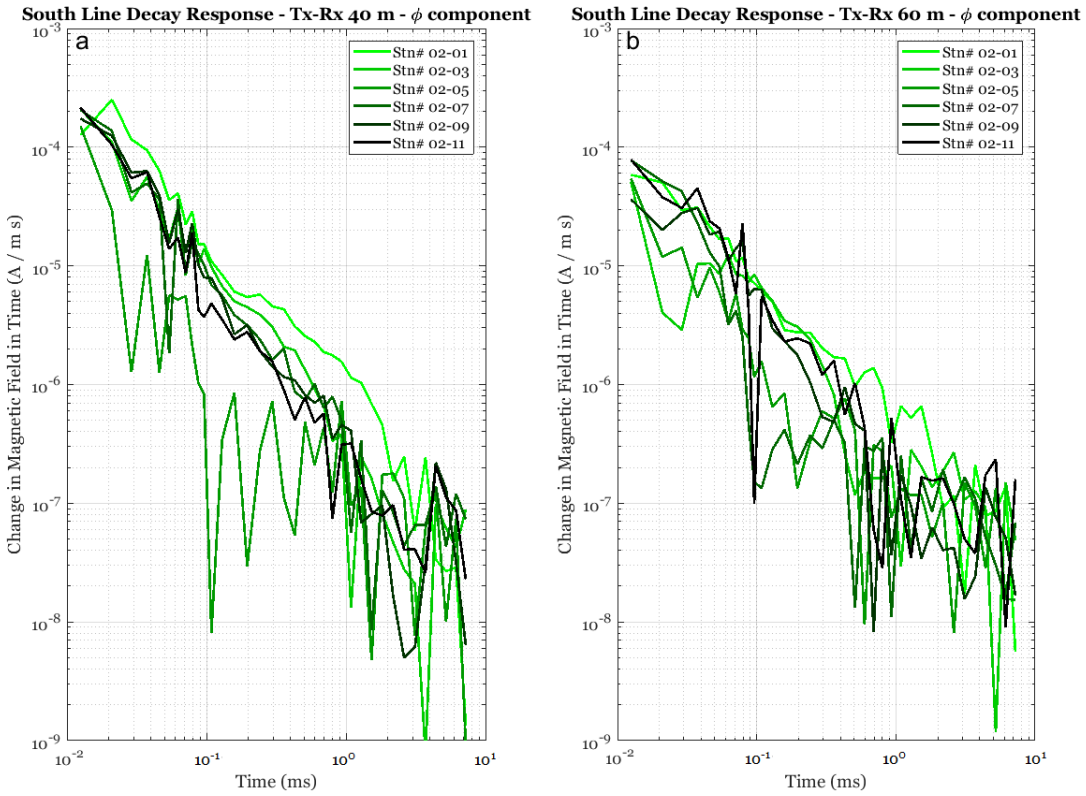

Figure 4.7: **2017 survey data. Decay view. Profile line 2; tangential field decay readings. Figure 4.7.a shows the readings at** 40 **m Tx-Rx separation, while figure 4.7.b shows the readings at** 60 **m Tx-Rx separation.**

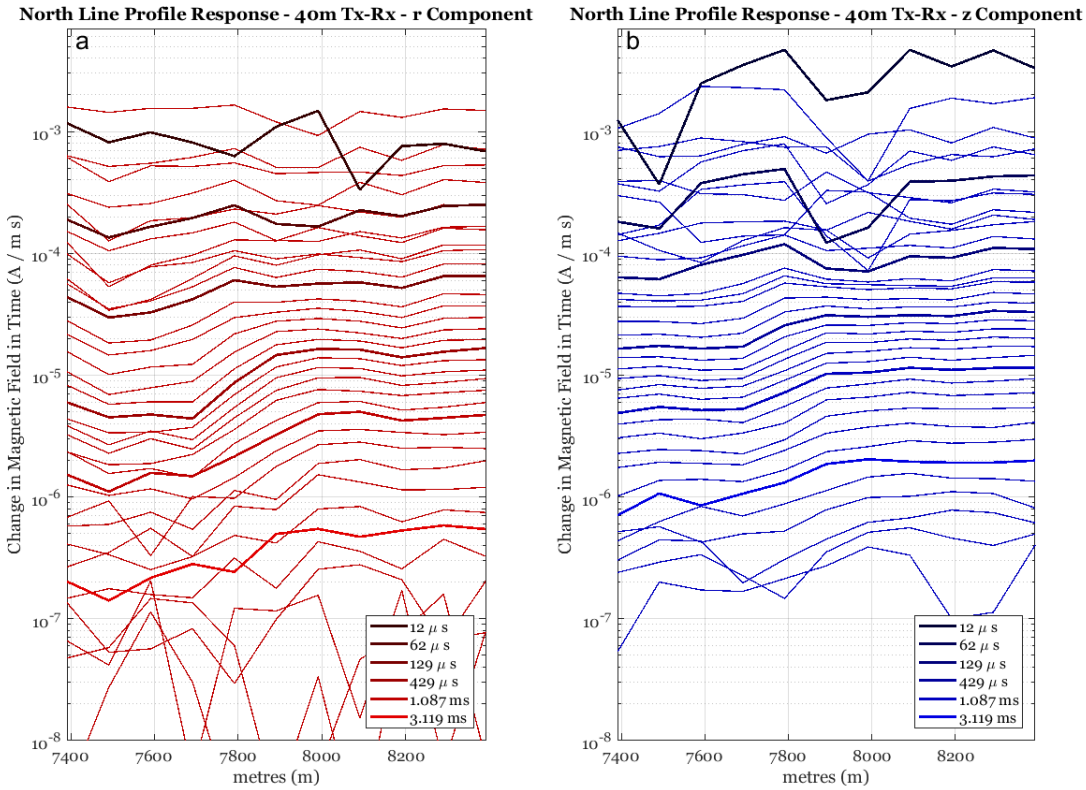

Figure 4.8: **North profile of the magnetic field decay. Shown here are all of the timegates, with specific highlighted ones in bold. Transmitter receiver separation at** 40 **m.**

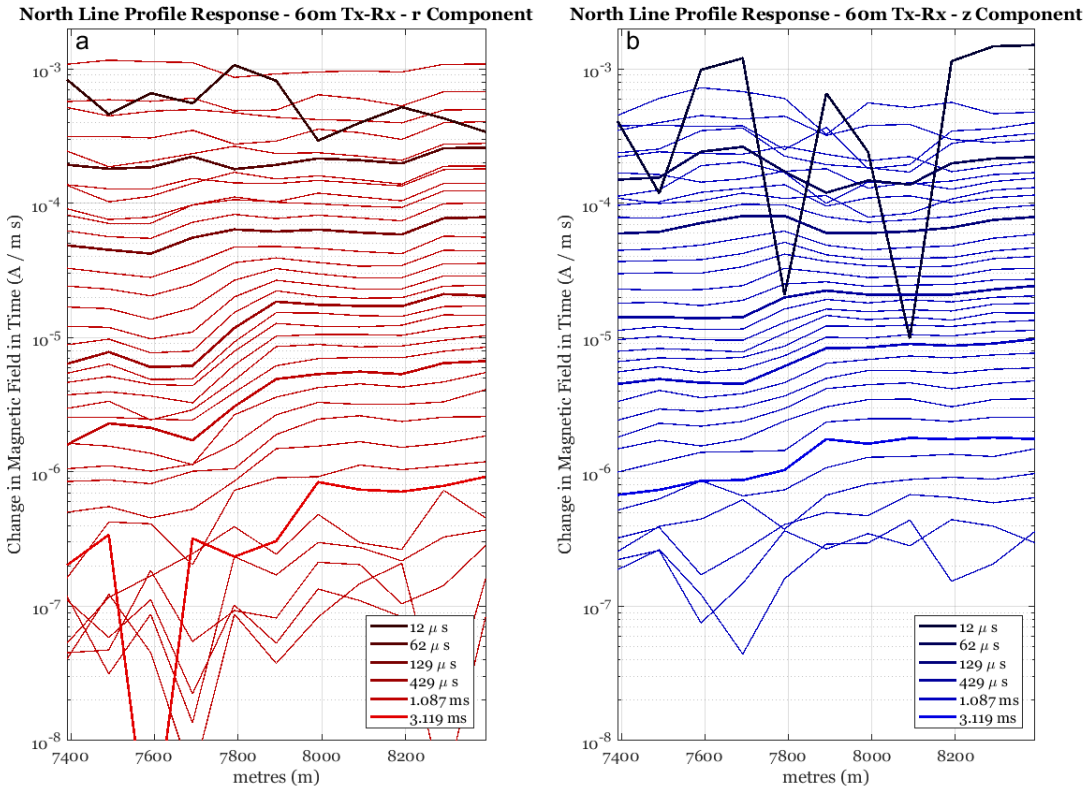

Figure 4.9: **North profile of the magnetic field decay. Shown here are all of the timegates, with specific highlighted ones in bold. Transmitter receiver separation at** 60 **m.**

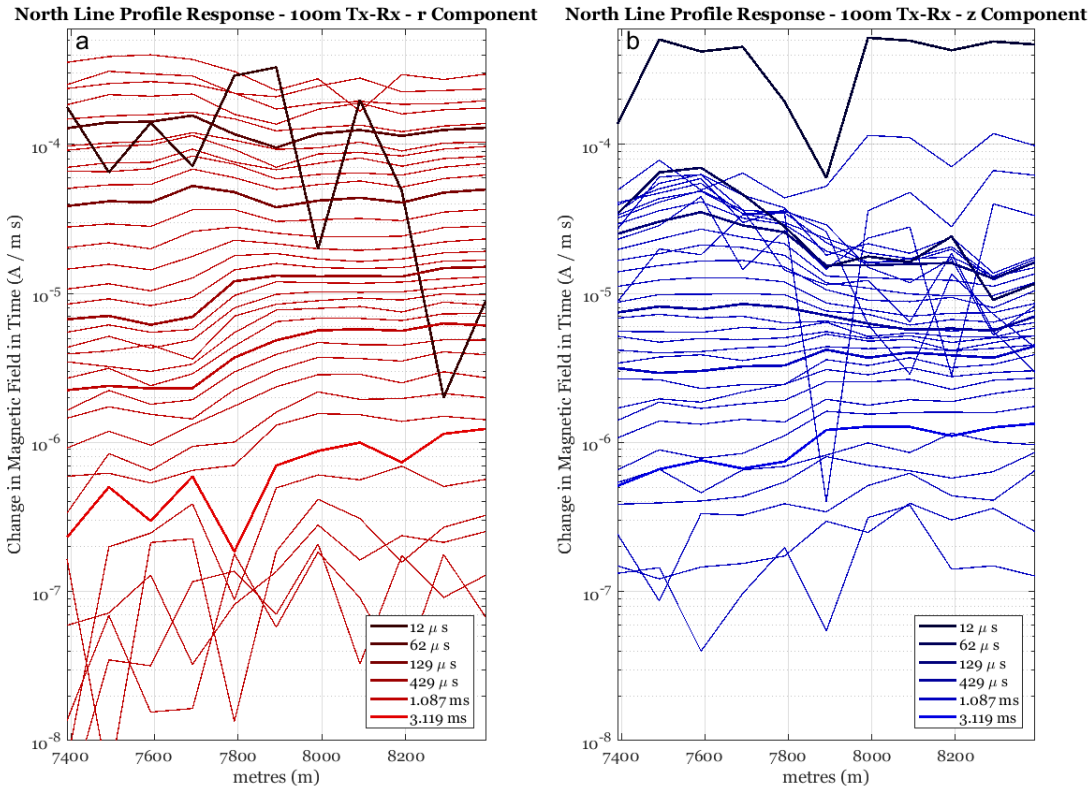

Figure 4.10: **North profile of the magnetic field decay. Shown here are all of the timegates, with specific highlighted ones in bold. Transmitter receiver separation at** 100 **m.**

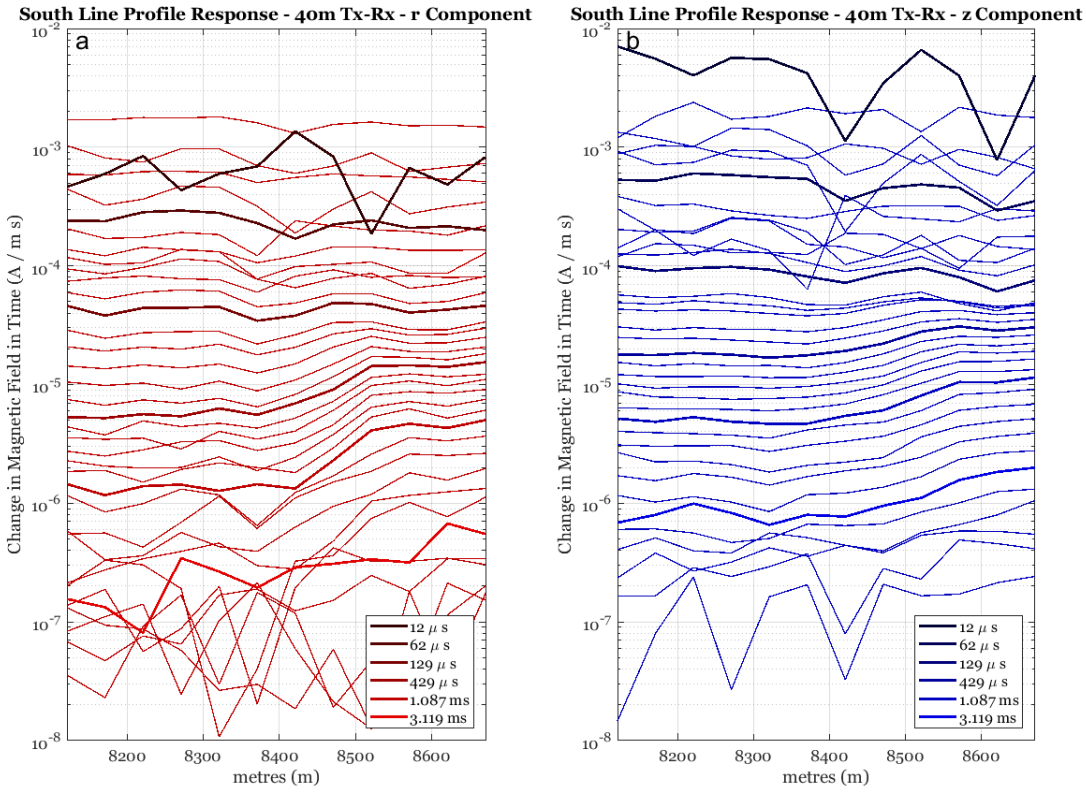

Figure 4.11: **South profile of the magnetic field decay. Shown here are all of the timegates, with specific highlighted ones in bold. Transmitter receiver separation at** 40 **m.**

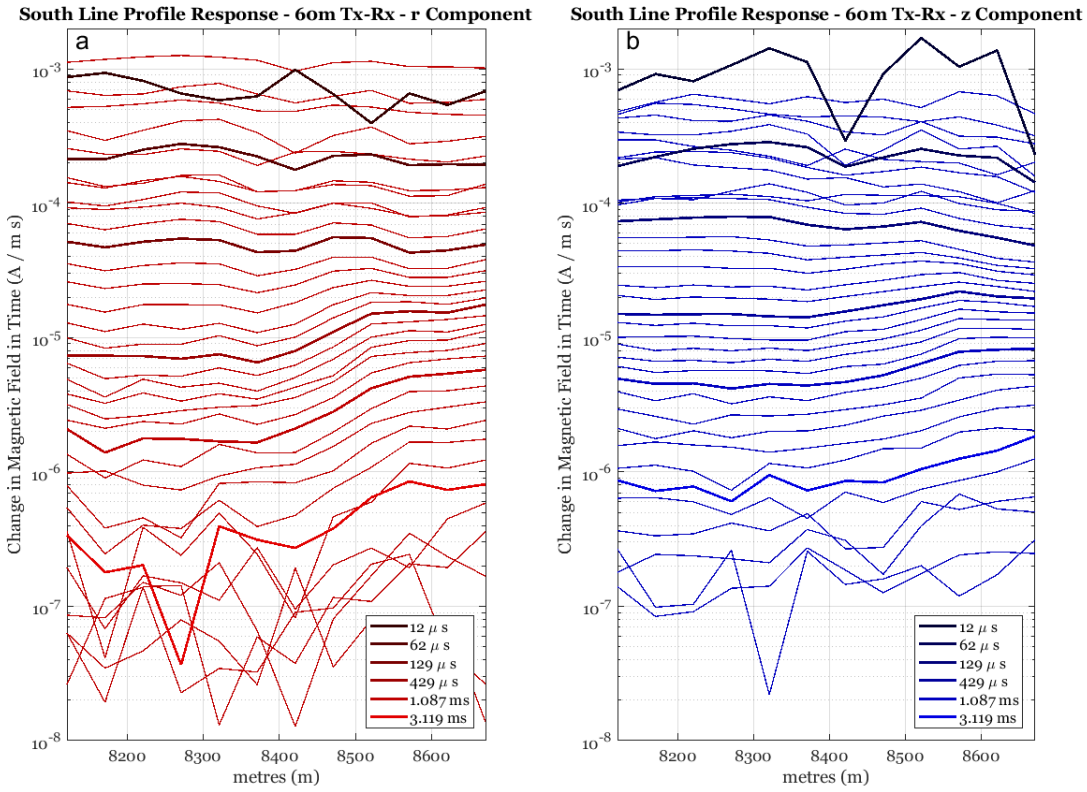

Figure 4.12: **South profile of the magnetic field decay. Shown here are all of the timegates, with specific highlighted ones in bold. Transmitter receiver separation at** 60 **m.**

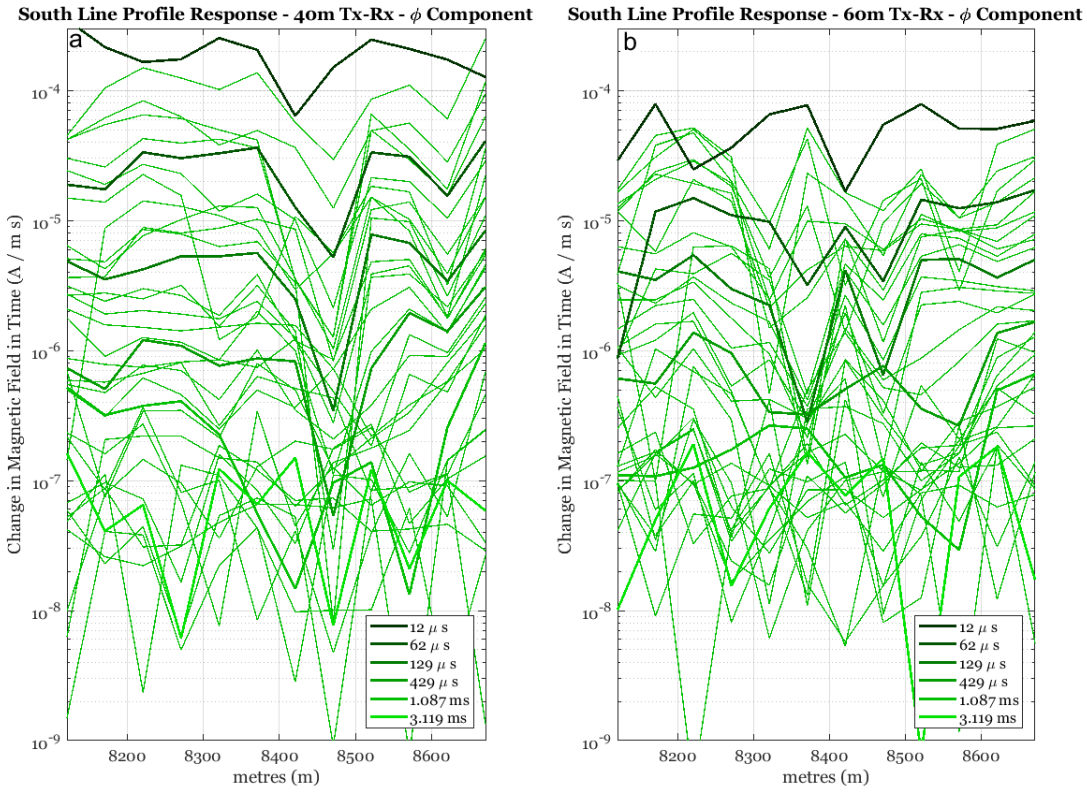

Figure 4.13: **South profile of the magnetic field decay - tangential field. Shown here are all of the timegates, with specific highlighted ones in bold. Transmitter receiver separation at both 40 m and 60 m.**

Mudge, 2014). The base station in this case was 01-01 or the westernmost transmitter set-up point as it was seen as the best baseline measurement from either survey line (i.e. farthest from the anomalous zone). Equation 4.1 shows this calculation. Letting Ψ stand for the time derivative of the magnetic field ($\Psi = \frac{\mathrm{d}H}{\mathrm{d}t}$).

$$\log_{10} \Psi_{relative} = \log_{10} \left| \frac{\Psi_{\hat{i}}}{\Psi_0} \right| = \log_{10} \left| \frac{\frac{\mathrm{d}H_{\hat{i}}}{\mathrm{d}t}}{\frac{\mathrm{d}H_0}{\mathrm{d}t}} \right|. \tag{4.1}$$

Relative responses of 0 show a normal - or consistent with the baseline - measurement. Values greater than 1 or less than 1 show an elevated or depressed measurement indicative of a conductive or resistive change in the environment respectively. Figures 4.14, 4.15, 4.16, 4.17, 4.18, and 4.19 show the log of the relative decay response at a set selection of timegates ranging between 0.096 and 2.179 ms. By removing the background or regional signal, we can see the transition segments on each line more easily, as well as get a quantitative value of the magnitude of the response from the target (or residual) signal. The transition zone appears to begin around 7720 m and ends around 8000 m on the north line and begins around station 8360 m and ends near station 8580 m on the south line. A plan view with an interpreted extent of the anomalous and transitional zones from the time-domain electromagnetics data is shown overlaid on a plan view of the survey in figure 4.20. The measured vertical field time decay at 100 m Tx-Rx separation decreases in early time magnitude relative to the reference baseline. This is a feature that accompanies the proximity in time to the current transferring below from one side of the receiver to the other, seen in the response signal as a sign change in the magnetic field decay. This phenomenon is illustrated through computer modelling in section 3.1.5.

Figures 4.21, 4.22, and 4.23 show the relative decay response over all timegates at select stations. These stations were selected from within the anomaly on both lines (stations 01-11 and 02-01), as well as stations from within the transition zone (station 01-05 and 02-05). From these we can see the time of peak relative response amplitude appears in the radial field consistently at around 0.5 ms across all Tx-Rx separations. The time of the peak relative decay response of the vertical field appears to shift in time as the Tx-Rx separation increases. At Tx-Rx of 40 m the peak time settles at around 1.1 ms, while at 100 m Tx-Rx

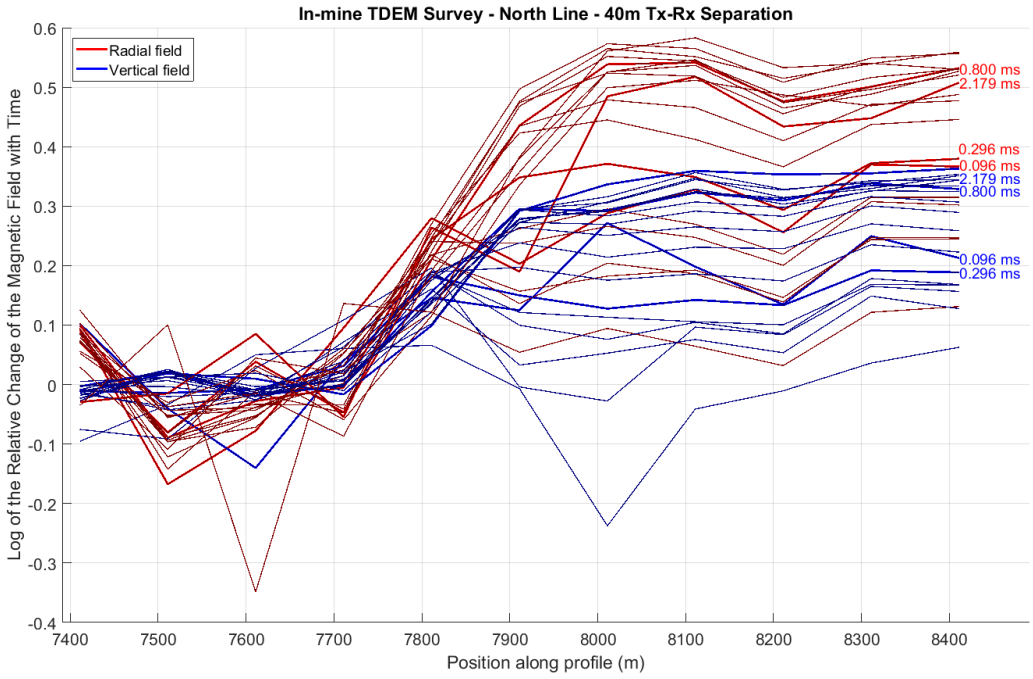

Figure 4.14: **North line, 40 metre Tx-Rx separation readings in profile with the background signal removed. Y-axis shows the ratio of the signal at each station to the normal conditions.**

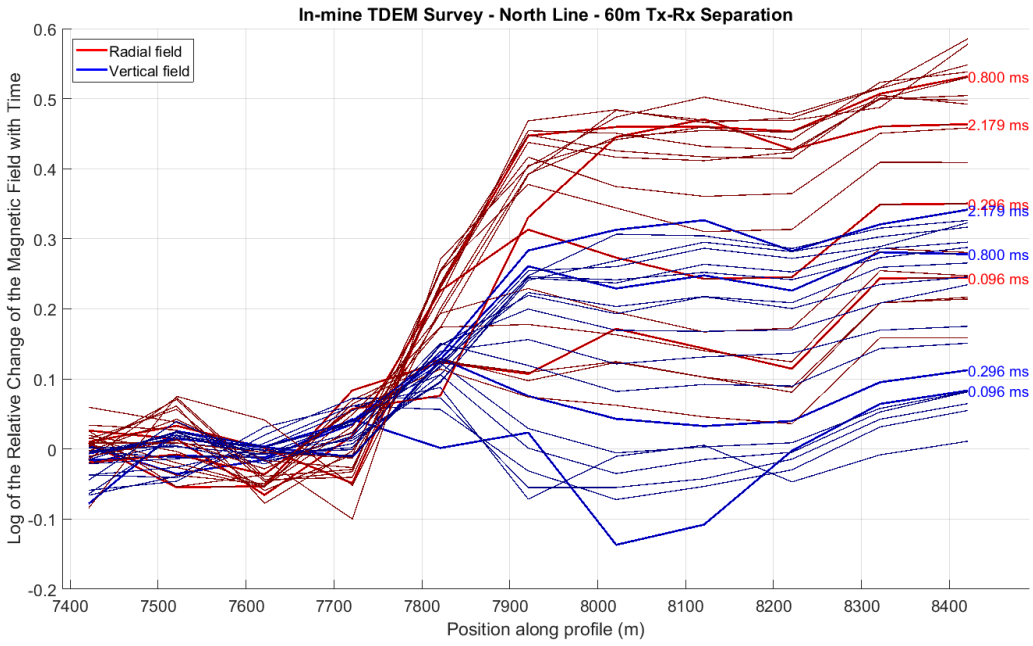

Figure 4.15: **North line, 60 metre Tx-Rx separation readings in profile with the background signal removed. Y-axis shows the ratio of the signal at each station to the normal conditions.**

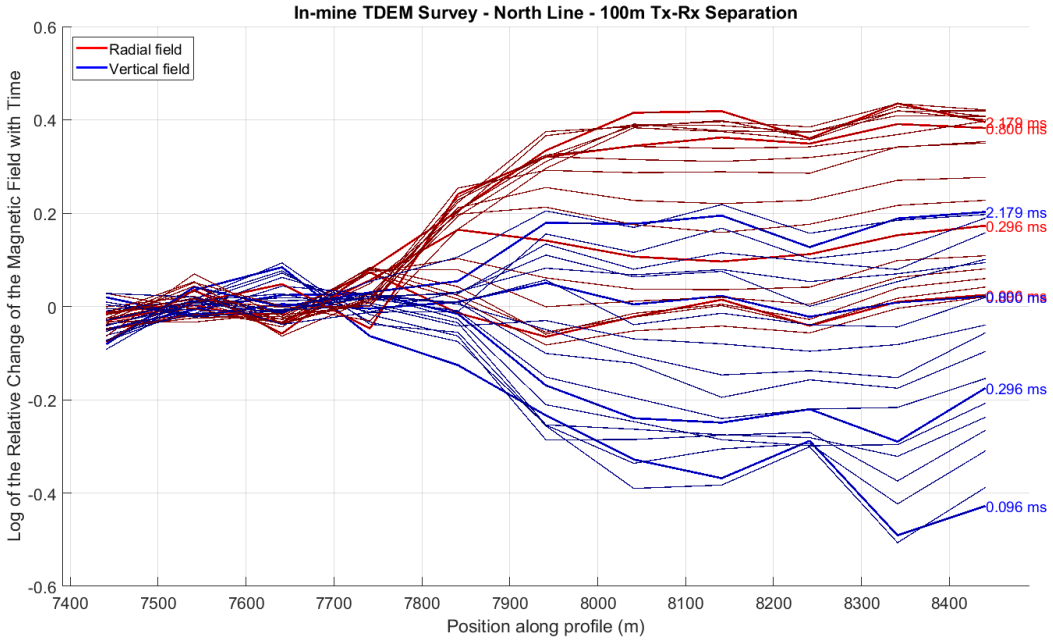

Figure 4.16: **North line, 100 metre Tx-Rx separation readings in profile with the background signal removed. Y-axis shows the ratio of the signal at each station to the normal conditions.**

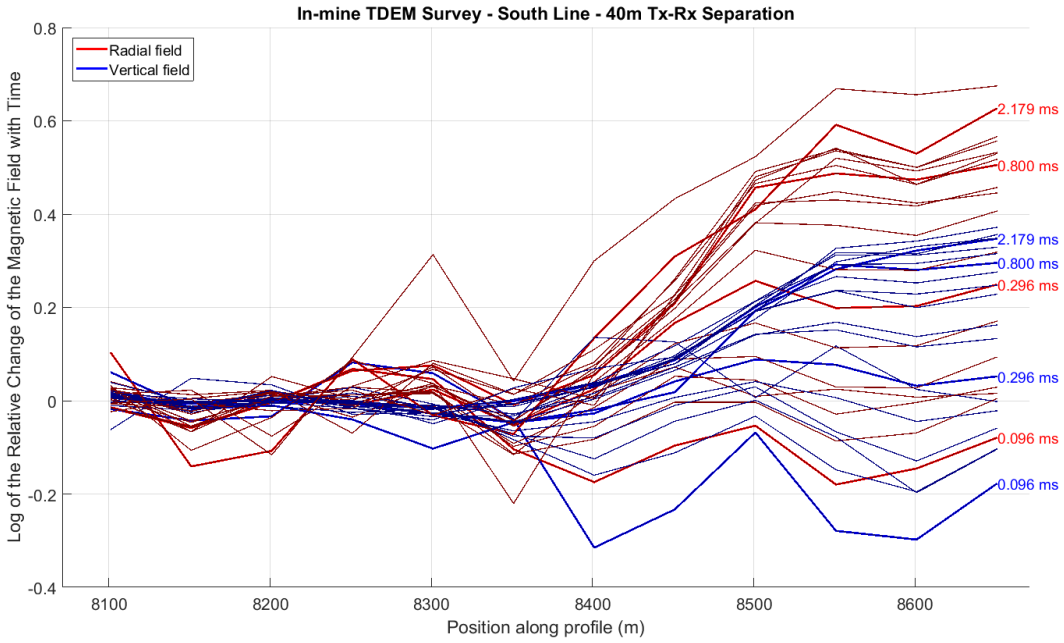

Figure 4.17: **South line, 40 metre Tx-Rx separation readings in profile with the background signal removed. Y-axis shows the ratio of the signal at each station to the normal conditions.**

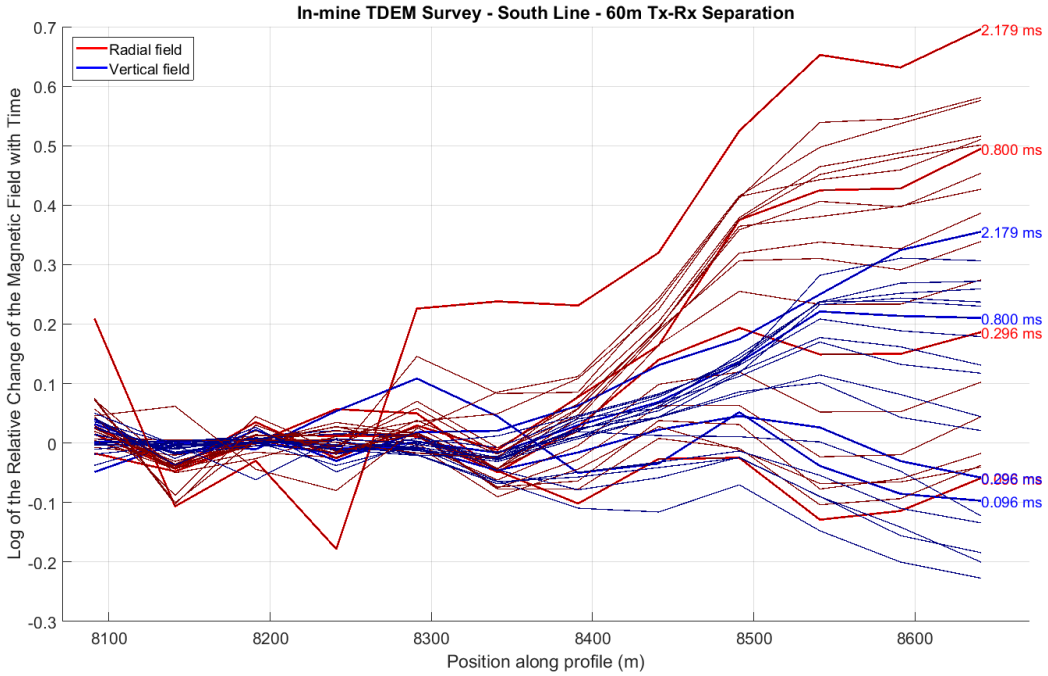

Figure 4.18: **South line, 60 metre Tx-Rx separation readings in profile with the background signal removed. Y-axis shows the ratio of the signal at each station to the normal conditions.**

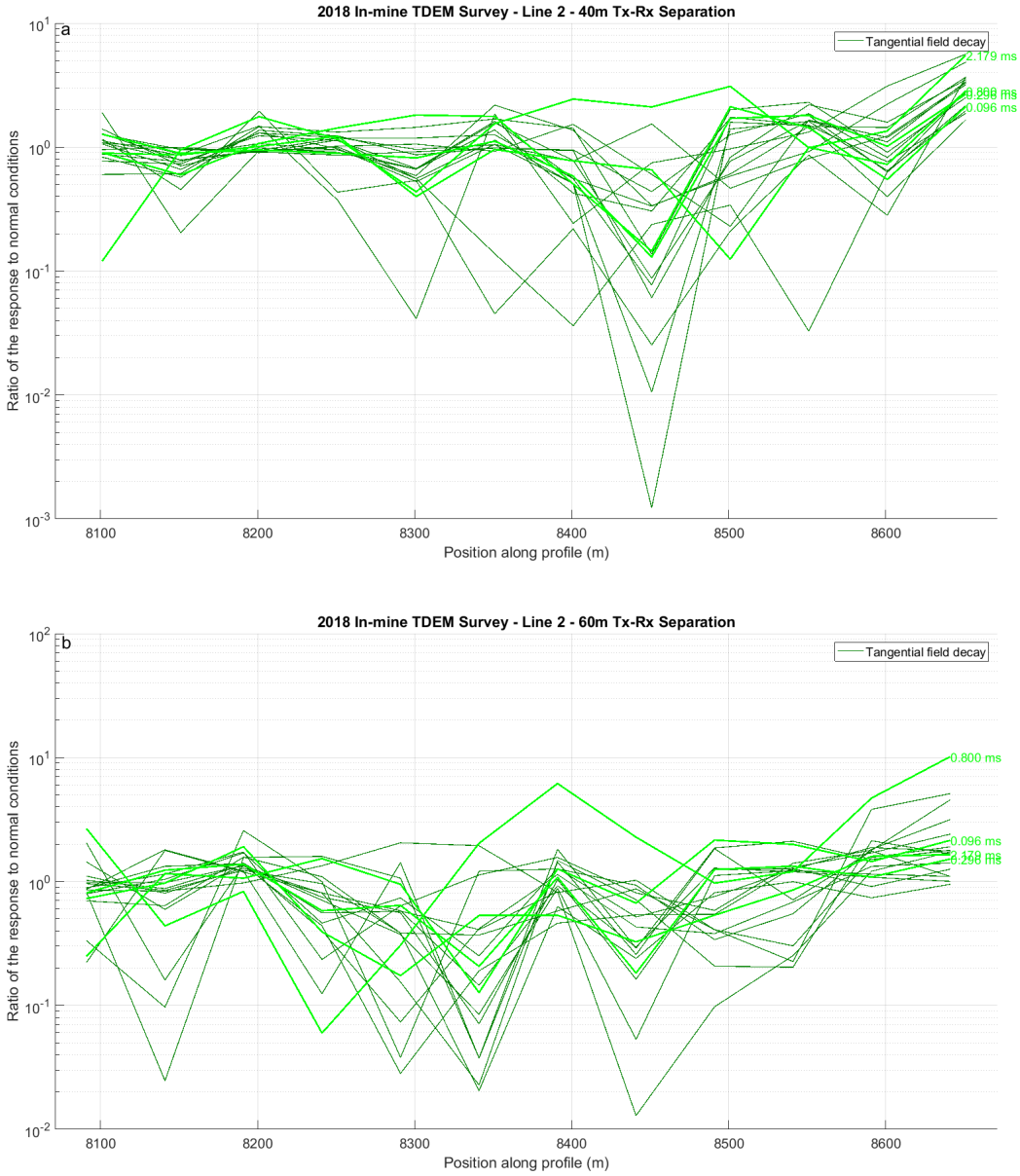

Figure 4.19: **South line, 40 and 60 metre Tx-Rx separation tangential field readings in profile with the background signal removed. Y-axis shows the ratio of the signal at each station to the normal conditions.**

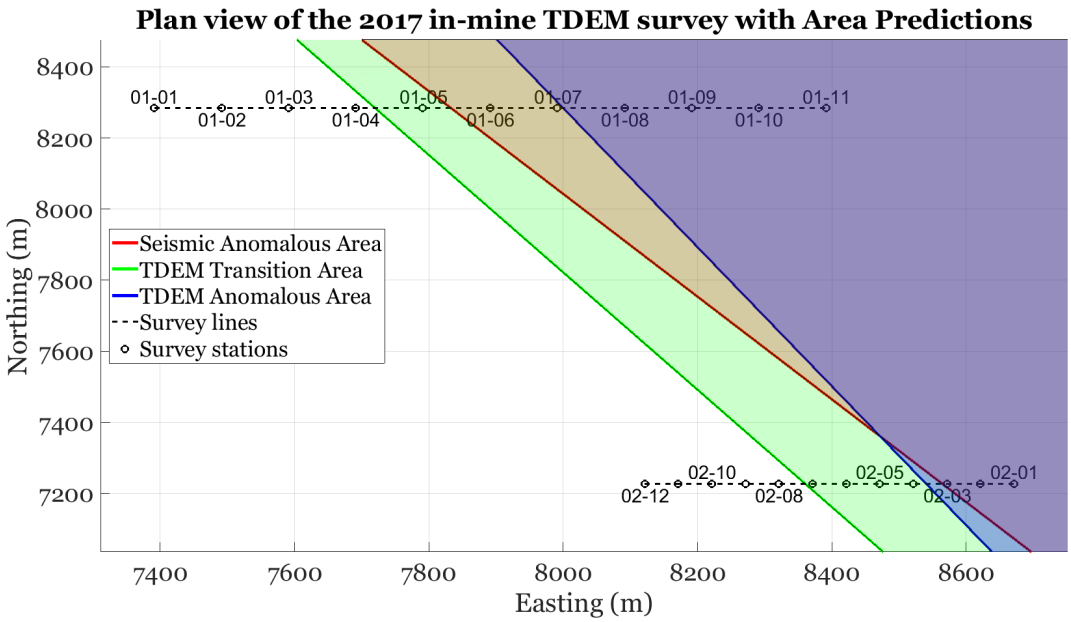

Figure 4.20: **Plan view of the TEM survey area including the TEM predicted anomalous (blue) and transitional (green) areas. Also shown is the anomalous zone as predicted by the earlier seismic surveys.**

the peak settles around 1.5 ms. Unfortunately, the noise level is quite high once the signal passes anywhere between 2 - 6 ms at any orientation or separation. In addition, at 100 Tx-Rx separation, the vertical field decay is still exiting early time as the measurements were recorded. This creates a cross-over between 0.1 and 1 ms where the conductive response is lower in amplitude than the resistive response (but still decaying at a much slower rate). In general, it appears that both lines produce similar relative decay responses, with the south line (station 02-01) being slightly more muted when compared with the response on the north line (01-11) - especially between 0.1 and 0.3 ms in the radial field measurements (slightly later for the vertical). The relative response from the intermediate zone (station 01-05) on the north line appears to be very similar to the anomalous zone north line station in the early timegates. However, at around 0.3 or 0.4 ms and later the signal diverges and becomes much lower in amplitude than in the anomalous zone. This feature appears in the intermediate zone reading on the south line as well (station 02-05).

The signal-to-noise ratio appears to be very high over many of the measured time-gates - though at the last several time-gates, more-so for the radial field, the signal-to-noise ratio drops noticeably. There are several features that control the time-gates at which the noise

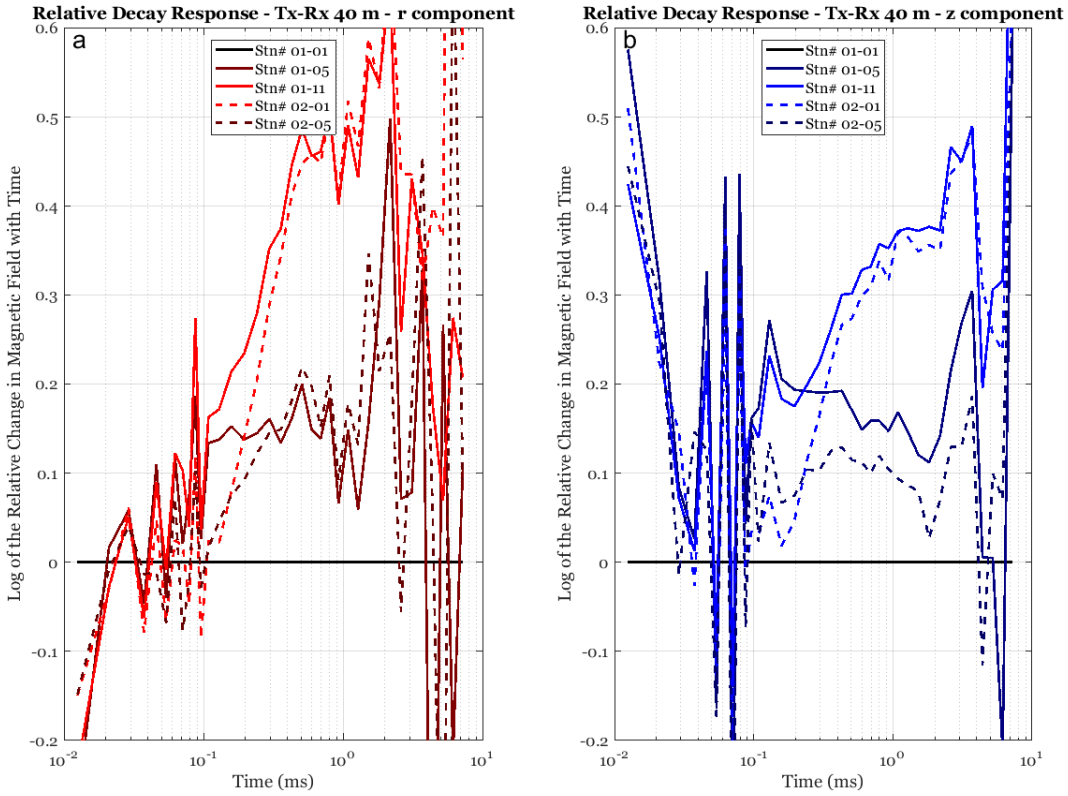

Figure 4.21: **2017 survey data. Relative decay of select stations. Transmitter receiver separation of 40 metres. Figure 4.21.a shows the relative radial field decay and figure 4.21.b shows the relative vertical field decay. Each figure displays a station from the anomalous zone from both the north and south lines (stations 01-11 and 02-01), as well as stations from the transition zone (stations 01-05 and 02-05).**

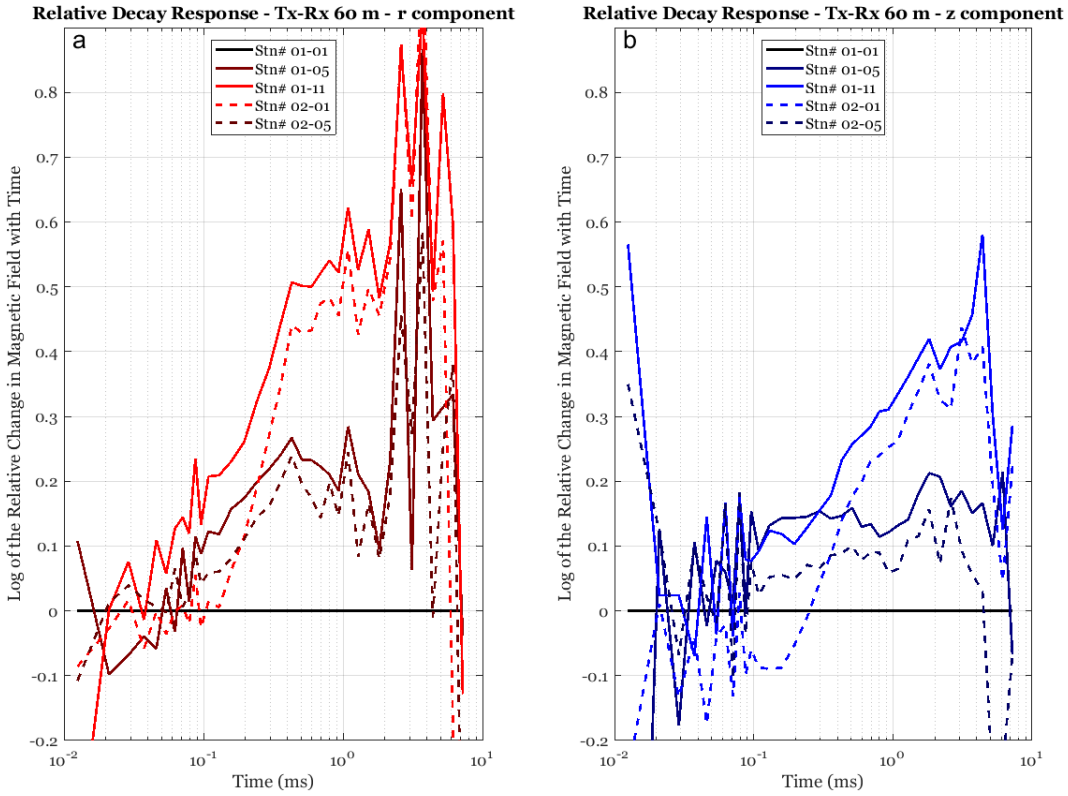

Figure 4.22: **2017 survey data. Relative decay of select stations. Transmitter receiver separation of 60 metres. Figure 4.22.a shows the relative radial field decay and figure 4.22.b shows the relative vertical field decay. Each figure displays a station from the anomalous zone from both the north and south lines (stations 01-11 and 02-01), as well as stations from the transition zone (stations 01-05 and 02-05).**

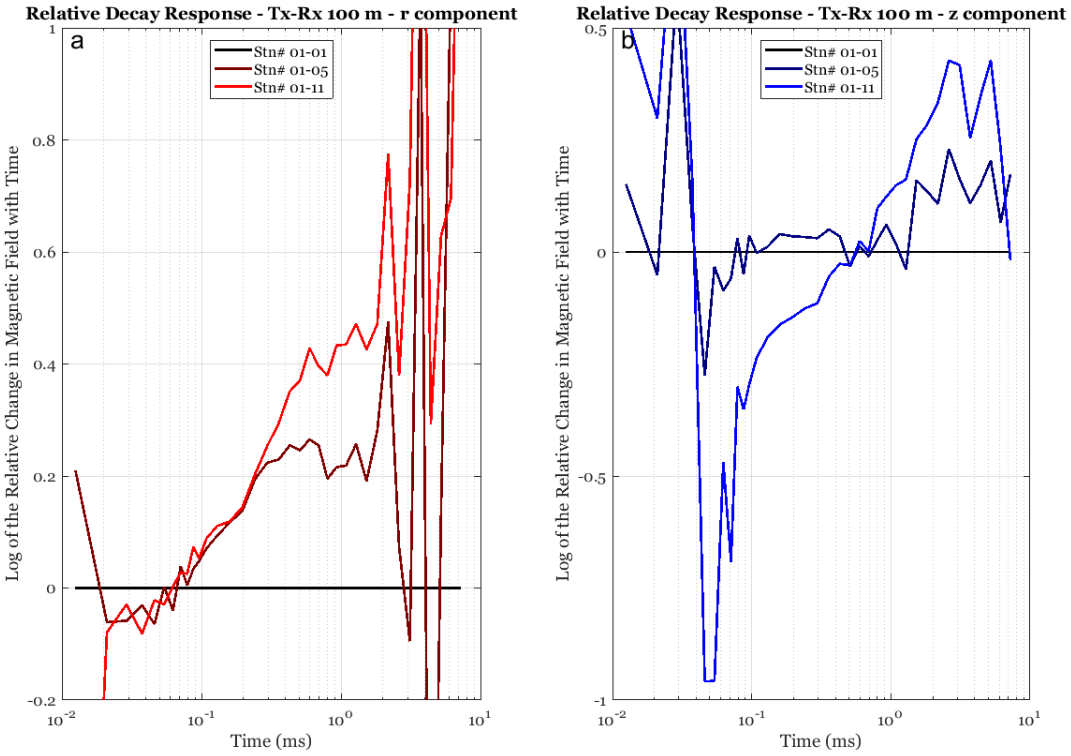

Figure 4.23: **2017 survey data. Relative decay of select stations. Transmitter receiver separation of 60 metres. Figure 4.23.a shows the relative radial field decay and figure 4.23.b shows the relative vertical field decay. Each figure displays a station from the anomalous zone from the north line (station 01-11), as well as a station from the transition zone (station 01-05).**

appears to overtake the signal. For one, the radial field time decay, as always, drops in signal at a faster rate than the vertical field. This shifts the point where the noise overwhelms the signal by roughly 1 ms later in time for the vertical field decay than the radial. This gives the vertical field decay a bit more depth of penetration per transmitted signal strength than the radial field decay. In addition, due to the elevated signal response in the anomalous region, the time-gate at which the noise level appears to overtake the signal shifts later in time by as much as 2 ms. The amplitude at which the noise overtakes the signal is relatively consistent across all of the station measurements. The point in amplitude that the signal appears to be exceeded by the noise is around 6×10^{-6} A m^{-1} s^{-1}. Note that this signal has been processed to remove the effects of the properties of the transmitter and receiver. This makes the amplitude depend on the mutual inductance of the system. This doesn't express the true noise level of the receiver used in the survey. To get this we will need to multiply the amplitude by the transmitter system parameters - this will remove the influence of the transmitter power on the receiver noise level and demonstrate the expected noise level of the receiver system given a transmitting magnetic moment of 1 A m^2. This can be seen in equation 4.2, where a is the area of the transmitter loop, and I_t is the current multiplied by turns within the wire loop. The area of the transmitting loop was 25 m^2 and the wire had 8 turns and a current of typically around 13 A. If we undo the transmitter correction done in processing, we get a better idea of the true detection level of the receiver system. This detection limit is calculated to be roughly 0.016 A m^{-1} s^{-1} (per unit of magnetic moment produced by the transmitter).

$$\text{absolute noise level}\left[\frac{\mathrm{d}H}{\mathrm{d}t}\right] = \text{relative noise level}\left[\frac{\mathrm{d}H}{\mathrm{d}t}\right] \times a \times I_t. \tag{4.2}$$

To get an idea of the noise level over the middle time-gates where the signal is much larger than the noise level, it is best to look at the data across the "normal" geological area where geological changes are thought to be quite small. In this kind of analysis we are observing not just the repeatability of the measurements, including the turn-off syncing between the transmitter and receiver, but also the background EM noise levels as well as the signal from spatial variations in nearby mining structure over the surveyed profile. The contribution of

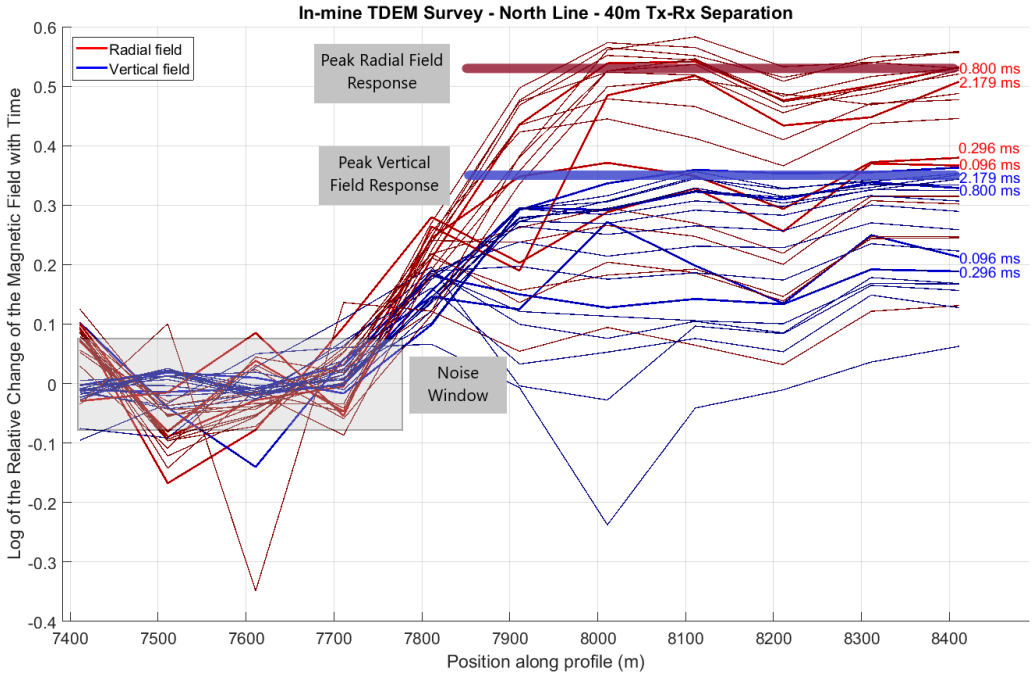

Figure 4.24: **Same as figure 4.14. Included on this figure are labels indicating the peak signal contrast between the anomalous and normal areas, as well as a qualitative approximation of the noise window within the normal area.**

such mining structure to the measured signal was thought to be minimal, as great care was taken prior to the survey to remove such features where possible - or note their presence when removal was impossible. Figure 4.24 helps illustrate the quality of the repeatability of the measurements - at least over the 400 m of the profile line that was in relatively "normal" and consistent geological conditions. Note that only the time-gates roughly between 0.1 ms and 2.2 ms are shown. These time-gates are not influenced by the drop in signal of late-time. The bulk of the noise over the first 400 m seems contained to a relative response of $\pm$0.075 in log space which equals a linear percent variation of around $\pm$18% in real space. In contrast, the response from the geologically anomalous area is around 0.54 for the radial field and 0.35 for the vertical field in log space - or roughly 350% and 225% increase in signal amplitude change respectively. From this we can see that the response from this particular geological anomaly is several orders of magnitude larger than the noise over the time-gates between 0.1 and 2.2 ms.

4.2 Forward Models

This section details the forward modelling performed in both COMSOL Multiphysics and Matlab. The parameters for these models were approximated from well-logs and refined through data inversions using the survey results previously discussed in section 4.1. An assortment of forward models were created in sets. These different sets of models were defined by setting the initial model to the same baseline parameters. The baseline parameters are shown in table 4.2. The subsequent models in each set were created by varying just one parameter from the baseline set. Sections 4.2.1, 4.2.2, 4.2.3, 4.2.4, and 4.2.5 discuss four of these parametric sweep model sets. They are broadly focused on analyzing the response in anomalous areas of salt thickness and Dawson Bay porosity. The thickness of the salt is analyzed in two sections. One looks at the salt-back thickness - i.e. the thickness of the Prairie Evaporite formation above the mine (section 4.2.3), and the other looks at thinning of the salt below the mine level (section 4.2.4). This thinning is caused by the presence of mounds - or "banks" - of the Winnipegosis formation. The Dawson Bay porosity is, of course, a more complicated phenomenon to model as it is a property change in the carbonate rock itself rather than a simple thinning or thickening. In an effort to keep the parameter sweep as simple as possible the anomalous zone was kept to the middle members of the Dawson Bay. Only the resistivities were allowed to vary; thicknesses were held constant. This was done in two separate sets. The first looked at just varying the Lower Dawson Bay - the larger, normally non-porous, more proximal member of the carbonate body (section 4.2.1). The other allowed the resistivity of the entire Dawson Bay carbonate body (both the lower and upper members) to vary in resistivity by the same factor (section 4.2.2). Lastly, in section 4.2.5 each of these anomalous responses are compared to one another and to the survey data from section 4.1. In all of these cases, the change in response from the parameter change arrived very early in time. Typical TEM targets in mineral exploration (for example) stretch in arrival times from 10 to 100 ms (Dentith and Mudge, 2014). Responses from all of these forward model parameter sweeps peaked well prior to 1 ms.

Three types of figures are used to display each of these sets of parameter sweeps. Figures 4.25, 4.29, 4.33, and 4.37 show the models in a standard time-decay view over their calculated

Layer	Thickness (m)	Resistivity (Ωm)
Upper half-space	∞	3.4
Davidson	13	1.4
First Red Bed	12	3.4
Hubbard	3	93.4
Upper Dawson Bay	10	**4.1***
Lower Dawson Bay	33	**74.9***
Second Red Bed	8	27.7
Prairie Evaporite (above)	**30****	806.7
Mine	2.6	∞
Prairie Evaporite (below)	**105*****	2007.7
Winnipegosis	10	141.3
Lower half-space	∞	43.5

Table 4.2: **Model parameters used for several of the following sections. Note the special signifiers around the following parameters: lower and upper Dawson Bay resistivity (*), Prairie Evaporite thickness above the mine (**), and the Prairie Evaporite thickness below the mine (***), all vary in their parameter sweeps in their respective sections.**

time-gates of 1 μ s to 10 ms. Figures 4.26, 4.30, 4.38, and 4.34 show a relative decay of the model responses over the time of evaluation. The relative decay was calculated using equation 4.1 (where H_0 is the calculated magnetic field response of the baseline model and H_i is the magnetic field response of the i-th model) and is simply the ratio of the logarithm of the decay response of each model over the decay response of the baseline model. The baseline model used the parameters found in table 4.2. Figures 4.27, 4.31, 4.39, and 4.35 show the relative magnetic field decay at several discretized time-gates over the parameters of the respective parametric sweeps. The chosen time-gates for these figures were spaced logarithmically between 10 μs and 10 ms.

4.2.1 Modelling of Anomalous Lower Dawson Bay

The porosity anomalies in the Dawson Bay and their accompanying conductivity increase is the primary focus of this research. Initially, it was thought that the conductivity increase would be relatively minor, however, the data inversions shown in section 4.3.2 illustrate a significant parameter change in order to match the data collected in the 2017 in-mine survey. The range these parameters varied in the inversions were between 9 Ω m and 75 Ω

m. The Ste. Martha well-log analyzed in section 3.4 suggested a more intermediary value of around 33 Ω m, though keeping in mind that more resistive carbonates have been difficult to constrain in inversion, as well as having a larger percent standard deviation in the well-log (see table 3.3 and figure 3.29). The adjacent Upper Dawson Bay layer also reported a change in resistivity from 4.3 Ω m to 0.5 Ω m in the data inversion. This suggests the possibility that the porosity anomaly that effects the Lower Dawson Bay might also influence the thinner Upper Dawson Bay as well. However, regardless of the source, the bulk conductivity contrast is quite high from one end of the survey to the other.

For this parameter analysis of the Lower Dawson Bay we will sweep logarithmically from 74.9 Ω m to 7.49 Ω m and leave all other parameters (such as layer thicknesses and all other layer resistivities) the same throughout (see table 4.2 for the values used).

4.2.2 Modelling of Anomalous Dawson Bay (both lower and upper)

The relative response of the parameter sweep in the previous section (4.2.1) showed a very early time-gate response to the conductive change - peaking at around the 0.1 ms point. The survey data recorded a much later peak conductive response (around 1.0 ms). This suggested that additional conductive bodies existed in the anomalous survey area outside of the Lower Dawson Bay. In order to keep the parameter sweep simple, a single factor term was created and applied to the resistivity of both the Lower and Upper Dawson Bay members. This factor varied logarithmically between 1 and 0.1 and was applied to both Dawson Bay layers equally. The Lower Dawson Bay resistivity, then, varied by the same amount as in section 4.2.1 - from 74.9 Ω m to 7.49 Ω m. The Upper Dawson Bay resistivity varied between 4.1 Ω m and 0.41 Ω m. This sweep left all other parameters as they are in the baseline model.

4.2.3 Modelling of Anomalous Salt-back Thinning

Another potential application of electromagnetics to potash mining would be mapping the thickness of the salt above the mine (salt-back). Salt-back thickness is an important element to monitor for mining operations as the salt ceiling forms a significant portion of the

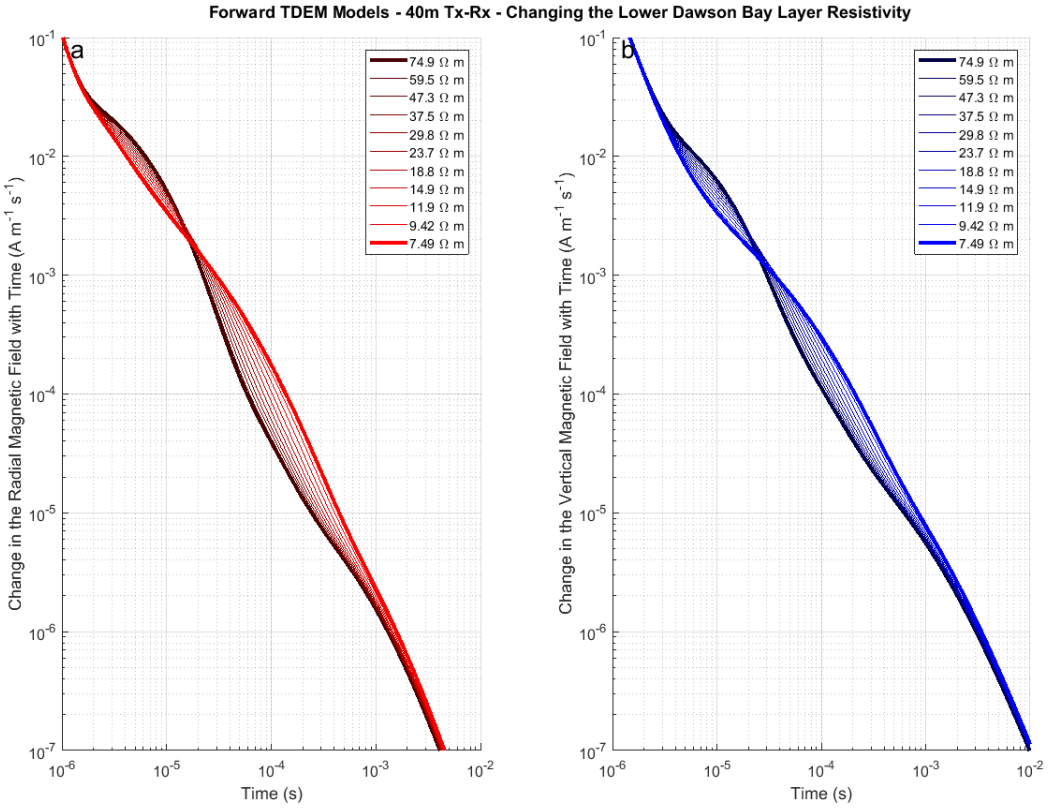

Figure 4.25: **Time-domain electromagnetic forward models of the 11-layer geological model with the Lower Dawson Bay resistivity varying. The response is calculated at 40 m separation between transmitter and receiver. The decay is calculated over the time period from 1 μs to 10 ms. The left side in red is the radial field time decay, while the right side in blue is the vertical field time decay. Each of the different models are in different shades of colour, with the darkest representing the "normal" or baseline conditions (in table 4.2) and the lighter colours show the models with increasing variation in the Lower Dawson Bay. The Lower Dawson Bay resistivity varies between 74.9 Ω m and 7.49 Ω m.**

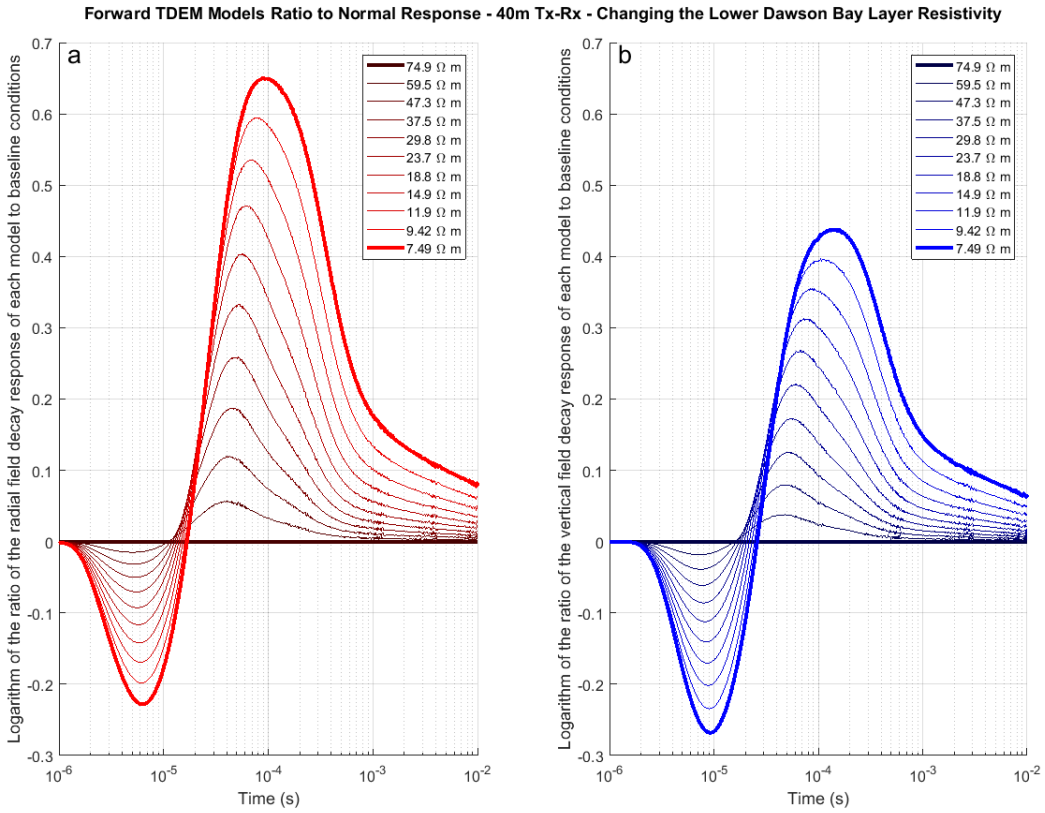

Figure 4.26: **Logarithm of the ratio of the magnetic field time decay of each of the models to the model with baseline conditions over the time-gates (1 μs to 10 ms). See equation 4.1. Transmitter to receiver distance is 40 m. The left side in red is the radial field relative time decay, while the right side in blue is the vertical field relative time decay. The shading of the lines indicate each how far the model ranges from the baseline (dark to light).**

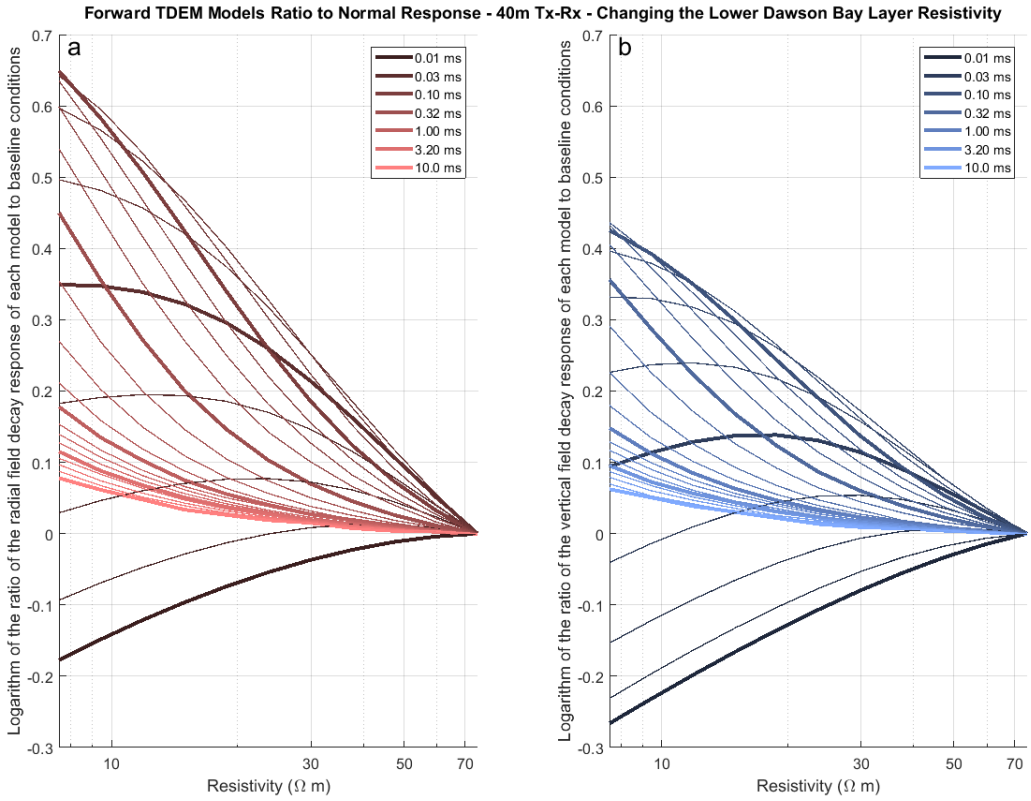

Figure 4.27: **Logarithm of the ratio of the magnetic field time decay of each of the models to the model with baseline conditions over the parameter sweep (74.9 Ω m to 7.49 Ω m). Transmitter to receiver distance is 40 m. The response ratio is compared against the varied parameter (Lower Dawson Bay resistivity). The shaded lines show each time gate from early to late (dark to light).**

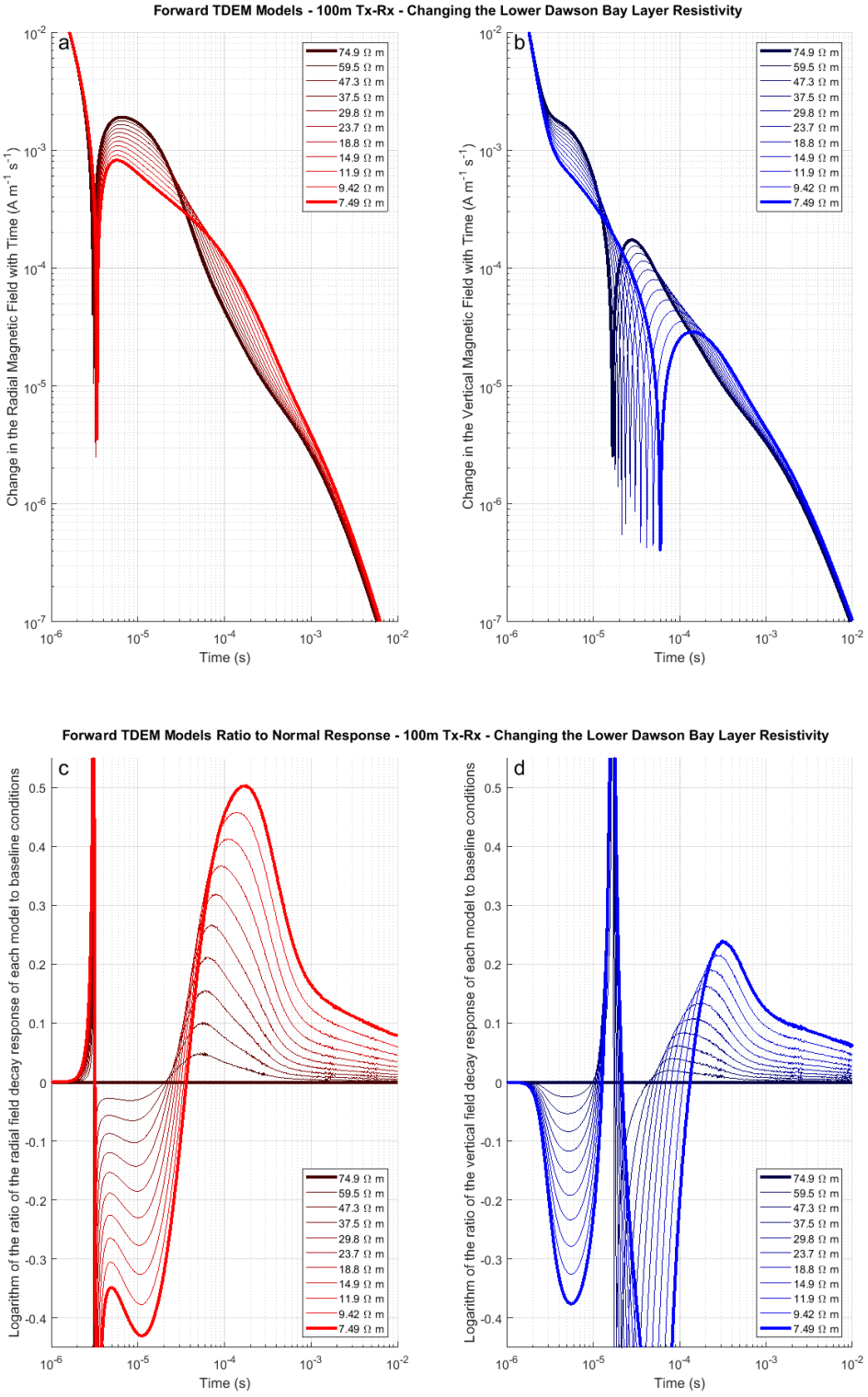

Figure 4.28: **All features are the same as with with figures 4.25 and 4.26 except that the transmitter receiver separation at** 100 **metres.**

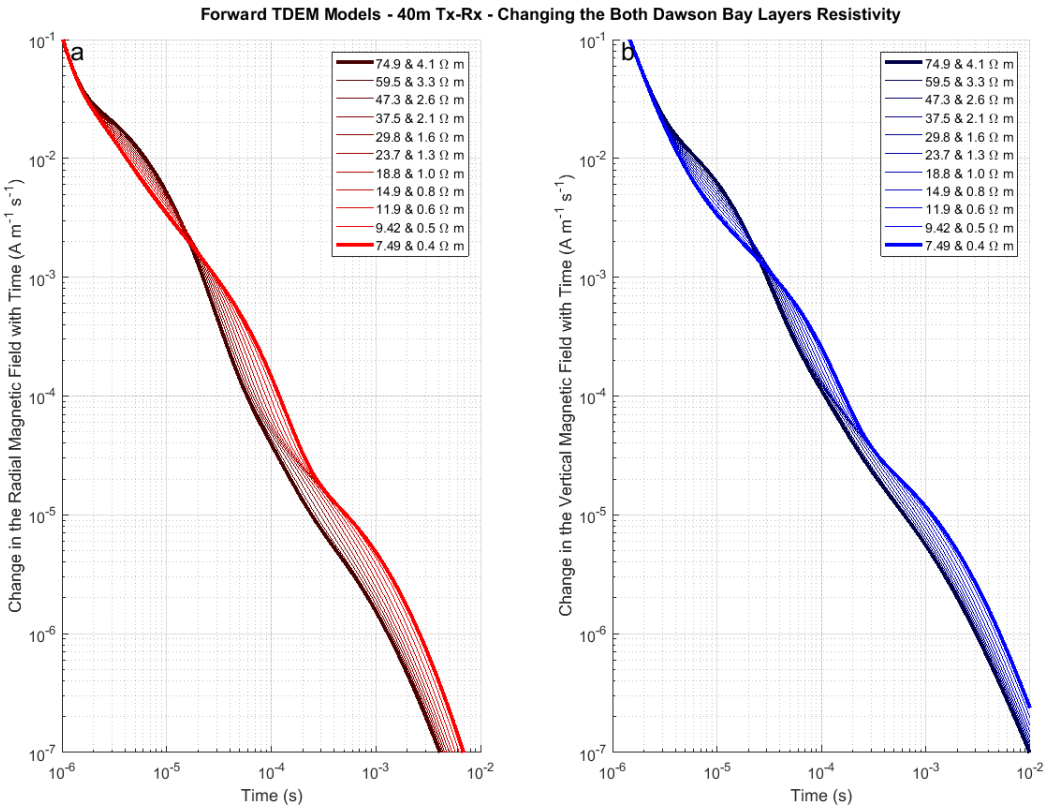

Figure 4.29: **Time-domain electromagnetic forward models of the 11-layer geological model with the Lower Dawson Bay resistivity varying. The response is calculated at 40 m separation between transmitter and receiver. The decay is calculated over the time period from 1 μs to 10 ms. The left side in red is the radial field time decay, while the right side in blue is the vertical field time decay. Each of the different models are in different shades of colour, with the darkest representing the "normal" or baseline conditions (in table 4.2) and the lighter colours show the models with increasing variation in the Dawson Bay layers. The Lower Dawson Bay resistivity varies between 74.9 Ω m and 7.49 Ω m and the Upper Dawson Bay 4.1 Ω m and 0.41 Ω m.**

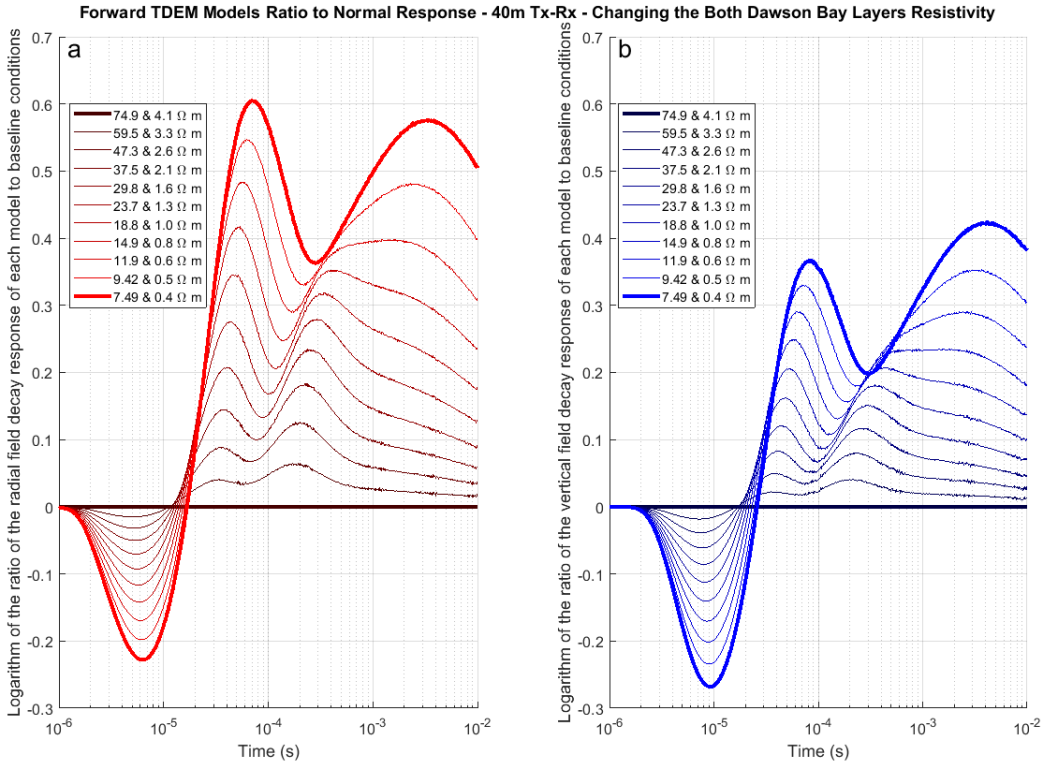

Figure 4.30: **Logarithm of the ratio of the magnetic field time decay of each of the models to the model with baseline conditions over the time-gates (1 μs to 10 ms). See equation 4.1. Transmitter to receiver distance is 40 m. The left side in red is the radial field relative time decay, while the right side in blue is the vertical field relative time decay. The shading of the lines indicate each how far the model ranges from the baseline (dark to light).**

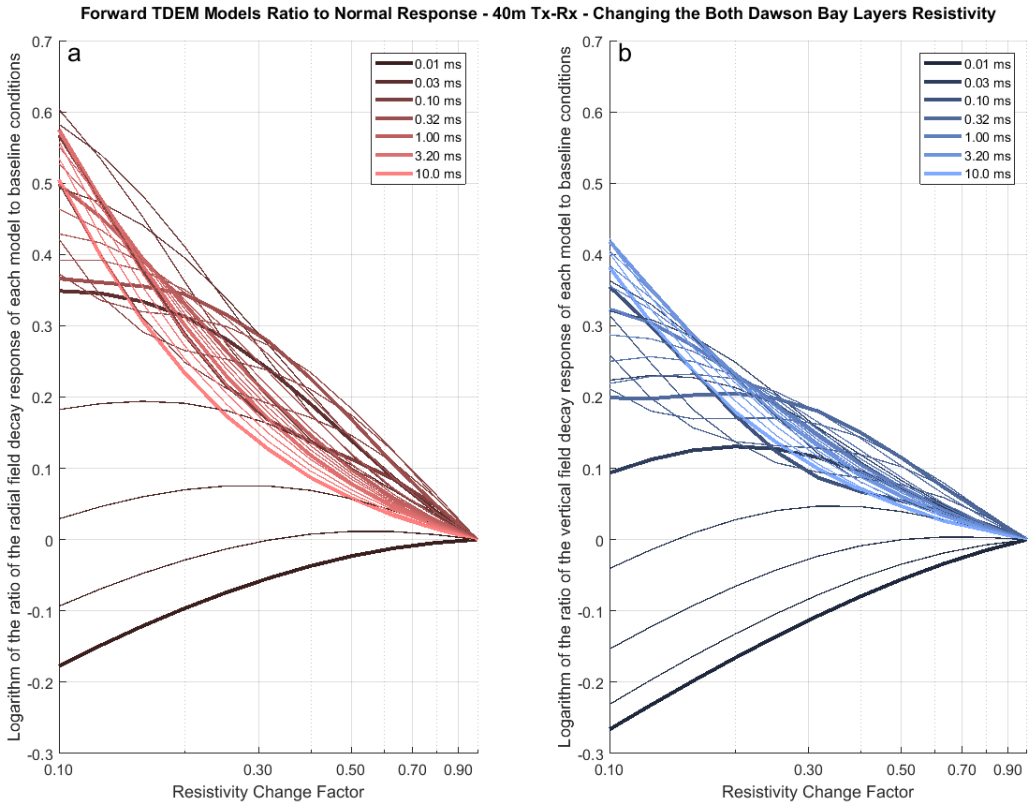

Figure 4.31: **Logarithm of the ratio of the magnetic field time decay of each of the models to the model with baseline conditions over the parameter sweep (1 to 0.1). Transmitter to receiver distance is 40 m. The response ratio is compared against the varied parameter (Lower and Upper Dawson Bay resistivity). The shaded lines show each time gate from early to late (dark to light).**

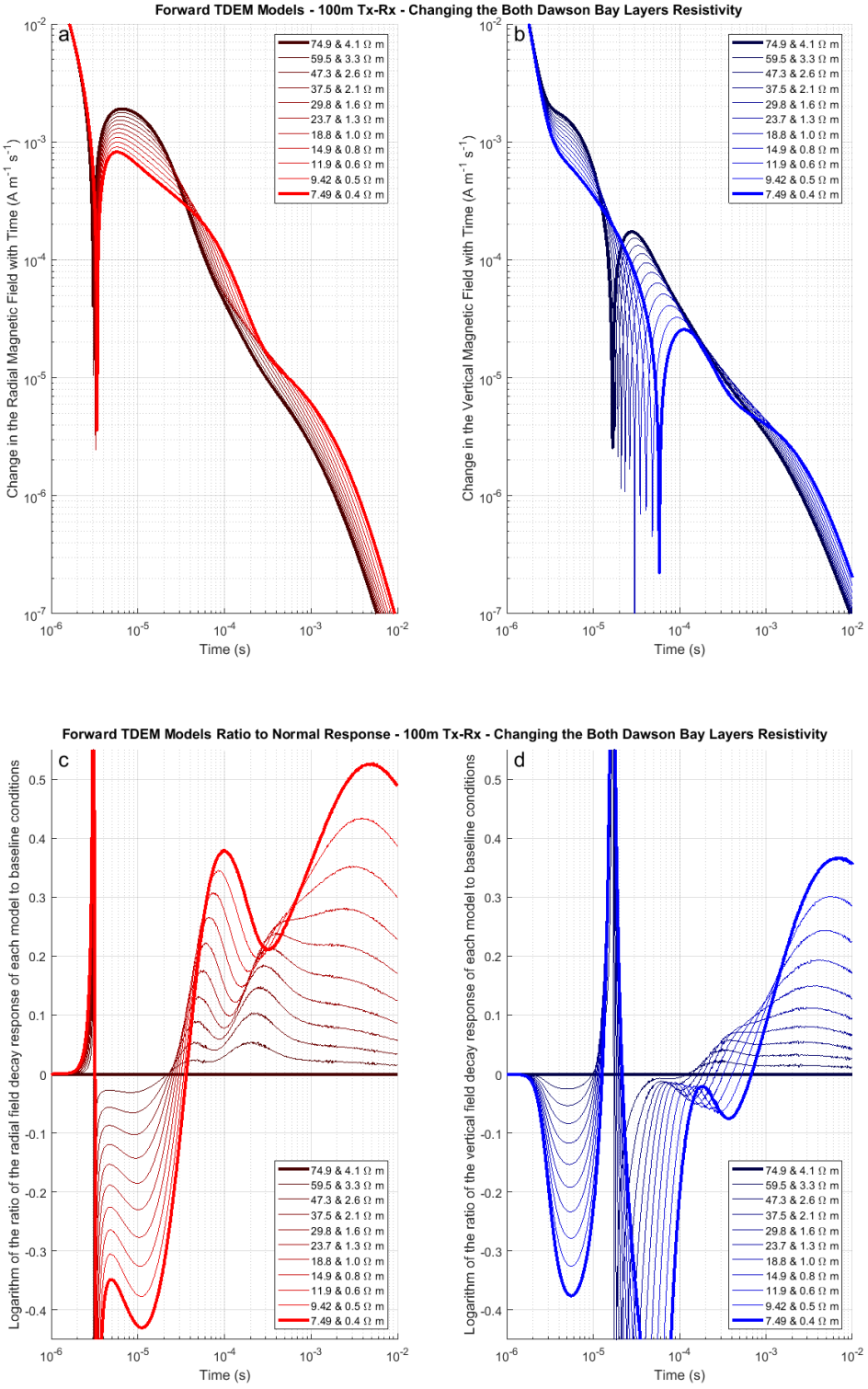

Figure 4.32: **All features are the same as with with figures 4.25 and 4.26 except that the transmitter receiver separation is set at** 100 **metres.**

protection to the mine itself. Previous studies have looked at using frequency-domain electromagnetics for this purpose (Gendzwill, 1967; Gendzwill and Pandit 1980). The parameter sweep results shown in figures 4.33 to 4.36 were constructed to investigate the TEM signal from a changing salt back thickness. This was done by linearly reducing the thickness of the Prairie Evaporite layer from the baseline of 30 m to 15 m. All other parameters were kept the same as in the baseline model.

The results of this parameter sweep suggest that a conductive response does occur at 15 m salt-back thickness, though the magnitude of this change is not very large. The peak change in the response also occurs very early in time - between 1 and 10 μs - which is earlier than most time-domain receivers can measure.

4.2.4 Modelling of Anomalous Winnipegosis Mounds

As discussed in sections 2.2.3 and 2.4, mounds in the underlying Winnipegosis formation are a concern to potash mine operations due to the established spatial relationship between the edges of these large scale features and collapse structures at or above the mine layers. As such, mining around these features is not commonly performed. Still, historically electromagnetics has been considered as a tool for mapping the Winnipegosis. These mounds in the Winnipegosis replace the salt of the Prairie Evaporite below the transmitting layer. This was simulated in the COMSOL model by both increasing the thickness of the Winnipegosis and decreasing the thickness of the Prairie Evaporite by equal amounts. This geological feature is illustrated in figures 6A to 6D in Gendzwill and Nilson (1987). This feature produced an interesting response in the radial field between $10 - 100$ μs where the signal dropped in the absence of the highly resistive salt below the transmitter-receiver points. Though for both the vertical and radial fields the variation from this model parameter sweep is quite small and would be very difficult to measure.

4.2.5 Comparing Forward Models to Survey Data

In this section I am going to focus on the peak relative magnetic field time decay between anomalous models and the baseline. I will be including results from section 4.1, specifically

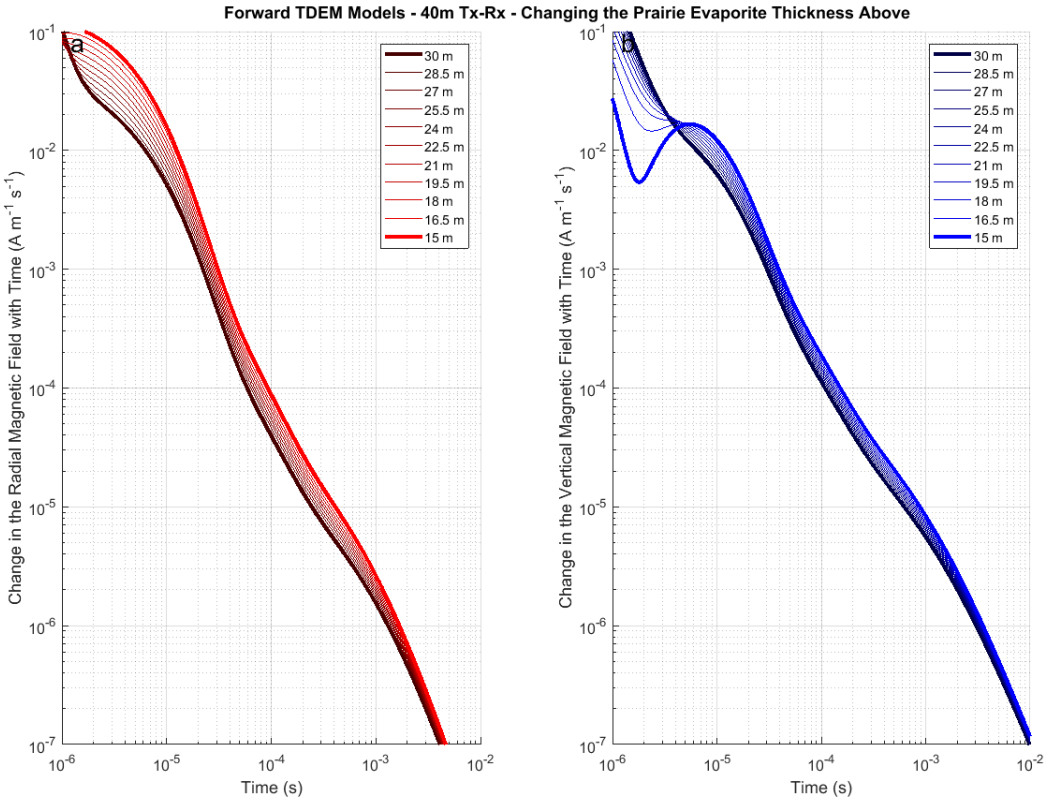

Figure 4.33: **Time-domain electromagnetic forward models of the 11-layer geological model with the Prairie Evaporite thickness varying. The response is calculated at 40 m separation between transmitter and receiver. The decay is calculated over the time period from 1 μs to 10 ms. The left side in red is the radial field time decay, while the right side in blue is the vertical field time decay. Each of the different models are in different shades of colour, with the darkest representing the "normal" or baseline conditions (in table 4.2) and the lighter colours show the models with increasing variation in the Prairie Evaporite. The Prairie Evaporite thickness varies between 30 m and 15 m.**

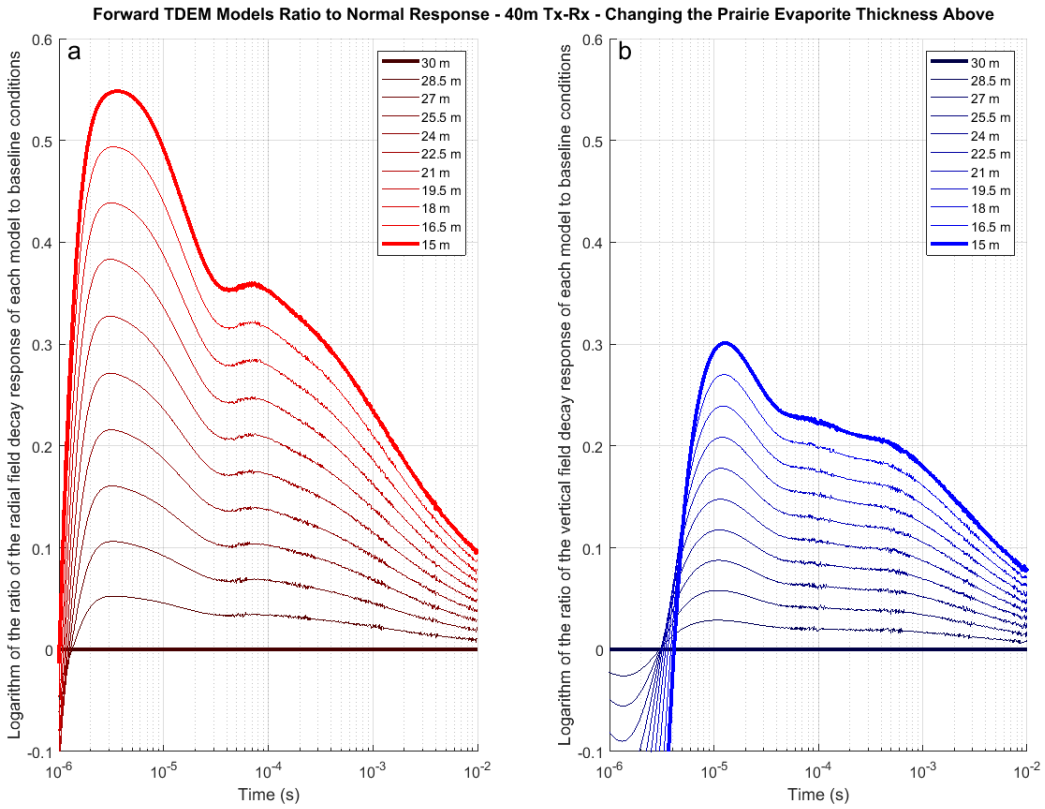

Figure 4.34: **Logarithm of the ratio of the magnetic field time decay of each of the models to the model with baseline conditions over the time-gates (1 μs to 10 ms). See equation 4.1. Transmitter to receiver distance is 40 m. The left side in red is the radial field relative time decay, while the right side in blue is the vertical field relative time decay. The shading of the lines indicate each how far the model ranges from the baseline (dark to light).**

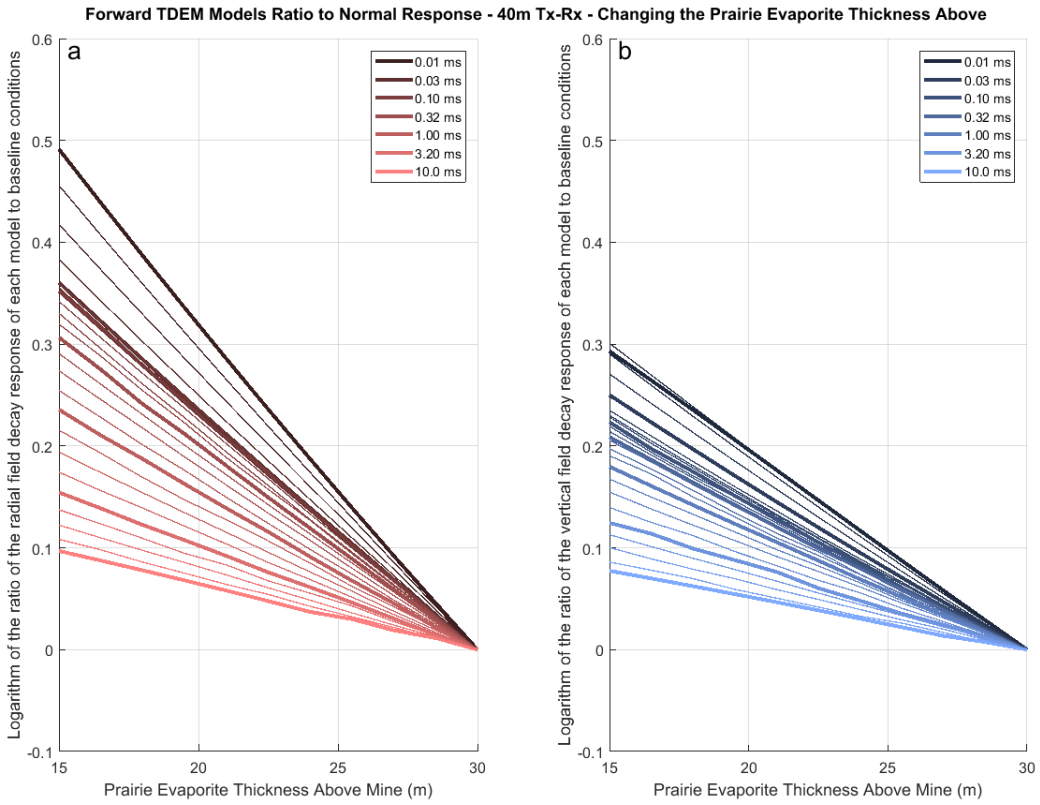

Figure 4.35: **Logarithm of the ratio of the magnetic field time decay of each of the models to the model with baseline conditions over the parameter sweep (30 m to 15 m). Transmitter to receiver distance is 40 m. The response ratio is compared against the varied parameter (Prairie Evaporite thickness above the transmitting layer). The shaded lines show each time gate from early to late (dark to light).**

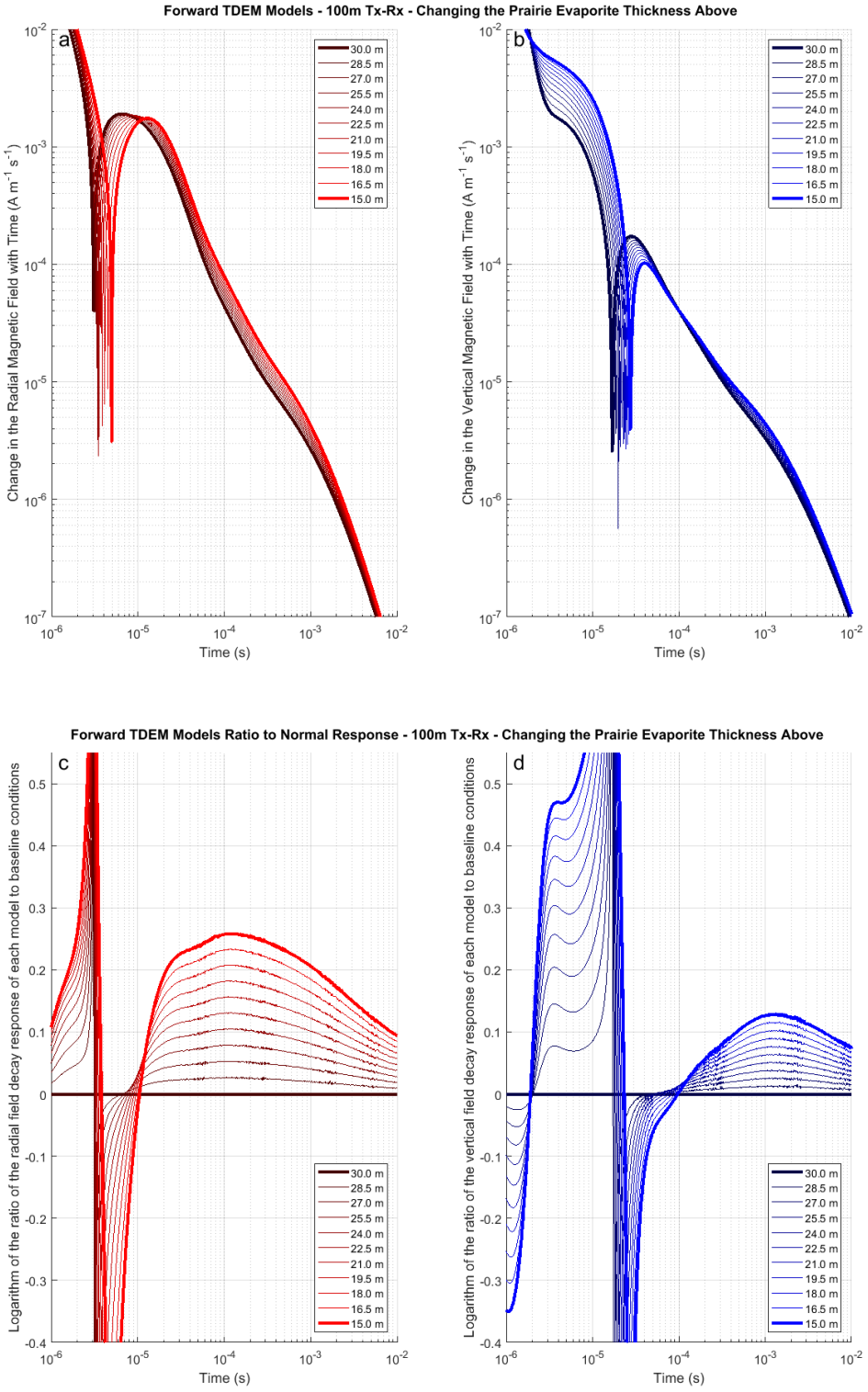

Figure 4.36: **All features are the same as with with figures 4.33 and 4.34 except that the transmitter receiver separation is set at** 100 **metres.**

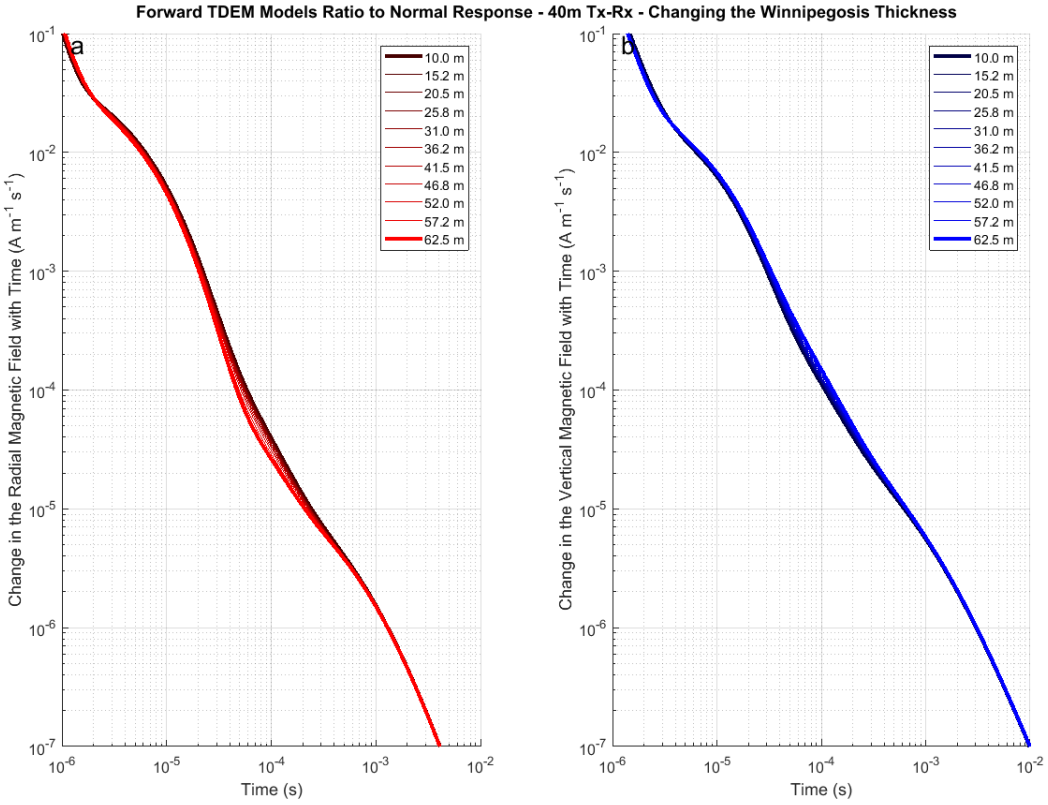

Figure 4.37: **Time-domain electromagnetic forward models of the 11-layer geological model with the Prairie Evaporite thickness varying. The response is calculated at 40 m separation between transmitter and receiver. The decay is calculated over the time period from 1 μs to 10 ms. The left side in red is the radial field time decay, while the right side in blue is the vertical field time decay. Each of the different models are in different shades of colour, with the darkest representing the "normal" or baseline conditions (in table 4.2) and the lighter colours show the models with increasing variation in the Winnipegosis. The Winnipegosis thickness varies between 10 m and 65 m.**

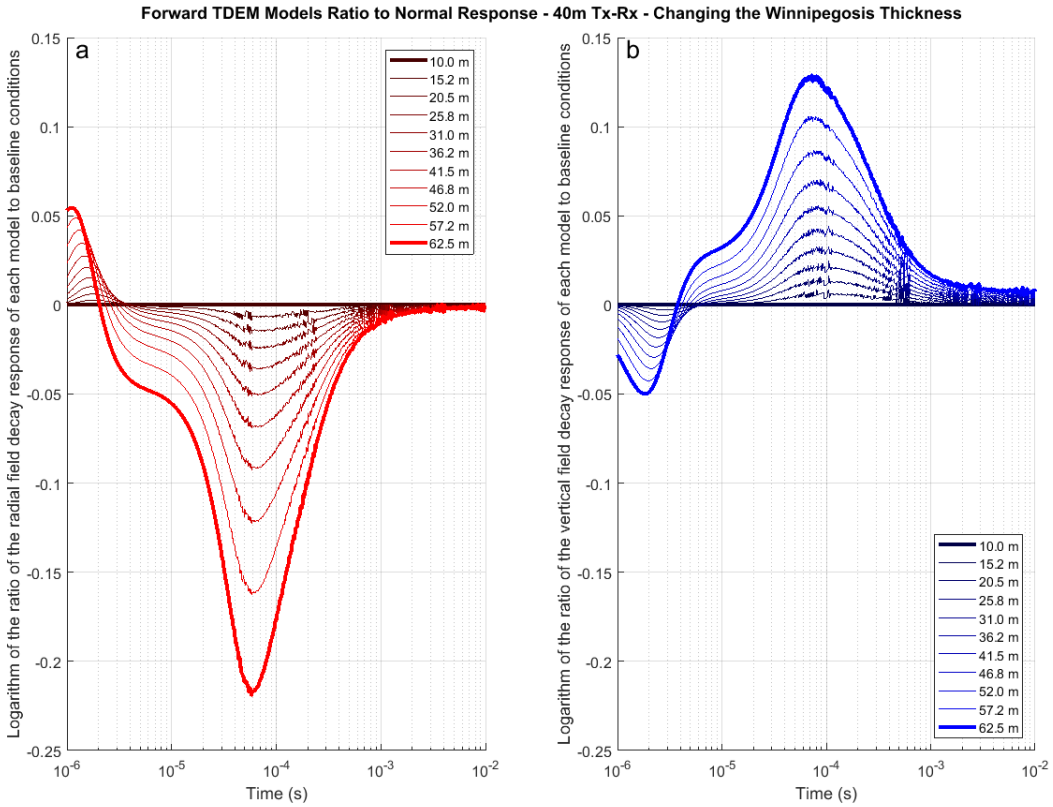

Figure 4.38: **Logarithm of the ratio of the magnetic field time decay of each of the models to the model with baseline conditions over the time-gates (1 μs to 10 ms). See equation 4.1. Transmitter to receiver distance is 40 m. The left side in red is the radial field time decay, while the right side in blue is the vertical field time decay. The left side in red is the radial field relative time decay, while the right side in blue is the vertical field relative time decay. The shading of the lines indicate each how far the model ranges from the baseline (dark to light).**

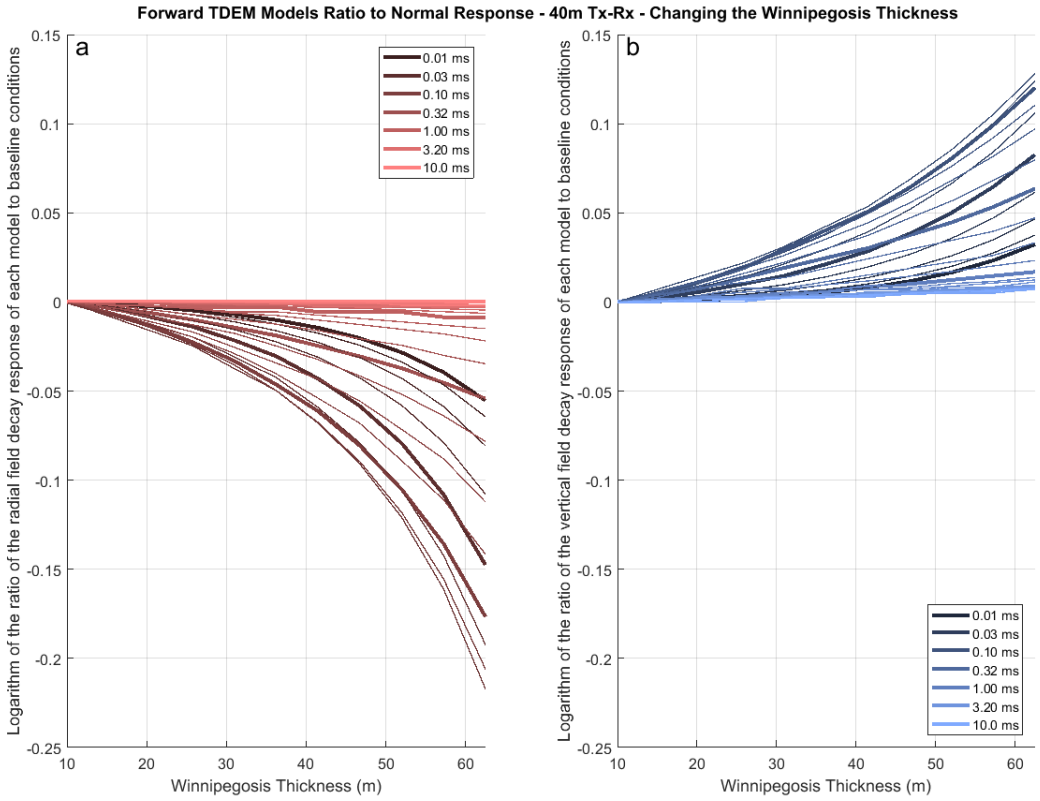

Figure 4.39: **Logarithm of the ratio of the magnetic field time decay of each of the models to the model with baseline conditions over the parameter sweep (30 m to 15 m). Transmitter to receiver distance is 40 m. The response ratio is compared against the varied parameter (thickness of the Winnipegosis below the transmitting layer). The shaded lines show each time gate from early to late (dark to light).**

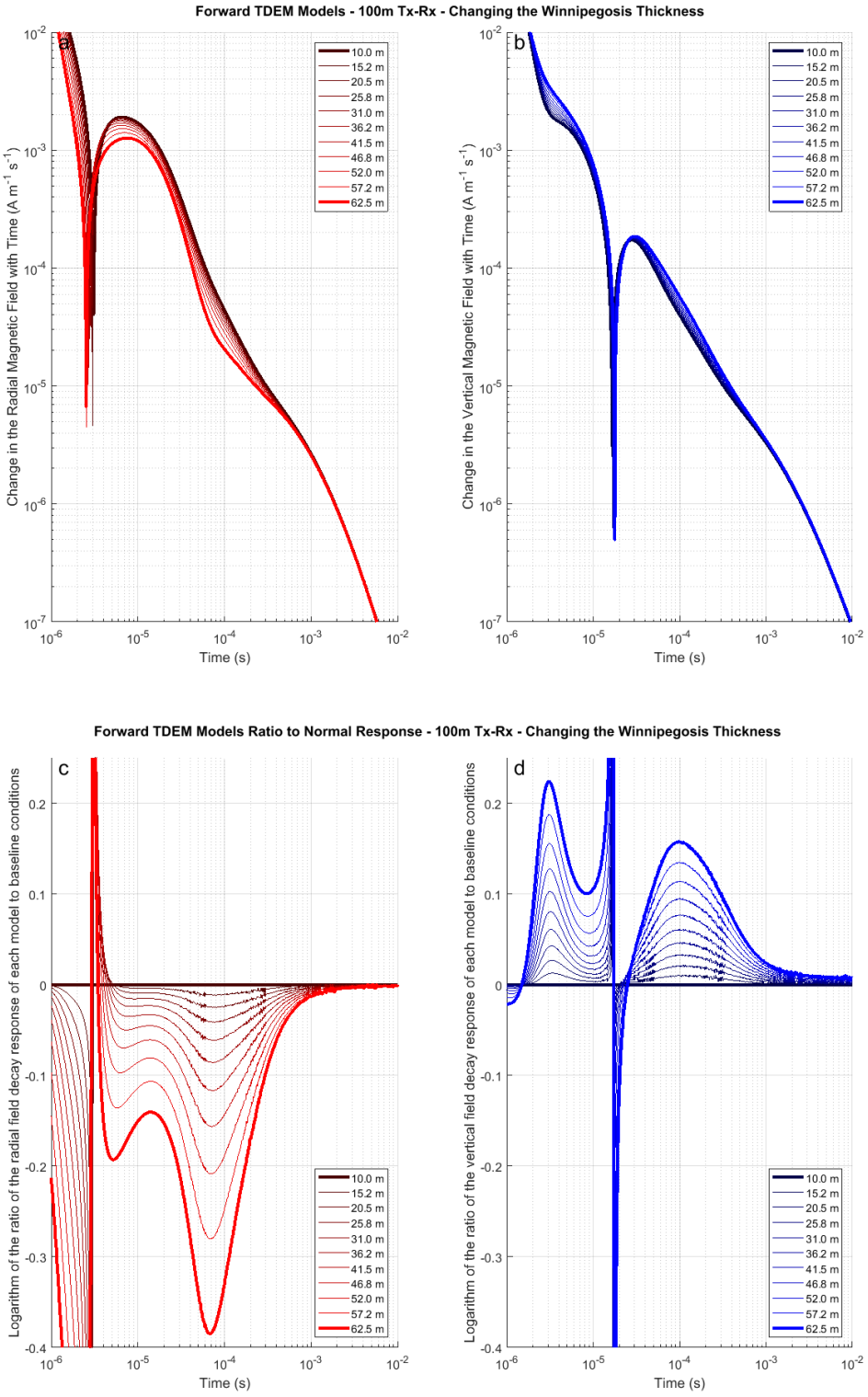

Figure 4.40: **All features are the same as with with figures 4.37 and 4.38 except that the transmitter receiver separation is set at** 100 **metres.**

the response measured at the north line western stations (01-01-40 and 01-01-100) and the response measured at the north line eastern stations (01-11-40 and 01-11-100). As with the forward models in the anomaly studies in previous sections, the survey data used for this section will include both 40 and 100 metre separated transmitter and receiver data. The west stations will be considered "normal" responses and used as the baseline result. The eastern stations will be considered the anomalous responses.

Figures 4.41 and 4.42 plot all of the anomalous parameter sweep models along with the baseline and the survey data. From these, we can see that the slopes of the decay curves diverge in the parameter sweep models earlier in time than in the survey data. In addition, there appears to be a later time slope change in the survey data that none of the models (except for the model where we adjusted the entire Dawson Bay formation's resistivity - the red curve) replicate.

Figures 4.43 and 4.44 show each of the relative responses of each of the anomalous models to the baseline. The relative anomalous survey data responses are calculated from the "normal" response measured at the opposite end of the survey line. From these we can begin to see the inaccuracies of the simple Lower Dawson Bay resistivity anomaly model when compared with the survey data. The variation in response from the Lower Dawson Bay parameter sweep arrives earlier in time than the variation in response from the survey data and dies out before the elevated response from the survey has run out. The last time-gate measured on the survey was at 7 ms. The conductive response does not appear to be returning to "normal" at that point, but the signal-to-noise ratio can be seen to be dropping long before 7 ms which makes predictions on how the signal is behaving at that point difficult, and implies that without increasing power in the transmitting signal we are unlikely to produce viable data much later than 7 ms even if the range of the time-gates were extended beyond this limit in future surveys.

In comparing the two model sweeps that play with the salt thickness - both above (green curve) and below (cyan curve), we can see that the relative responses are not highly distinct and peak very early in time (between 10 and 100 μs). This would make mapping these phenomena with time-domain electromagnetics extremely challenging. This early response is likely due to the extremely high resistivity of the salt. The signal travels through the salt in

a matter of microseconds. To observe the degree to which conductivity of the layers controls diffusion velocity and current density and to analyze differences between the Dawson Bay anomaly model and the baseline, figures 4.45, 4.46, and 4.47 were created. They show the current density around the transmission layer at three separate points in time (94.4 μs, 312 μs, and 4.51 ms). Figure a) shows the current density in the baseline model, while figure b) shows the current density in the end case model that describes the resistivity decrease in both Dawson Bay layers. The colour scale has been stretched to include the extremes of both models and is the same for both figures. In this we can see that the current in the Dawson Bay anomaly model travels much less distance, and maintains a relatively high level even until 4 ms when compared with the baseline model. This is due to the drop in resistivity of the two layers between 41 and 84 metres. Also, note how in both models, even at the earliest time-gate plotted, the two large zones (one below 0 metres and one between 2 and 32 metres) that model the salt do not have discernible current remaining in them due to their high resistivity.

In analyzing the point of peak relative response in the anomalous models, it is important to note that the relative amplitude of the response in each of these models can be misleading. This relative change is controlled by the amount of parametric change in the models themselves. However, effort was made not to change these parameters any more than could be realistically expected geologically. For the thicknesses of the layers, 50% decrease in the salt-back is reasonable as it is unlikely that mining operations would ideally continue at anything less than 15 metres. For the thickness increase in the Winnipegosis formation a terminal parameter was set at 65 metres. Mounds can extend several kilometres and have thicknesses up to 105 metres according to Gendzwill and Wilson (1987). However, a more muted value of 65 metres total thickness for the Winnipegosis and a correlating decrease in the thickness of the Prairie Evaporite formation below the transmitting layer to 55 metres was seen as appropriate given the unlikelihood of mining operations nearing the largest of these Winnipegosis structures. The Dawson Bay resistivity variation was set at one order of magnitude partly due to the difference in resistivity seen in well-logs between normally tight carbonate layers and normally porous ones - i.e. the lower and upper Dawson Bay, and the upper and lower Davidson (see table 3.3 and figure 3.29). In addition, the change in

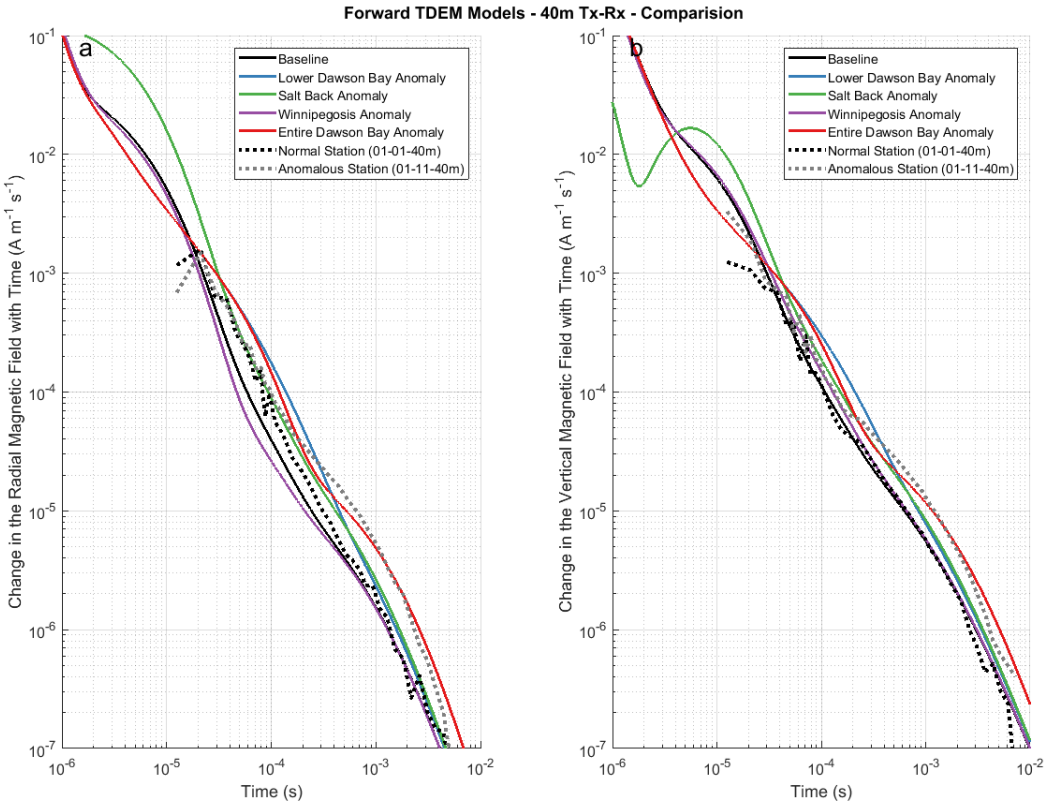

Figure 4.41: **Comparing the time-domain responses of the end cases from each of the forward model parameter sweeps previously discussed. The response is calculated at 40 m separation between transmitter and receiver. The end cases are compared against the survey data from section 4.1. Sub-figure a) is the radial magnetic field time decay, while sub-figure b) is the vertical magnetic field time decay.**

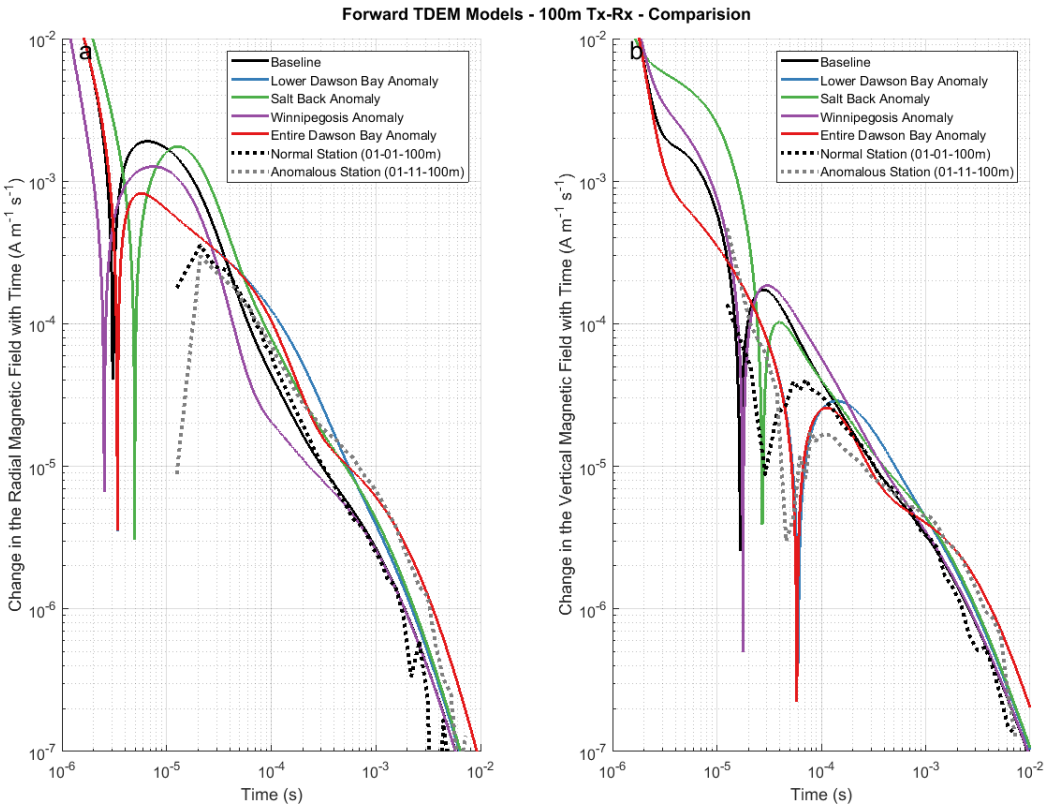

Figure 4.42: **Comparing the time-domain responses of the end cases from each of the forward model parameter sweeps previously discussed. The response is calculated at 100 m separation between transmitter and receiver. The end cases are compared against the survey data from section 4.1. Sub-figure a) is the radial magnetic field time decay, while sub-figure b) is the vertical magnetic field time decay.**

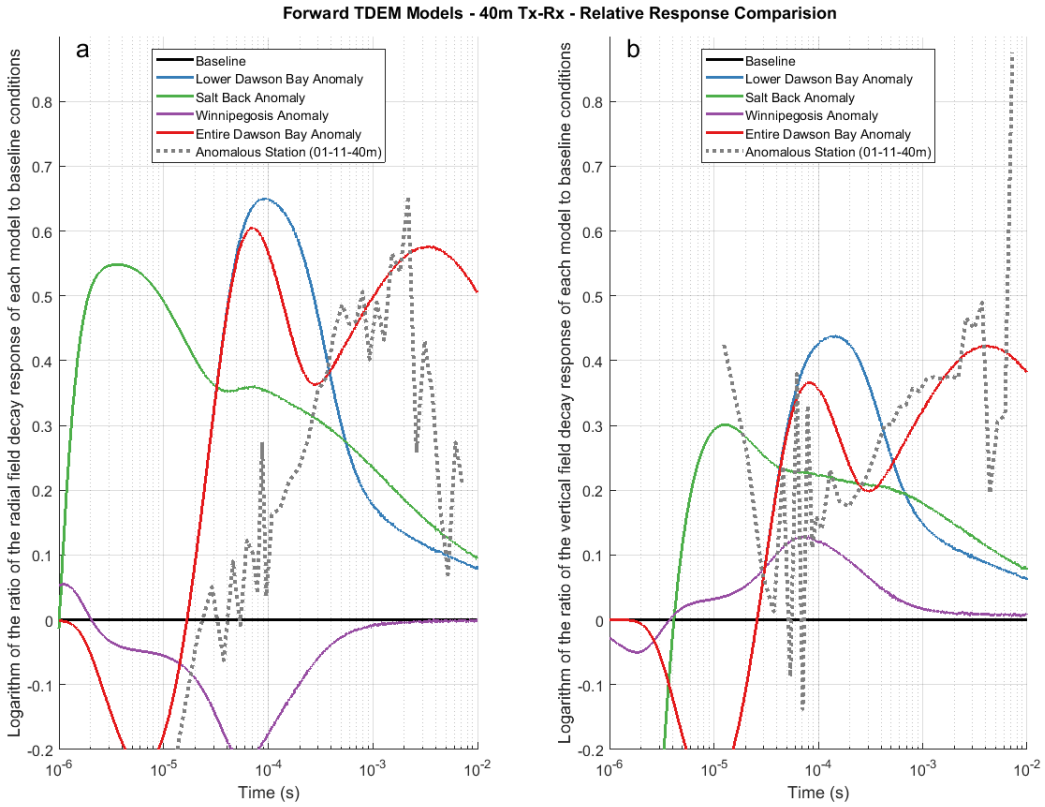

Figure 4.43: **Comparing the log of the relative magnetic field time decay responses of the end cases from each of the forward model parameter sweeps previously discussed. The response is calculated at 40 m separation between transmitter and receiver. The end cases are compared against the survey data from section 4.1. Sub-figure a) is the radial magnetic field time decay, while sub-figure b) is the vertical magnetic field time decay.**

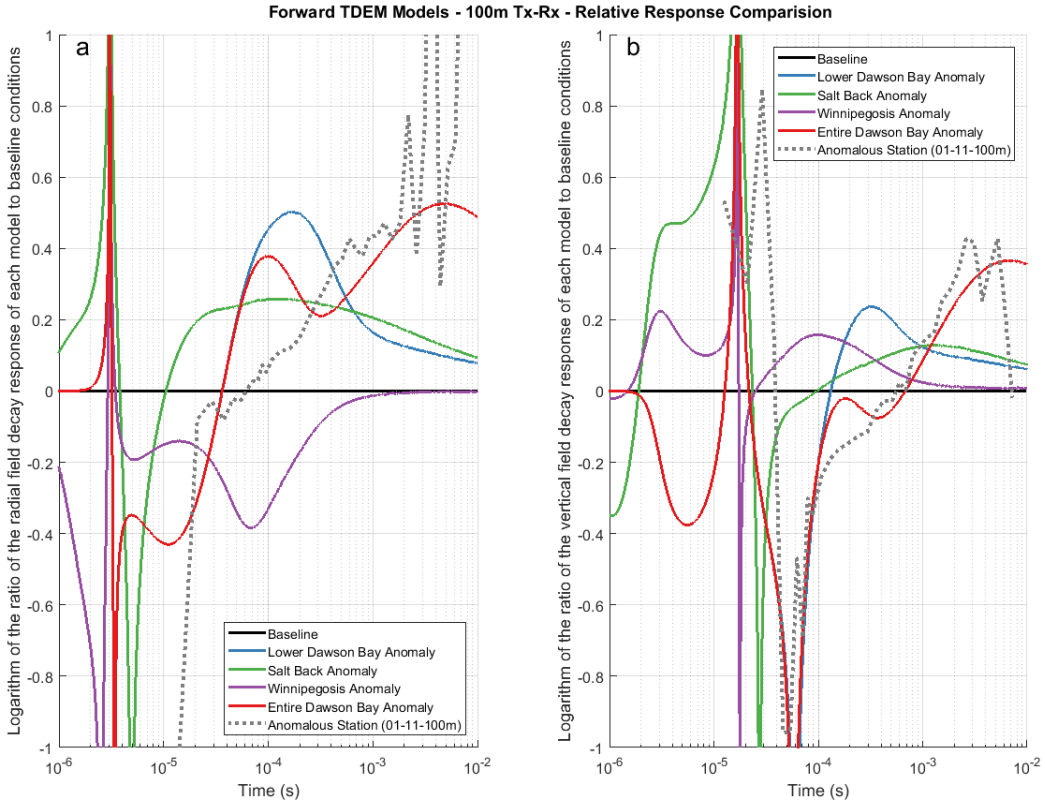

Figure 4.44: **Comparing the log of the relative magnetic field time decay responses of the end cases from each of the forward model parameter sweeps previously discussed. The response is calculated at 100 m separation between transmitter and receiver. The end cases are compared against the survey data from section 4.1. Sub-figure a) is the radial magnetic field time decay, while sub-figure b) is the vertical magnetic field time decay.**

resistivity found in the inversion method (described in section 4.3.2) also suggested around an order of magnitude change in resistivity.

In conclusion, the relative magnetic field decay for each of these models is useful in getting an idea of the amount of response one could expect while surveying into an area of one of these phenomena. In addition, the time gates at which these responses are recorded are very important as they inform the ideal amount of transmitting power, transmitter-receiver separation, and the assigned time-gate density and start point/end points. Early time response changes (< 0.1 ms) will be undetectable if time-gates are not defined sufficiently early or densely enough. Even if they are, however, high-power in the transmitter combined with a small transmitter-receiver separation can make detection impossible due to high noise from the transmitter. Transmitter receiver separation being too large can introduce it's own additional problems, which include losing some degree of lateral spatial resolution and moving the early-to-late time transition to a later time-gate.

While there are other considerations to make regarding TEM analysis, such as multiple peaks in response, length of peak response, noise level at early and late time gates, etc., table 4.3 was built to highlight the difference in response time and amplitude of the different geological models for simple comparison purposes. In this table, the point in time that the relative $\frac{\mathrm{d}H}{\mathrm{d}t}$ response occurs in each of the models as well as the relative amplitude itself (which can be expressed as a ratio or percentage) are detailed in their respective columns. As a reminder, in the final column (Δ m), the percent change of the model parameter used in the end case of each of the parametric sweeps is listed.

4.3 Inverse Modelling

This section details the inversions applied to the in-mine survey data supplied by *Potash Corporation of Saskatchewan Inc.*. These survey results are detailed in section 4.1. The inversions followed the approach outlined in section 3.3. For all inversions, the layer thicknesses were kept constant in the model. This was seen as acceptable since - while electromagnetic responses are produced by a combination of resistivity and thickness variation - all of the formations near potash mines in Saskatchewan are sedimentary formations. As such, in small

40 **m Tx-Rx**	**Peak** $\frac{\mathrm{d}H_r}{\mathrm{d}t}$		**Peak** $\frac{\mathrm{d}H_z}{\mathrm{d}t}$		
Anomaly Type	**t (s)**	**Rel. Amp**	**t (s)**	**Rel. Amp**	**Δm**
Lower Dawson Bay	9.4e-5	0.65	1.4e-4	0.44	−90%
Salt back thinning	3.8e-6	0.55	1.3e-5	0.30	−50%
Winnipegosis Mounds	5.8e-5	-0.22	7.5e-5	0.13	+650%
Dawson Bay (both)	6.8e-5	0.60	8.4e-5	0.37	−90%
	3.7e-3	0.57	4.0e-3	0.43	− − −
Survey data	2.2e-3	0.65	5.2e-3	0.49	− − −

100 **m Tx-Rx**	**Peak** $\frac{\mathrm{d}H_r}{\mathrm{d}t}$		**Peak** $\frac{\mathrm{d}H_z}{\mathrm{d}t}$		
Anomaly Type	**t (s)**	**Rel. Amp**	**t (s)**	**Rel. Amp**	**Δm**
Lower Dawson Bay	1.7e-4	0.50	3.1e-4	0.24	−90%
Salt back thinning	1.0e-4	0.26	9.9e-5	0.16	−50%
Winnipegosis Mounds	6.3e-5	-0.38	1.2e-3	0.13	+650%
Dawson Bay (both)	9.9e-5	0.38	3.8e-4	0.08	−90%
	5.0e-3	0.52	6.5e-3	0.36	− − −
Survey data	3.1e-3	0.73	3.1e-3	0.42	− − −

Table 4.3: **Comparing the peak relative time-domain electromagnetic responses for each of the four different geological models. The results use the relative response for the end (most extreme) cases from each model parameter sweep. The "t" and "Rel. Amp." columns are the points of peak relative response in the anomalous models with "t" being the time of peak decay from the baseline, and the "Rel. Amp" being the peak relative amplitude of the response at these points in time. The "m" column shows the percentage of parameter change for each of these models. Detailed descriptions of each of these models are shown in the previous sections (4.2.1 to 4.2.4).**

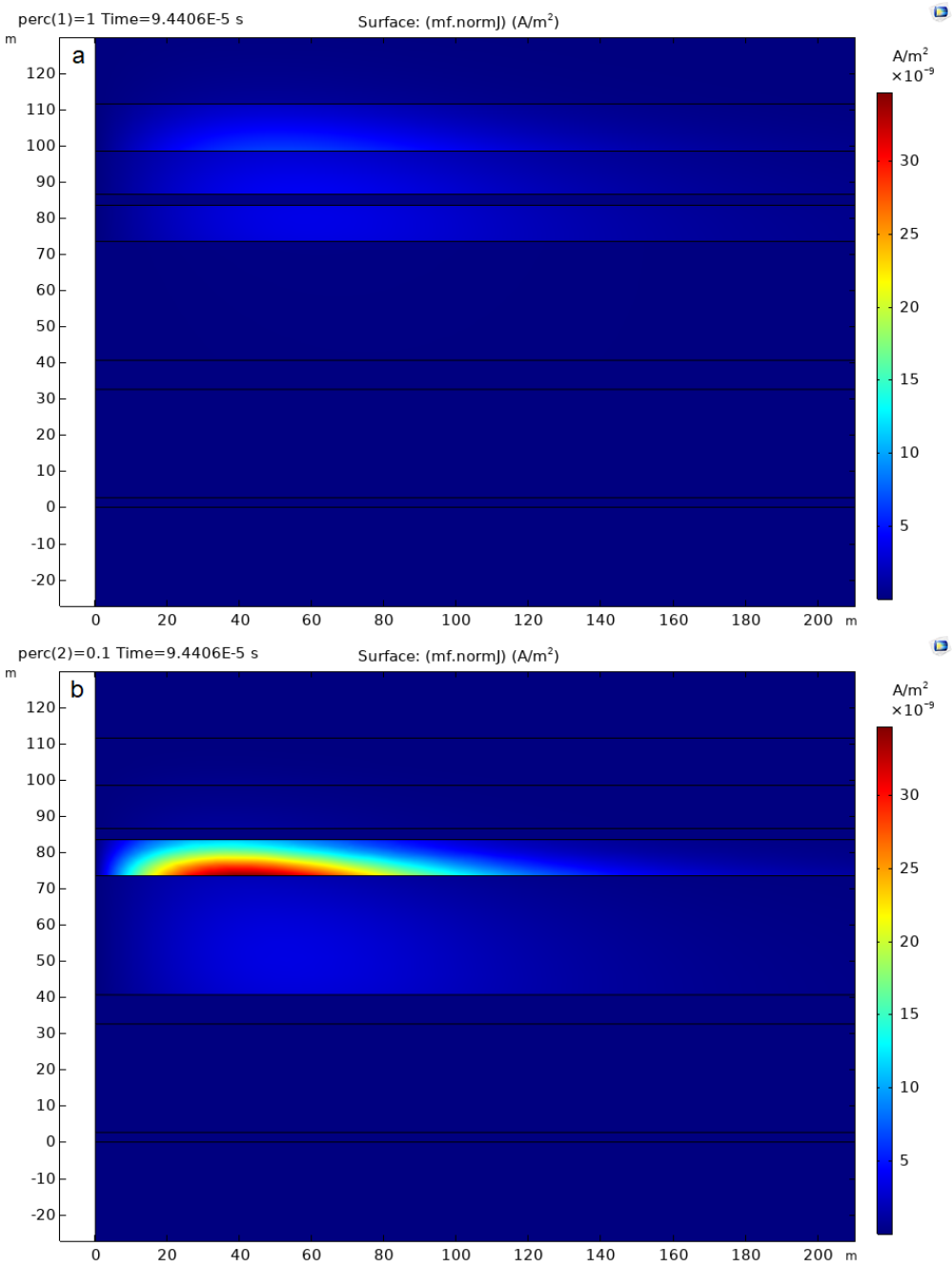

Figure 4.45: **Showing a cross-section of the current density at** 94.4 μ**s from both a) the baseline model and b) the end model for the Upper and Lower Dawson Bay resistivity sweep. The Dawson Bay layers extend between** 41 **m and** 84 **m.**

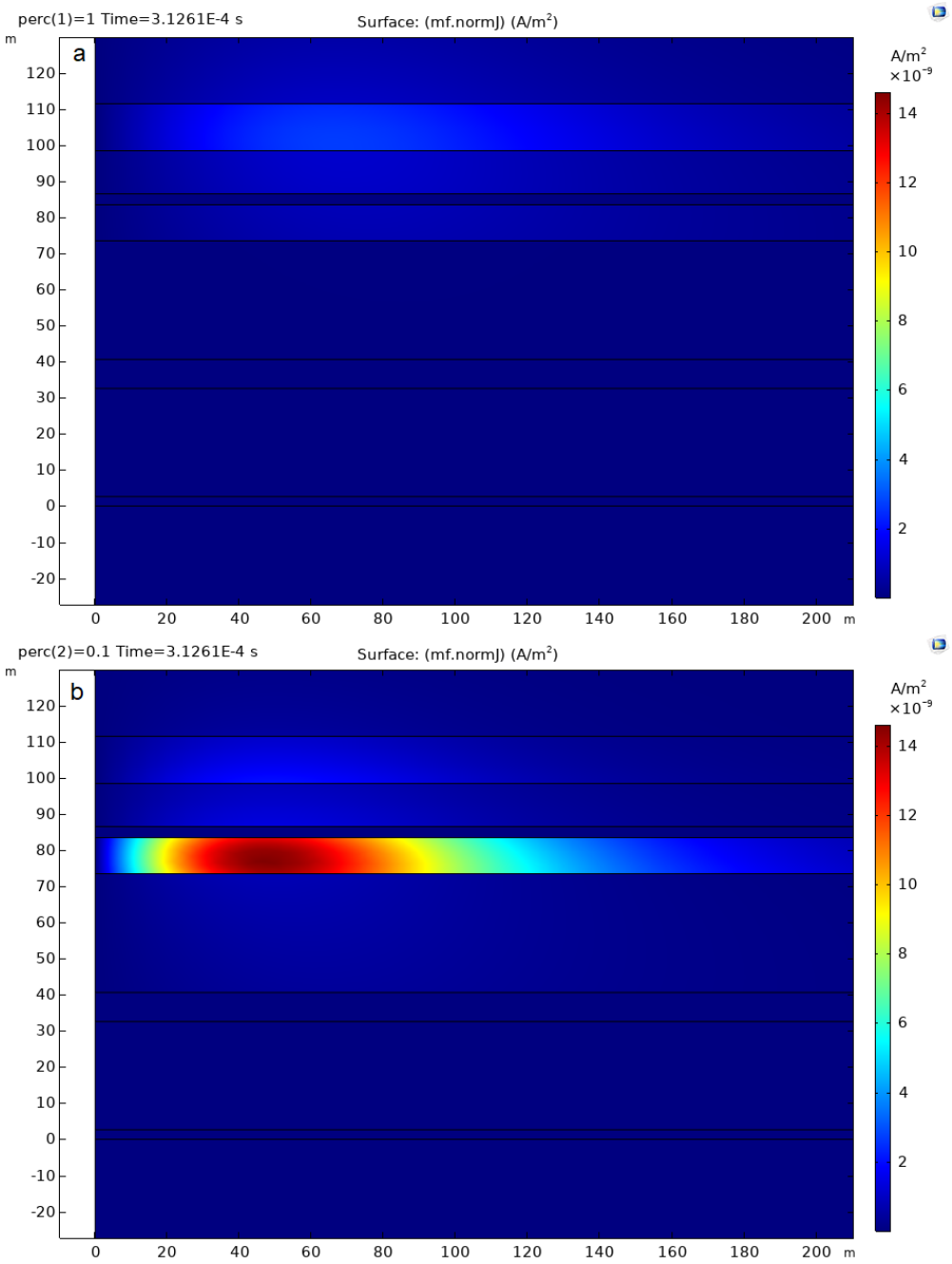

Figure 4.46: **Showing a cross-section of the current density at** 312 μ**s from both a) the baseline model and b) the end model for the Upper and Lower Dawson Bay resistivity sweep. The Dawson Bay layers extend between** 41 **m and** 84 **m.**

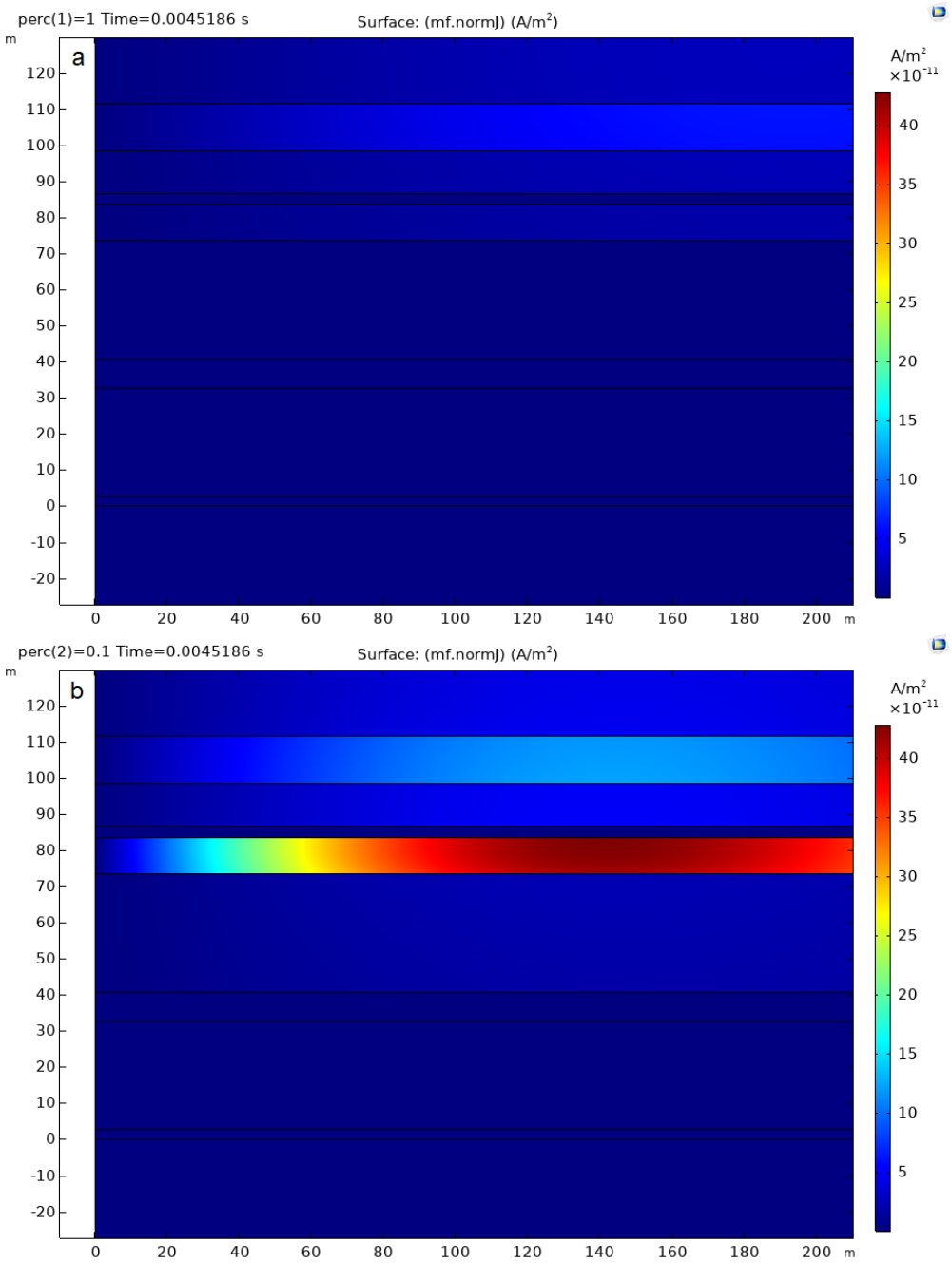

Figure 4.47: **Showing a cross-section of the current density at** 4.51 **ms from both a) the baseline model and b) the end model for the Upper and Lower Dawson Bay resistivity sweep. The Dawson Bay layers extend between** 41 **m and** 84 **m.**

surveyed areas, it is a fair assumption that resistivity would vary at higher degrees than layer thicknesses. Any small changes in layer thicknesses would be subsumed to a degree into the changing resistivity parameters. In making this assumption, the number of parameters in the inversion were halved - dramatically reducing the time needed for the inversion to run.

This inversion section describes three different approaches to inverting the datasets. The first step in the inversion process was to find an acceptable model in the area with the most "normal" conditions, as far from the anomalous Dawson Bay environment as possible. This effort is detailed in section 4.3.1. Once a baseline model of the near-mine geological features was arrived at, the next goal was to proceed to develop tools to analyze the datasets located in both the transitional and anomalous zones on both the north and south line. Two methods were developed for this purpose. The first, detailed in section 4.3.2, used an approach to reduce the number of parameters in the inversion by only allowing the Dawson Bay layers (upper and lower) to vary. With the reduction of the number of parameters, equivalency issues and run-away model parameters were more-or-less resolved. The second approach was to use the same damping controls used on the "normal" area inversion on each subsequent station. This somewhat artificially tied the model parameters to "normal" area values while inverting for data taken in "anomalous" areas. However, it had the benefit of allowing a large degree of freedom for the parameters to vary without showing favouritism to any set of layers. Section 4.3.3 details these results.

4.3.1 Inverting the Dataset in Normal Geological Conditions

In order to find a parameter set that could explain the signal measured in the "normal" area, the three westernmost stations on the north line were selected. These three stations represented a wide range of area (over 200 m) with which to determine a background electromagnetic signal for the survey. Each of these stations had three readings at different transmitter/receiver spacings, with measurements of both the vertical and radial field decays. This allowed the inversion to use 18 datasets in total. This inversion allowed the resistivity of each of the geological layers to vary under damping constraints outlined in section 3.3.2. The layers' starting parameters, both invariant thicknesses and varying resistivities, were determined largely from the well-log analysis outlined in section 3.4. These

starting resistivities also formed the basis for the damping constraint.

One critical control on the inversion is the magnitude of the C coefficient used in the damping term (shown in equations 3.56). A C value too low will result in not enough control of the parameters in the inversion. Attempts made with full unconstrained ($C = 0$) inversions led to many of the parameters, especially the ones tending toward the more resistive end of the scale, to vary to extreme degrees. A C value too large, on the other hand, will result in a final solution that is overly controlled by the user, leading to a meaningless result. Several attempts at resolving an inversion of the normal conditions were performed with varying weights placed on the damping term in the objective function in order to establish a relationship between the value used for C, the amount of parameter change from the initial values, and the misfit between the final model and the datasets. Figure 4.48.a shows the percentage average difference between the starting set of parameters and the final values compared against the misfit between the final model and the datasets (in percent of the starting misfit). Figure 4.48.b shows the C value compared against the percent of the damping term in the overall final objective function value. In both figures, the ultimate value for C that was used is highlighted by a black circle ($C = 0.0039$). This point lies near the elbow of the trade off between the amount of misfit between the inverse solution model and the data and the final change in the initial values of the parameter set.

The results of the inversion are shown in figure 4.49. This figure shows the path each parameter took during the inversion, as well as the percentage of both damping and misfit terms in the objective function with respect to the starting values over the iterations of the inversion process. Table 4.3.1 shows the parameters for the initial and final models in the inversion for each of the geological layers. Of all of the parameters, the largest changes came from the upper layers in the model (Davidson and the upper half-space) in a more conductive direction, as well the Lower Dawson Bay and Second Red Bed drifting in a more resistive direction. Some degree of correlation to the parameter paths in the inversion can be seen in figure 4.49. As such a principle component and covariance analysis was performed on the data. Figure 4.50 and table 4.5 show the covariance between the parameters within the inversion. One covariant set appears to include the upper half-space, the red bed layers and the Prairie Evaporite. Another covariant group includes the middle carbonate layers

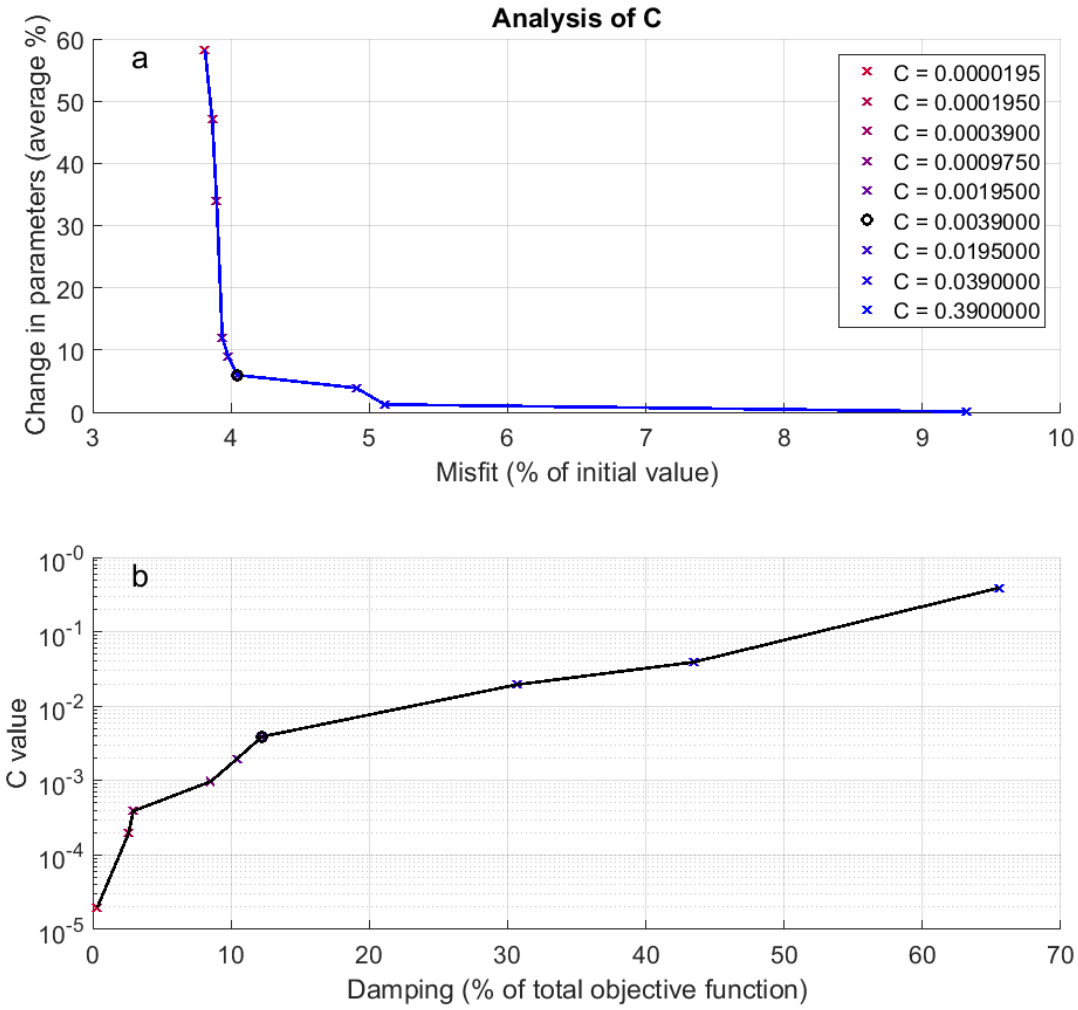

Figure 4.48: **Analysis of 11-layer inversions with varying damping values. The black circle indicates the C values used for later inversion sets. a) shows the misfit versus the change in value from the initial parameters. b) shows the damping contribution versus the value used for the damping coefficient term.**

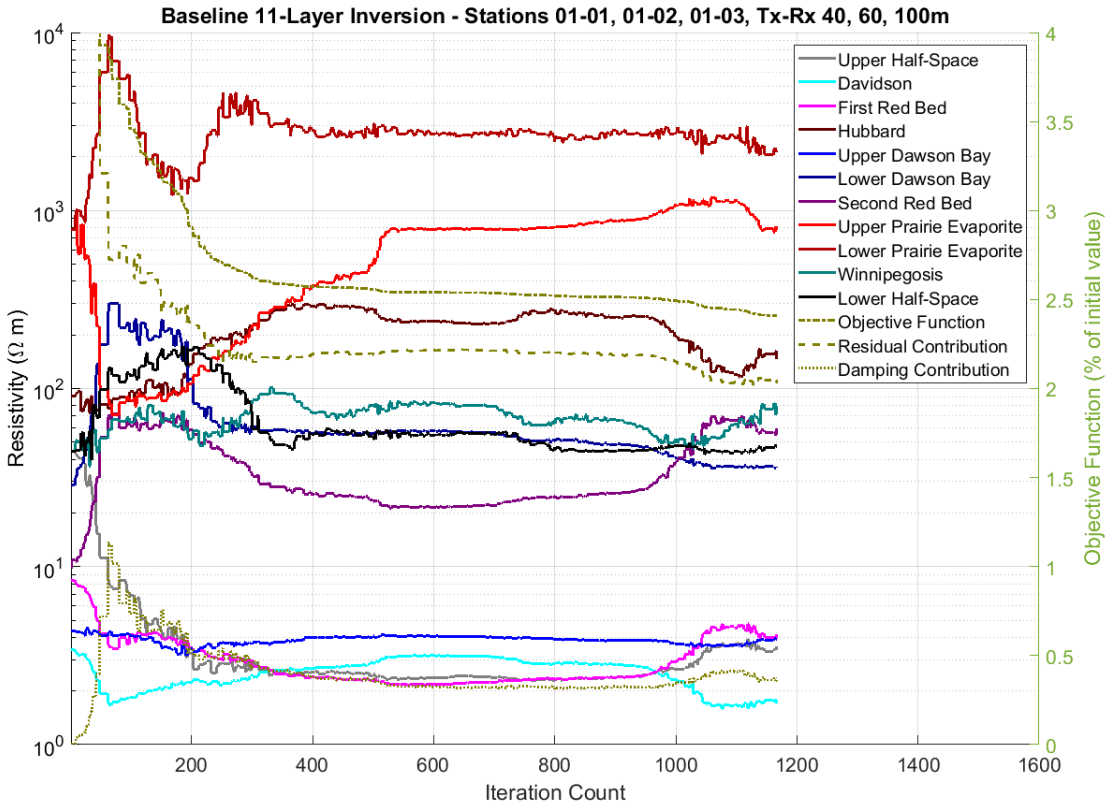

Figure 4.49: **Inversion establishing parameters for the normal conditions in the survey area. This inversion used data from three stations on the north line (line 01, stations 01, 02, and 03), with transmitter-receiver separations of 40, 60, 100 m from each station, leading to a total of 18 datasets. Each dataset was given equal weighting in the inversion.**

above the transmitting layer: Dawson Bay carbonates and the Lower Davidson. These covariant trends are likely related to spatial relationships between the resistivity parameters. In general, there does appear, both from the inversion paths and from the covariance analysis, that there is a large degree of equivalency between the parameters, leading to a variety of potentially equally valid solutions. Though, as can be seen in the forward model comparisons in figures 4.51, 4.52, and 4.53, the forward models produced by the final parameter products of the inversion are a substantial improvement on the forward models produced from the initial parameters derived from the well-log and match the data very well.

Sensitivity analysis was performed on the inversion products derived for the "normal"

Layer	Thickness (m)	Resistivity (Ω m)	
		Initial	Final
Souris River (upper half-space)	∞	44.53	3.56
Davidson Carbonate	13	3.41	1.71
First Red Bed	12	8.37	4.20
Hubbard Evaporite	3	90.72	145.6
Upper Dawson Bay (Nealy)	10	4.35	3.88
Lower Dawson Bay (Burr)	33	28.80	35.78
Second Red Bed	8	9.79	59.88
Prairie Evaporite (above mine)	30	787.3	815.7
Mine Layer	2.6	∞	∞
Prairie Evaporite (below mine)	105	787.3	2163.9
Winnipegosis	10	44.53	79.48
Lower half-space	∞	44.53	46.80

Table 4.4: **Inversion result attempting to constraint near-mine electrical parameters in normal conditions. The datasets used for this inversion included the results from the westernmost three stations on the north line, using all three available transmitter/receiver separations (40 m, 60 m, and 100 m).**

	UHS	LD	FRB	Hub	UDB	LDB	SRB	PE^+	PE^-	Win	LHS
UHS	**1.00**	-	-	-	-	-	-	-	-	-	-
LD	-0.97	**1.00**	-	-	-	-	-	-	-	-	-
FRB	0.98	-0.99	**1.00**	-	-	-	-	-	-	-	-
Hub	-0.97	0.92	-0.95	**1.00**	-	-	-	-	-	-	-
UDB	-0.73	0.85	-0.82	0.72	**1.00**	-	-	-	-	-	-
LDB	-0.89	0.97	-0.94	0.83	0.90	**1.00**	-	-	-	-	-
SRB	0.97	-1.00	0.99	-0.93	-0.86	-0.97	**1.00**	-	-	-	-
PE^+	0.65	-0.72	0.71	-0.68	-0.89	-0.78	0.75	**1.00**	-	-	-
PE^-	-0.60	0.60	-0.60	0.53	0.42	0.57	-0.60	-0.22	**1.00**	-	-
Win	-0.37	0.55	-0.50	0.33	0.82	0.69	-0.56	-0.79	0.08	**1.00**	-
LHS	-0.48	0.63	-0.58	0.36	0.78	0.74	-0.62	-0.63	0.38	0.67	**1.00**

Table 4.5: **Covariance of the inversion parameters in the "normal" area dataset. Same as in figure 4.50. Legend for table: Upper half-space / Upper Davidson (UHS), Lower Davidson (LD), First Red Bed (FRB), Hubbard (Hub), Upper Dawson Bay (UDB), Lower Dawson Bay (LDB), Second Red Bed (SRB), Prairie Evaporite above mine (PE^+), Prairie Evaporite below mine (PE^-), Winnipegosis (Win), & Lower half-space / Ashern and lower (LHS).**

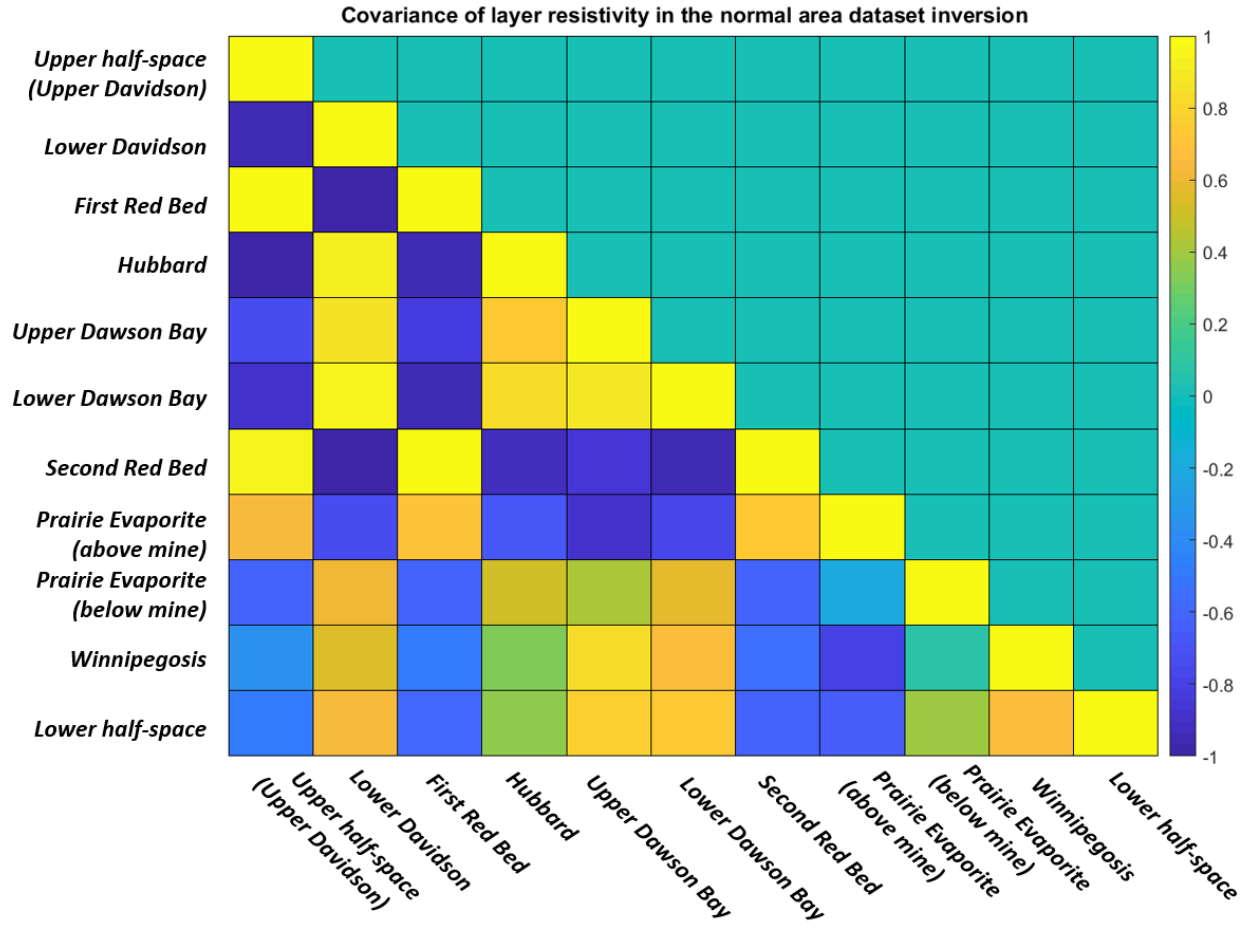

Figure 4.50: **Results of covariance analysis on the inversion paths the resistivity parameters took in the inversion of the "normal" area. Yellow cells indicate a high positive covariance, and dark blue indicates a strong negative covariance.**

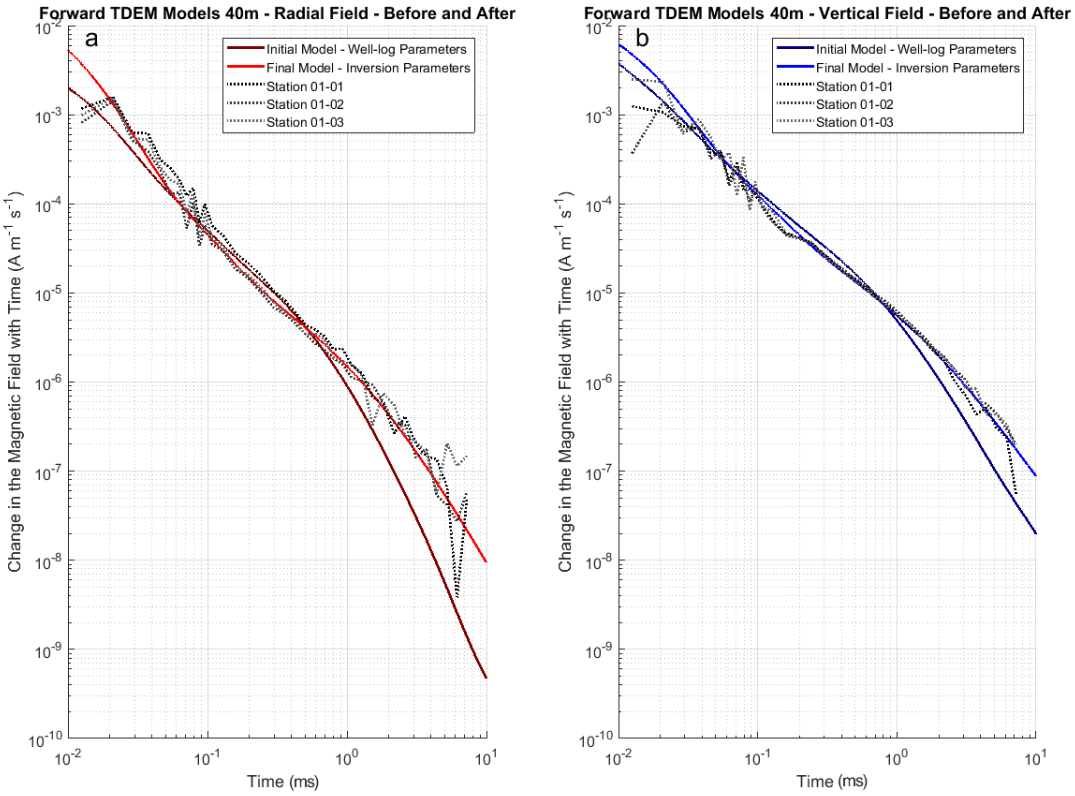

Figure 4.51: **Contrasting the forward models calculated using the parameters derived both from the well-log (starting point for the inversion) and from the final parameters derived from the inversion process. Transmitter/receiver separation at 40 m. Also shown are the decay curves from the TEM survey used in for this inversion process.**

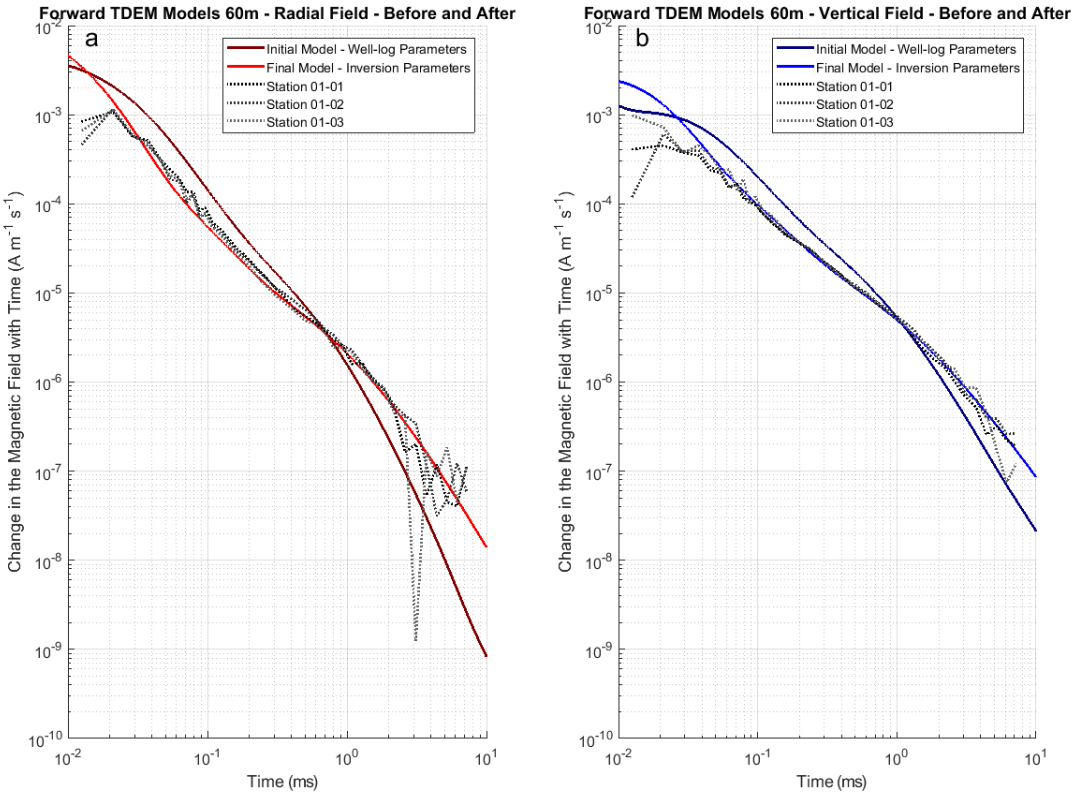

Figure 4.52: **Contrasting the forward models calculated using the parameters derived both from the well-log (starting point for the inversion) and from the final parameters derived from the inversion process. Transmitter/receiver separation at 60 m. Also shown are the decay curves from the TEM survey used in for this inversion process.**

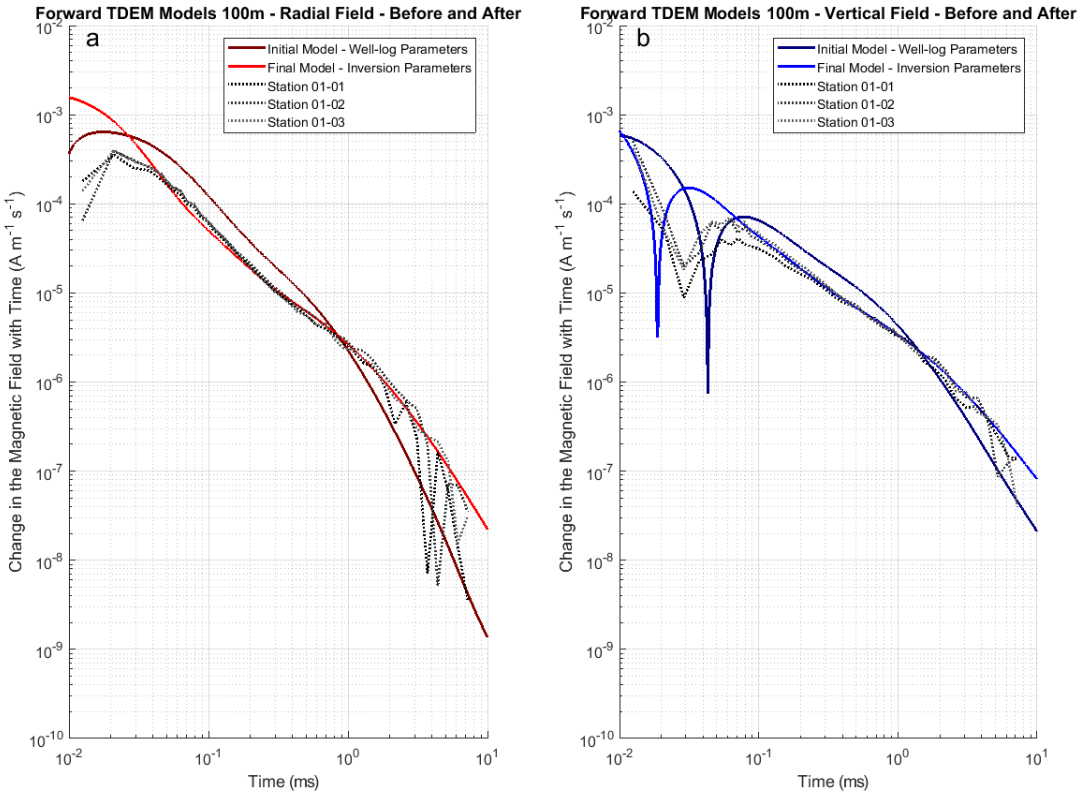

Figure 4.53: **Contrasting the forward models calculated using the parameters derived both from the well-log (starting point for the inversion) and from the final parameters derived from the inversion process. Transmitter/receiver separation at 100 m. Also shown are the decay curves from the TEM survey used in for this inversion process.**

area. The sensitivity was calculated from modifying each of the layer resistivities independently and calculating the resulting change in the time derivative of the magnetic field (here the time derivative of the magnetic field is represented by Ψ). The sensitivity value (S) was normalized to the amplitude of the decay at each point in time to allow for comparison across all time-gates and signal amplitudes. As such the sensitivity equation (eq. 4.3) calculated a ratio change in the magnetic field time derivative per change in parameter value at each of the k-th time-gates. Each of the j-th layer resistivities in the model were perturbed individually by 25%. As such 11 different sensitivity calculations were made.

$$S_{j,k} = \frac{\frac{\Delta\Psi_{j,k}}{\Psi_{0,k}}}{\Delta\rho_j} = \frac{\frac{\Psi_{j,k}-\Psi_{0,k}}{\Psi_{0,k}}}{1.25\rho_j}. \tag{4.3}$$

Figure 4.54 shows the resulting sensitivity for each layer at specific time-gates (ranging from 0.032 ms to 1.778 ms). In general, the main trend is that with lower resistivity the layers maintain a higher relative sensitivity (making the porous carbonate and shale layers more sensitive than the salt layers). Other trends that appear include an increasing sensitivity with time in the layers above the Dawson Bay carbonates (including the Upper Dawson Bay), while the layers near mine and below appear to have a decreasing sensitivity with time.

4.3.2 Two-layer Inversion Profile of the Dawson Bay

In order to determine plausible explanations for the signal variation measured across the survey profiles, one technique was developed to sweep through each dataset individually allowing only two parameters of the model to vary in the inversions: the lower and upper Dawson Bay resistivities. This technique, of course, relies heavily on the starting point derived in the earlier section, and equally depends on our assumption that the primary source of the conductive response we observed is exclusive to the Dawson Bay. However, it does give us insight into the degree of influence the Dawson Bay layers have into the misfit, as well as the amount of parameter change over the area of the survey - under certain background and geological assumptions. Several benefits of this method include speed of

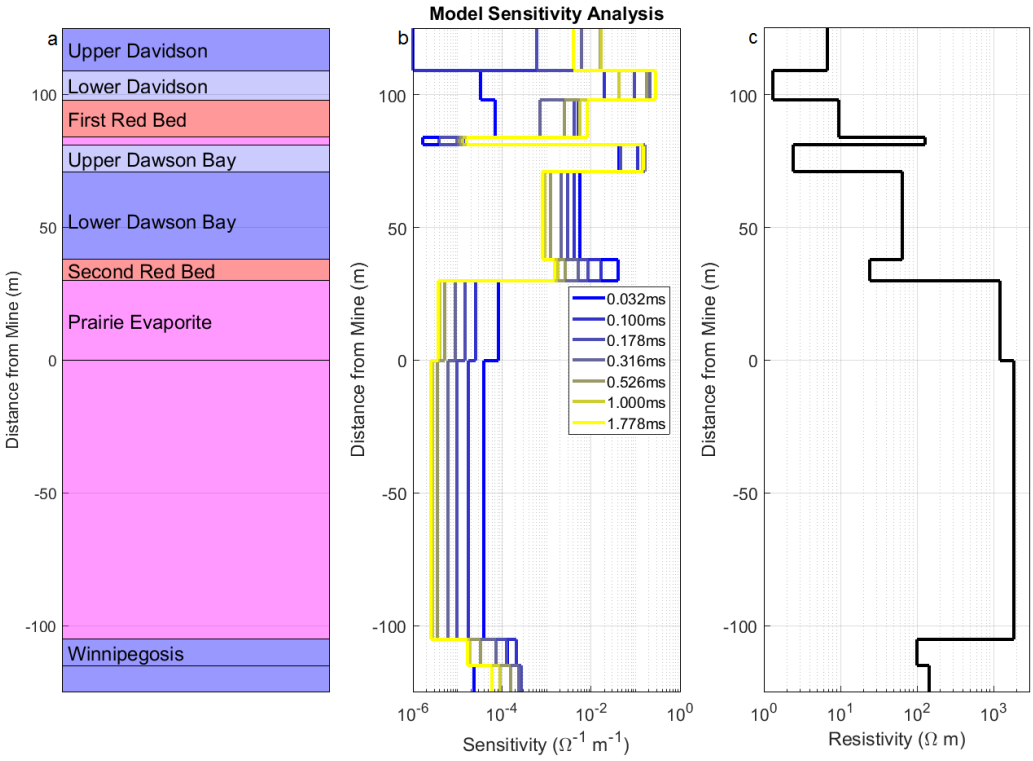

Figure 4.54: **Sensitivity analysis of the inversion products of the normal near mine parameters. Sub-figure a) shows the labels of the layers, b) the sensitivity at several time-gates, and c) the initial resistivity of each of the layers. The sensitivity was calculated by taking the normalized change in the magnetic field time derivative over the change in the resistivity of each layer.**

operation - each inversion set took a fraction of the time of an 11-layer parameter inversion - and the need for a damping control on the parameters dropped precipitously (leading to a value of 0 being used for C).

Figures 4.55 and 4.56 show the results of the two-layer inversion on the datasets from the north and south profile lines respectively. These show a drop in the resistivity of both of the Dawson Bay layers, as well as a substantial improvement in the misfit. There is a small increase in the final objective function (misfit) in the anomalous area over the final misfit in the normal area. This seems to suggest that the relatively simple conductive two-layer model does not - in isolation - completely explain the signal change in the anomalous area; however, the improvement in the misfit is still significant.

The north line at 100 m Tx-Rx separation was the one dataset in the inverse models on either line that produced very different results. In this dataset inversion, the Upper Dawson Bay resistivity parameter behaved exactly as the other two separation datasets on the north line, as well as the datasets on the south line (100 m Tx-Rx separation readings were not taken on the south line). However, the Lower Dawson Bay resistivity parameter behaved erratically and possibly contributed to producing a higher misfit in both the inversion end result and starting models. This is possibly due to 2D features in the geology altering the signal to a degree our 1D models cannot replicate. Or it is possible that since the inversion was not optimized to effectively deal with the early time signals the 100 m Tx-Rx separation results feature that the results were inevitably compromised. This suggests that the methods used in the inverse modelling for this project are possibly best reserved for late-time signals only.

4.3.3 Eleven-layer Inversion Profile

The other technique that this project used to invert datasets in the anomalous and transitional areas was to apply the same 11-layer method that was used on the "normal" area on each of the 40 m transmitter/receiver separated datasets on both survey lines. This included using the same damping coefficient ($C = 0.0039$) as the one used in the normal area as shown in section 4.3.1. This somewhat artificially tied the parameters in each dataset to the parameters found in the well-log. Since the well-log is assumed to be in a "normal"

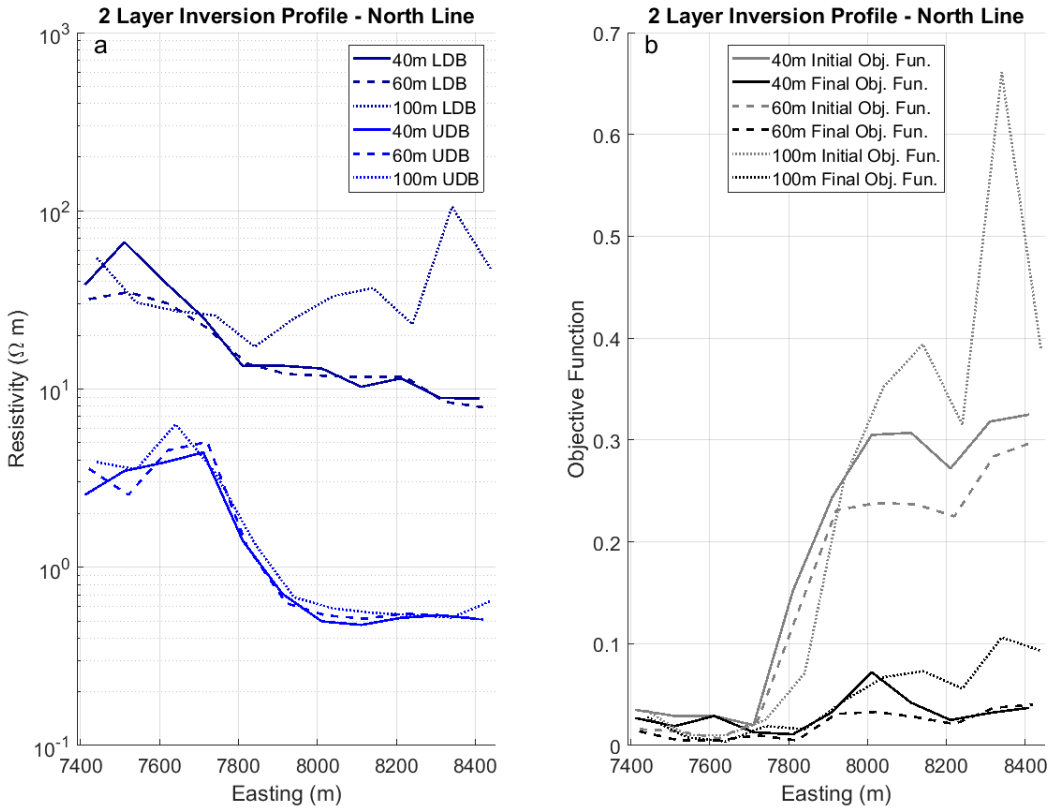

Figure 4.55: **Figure detailing the results of the two-layer inversion on the north profile line. Figure a shows the final parameters derived by the inversions at each station. Figure b shows both the initial and final objective function values at each station.**

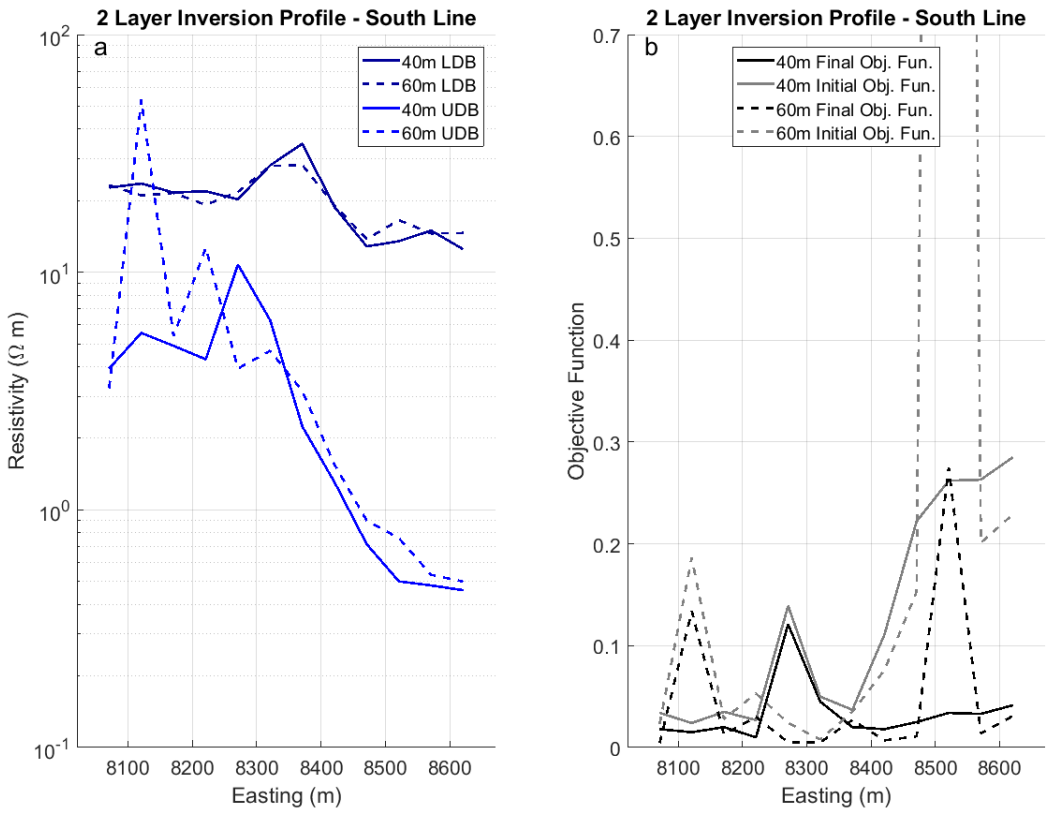

Figure 4.56: **Figure detailing the results of the two-layer inversion on the south profile line. Figure a shows the final parameters derived by the inversions at each station. Figure b shows both the initial and final objective function values at each station.**

area, the damping control had no consideration of the fact that the area was anomalous - or what features would be considered anomalous. As such, the forward models that these inversions produce are somewhat biased toward the "normal" conditions derived from the earlier well-log analysis. No parameter was weighted differently than any other. While some geological layers are far more likely to vary than others (for example, carbonates are much more susceptible to porosity changes than shale bodies), such unequal weighting was not introduced because I did not want to direct the parameter results any more than absolutely necessary.

Figures 4.57 and 4.58 show the final products for these 1D inversions. Note that this is a series of 1D inversions stitched together to form a 2D cross-section. The mine layer is at 0 m and vertical distance from the mine layer is on the y-axis. Figure 4.59 shows the same results in graph form. Included on this figure is the final component values for the objective function - both the residual and the damping terms. As one would expect, there is an increase in both the controlling damping term and the residual in the anomalous area. However, this increase is not extremely high - indeed, it appears that there is a higher objective function in the transition area than in the anomalous area, especially on the north line where the line extends deeper into the anomaly. Given that no parameter was guided to vary in any direction any more than any other in this inversion, it is very interesting to observe that among the parameters that appear to have a spatial link to the anomalous area, the ones that have a conductive relationship are the two Dawson Bay layers. The Lower Dawson Bay drops from about 50 Ω m on the north line and 43 Ω m on the south line to around 19 Ω m on the north line and 14 Ω m on the south line. The Upper Dawson Bay drops even more precipitously, from 4.0 Ω m on the north line and 3.8 Ω m on the south line to about 0.54 Ω m on the north line and 0.51 Ω m on the south line. There were some other spatial relationships that are noticeable. Both the upper half-space (Upper Davidson) and the Lower Davidson layers had an increasing resistivity trend with the survey lines. Other than those four layers, there did not appear to be any consistent spatial relationship between the anomalous area and the inverted parameters. The layer resistivities that demonstrated a trend with the profile lines (either positive or negative) are bold in figure 4.59.

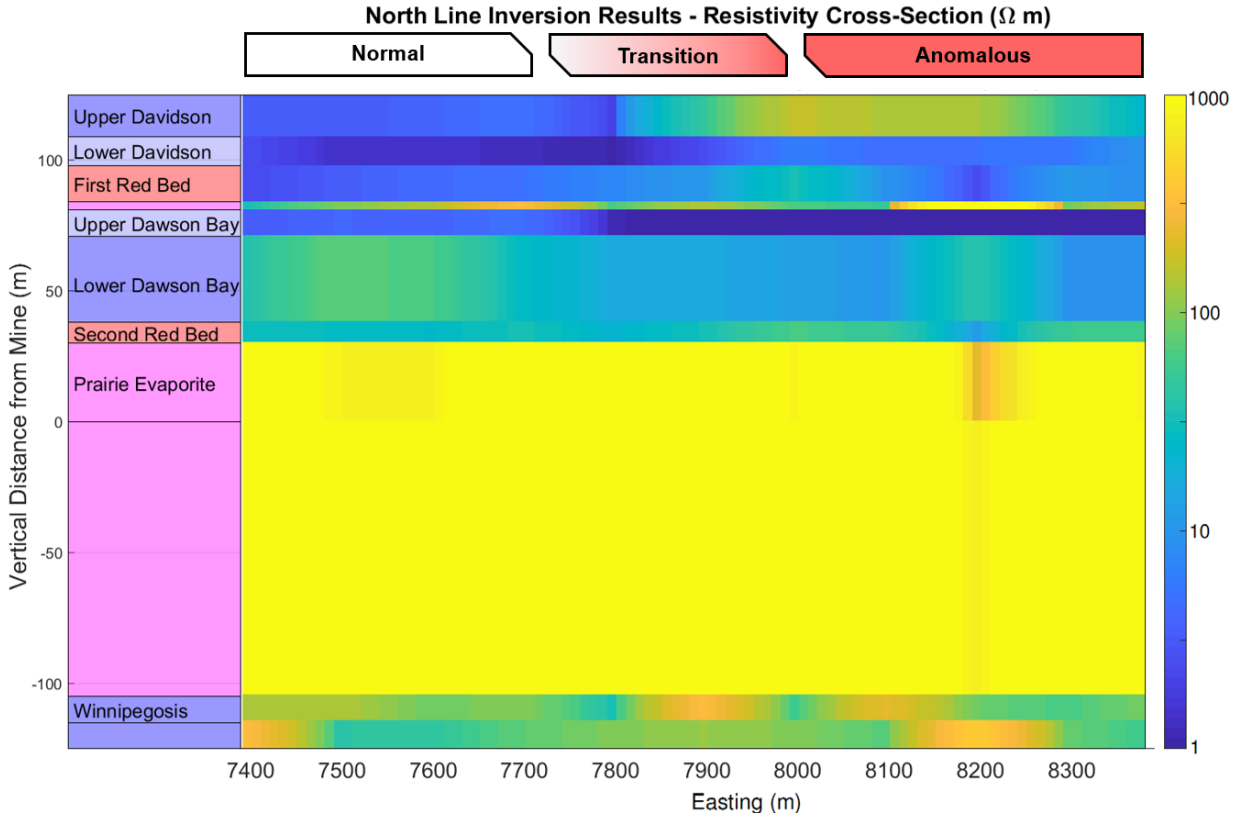

Figure 4.57: **Cross-section of the resistivities found by the inversions on each 40 m Tx-Rx datasets on the north line. Note this figure represents a series of eleven 1D inversions. The spaces in-between each inversion are linearly smoothed and interpolated.**

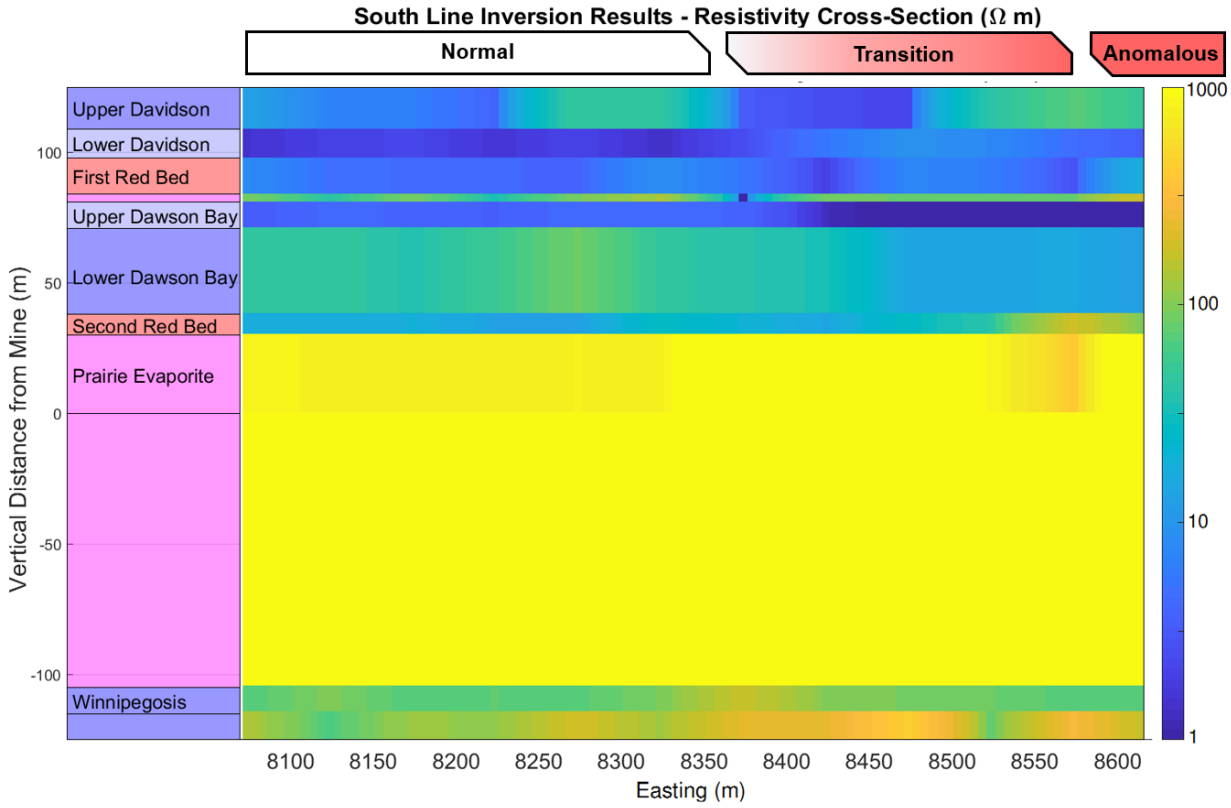

Figure 4.58: **Cross-section of the resistivities found by the inversions on each 40 m Tx-Rx datasets on the south line. Note this figure represents a series of twelve 1D inversions. The spaces in-between each inversion are linearly smoothed and interpolated.**

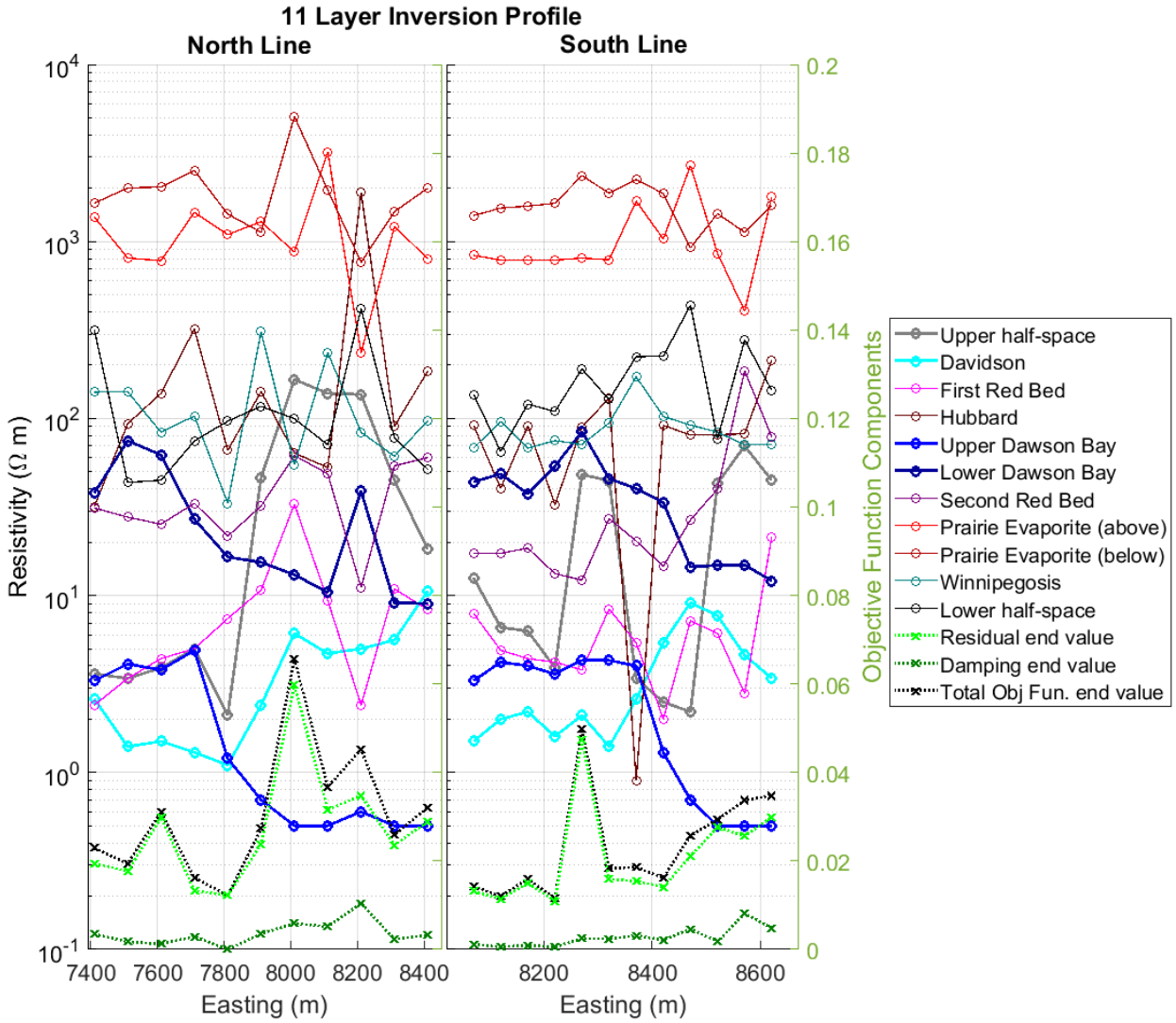

Figure 4.59: **North and south line profiles the resistivities found by the 11-layer inversions on 40 m Tx-Rx datasets (left y-axis). Also plotted are the components in the final objective functions for the inversion - both the residual and damping terms (right y-axis).**

4.3.4 Comparing Inversion Results and Forward Models

Figure 4.60 shows the results of the 40 m transmitter receiver separated dataset inversions on both profile lines using the 2-layer and 11-layer methods described in the earlier sections. Since the 2-layer inversion only had two varying parameters and had no damping term applied, only the Upper and Lower Dawson Bay resistivity and the residual are compared across the profiles. The results show an extremely high correlation between the two parameter sets, including the end value residuals, all along each of the profile lines. This came as a surprise as both methods approach the problem in fairly different ways. While the 11-layer inversion did tie the parameters to initial values, they were the values derived from the well-log analysis and were not the same values the 2-layer inversion used for the surrounding layers. Figures 4.61 and 4.62 show various radial and vertical time decay forward model results using the final inversion products from the two techniques. The a) sub-figures show the 11-layer inversion end case forward models and the b) sub-figures show the 2-layer inversion end case forward models.

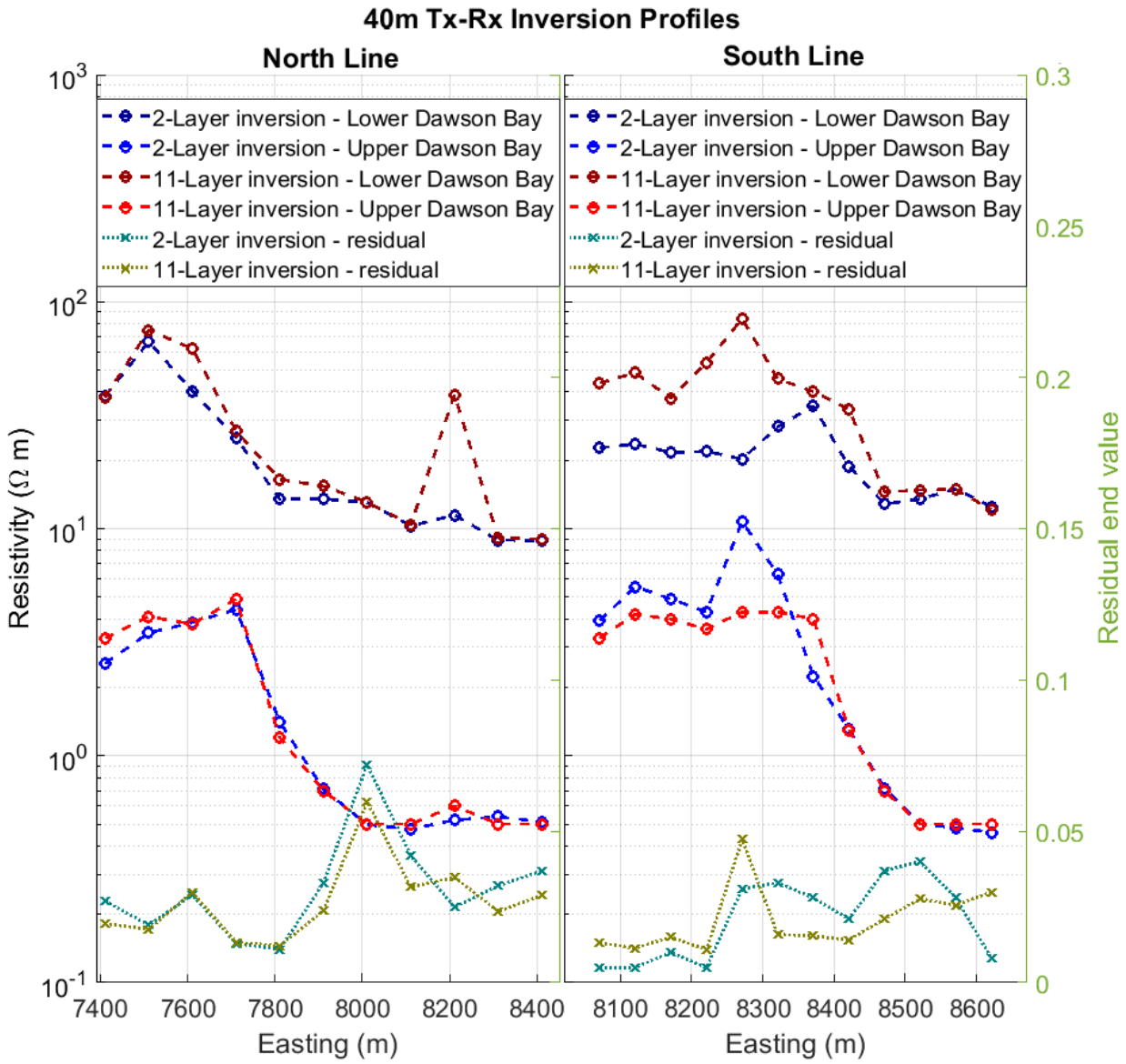

Figure 4.60: **Comparison between the 2-layer and 11-layer inversion results on the 40 transmitter-receiver separation datasets. The left y-axis plots the resistivity products, while the right y-axis plots the residual component of the final misfit value.**

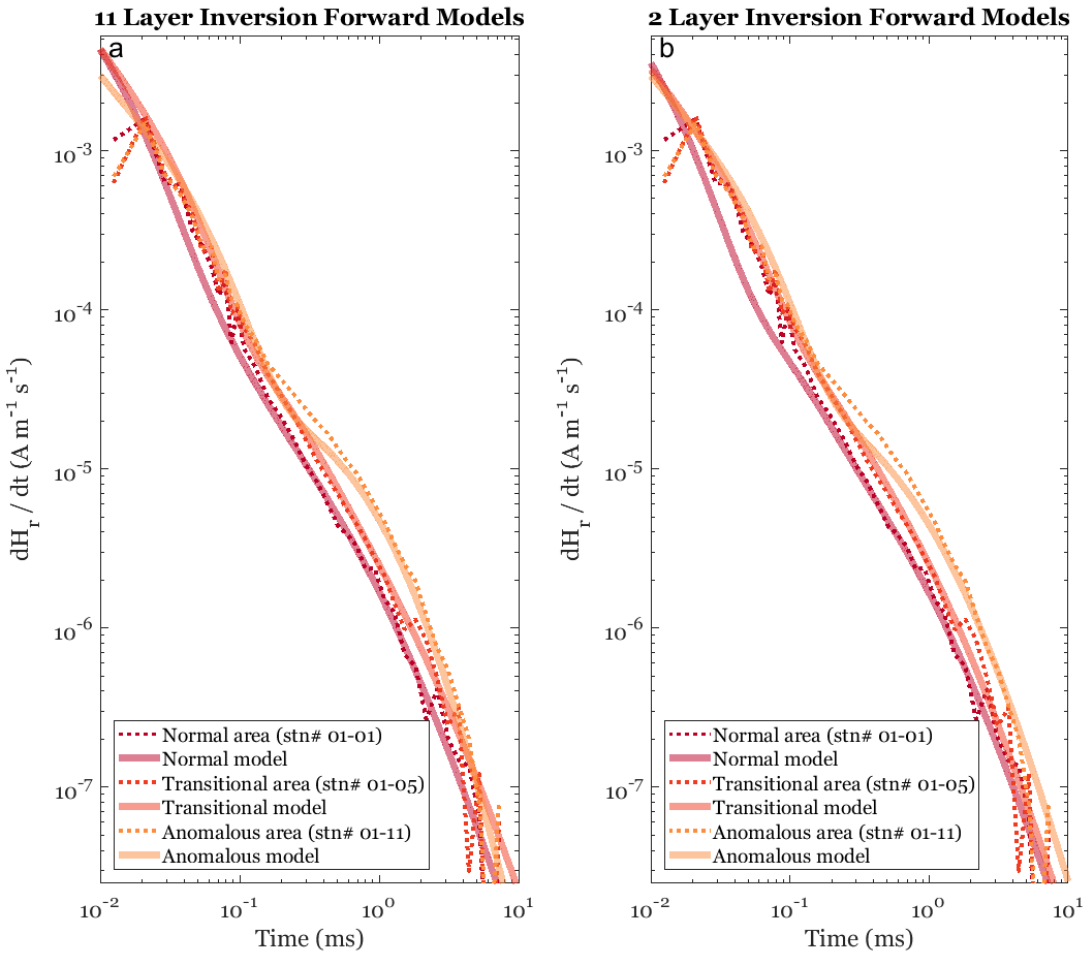

Figure 4.61: **Radial field time-domain EM Forward models using the inversion products produced from the two different inversion methods. a) shows the 11-layer inversion and b) shows the 2-layer inversion. TEM survey results from stations in three different areas of the survey - on the north line - are depicted. Station 01-01 represents normal conditions, station 01-05 represents the transition zone, and station 01-11 represents the anomalous conditions. Forward models from each of the inversions performed on these datasets are also depicted.**

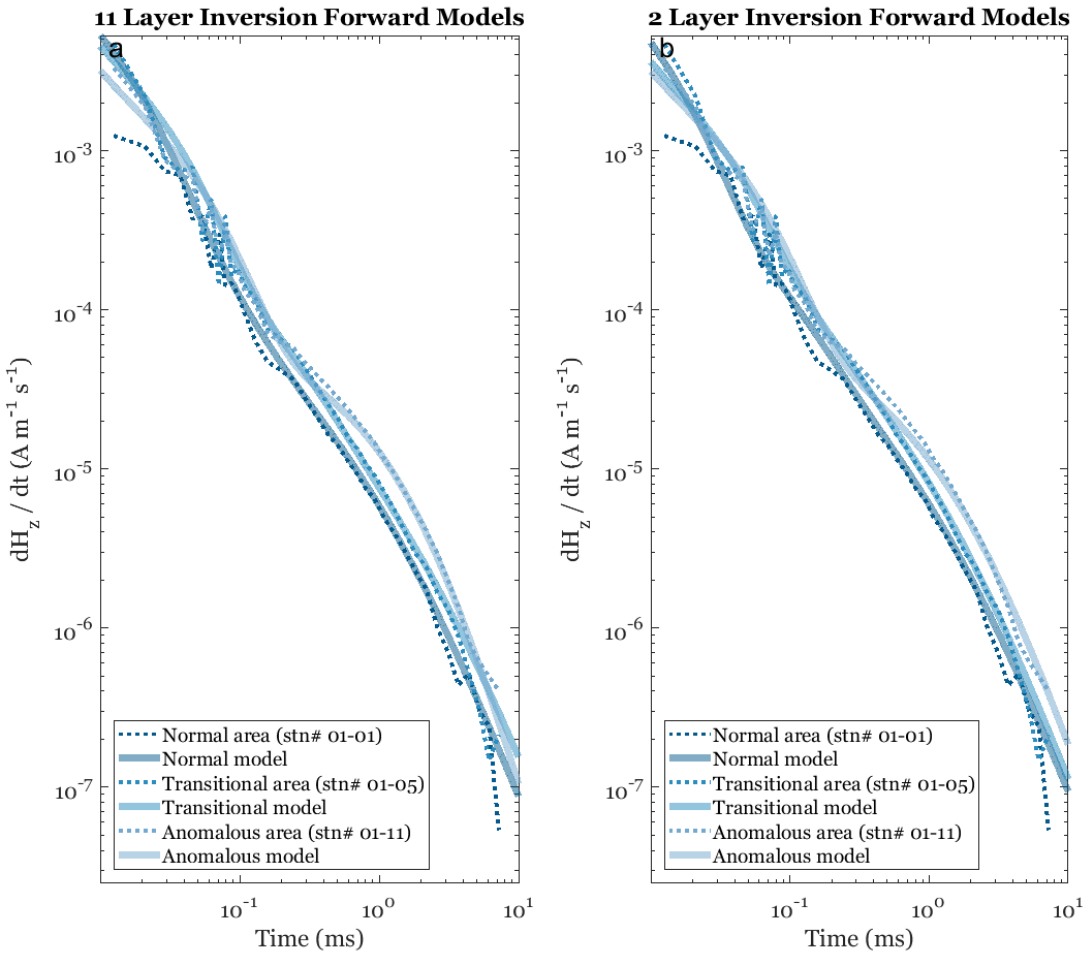

Figure 4.62: **Vertical field time-domain EM Forward models using the inversion products produced from the two different inversion methods. a) shows the 11-layer inversion and b) shows the 2-layer inversion. TEM survey results from stations in three different areas of the survey - on the north line - are depicted. Station 01-01 represents normal conditions, station 01-05 represents the transition zone, and station 01-11 represents the anomalous conditions. Forward models from each of the inversions performed on these datasets are also depicted.**

Chapter 5

Conclusions and Discussion

This chapter will outline the scope of the problem, specifically focus on the elements of the problem relevant to this thesis; detail conclusions based on the results derived from the forward and inverse modelling, as well as the data collected over the 2017 in-mine survey included in this project; and, finally, suggest areas of future exploration on the topic, specifically relating to future surveying, 3D forward modelling, and suggested improvements to the inversion algorithm used for this project.

5.1 Summary of the Problem

The core of this project was designed around developing geophysical techniques - specifically, time-domain electromagnetics (TEM) - for remote detection of anomalous water bodies near underground conventional potash mines. The elements that this project focused on to address this goal included a wide degree of computer modelling - both forward and inverse - and analysis in-mine survey TEM data collected in an area of a suspected anomaly. This project relied extensively on multidisciplinary work related to this problem over the years, including older and more recent geophysical surveys, core and well-logs from downhole surveys, and earlier modelling work performed by other researchers in order to both guide geological understanding and to properly direct modelling efforts.

Geologically anomalous bodies near mines, including the water bearing ones, are varied, and several of these have been the focus of elements of this project. However, the primary focus and bulk of the work was placed on detecting anomalous carbonate members in the Dawson Bay formation. Detection of carbonate member anomalies is challenging for both the

position of the Dawson Bay - situated as it is between conductive shales and on the other side of a highly resistive salt layer - as well as for the expected lower resistivity contrast between wet or porous carbonate and dry or tight carbonate. When water anomalies are located in the salt near the mine, the physical contrast is extremely high and a wide variety of geophysical tools have been known to provide delineation of such features.

5.2 Study Conclusions

Effective detection of anomalous geological features through geophysical methods has two primary controls. One is the sensitivity and resolution that the geophysical surveying equipment is capable of. The other is the degree and kind of physical property variation in the geological lithology. The second issue is a complex question and is the focus of a large degree of the computer modelling in this project. The first issue, on the other hand, relies to some degree on the parameters of the survey and to a larger degree on the quality and power of the survey equipment. Extensive surveying will be required to answer this question in full; however, with the given equipment and parameters used for the survey that was the focus of section 4.1, it is shown that time-domain electromagnetics can be collected in a full-space environment to effectively delineate a target located relatively close to a mine.

The issue of equipment sensitivity and resolution was addressed in large part by the success of the in-mine survey. Though, beyond selection of the survey area, the only elements that can be controlled by survey operators are the survey equipment and the operational parameters. Despite the restrictions imposed on in-mine TEM surveys when it comes to transmitter power and transmitter loop size, the survey produced extremely repeatable responses across both survey lines, as well as a very large change in response when surveying under the expected geological anomaly. The test for the repeatability of the TEM survey can partly be demonstrated by observing the consistency of the measurements across the profile lines. This consistency can especially be seen in figures 4.14, 4.15, 4.16, 4.17, and 4.18. Across most of the time-gates measured the signal appears highly consistent - particularly those time-gates that were most sensitive to the geological changes (roughly between 0.1 and 2.2 ms). The elevated response in the anomalous area appeared to peak around 0.54 in log space or 3.5 times higher than the background levels and around 0.35 in log space

or 2.5 times higher in the vertical field response. The peak response also occurred slightly earlier in time in the radial field (around 0.80 ms) than in the vertical field (2.2 ms). The fluctuation (or noise) in the relative signal hovered around $\pm$1.8 times the background - or 0.075 in log space. This shows that the measured values were highly repeatable with the survey equipment and parameters that were used - and that the anomaly was large enough to provide a significant target for the TEM induction technique.

Through a series of tests and predictive computer modelling done prior to the survey, it was determined that the signal from the target would arrive relatively early in time. This is due to a combination of the resistive environment as well as the proximal nature of the target (40-60 m, rather than hundreds of metres that are typical in mineral exploration TEM surveying). These issues are common in geophysical applications in environmental or engineering fields. It was also observed in modelling that the radial component of the change in the magnetic field would be very useful in analysis. Commonly, the radial field is measured when conducting surveys on the surface of the Earth. The contrast between the sub-surface resistivity and the approaching infinite resistivity of the atmosphere cause the magnetic field to tilt in direction as the current diffuses through the environment. This produces a sizable and very diagnostic radial field response. In-mine surveys previously performed focused on measuring the vertical field - sometimes exclusively. This was likely done as the field in a homogeneous full-space exhibits no radial field in the plane of the transmitter. As such it could be assumed that the radial field response would be of minor diagnostic value when surveying underground. However, due to the large size of the salt of the Prairie Evaporite below the survey, as well as the resistivity contrast between the salt and the shales and carbonates, a significant radial field decay is observed in the basic computer models. This was later confirmed by the survey results. Challenges still exist in analyzing the radial field due to the high decay rate compared with vertical field measurements. This means that the radial component of the signal drops below the noise level earlier in time than the vertical component signal. The combination of computer modelling done in conjuncture with in-mine surveying, both in pre- and post-survey, proved to be highly effective in combination with one another.

A series of parameter sweeps were conducted in forward TEM computer models to get

an understanding of the expected amplitude of signal variation in a variety of geologically anomalous areas near potash mines in Saskatchewan (described in section 4.2). The geological anomalies that were tested included salt-back thinning above the mine, mounds or "banks" in the Winnipegosis below the mine, and increases in Dawson Bay porosity (simulated by decreasing the resistivity of the material). Separate model sweeps were done for the Dawson Bay for the case that only the lower carbonate member is influenced by the geological changes and for the case where both the upper and lower carbonate members were influenced. Each of these parameters were varied separately and compared against the baseline model. These baseline model parameters were constructed from a combination of well-logs and "normal" area inverse modelling results (described in section 4.3).

The results of these parameter sweeps indicated that for any mapping of the geological layers near the salt (either above or below the mine) early time measurements would be required. The peak variation in the end case anomalous model responses occurred very early in time (< 0.1 ms) and the amplitude variation was low. The parameter change for these models was 30 m to 15 m for the salt-back thinning and 10 m to 65 m for the Winnipegosis mounds. Of course, if these parameters were extended to the extremes, the amplitude of the variation in response would increase in kind. This preliminary modelling suggests that to investigate changes in the thickness of the salt near mine would require quite small transmitter-receiver separations along with very early time-gate measurements for an effective time-domain EM investigation.

For the Dawson Bay porosity parameter sweeps, the resistivity of the layer(s) were varied logarithmically by one order of magnitude. As described, two separate sweeps were performed: one varying the Lower Dawson Bay in isolation and one varying both of the Dawson Bay carbonate members. This was done as the degree to which each of the members of the Dawson Bay formation are influenced by the anomalous water bearing zones is somewhat ambiguous. The large lower carbonate member is normally tighter (lower porosity and water content) than the upper member, so it is reasonable to expect a significant change in response from this layer in areas where anomalous water content has been introduced in the Dawson Bay and in younger formations above. However, it is likely that this water content alters the other carbonate layers beyond just the Lower Dawson Bay. The resulting signal

contrast in the anomalous models - in both cases - produced a positive variation at earlier time-gates than the in-mine survey data produced. In the model sweep, however, where both carbonate Dawson Bay layers' resistivity were varied, the time at which the conductive response terminates is very close to the time-gate where the surveyed response in the anomalous area terminated as well. In addition, the response amplitude of the modelled conductive anomaly was very similar to the surveyed data amplitude as well - indicating that the chosen parameter change was not too extreme. This approach implies that the very simple forward model parameter sweep can be a fairly accurate approximation of the physical variations near mine. This is a process that can be quickly performed and is not a complex procedure. The only consideration is that the near-mine parameters in the surveyed area need to be well-understood and appropriate or else the forward model sweep will produce less reliable results.

Inverse modelling in this project took two approaches to offset the problem with over-fitting that a large number of parameters can introduce. For TEM inverse modelling, this problem is amplified by equivalency between parameters and the exceptionally low signal from resistive layers. This was observed in the inverse modelling process by the algorithm drifting in several layers to extremely high resistivity in the solutions. This problem was circumvented with two different approaches to inverse modelling. One was to severely restrict the number of parameters allowed to vary in the inversion. The other was to apply a damping term to the minimization algorithm within the inversion - flexibly tying the parameters to their starting values.

The first step in the inversion process was to define the "normal" near mine parameters in the survey area. This "normal" signal can be seen in the responses over most of the first four or five stations on the north line and the first six or seven stations in the south line. For this inversion, a damping term was tested for optimization at different magnitudes and applied to the algorithm. The parameters observed in the well-log (analyzed in section 3.4) were used as the starting values and the damping constraints. Radial and vertical field responses from three stations (01-01, 01-02, and 01-03) on the west side of the north profile line were used in the data inversion. These included datasets from 40, 60, and 100 m transmitter-receiver separations for a total of 18 datasets. This allowed a much more

smoothed or averaged combined dataset for determining the generic background resistivity profile. The final solution managed to drop the objective function to just over 2% of the initial objective function value when using the parameters observed in the well-log.

For inverting the stations over both profile lines, two approaches were used, following the two techniques outlined previously. One was to reduce the number of parameters in the inversion to just the resistivity of the Dawson Bay carbonate members, and the other was to retain the damping system used for determining the set of background resistivity parameters and apply it across the surveyed lines. One negative to using the first method is that it relies heavily on operator *a priori* understanding of the anomalous area that is being surveyed. Assumptions are required as to which specific layers - and which parameters - are changing over the length of the survey. While this method was relatively simplistic, it dramatically reduced operating time of the inverse modelling algorithm and prevented almost all of the runaway parameter problems elsewhere encountered. The second approach required a reliable set of starting parameters, as well as establishing the most effective damping coefficient. A low value would allow the parameters too much leeway and over-constraining with a high coefficient would lead to the parameter products being too much controlled and directed by the operator.

The first approach to inverting the entire length of surveyed stations on both lines relied on the assumption that the geological anomaly over which the survey operated was locally tied to the Dawson Bay carbonates to a sufficiently large degree that the number of changing parameters could be reduced to just the resistivity of the lower and upper Dawson Bay carbonates alone. This inverse model resulted in a large resistivity drop in both layers - but even more extremely in the thinner upper Dawson Bay member - over the length of both survey lines. On the north line (which was the longer surveyed line and the one which stretched the farthest into the anomaly), the resistivity drop over the length of the survey was from around 38 Ω m to 8 Ω m for the Lower Dawson Bay member, and 4 Ω m to 0.5 Ω m for the upper member. On the south line, the Lower Dawson Bay member dropped from around 23 Ω m to 12 Ω m, and the upper member dropped from about 4 Ω m to 0.5 Ω m. The improvement on the misfit between the parameters used for the "normal" area and the ones solved by the inverse model for the anomalous area were around 11% to 14% of the original

misfit. The end solution misfit in the anomalous area was higher than in the "normal" area - especially for the 100 m transmitter receiver separated data - which implies the simple two-parameter approach did not explain the anomaly in its entirety. However, given the large improvement in the objective function, this simple inverse modelling approach did account for a large portion of the signal change with only a few parameters being introduced.

The second approach tied the set of resistivity parameters for all eleven geometric layers near mine to the ones determined from well-logs. It used the same procedure as the one used for determining the "normal" resistivity profile. In this case, only the 40 m transmitter-receiver separated datasets were used. These datasets were inverted individually, making this attempt at inversion one-dimensional. There are shortcomings for this method. For one, it is quite computationally exhaustive (eleven parameters). For another, it does not allow parameters to vary from their assumed background values, making the solution set that the inversions arrive at in the anomalous areas not as extreme as they most likely are in reality. Despite these shortcomings, this method produced highly interesting results. An effort was made by the author to not direct the inversion in any way. As such, each layer was equally allowed to vary (for example, carbonates were not penalized less than shales). Even with this, both Dawson Bay carbonates demonstrated significant resistivity drops over the length of both profile lines. The lower Dawson Bay demonstrated a decrease in resistivity from around 40 Ω m in the "normal" area to 9 Ω m on the north line and 44 Ω m to 12 Ω m on the south line. The upper Dawson Bay demonstrated a decrease from 3.3 Ω m in the "normal" area to 0.5 Ω m in the anomalous area on both lines. These results are extremely similar to the two-layer, unconstrained inversion for both of these layers. This is in spite of the large differences in the inversion design for both methods. The only other relationship discovered through this inversion technique between the solved parameters and the length of the survey lines was the upper half-space layer. This layer represented the upper Davidson carbonate and above. The layer maintained a relatively consistent positive relationship with the length of the surveys (i.e. resistivity went up in the anomalous area). The resistivity of the upper half-space increased from around 5 Ω m to around 40 Ω m - or even higher in the transitional areas. One possible explanation is that the damping term for the upper half-space was set at 44.4 Ω m. The background resistivity inversion determined a much

higher conductivity in the layer. By decreasing this in the anomalous and transitional areas, the inversion decreased the penalty for that layer in the algorithm.

5.3 Future Work

For future study on this topic, I will divide it into two broad sections of discussion. On the one hand, there is the practicality of performing these types of surveys in-mine. The more data that can be collected and compiled the more of an understanding can be developed of the sensitivity of geophysical techniques - specifically, TEM - to near mine lithological changes. This is primarily a technical and engineering problem, of course. But projects such as this - especially from an academic perspective - bring a different set of considerations and goals to TEM analysis; shifting the focus from short term engineering considerations to long term scientific inquiry. This longer term analysis brings with it added value across multiple projects that can offset some of the costs inherent in acquiring such data in the first place. As such the more in-mine geophysical data - TEM and other - that can be shared, analyzed, and saved for posterity between industry and academia the better - especially since such data is historically sparsely collected, difficult and expensive to acquire, and often not shared widely or even lost over time.

One very important future area of research would be performing TEM surveying and computer modelling in northern Saskatchewan potash mines, such as those near Saskatoon. The physical properties of the lithology near northern mines is markedly different than that of southern mines (the area of this paper). These differences include but are not limited to thinner (and generally more resistive) Dawson Bay carbonates, thinner salt-back coverage, and a non-porous, non-conductive Lower Davidson carbonate member. The three features of importance to TEM are the more proximal and thinner nature of the target body (Dawson Bay) and the higher resistivity in general in the areas of northern mines. All of these features will push back in time the signal from any sources in the Dawson Bay. This will make acquiring the full time-domain waveform more challenging - as well as potentially having a smaller amplitude due to the thinner Dawson Bay member. This makes broadening the areas of focus in this subject to include more potash mine environments a worthwhile and potentially useful endeavour for both industry and academia - as well as for geophysical

instrumentation developers.

From a modelling perspective there are a number of avenues to explore. The first and foremost would be creating full 3D near-mine EM forward models. By allowing the EM model to include geometric property variation in three-dimensions, several advantages are brought to the analysis. These include developing an understanding of the effects of 3D geometry on the radial and tangential EM decays in full-space environments. These horizontal fields are strongly influenced by property variation orthogonal to them. In the case of the radial field, changes in decay response is produced through the variation in resistivity in horizontal layers above and below the signal, even in the full-space of a potash mine. However, 3D modelling would allow analysis to note variation in the magnetic radial field time decay that cannot be purely explained by variation in resistivity of the vertical layers. This might be highly valuable for analysis especially of areas of transition where the lithological properties are in flux spatially. In addition, including 3D features will allow for analyzing the tangential field time decay signal. In 2D-axisymmetric analysis, for a vertical signal source, the tangential field is zero in all locations. Analyzing the tangential field decay can be useful in areas where a mine panel does not penetrate an anomalous area at a near orthogonal direction. Such highly acute angled (or oblique, if you prefer) surveys to anomalous areas would extend the transitional zone along the surveyed profile, as well as, theoretically produce a peak tangential field in the boundary area. The amplitude of this signal needs, of course, to exceed the noise level in the instrumentation used to be measurable and of any value. As such, more predictive computer modelling would be of high benefit for this area of research. The survey analyzed in this project did perform tangential field measurements on the south profiled line. This line was thought to cut the anomaly at an angle less than 90 degrees. While it seems possible that there may have been a small signal due to this feature in the tangential field, the noise level was exceptionally high and made analysis unreliable. An additional feature to consider when the signal is that low is the orientation of the receiver, which in the 2017 survey was only positioned by eye, as well as the presence of non-survey equipment or metal nearby. Certainly, although evidence suggests that lithology near potash mines is sufficiently 2D that radial and vertical field measurements are by far the most valuable for analytical purposes, additional modelling would still be highly beneficial.

In terms of inverse modelling, several possible routes could be taken to improve the process. For one, more stringent tests could be run on the datasets to determine the level of information content. For another, construction of the damping term in the inversion algorithm that controls the selection penalty of the values of the parameters could be refined. For this project, I used a penalty equally weighted across the logarithm of resistivity and geological layers, as well as universally tied to the highest quality log data I could find. However, more fine-tuned approaches could be used. One approach would be to include more stringent penalties for lithological layers that experience little porosity change such as shales, while decreasing the penalty for layers that are potentially more susceptible to porosity increase, such as carbonates and evaporites. This would perhaps make inverse models more geologically accurate. Another approach would be to only penalize large increases in resistivity, leaving decreases in resistivity with no penalty. This would allow the algorithm more freedom while focusing on restricting the much more troublesome resistive end of the spectrum. A third approach might be to rely on the inverse model results to generate (and regenerate) the parameter values for the damping penalty throughout the profile line. This would make each station's starting inversion parameters dependent on the previous station's products rather than on the well-log parameters. This would perhaps make the inversion results more consistent with itself over the length of a survey profile, while potentially also increasing the self-conformation bias following the inversion's first several algorithms. Ideally, such an attempt would be self-correcting in some way to reduce the effects due to bias - moving toward a 1.5D or full 2D inversion. Finally, other improvements to the inverse modelling could include some degree of weighting based on noise levels or by applying a smoothing filter on the higher noise time-gates. This would allow more of the time-gates to be included in the inverse models. Of more importance, however, is the early time polarity shifts in the 100 m Tx-Rx separation datasets. To properly invert parameters for this dataset, a moving window in time should be included such that the algorithm will be able to quantify improvements in placing the early time polarity shift while not requiring a near perfect match with the data. Since polarity shifts occur over a scale of microseconds with such rapid magnitude changes, inverting on a purely one-to-one difference at each time-gate in the algorithm proved to be too restrictive.

Appendix A

A.1 Frequency-Domain Forward Models

Frequency-domain electromagnetics (FEM) does suffer from limitations when compared with transient (TEM) systems These include the active primary magnetic field dominating the relatively weak secondary field, and additional noise introduced by the orientation and placement of the transmitter and receiver relative to one another. Despite this, FEM systems are still deployed quite regularly in applications related to ground-water mapping, and in various shallow earth engineering and archaeological areas of interest (Dentith and Mudge, 2014). As part of this project, some preliminary modelling was performed early on to judge the effectiveness of using FEM for determining near-mine features for potash mines. This work was not as thorough as would be preferred, and as such it has been moved to this appendix as a stub. It is strongly recommended that additional work be done in modelling frequency-domain EM signals to determine if a viable FEM product on the market would perform as capably as the TEM Nordic EM24 and Geonics TEM57-MK2 performed. Especially given the prevalence of FEM systems in other engineering applications performed around the world.

In analyzing FEM signals, there are two components that are considered. Both are tied to the secondary field that is produced by the Earth in response to the primary field from the transmitter. One of which is the amplitude of the response that is in-phase (IP) with the primary (or at 180 degrees with respect to the transmitter), and the other is the amplitude of the response that is out of phase with the primary (quadrature - or quad). In addition, since the the primary field is active during measurement it needs to be subtracted out of the measure signal. This primary field is entirely in-phase with the current in the transmitter,

so the quadrature component needs no correction in this regard. The measured signal is also usually normalized by the size of the transmitting signal, so as to allow measurements from multiple different FEM systems to be compared alongside one another. Equations A.1 and A.2 shows the calculation for the in-phase and quadrature components respectively.

$$\mathrm{IP}_{secondary} = \frac{\mathrm{IP}_{primary} - \mathrm{IP}_{measured}}{\mathrm{IP}_{primary}}. \tag{A.1}$$

$$\mathrm{Quad}_{secondary} = \frac{\mathrm{Quad}_{measured}}{\mathrm{IP}_{primary}}. \tag{A.2}$$

The first set of models looked at the thickness of the salt-back. The salt-back is the Prairie Evaporite rock above the mining horizon and below the Second Red Bed. Several models were created for this purpose, ranging the thickness of the salt-back between 28 m to 12 m. The 20 m model is contrasted with the median conditions (here 28 m are used) in Figure A.1. Each individual component is shown individually. It appears that the highest signal variation occurs between 10kHz and 100kHz. For the quadrature responses, the amplitude of the secondary field appears to be lower than the in-phase, but also the maximum variation occurs at lower frequencies. In general, these results suggested a very high frequency would be required to detect variations in salt-back thickness. For these calculations, the receiver was radially offset by 20 metres from the transmitter, with near zero vertical offset.

The second set of models look at resistivity variations in the Dawson Bay layers. A series of models were created to test the response to a harmonic dipole in a variety of resistivities for the Lower Dawson Bay (Burr Member). The resistivity varied between the expected value of 38.15 Ω m and 6.95 Ω m. The variation was small, less than 1% for most of the frequencies. The frequencies of max variation were much lower than the varying salt-back thickness models. The transmitter-receiver separation was 20 metres with only a small vertical offset.

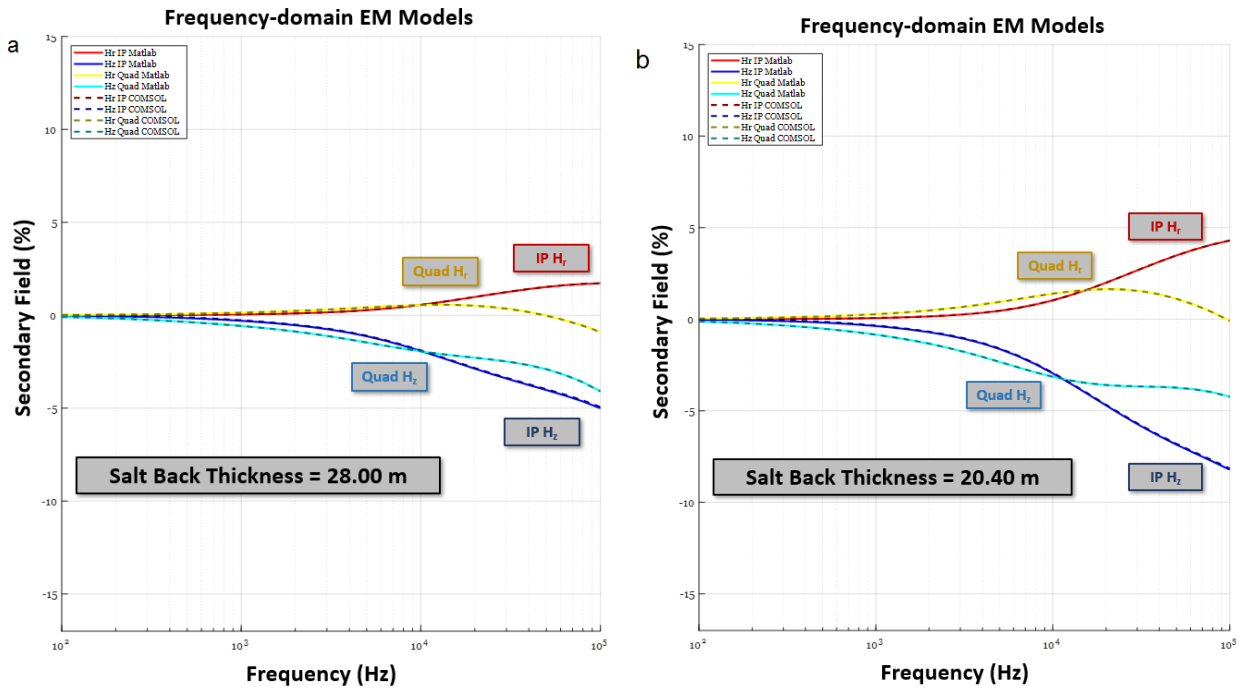

Figure A.1: **Contrasting the frequency response from varying the thickness of the salt-back from 20.40m to 28.00m. The normal conditions (28.00m) are in a). The blue/cyan lines are the vertical fields and the red/yellow are the radial fields. The darker dashed lines are the COMSOL results while the solid lighter lines are the Matlab results.**

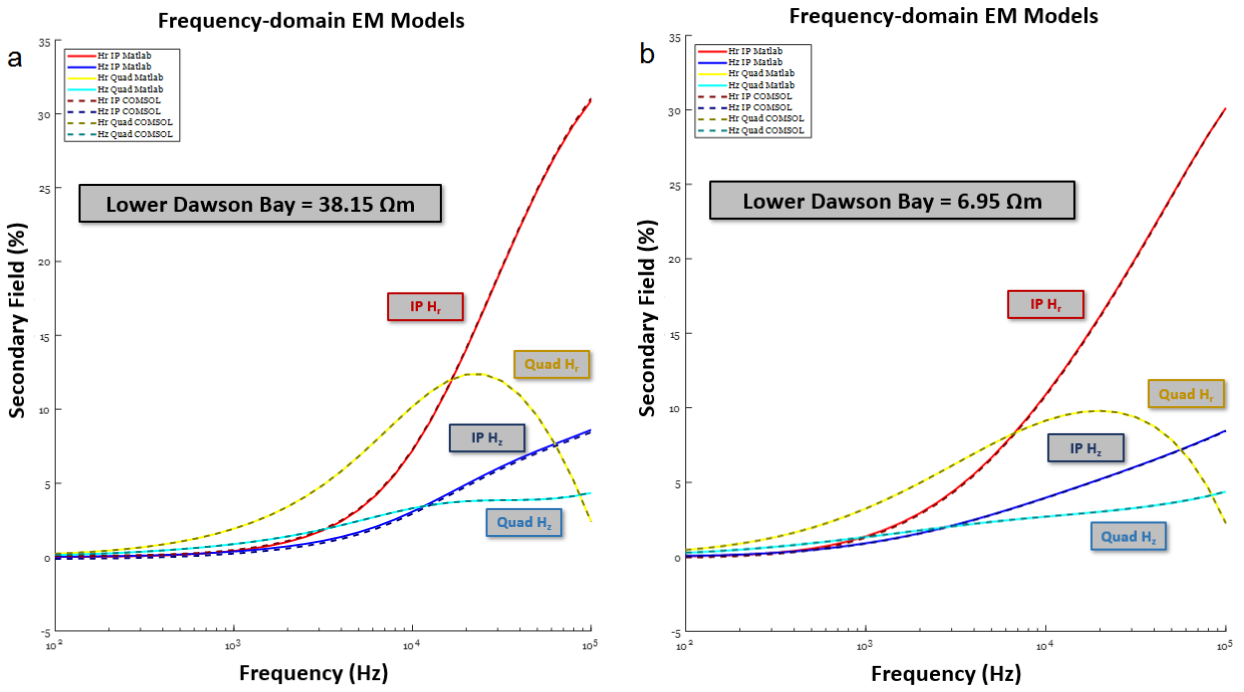

Figure A.2: **Contrasting the frequency response from varying the resistivity of the Burr member of the Dawson Bay from 38.15 Ω m to 6.95 Ω m. The normal conditions are in a). The blue/cyan lines are the vertical fields and the red/yellow are the radial fields. The darker dashed lines are the COMSOL results while the solid lighter lines are the Matlab results.**

References

Alhstrom, J. H. (1992), Geology And Diagenesis Of The Dawson Bay Formation In The Saskatoon Potash Mining District, Saskatchewan.

Butler, S., and G. Sinha (2012), Forward modeling of applied geophysics methods using comsol and comparison with analytical and laboratory analog models, *Computers & Geosciences*, *42*, 168 – 176, doi:https://doi.org/10.1016/j.cageo.2011.08.022.

Butler, S. L., and Z. Zhang (2016), Forward modeling of geophysical electromagnetic methods using comsol, *Computers & Geosciences*, *87*, 1–10.

Campbell, D. L., and D. V. Fitterman (2000), Geoelectrical methods for investigating mine dumps, in *Proceedings of the 5th International Conference on Acid Rock Drainage (ICARD 2000), Denver, Colo*, vol. 2, pp. 1513–1523, Citeseer.

Chouteau, M., G. Phillips, and A. Prugger (1997), Mapping and monitoring softrock mining, in *Fourth Decennial International Conference on Mineral Exploration edited by AG Gubins*, vol. 927, p. 940.

Das, U. C. (1995), A reformalism for computing frequency-and time-domain em responses of a buried, finite-loop source in a layered earth, in *SEG Technical Program Expanded Abstracts 1995*, pp. 811–814, Society of Exploration Geophysicists.

Duckworth, K. (1992), Detection of brine layers overlying potash mine operations by means of electromagnetic surveys, *Canadian Society of Exploration Geophysicists*, *28*, 109–116.

El-Kaliouby, H. M., S. A. Hussain, A. E.-R. Bayoumi, E. A. El-diwany, and E. A. Hashish (1995), Effect of clayey media parameters on the negative response of a coincident loop 1, *Geophysical prospecting*, *43*(5), 595–603.

Eso, R., D. Oldenburg, and M. Maxwell (2006), Application of 3d electrical resistivity imaging in an underground potash mine, in *SEG Technical Program Expanded Abstracts 2006*, pp. 629–632, Society of Exploration Geophysicists.

Ezersky, M., and I. Goretsky (2014), Velocity–resistivity versus porosity–permeability interrelations in dead sea salt samples, *Engineering geology*, *183*, 96–115.

Farquharson, C. (2006), Background for program em1dtm version 1.0, developed under the consortium research project: Time domain inversion and modeling of electromagnetic data, *Geophysical Inversion Facility, Department of Earth & Ocean Sciences, University of British Columbia (UBC–GIF), Vancouver, Canada*.

Farquharson, C., and D. Oldenburg (1993), Inversion of time-domain electromagnetic data for a horizontally layered earth, *Geophysical Journal International*, *114*(3), 433–442.

Farquharson, C., and D. Oldenburg (1998), Non-linear inversion using general measures of data misfit and model structure, *Geophysical Journal International*, *134*(1), 213–227.

Farquharson, C., D. Oldenburg, and P. Routh (2000), Simultaneous one-dimensional inversion of electromagnetic loop-loop data for both magnetic susceptibility and electrical conductivity, *GeoCanada 2000, Expanded Abstracts*, pp. 1–4.

Gendzwill, D. (1967), Electromagnetic measurement of salt formation thickness, *Physics Division - Saskatchewan Research Council*.

Gendzwill, D. (1978), Winnipegosis mounds and prairie evaporite formation of saskatchewan–seismic study, *AAPG Bulletin*, *62*(1).

Gendzwill, D. (1982), Report to potash company of america for electromagnetic survey of november, 1981, *Gendzwill Consulting LTD.*

Gendzwill, D., and N. Martin (1996), Flooding and loss of the patience lake potash mine, *CIM Bulletin*, *89*(1000).

Gendzwill, D., and B. Pandit (1980), A computer study of electromagnetic sounding in a potash mine, *Canadian Society of Exploration Geophysicists*, *16*, 45–55.

Gendzwill, D., and D. Stead (1992), Rock mass characterization around saskatchewan potash mine openings using geophysical techniques: a review, *Canadian Geotechnical Journal*, *29*(4), 666–674.

Gendzwill, D., and N. Wilson (1987), Form and distribution of winnipegosis mounds in saskatchewan.

Jiang, G., C. Jia, Y. Mu, and D. Chen (2015), Full space processing and 3-d interpretation technique of mine transient electromagnetic method, *Progress in Geophysics*, (5), 2164–2170.

Jin, J., and K. M. Bergman (1999), Sequence stratigraphy of the middle devonian winnipegosis carbonate-prairie evaporite transition, southern elk point basin, *Carbonates and Evaporites*, *14*(1), 64.

Kendall, A. (1976), Bedded halites in the souris river formation (devonian): potash mining district around saskatoon, *Summary of investigations*, pp. 84–86.

Kreis, L., P. Thomas, R. Burke, and S. Whittaker (2003), Devonian isopach and structure maps: Initial results of the iea weyburn co2 monitoring and storage project area, *Summary of Investigations*, *1*, 2003–4.

Krivochieva, S., and M. Chouteau (2002), Whole-space modeling of a layered earth in time-domain electromagnetic measurements, *Journal of Applied Geophysics*, *50*(4), 375–391.

Lagarias, J. C., J. A. Reeds, M. H. Wright, and P. E. Wright (1998), Convergence properties of the nelder–mead simplex method in low dimensions, *SIAM Journal on optimization*, *9*(1), 112–147.

Lane, D. (1959), *Dawson Bay Formation in the Quill Lakes-Qu'Appelle Area Saskatchewan*, Saskatchewan Department of Mineral Resources.

McNeill, J. (1994), *Principles and application of time domain electromagnetic techniques for resistivity sounding*, Geonics.

Murphy, E. C., S. H. Nordeng, B. J. Juenker, and J. W. Hoganson (2009), North dakota stratigraphic column, *North Dakota Geological Survey*.

Napier, S. (2007), Practical inversion of 3d time domain electromagnetic data, Ph.D. thesis, University of British Columbia.

Nelder, J. A., and R. Mead (1965), A Simplex Method for Function Minimization, *The Computer Journal*, *7*(4), 308–313, doi:10.1093/comjnl/7.4.308.

Raiche, A., and R. Gallagher (1985), Apparent resistivity and diffusion velocity, *Geophysics*, *50*(10), 1628–1633.

Salem, H. S. (2001), The influence of clay conductivity on electric measurements of glacial aquifers, *Energy sources*, *23*(3), 225–234.

Siemon, B., A. Ullmann, M. Vasterling, U. Meyer, W. Beer, and J. Plümacher (2010), Airborne electromagnetic survey of the groundwater mineralisation in the potash mining district of the werra river, ger, in *Near Surface 2010-16th EAGE European Meeting of Environmental and Engineering Geophysics*, pp. cp–164, European Association of Geoscientists & Engineers.

Smith, B. D., A. E. McCafferty, R. R. McDougal, and S. Church (2000), Utilization of airborne magnetic, electromagnetic, and radiometric data in abandoned mine land investigations, in *Proceedings of the Fifth International Conference on Acid Rock Drainage, Denver, Colorado*.

Wait, J. (1955), Mutual electromagnetic coupling of loops over a homogeneous ground, *Geophysics*, *20*(3), 630–637.

Wardlaw, N. C., and G. E. Reinson (1971), Carbonate and evaporite deposition and diagenesis, middle devonian winnipegosis and prairie evaporite formations of south-central saskatchewan, *The American Association of Petroleum Geologists Bulletin*, *55*(10), 1759–1786.